



**HAL**  
open science

# Deciphering the biological effects of ionizing radiations using charged particle microbeam : from molecular mechanisms to perspectives in emerging cancer therapies

Giovanna Muggiolu

## ► To cite this version:

Giovanna Muggiolu. Deciphering the biological effects of ionizing radiations using charged particle microbeam : from molecular mechanisms to perspectives in emerging cancer therapies. Cancer. Université de Bordeaux, 2017. English. NNT : 2017BORD0599 . tel-01820606

**HAL Id: tel-01820606**

**<https://theses.hal.science/tel-01820606>**

Submitted on 22 Jun 2018

**HAL** is a multi-disciplinary open access archive for the deposit and dissemination of scientific research documents, whether they are published or not. The documents may come from teaching and research institutions in France or abroad, or from public or private research centers.

L'archive ouverte pluridisciplinaire **HAL**, est destinée au dépôt et à la diffusion de documents scientifiques de niveau recherche, publiés ou non, émanant des établissements d'enseignement et de recherche français ou étrangers, des laboratoires publics ou privés.

THÈSE PRÉSENTÉE  
POUR OBTENIR LE GRADE DE  
**DOCTEUR DE**  
**L'UNIVERSITÉ DE BORDEAUX**

ÉCOLE DOCTORALE DE SCIENCE DE LA VIE ET DE LA SANTÉ  
SPÉCIALITÉ : BIOLOGIE CELLULAIRE ET PHYSIOPATHOLOGIE

Par Giovanna MUGGIOLU

**Deciphering the biological effects of ionizing radiations  
using charged particle microbeam: from molecular  
mechanisms to perspectives in emerging cancer therapies**

Sous la direction de : Hervé SEZNEC

Soutenue le :

Membres du jury :

M. MORETTO, Philippe  
M. POUGET, Jean-Pierre  
Mme RODRIGUEZ-LAFRASSE, Claire  
M. KANTOR, Guy

Professeur, Université Bordeaux  
Chargé de recherche, INSERM  
Professeur, Université Lyon 1  
Professeur, Université Bordeaux

Président  
Rapporteur  
Rapporteur  
Examineur



# Acknowledgements

Je tiens ici à remercier toutes celles et ceux qui ont contribué de près ou de loin à ce projet et qui m'ont permis de le mener à la fin. Que ceux que je pourrais oublier acceptent déjà mes excuses et soient assurés de toute ma reconnaissance.

Firstly, I would like to thank all members of the SPRITE project. They contributed to open my mind to other different fields. All along these three years, during numerous training courses shared together, I learnt a lot of things (scientific and not) from all of them.

Je remercie Philippe Moretto comme Directeur du laboratoire de m'avoir accueillie au CENBG et aussi comme membre du jury avec Mme Claire Lafrasse-Rodriguez, M. Jean-Pierre Pouget et M. Guy Kantor que je tiens à remercier pour le temps consacré à l'évaluation de ce travail.

Toute ma gratitude s'adresse à Hervé Seznec, mon directeur de thèse, qui m'a guidée, encadrée et encouragée tout au long de cette thèse. Je le remercie d'avoir accepté mon côté « italienne » un peu trop bruyant, dramatique et un peu espiègle. Merci beaucoup pour toutes les choses que tu m'as apprises ou que tu as essayées de m'apprendre comme par exemple l'organisation (ce n'est pas ta faute mais vraiment je ne peux pas être organisée, désolée). Il faut bien accepter que l'élève dépasse le maître (encore désolée si mes cellules sont bien meilleures que les tiennes). Je tiens également à remercier beaucoup Philippe Barberet pour toute son aide, sa patience (tu as dû me répéter des milliers de fois des concepts de base de physique sans me faire me sentir ridicule) et pour les bons moments partagés pendant les conférences. Je n'oublierai pas comment c'est possible de risquer la mort en traversant la route, de manger super-pimenté avec 40 degrés à l'extérieur et comment dire thé en chinois. Je n'oublie pas de remercier Guillaume Devès pour avoir essayé de me convaincre que la statistique est fondamentale et qu'on ne peut pas survivre sans le logiciel R. Peut-être qu'un jour je saurai l'utiliser ou peut-être tu vas encore recevoir mes mails en demandant de l'aide. Un très grand merci je le dois dire à Marina Simon, une super collègue. Merci pour toutes les journées, discussions, manips (diurnes et nocturnes) accompagnées de fous rires, blagues, moqueries et bien sûr aussi pleines de réflexions scientifiques (il faut bien dire ça dans une thèse). J'ai passé trois années au top aussi grâce à toi. Tu ne vas pas te débarrasser de moi très facilement ! Ana est née un jour avant moi donc tous les ans tu vas te rappeler de moi aussi. Tu es vraiment super et je te souhaite d'obtenir tout ce que tu désires le plus (sans oublier qu'il faut se dépêcher vu que tu as un certain âge).

Blagues à part, je vous remercie infiniment pour tout le bon temps que vous m'avez fait passer au CENBG.

Merci aux autres membres du groupe iRiBio que j'ai eu la chance de rencontrer : Sebastien Incerti, Claire Michelet, Christophe Champion et Douatsu, Florian, Nathanael pour l'accueil, la gentillesse et surtout les pause-café. À la nouvelle doctorante Eva, même si elle est physicienne, je souhaite une bonne continuation dans la recherche aussi s'il sera difficile de faire comme moi ! Reste souriante comme tu l'es.

Merci également à tout le personnel du CENBG surtout à Nathalie et Sylvie pour leurs explications concernant la bureaucratie française et celle du labo. Je voudrais citer tout le monde mais ça serait

trop long et surtout par peur d'en oublier (moi aussi j'ai un certain âge). Je dis simplement : MERCI à tous. À une personne particulièrement je voudrais adresser un merci et un bisou (elle a besoin toujours d'un contact physique) : Paola. Merci d'abord pour parler italien (parmi tous ces françaises), pour ta joie, pour parler plus fort que moi, pour les dîners après le boulot et tout le temps passé à rigoler mais aussi à discuter sérieusement. Merci Paola et bon courage pour la suite !

Une partie de ce travail n'aurait pas été possible sans la collaboration avec L'Institut Bergonié. Merci à Frédéric Chibon et à toute son équipe pour m'avoir accueillie et initiée à travailler avec les sarcomes. Merci à tous les doctorants et post-docs qui m'ont aidée, montrée et expliquée les fonctionnements de l'équipement du labo mais surtout pour les after-works passés devant des boissons réfléchissantes. Plus particulièrement, merci à Guy Kantor pour m'avoir offert l'opportunité de travailler avec le service de Radiothérapie de l'Institut Bergonié. Un énorme merci à Mikael Antoine pour avoir participé activement à toutes les manipulations d'irradiation et aux discussions sur les résultats obtenus.

À tous les amis rencontrés à Bordeaux pendant ces années, je n'ai pas de mots pour exprimer à quel point vous m'avez fait passer des très bons moments. Je vous dis merci pour toutes les choses que nous avons partagées et pour avoir rendu ces années à Bordeaux très agréables. J'ai appris beaucoup sur la culture grecque, arabe ou nord-africaine (comme vous préférez) mais aussi sur le centre de l'Italie. En réalité je retiendrai toutes les spécialités culinaires : le couscous, les bricks, les souvlakis, les courgettes, etc.... Merci pour tout ça !

Pendant ces années, je n'ai pas seulement « voyagé » à travers la Méditerranée. Une autre île est également rentrée dans ma vie : la Martinique. Camille, qu'est-ce que tu m'as appris pendant ces années de coloc ? Trop de choses pour pouvoir les lister mais je dois absolument te remercier de m'avoir fait goûter des fruits et légumes « bizarres » (cristophines, banane plantaine, et mon épice préférée le piment oiseau). Merci de m'avoir initiée à la musique française et étrangère de très haute qualité (Maître Gims, Macassi, Justin Bieber, etc..) et à la danse des Antilles. Surtout merci de m'avoir fait découvrir ma boisson préférée : le Ti-punch. Merci pour tout ça tu as rendu ces années super ! Je t'attends en Sardaigne et j'espère qu'on va rester en contact (on ne va pas s'appeler tous les jours par contre)!

Naturalmente non posso dimenticare le mie origini Italiane e sarde! Ringrazio tutti i miei amici e amiche che sono stati presenti durante questi faticosi anni di adattamento alla cultura e alla lingua francese. Chi più chi meno, chi é venuto a trovarmi anche se per un breve periodo o chi ha anche solo pensato di farlo. Grazie a chi ha contribuito a farmi sentire a casa nei periodi di vacanza! In ogni caso grazie a tutti!

Un grazie speciale é rivolto a tutta la mia famiglia. Sono loro le persone sulle quali sai che puoi sempre contare anche se lontane.

Infine Stefano, grazie per sopportare i miei cambiamenti, i cambiamenti di città, stato, lingua; grazie per accettare (anche se a volte a malincuore) le nuove abitudini alimentari, gli amici, e il nuovo stile di vita. Grazie per essere stato sempre presente e per esserlo in futuro ☺! Spero che anche tu possa approfittare delle esperienze che questa nuova avventura ti offrirà!

**GRAZIE! MERCI! THANK YOU!**



# Deciphering the biological effects of ionizing radiations using charged particle microbeam: from molecular mechanisms to perspectives in emerging cancer therapies

---

## Abstract

Few years ago, the paradigm of radiation biology was that the biological effects of ionizing radiations occurred only if cell nuclei were hit, and that cell death/dysfunction was strictly due to unrepaired/misrepaired DNA. Now, next this “DNA-centric” view several results have shown the importance of “non-DNA centered” effects. Both non-targeted effects and DNA-targeted effects induced by ionizing radiations need to be clarified for the evaluation of the associated radiation resistance phenomena and cancer risks. A complete overview on radiation induced effects requires the study of several points: (i) analyzing the contribution of different signaling and repair pathways activated in response to radiation-induced injuries; (ii) elucidating non-targeted effects to explain cellular mechanisms induced in cellular compartments different from DNA; and (iii) improving the knowledge of sensitivity/resistance molecular mechanisms to adapt, improve and optimize the radiation treatment protocols combining ionizing radiations and nanoparticles.

Charged particle microbeams provide unique features to answer these challenge questions by (i) studying *in vitro* both targeted and non-targeted radiation responses at the cellular scale, (ii) performing dose-controlled irradiations on a cellular population and (iii) quantifying the chemical elements distribution in single cells after exposure to ionizing radiations or nanoparticles.

By using this tool, I had the opportunity to (i) use an original micro-irradiation setup based on charged particles microbeam (AIFIRA) with which the delivered particles are controlled in time, amount and space to validate *in vitro* methodological approaches for assessing the radiation sensitivity of different biological compartments (DNA and cytoplasm); (ii) assess the radiation sensitivity of a collection of cancerous cell lines derived from patients in the context of radiation therapy; (iii) study metal oxide nanoparticles effects in cells in order to understand the potential of nanoparticles in emerging cancer therapeutic approaches.

Keywords: Targeted irradiation, DNA damage, low/high LET irradiations, Radiation sensitivity, Nanoparticles

# Etude des effets biologiques radio-induits et micro-irradiation par particules chargées. Des mécanismes moléculaires aux thérapies émergentes anti-cancéreuses

---

## Résumé

Ces dernières années, le paradigme de la radiobiologie selon lequel les effets biologiques des rayonnements ionisants ne concernent strictement que les dommages à l'ADN et les conséquences liées à leur non réparation ou à leur réparation défectueuse, a été remis en question. Ainsi, plusieurs études suggèrent que des mécanismes «non centrés» sur l'ADN ont une importance significative dans les réponses radio-induites. Ces effets doivent donc être identifiés et caractérisés afin d'évaluer leurs contributions respectives dans des phénomènes tels que la radiorésistance, les risques associés au développement de cancers radio-induits, les conséquences des expositions aux faibles doses. Pour ce faire, il est nécessaire : (i) d'analyser la contribution de ces différentes voies de signalisation et réparation induites en fonction de la dose et de la zone d'irradiation; (ii) d'étudier les réponses radio-induites suite à l'irradiation exclusive de compartiments subcellulaires spécifiques (exclure les dommages spécifiques à l'ADN nucléaire); (iii) d'améliorer la connaissance des mécanismes moléculaires impliqués dans les phénomènes de radiosensibilité/radiorésistance dans la perspective d'optimiser les protocoles de radiothérapie et d'évaluer *in vitro* de nouvelles thérapies associant par exemple les effets des rayonnements ionisants et de nanoparticules d'oxydes métalliques.

Les microfaisceaux de particules chargées offrent des caractéristiques uniques pour répondre à ces questions en permettant (i) des irradiations sélectives et en dose contrôlée de populations cellulaires et donc l'étude *in vitro* des effets « ciblés » et « non ciblés » à l'échelle cellulaire et subcellulaire, (ii) de caractériser l'homéostasie de cultures cellulaires en réponse à des expositions aux rayonnements ionisants et/ou aux nanoparticules d'oxydes métalliques (micro-analyse chimique multi-élémentaire).

Ainsi, au cours de ma thèse, j'ai validé et exploité des méthodes d'évaluation qualitatives et quantitatives (i) *in cellulo* et en temps réel de la réponse radio-induite de compartiments biologiques spécifiques (ADN, mitochondrie, ...); (ii) *in vitro* de la radiosensibilité de lignées sarcomateuses issues de patients; et (iii) *in vitro* des effets induits par des expositions à des nanoparticules d'oxydes métalliques afin d'évaluer leur potentiel thérapeutique et anti-cancéreux.

Mots-clés: Micro-irradiation ciblé, Dommages ADN radio-induits, Irradiations bas/haut TEL, Radiosensibilité, Nanoparticules



# Résumé substantiel

La radiobiologie est le domaine des sciences médicales qui étudie l'influence des rayonnements ionisants (RI) sur les cellules, les tissus biologiques et les organismes vivants. Depuis de nombreuses années, le « dogme classique » de la radiobiologie considère que l'ADN est la cible « critique » et que les conséquences radio-induites ne se produisent que si les noyaux cellulaires sont effectivement touchés et que la mort/dysfonction cellulaire est strictement liée à un défaut ou à une absence de réparation de l'ADN. Aujourd'hui, cette vision « centrée » sur l'ADN (« *targeted* » effect) est remise en question et de nombreuses études suggèrent l'importance des effets « non centrés » sur l'ADN (« *non targeted effect* », NTE). Ainsi, il apparaît que des facteurs tels que le microenvironnement cellulaire/tumoral, la génétique, l'adaptation et la signalisation impliquées dans les réponses aux RI ont un rôle fondamental. De fait, ces mécanismes radio-induits doivent être identifiés afin de permettre une meilleure évaluation du risque associé à l'exposition aux RI (cancer) et ce, aussi bien dans le cadre des fortes et faibles doses d'exposition.

Pour ce faire, il est nécessaire : (i) d'analyser la contribution de ces différentes voies de signalisation et réparation induites en fonction de la dose et de la zone d'irradiation; (ii) d'étudier les réponses radio-induites suite à l'irradiation exclusive de compartiments subcellulaires spécifiques (exclure les dommages spécifiques à l'ADN nucléaire); (iii) d'améliorer la connaissance des mécanismes moléculaires impliqués dans les phénomènes de radiosensibilité/radiorésistance dans la perspective d'optimiser les protocoles de radiothérapie et d'évaluer *in vitro* de nouvelles thérapies associant par exemple les effets des RI et de nanoparticules d'oxydes métalliques. Les nanoparticules sont en effet des agents très intéressants permettant d'augmenter localement la dose délivrée dans la tumeur lors de traitements en radiothérapie externe. Cependant, l'exploitation de leurs propriétés de « dose-enhancers » nécessite le développement de protocoles destinés à quantifier l'internalisation et la toxicité des nanoparticules dans les cellules.

L'amélioration des connaissances des mécanismes fondamentaux des réponses radio-induites en fonction de la dose d'exposition nécessite une étude profonde de tous les domaines mentionnés ci-dessus. Dans ce but, il faut répondre à plusieurs questions: (i) quels mécanismes moléculaires doivent être pris en considération pour une évaluation des effets radio-induits à court et long terme ? (ii) quels sont les effets radio-induits suite à une irradiation non ciblée sur l'ADN ? (iii) comment définir la notion de «dose» moyenne dans le cadre d'exposition *in vitro* ou l'organisme biologique est une population cellulaire et non un organe ? (iv) comment exploiter des données *expérimentales in vitro* afin de valider de nouveaux protocoles thérapeutiques ? etc, ...

Cette thèse s'est donc concentrée sur la caractérisation moléculaire et cellulaire des effets biologiques radio-induits et sur l'exploitation potentielle de ces mécanismes dans le cadre de nouvelle thérapie anti-cancéreuse. Plusieurs thèmes sont abordés dans ce travail de thèse et il s'organise en trois parties. La première partie concerne la mise en œuvre des approches méthodologiques *in vitro* pour évaluer la radiosensibilité de différents compartiments cellulaires (ADN et cytoplasme) suite à des expositions contrôlée en dose, dans le temps et à l'échelle cellulaire à l'aide de l'utilisation d'un microfaisceau de particules chargées (AIFIRA). La seconde partie concerne l'évaluation *in vitro* de la radiosensibilité d'une collection de lignées cellulaires cancéreuses provenant de patients (lignées sarcomateuses). Enfin, la troisième et dernière partie porte sur l'étude des effets biologiques induits en réponse à des expositions à des nanoparticules d'oxydes métalliques afin de caractériser leur potentiel thérapeutique (thérapie anti-cancéreuse).

L'objectif de la première partie de cette étude concerne la caractérisation des effets biologiques radio-induits en fonction de la dose délivrée et de la cible irradiée (ADN, mitochondries). Dans cette étude, les réponses biologiques ont également été évaluées en fonction du transfert d'énergie linéique des particules considérées : proton et particule  $\alpha$ .

Cette étude a ainsi permis de caractériser la dynamique et la cinétique de réponse de protéines impliquées dans les mécanismes de reconnaissance et de réparation des cassures ADN induites par des particules chargées de basse énergie (3 MeV protons - particules  $\alpha$ ). Dans ce sens, une collection de lignées cellulaires exprimant des protéines fluorescentes recombinées avec la GFP (green fluorescent protein) a été établie. J'ai ainsi étudié les réponses radio-induites des protéines GFP-XRCC1 et GFP-RNF8 en fonction (i) de l'énergie déposée et (ii) du TEL (Transfert d'Énergie Linéique) des particules. Pour ce faire, j'ai contribué à la validation d'un système de détection original qui permet d'irradier de manière sélective et contrôlée des cellules avec la dose « ultime » d'une seule particule  $\alpha$  par noyau. Ce dispositif permet de détecter des particules  $\alpha$  individuelles sans interférer avec l'énergie et la taille du microfaisceau. En utilisant notre système d'irradiation, j'ai mesuré que la protéine GFP-RNF8 s'accumule continuellement sur des traces de particules  $\alpha$  pendant les 30 premières minutes après l'irradiation (1). J'ai ensuite pu évaluer que la protéine GFP-RNF8 est recrutée sur les sites endommagés d'une manière dépendante du TEL et que sa vitesse de recrutement est 10 fois inférieure à celle observée pour la protéine GFP-XRCC1 (2).

Ensuite, pour étudier les « effets non ciblés », j'ai collaboré avec l'*Université de Bundeswehr de Munich* et la plateforme d'irradiation SNAKE (consortium Marie-Curie, SPRITE) dans un projet visant à cibler les mitochondries et à évaluer leur réponse suite à une irradiation locale, ciblée et contrôlée en dose. La difficulté de ce projet résidait dans la capacité à (i) micro-irradier sélectivement des

mitochondries, (ii) à réaliser des expériences similaires entre 2 facilités d'irradiation en terme de dépôt d'énergie et de modalité d'irradiation. Les résultats, obtenus lors de ces expériences, ont montré une dépolarisation locale des mitochondries en réponse à des micro-irradiations ciblées à l'aide de carbone (55 MeV, SNAKE) et de protons (3 MeV, AIFIRA). Les mécanismes induisant la dépolarisation des mitochondries restent encore inconnus mais nous avons observé que cette dépolarisation n'était pas due à la rupture de la membrane mitochondriale. En fait, afin de valider le maintien de l'intégrité de la membrane, j'ai établi des cellules transfectées exprimant une protéine de la matrice mitochondriale appelée Matrix-roGFP2. Suite aux irradiations réalisées au SNAKE et à AIFIRA, aucune modification n'a pu être observée (pas de modification de la localisation et de l'intensité de la fluorescence de la matrice mitochondriale) (3).

Enfin, la mobilisation et les interactions des molécules impliquées dans la réponse cellulaire aux RI peut être aussi mesurée avec des expériences de FRAP pour « Fluorescence Recovery after Photobleaching ». Pour réaliser ces expériences, le système d'irradiation de la ligne de microfaisceau a été complété avec une source laser équipée d'un système de balayage permettant de réaliser le photoblanchiment de marqueurs fluorescents. J'ai été donc impliqué dans la validation de ce dispositif expérimental en développant de lignées cellulaires d'intérêts telle que GFP-H2B et GFP-Nop52 afin de permettre l'étalonnage de ce nouveau système en termes d'intensité de « bleaching », de résolution et de ciblage.

Les objectifs de la deuxième partie de ma thèse ont été de développer des protocoles *in vitro*, en utilisant un faisceau d'ions caractérisé et avec d'études dosimétriques pour mieux comprendre les mécanismes biologiques induits par les électrons, les photons (couramment utilisés en radiothérapie conventionnelle) et les protons mais également l'impact de différentes modalités d'irradiation en terme de distribution spatiale en énergie (à l'échelle cellulaire) sur les lignées cellulaires cancéreuses issues des patients (sarcome). Deux lignées cellulaires, issues d'une collection unique établie par F. Chibon, ont été sélectionnées pour leur histologie et leurs caractéristiques génétiques afin d'en étudier l'influence sur la réponse intrinsèque aux rayonnements. En collaboration avec le service de radiothérapie de l'Institut Bergonié, j'ai développé et adapté des protocoles d'irradiation *in vitro* pour estimer l'efficacité d'un faisceau médical de haute énergie (électrons de 9 MeV et photons de 6 MV) et l'efficacité de un faisceau de protons de basse énergie (3 MeV). Les irradiations d'électrons et de photons ont été réalisées avec un accélérateur linéaire médical. Les irradiations de protons ont été réalisées avec un microfaisceau, ce qui offre la possibilité d'étudier les effets de deux distributions d'énergie où l'énergie peut être déposée de manière très focalisée à l'échelle cellulaire ou bien de manière plus homogène sur la totalité de la surface cellulaire (faisceau focalisé *versus* faisceau large).

La dosimétrie assure que la même dose a été administrée par cellule au cours de ces différentes modalités d'irradiation. Les paramètres biologiques, tels que la quantification et la persistance dans le temps des dommages à l'ADN, la prolifération et la survie clonogénique, ont été analysées pour l'évaluation de la radiosensibilité de ces lignées cellulaires. Pour réduire les erreurs expérimentales, j'ai validé deux méthodes de comptage automatique développées avec le logiciel *ImageJ* qui permettent à la fois la quantification des dommages radio-induits (foci  $\gamma$ H2AX et P-ATM) et le comptage des colonies et du nombre de cellules par colonie. En utilisant ces approches, j'ai observé que les protons induisent des effets plus délétères que les électrons, indépendamment de la distribution d'énergie à l'échelle cellulaire et qu'une lignée cellulaire est plus radiosensible pour les paramètres biologiques analysés et cette radiosensibilité semble être en relation avec les caractéristiques génomique (4).

Dans une prochaine étape, ces établis protocoles *in vitro* peuvent être adaptés pour évaluer la potentialité de nouvelles approches thérapeutiques combinant RI et nanoparticules d'oxydes métalliques. Comme déjà mentionné, les nanotechnologies sont des domaines émergents étudiés afin d'augmenter localement la dose délivrée et ensuite, améliorer l'efficacité thérapeutique de la radiothérapie. L'un des points les plus importants qui contribue à disséquer les effets biologiques radio-induits en présence des nanoparticules est d'évaluer la concentration internalisée et la localisation des nanoparticules à l'échelle de la cellule unique.

Dans ce contexte, la troisième partie de mon manuscrit a été consacrée au développement de nouveaux protocoles qui combinent l'analyse par faisceau d'ions et les techniques de microscopie en fluorescence pour quantifier la distribution des éléments chimiques à l'échelle de la cellule unique. Une microsonde nucléaire présente au CENBG permet de détecter, quantifier et localiser la présence d'éléments chimiques dans différents tissus et dans des populations cellulaires à l'échelle de la cellule unique. Dans ce contexte particulier, j'ai participé au développement d'une méthodologie d'imagerie originale qui combine l'analyse par faisceau d'ions et la microscopie de fluorescence et utilisant cette méthodologie, nous avons montré que les nanoparticules de dioxyde de titane ( $\text{TiO}_2$ ) s'accumulent dans le cytoplasme tout autour du noyau et sont exclues du noyau et des mitochondries. Nous avons également observé que le contenu intracellulaire des nanoparticules peut être très hétérogène avec des variations très importantes de l'ordre de 10 fois entre différentes cellules d'une même population exposée. De plus, nous avons observé une altération de l'homéostasie cellulaire avec une augmentation d'ion intracellulaire, tel que le calcium, directement corrélée à la teneur de nanoparticules de  $\text{TiO}_2$  (5).

Ces données suggèrent une altération de l'homéostasie cellulaire induite par la présence de nanoparticules de  $\text{TiO}_2$ . Donc, pour définir les mécanismes moléculaires et cellulaires impliqués dans la toxicité des nanoparticules dans les cellules eucaryotes, j'ai participé au projet de Marina Simon qui vise à étudier les réponses de l'homéostasie cellulaire induite par différentes nanoparticules de  $\text{TiO}_2$  (en termes de forme, de taille et de réactivité de surface) dans différentes populations de cellules humaines primitives et immortalisées. Nous avons observé qu'une concentration intracellulaire minimale de nanoparticules de  $\text{TiO}_2$  (seuil minimal) est nécessaire pour (i) induire une altération de l'homéostasie cellulaire à travers l'altération du calcium et (ii) induire une voie de stress spécifique comme celle du réticulum endoplasmique associée à une dysfonction mitochondriale. De plus, nous avons observé que la fonction cellulaire (endothéliale *versus* épidermique), le type cellulaire (primaire *versus* immortalisé/cancéreuse) et l'hétérogénéité de la distribution intracellulaire de nanoparticules de  $\text{TiO}_2$  dans une population modifient profondément la réponse cellulaire (6).

En résumé, j'ai (i) validé de nouveaux systèmes et protocoles pour étudier les effets radio-induits sur l'ADN et les mitochondries, (ii) exploré les mécanismes spatio-temporels activés dans les cellules en réponse aux IR, (iii) réalisé des analyses multiparamétriques pour extraire des informations biologiques sur la réponse intrinsèque des lignées cellulaires cancéreuses aux RI, et (iv) en collaboration avec mes collègues, j'ai analysé les altérations des éléments chimiques induites par les nanoparticules et/ou les RI.

## List of publications

- (1) **G. Muggiolu**, M. Pomorski, G. Claverie, G. Berthet, C. Mer-Calfati, S. Saada, G. Devès, M. Simon, H. Seznec and P. Barberet. "Single  $\alpha$ -particle irradiation permits real time visualisation of RNF8 accumulation at DNA damaged sites". *Sci. Rep.* 7, 41764; doi: 10.1038/srep41764 (2017).
- (2) **G. Muggiolu**, E. Torfeh, M. Simon, G. Devès, S. Incerti, N. Lampe, P. Barberet, and H. Seznec. "Microdosimetric simulations rationalize *in situ* radiation-induced spatiotemporal dynamics of GFP-tagged DNA repair proteins at cellular scale". In preparation for submission.
- (3) D.W.M. Walsh, C. Siebenwirth, C. Greubel, K. Ilicic, J. Reindl, S. Girst, **G. Muggiolu**, M. Simon, P. Barberet, H. Seznec, H. Zischka, G. Multhoff, T.E. Schmid, G. Dollinger. "Live cell imaging of mitochondria following targeted irradiation *in situ* reveals rapid and highly localized loss of membrane potential". *Sci. Rep.* 7, 46684; doi: 10.1038/srep-46684 (2017).
- (4) **G. Muggiolu**, M. Simon, G. Devès, E. Torfeh, A. Mikael, G. Kantor, F. Chibon, P. Barberet and H. Seznec. "Multiparametric analysis of radiation sensitivity of two sarcoma cell lines derived from patients after both electron and proton irradiation". Submitted on 20/02/2017 to *Scientific Reports*
- (5) **G. Muggiolu**, M. Simon, N. Lampe, G. Devès, P. Barberet, C. Michelet, M.H. Delville, H. Seznec. "*In situ* detection and single cell quantification of metal oxide nanoparticles using Nuclear Microprobe Analysis". Under revision *JoVe*.
- (6) M. Simon G. Saez, **G. Muggiolu**, M. Lavenas, Q. Le Trequesser, C. Michelet, G. Devès, P. Barberet, E. Chevet, D. Dupuy, M.H. Delville and H. Seznec. « In situ quantification of diverse titanium dioxide nanoparticles unveils selective endoplasmic reticulum stress-dependent toxicity. *Nanotoxicology*, 11:1, 134-145, DOI: 10.1080/17435390.2017.1278803 (2017).

# Table of Contents

INTRODUCTION .....	17
BIBLIOGRAPHY .....	27
<b>PART I: BIOLOGICAL EFFECTS INDUCED BY IONIZING RADIATIONS. STUDY OF DOSE-EFFECT PROTEINS KINETICS AND NON-TARGETED EFFECTS .....</b>	<b>29</b>
BACKGROUND .....	32
Chapter 1: Ionizing radiations and matter interactions .....	32
Linear Energy Transfer	
Absorbed Dose	
Relative Biological Effectiveness	
Chapter 2: An original tool to observe ionizing radiation effects: Charged Particle Microbeam .....	35
Study of biological effects of single charged particles in single cells	
Study of DNA damage response	
Cellular compartment targeting	
Study of non-targeted effects	
Development of approaches for tumor therapy	
Chapter 3: Ionizing radiations induce cluster of DNA lesions .....	42
Base Excision and Single Strand Break Repair	
Double Strand Break Repair	
Chapter 4: Ionizing radiation and non-targeted effects .....	48
QUESTIONS ADDRESSED IN THIS WORK .....	50
EXPERIMENTAL RESULTS .....	51
DISCUSSION AND PERSPECTIVES .....	60
ANNEX	
<b>Manuscript 1:</b> Single $\alpha$ -particle irradiation permits real-time visualization of RNF8 accumulation at DNA damaged sites .....	63
<b>Manuscript 2:</b> Microdosimetric simulations rationalize <i>in cellulo</i> radiation-induced spatiotemporal dynamics of GFP-tagged DNA repair proteins at cellular scale .....	75

<b>Manuscript 3:</b> Targeted mitochondrial micro-irradiation induces depolarization without persistent membrane alteration .....	99
BIBLIOGRAPHY .....	111
<b>PART II: IN VITRO EVALUATION OF RADIATION SENSITIVITY OF SARCOMA CELL LINES DERIVED FROM PATIENTS</b> .....	119
BACKGROUND .....	123
Chapter 1: Sarcoma: a particular types of cancer .....	124
Chapter 2: Radiation biology for studying <i>in vitro</i> radiation resistance and radiation sensitivity. ....	126
Chapter 3: Microbeam for radiation biological approaches .....	129
QUESTIONS ADDRESSED IN THIS WORK .....	131
EXPERIMENTAL RESULTS .....	132
DISCUSSION AND PERSPECTIVES .....	136
ANNEX	
<b>Manuscript 4:</b> Electron and proton irradiations reveal different radiation sensitivity of two sarcoma cell lines derived from patients. ....	139
BIBLIOGRAPHY. ....	166
<b>PART III: IN SITU AND IN CELLULO DETECTION AND QUANTIFICATION OF METAL OXIDE NANOPARTICLES. TOWARD THE ELUCIDATION OF NANOTOXICITY MECHANISMS AND PERSPECTIVES FOR CANCER THERAPY</b> .....	169
BACKGROUND .....	172
Chapter 1: Nanoparticles in nanomedicine. ....	172
Nanoparticles in radiation therapy	
TiO <sub>2</sub> Nanoparticles	
Chapter 2: Nuclear microprobe techniques for chemical multi-elements micro-analysis . .	176
PIXE: Particle-Induced X-Rays Emission	
RBS: Rutherford Backscattered Spectrometry	
STIM: Scanning Transmission Ion Microscopy	



QUESTIONS ADDRESSED IN THIS WORK .....	179
EXPERIMENTAL RESULTS .....	180
DISCUSSION AND PERSPECTIVES .....	182
ANNEX	
<b>Manuscript 5:</b> <i>In situ</i> detection and single cell quantification of metal oxide nanoparticles using nuclear microprobe analysis .....	185
<b>Manuscript 6:</b> <i>In situ</i> quantification of diverse titanium dioxide nanoparticles unveils selective endoplasmic reticulum stress-dependent toxicity .....	203
BIBLIOGRAPHY .....	224
<b>CONCLUSIONS AND PERSPECTIVES</b> .....	227

# INTRODUCTION



The path to the discovery of ionizing radiations is paved by important physics discoveries. In 1895, the German physicist Röntgen discovered a “new kind of ray”, that he called temporarily X-Rays as a designation of something “unknown”, and with which he took the first picture of his wife’s hand and skeletal structure. In 1896, Becquerel discovered that uranium compounds naturally emitted similar rays, and the adverse health effects due to exposure to X-Rays, were soon reported. Inadvertently, he left a radium container in his vest pocket and he described the skin erythema appeared 2 weeks later. Two years later, Pierre and Marie Curie named this phenomenon radioactivity. They isolated the radioactive polonium and radium that, within few years, was used for the treatment of cancer. Marie Curie died in 1934 of aplastic anemia probably developed from extended exposure to various radioactive materials.

These are few examples of the applications or effects that ionizing radiations (IR) could cause in cells, organs and tissues of the human body. It is clear that there are health risks for humans exposed to radiations, despite the considerable benefits obtained from the use of radiations in medicine<sup>1</sup>. Everyday a person, group of people or even an entire population might be chronically or acutely exposed to ionizing radiations and suffer from acquired damages. These IR come from nuclear accidents, natural sources or produced for medical purposes, energy production and other industrial uses. Nuclear bombings of Hiroshima and Nagasaki by USA during World War II in 1945 are examples for nuclear warfare. Nuclear reactor accidents, such as Chernobyl in 1986, affected staff, clean-up workers, and the population of the region. There are also natural sources of IR, such a cosmic rays and radiation from elements present in the earth’s crust (for example radon). Other examples of expositions to IR are in medicine for both imaging/nuclear medicine and for cancer treatment (radiotherapy) where damaged is caused not only in cancerous cells but also in healthy tissues.

For all these and many other reasons, **the knowledge of interaction between IR and living tissues has an important role in many fields, such as health risks associated to low dose exposure from natural or working environment, the appearance of radiation-induced tumors, and the new cancer therapeutic approaches.**

IR are electromagnetic waves or massive particles that carry enough energy to ionize (*i.e.* removes an electron from) an atom or a molecule of the medium through which it propagates. **These changes can induce a variety of biological effects depending on the physical nature, duration, dose and dose-rate of exposure.** Low doses of IR can be found in natural (cosmic gamma rays, ingestion of potassium-40, radon exposure) and industrial environment (nuclear power plants, waste processing plants, medical environment). Thus, we are increasingly exposed to radiation during the course of

our lives from routine medical usage, such as diagnostic X-Rays and computed tomography (CT) scanning, from the increased frequency of flying, and from radiotherapy treatments<sup>2,3</sup>. The elevated usage of radiation for medical purposes and nuclear power for energy enhances the risk of accidental exposure from industrial accidents and for workers in the radiation industry<sup>4</sup>.

Worldwide, the average human exposure to radiation from natural sources is 2.4 mSv per year, about half of which is due to the effects of radon progeny (daughters) (radioactive elements produced by the decay of <sup>222</sup>Ra). Diagnostic medical exposures add about 0.4 mSv per year, atmospheric nuclear testing about 0.005 mSv per year, the Chernobyl accident fallout 0.002 mSv per year, and nuclear power production about 0.0002 mSv per year<sup>5,6</sup>. However, the magnitude of health risks at low doses and dose-rates (below 100 mSv and 0.1 mSv.min<sup>-1</sup>, respectively) remains controversial due to the difficulty of direct data collection<sup>7</sup>. To date, this issue cannot be addressed by epidemiological studies because it is difficult to accurately assess the risk of a population exposed to various carcinogens: it is well established that low-dose effects of IR are more difficult to measure than high-dose effects. The most important of the epidemiological studies for risk assessment is the Life Span Study of the survivors of the atomic bombings of Hiroshima and Nagasaki<sup>8,9</sup>. These epidemiological studies of the survivors provide strong evidence of increased risk of developing both solid cancers and leukemia from high doses and high dose-rates of radiation. However, significantly increased cancer risk is also observed in atomic bomb survivors exposed to lower doses of radiations<sup>1,10,11</sup>. Another convincing evidence of low-dose effects comes from studies of *in utero* exposure, which suggest that there are elevated risks of leukemia and most other cancer types following 10-20 mGy diagnostic exposure<sup>12,13</sup>. The radiation risks (per unit dose) implied by these studies are similar in magnitude to those following much higher dose exposure in early life in the Japanese atomic bomb survivors<sup>14</sup>.

Although the link between the initial damage and cancer remains elusive, the target theory is the basis for the model describing risk of cancer and heritable effects, and it has been used to establish international rules and standards of radiation protection. These assumptions are described collectively as the linear no-threshold (LNT) model, where the risk of low doses is extrapolated from the risk assessed at high doses. The LNT relationship implies a proportionality between the dose and the cancer risk<sup>7</sup>. The validity of using this dose-response model is controversial because accumulated evidences indicated that living organisms respond differently to low dose radiation than they do to high dose radiation<sup>15</sup>. The range in sensitivity between individuals is, perhaps, best illustrated by the response to radiotherapy where 1–5% of treated patients have a more dramatic response compared

to the average individual. This represents the response to high-dose exposure but current evidence suggests that there will be individuals with enhanced sensitivity to low-dose exposure.

Therefore, while some progress has been made in understanding these phenomena, **the knowledge has yet to be assembled into a coherent body of understanding that can be readily applied to the assessment of low-dose risk.** However, it is recognized that epidemiological studies can be limited in statistical power to detect excess risk under these conditions. This is because the population size required to detect added risk becomes enormous when very small increases in risk are being investigated. The advances in radiation biology during the past two decades, the understanding of carcinogenesis, and the discovery of defenses against carcinogenesis challenge the LNT model, which appears nowadays outdated<sup>16,17</sup>.

Quite a lot is currently known about the general mechanisms of action of radiation. However, much remain to be learnt about the specific mechanisms by which radiations exert their effects, in particular the effects of low doses over long periods of time. Improved knowledge of genetic and epigenetic mechanisms involved in radiation sensitivity will allow a better definition of radiation protection rules and the development of more effective treatment plans in case of deleterious exposure.

The absorption of IR by living cells can directly disrupt atomic structures, producing physical, chemical and biological changes (direct effects). It can also act indirectly through radiolysis of water, thus generating reactive chemical species that may damage nucleic acids, proteins and lipids (the so-called indirect effects)<sup>18</sup>. Since the discovery of the DNA (in 1953, by Watson and Crick) and the discovery that radiations could introduce strand breaks into DNA double helix (in 1961, by Lett and colleagues), the DNA was considered as the main target of IR<sup>19</sup>. It was assumed that the amount of DNA damages is proportional to the radiation dose received, and there is a clear relationship between DNA damages, mutations and cancer development, which drive to a DNA-centered paradigm, known as 'the target theory'<sup>20</sup>. Indeed, upon DNA damages induction by IR, there is an extensive response in the chromatin surrounding the break. Hundreds of molecules and DNA damage response proteins accumulate at DNA damaged sites, forming large nuclear aggregates, that appear as ionizing radiation-induced nuclear foci (IRIF)<sup>21</sup>. **Of particular importance is to analyze the contribution of these different signaling and repair pathways activated in response to radiation-induced injuries that can affect human health and promote cancer development**<sup>6,17</sup>.

Alongside the damages induced directly to DNA, it has been put-forward that the radiation-induced effects can be mediated by 'Non-Target Effects' (NTE). NTE occur when IR energy has not been

deposited in the DNA or the DNA has not been targeted. In 1990's the 'membrane theory', where membranes are considered as a second major target of radiation effects, challenges the 'DNA-centered theory'. Furthermore, early effects of lipid soluble vitamins under radiation response were observed<sup>22</sup>. In those years, it raised the idea that the signaling of damage from irradiated cells could be induced in non-hit cells, calling this phenomena 'bystander effects'. Nowadays, the distinct classes of NTE are identified in genomic instability, bystander effect, adaptive response, and low dose radiation-induced hypersensitivity.

**Elucidating the mechanisms of NTE calls for further researches; moving away from the conventional DNA targeted framework, it is necessary to develop new experimental strategies to evaluate the impact of IR on specific targets different from DNA.**

As well as the effects of IR at low doses need to be clarified for the evaluation of the associated cancer risks<sup>23</sup>, understanding how high doses of IR interacts with molecular mechanisms responsible for the radiation resistance phenomena (that could be innate or derived from a previous radiation therapy treatment) remains a challenge. **Improving the knowledge of sensitivity/resistance molecular mechanisms is useful to adapt, improve and optimize the radiation treatment protocols.** Indeed, radiation therapy exploits the capability of IR to kill cells. The effectiveness of radiation therapy depends not only on the type of radiation (X-Rays or protons) but also, on the nature of cancer, on the individual patient, and on the combination of radiations with other treatments.

The evolution of radiotherapy has been strongly correlated with the development of imaging techniques, which allow radiologists to determine the location of both internal organs and tumor<sup>24</sup>. However, when using conventional external-beam radiotherapy (photons and electrons), healthy tissues are exposed to radiations. Several strategies investigate the use of heavy charged particles (hadrons)<sup>25</sup>, and the addition of radiation sensitizing agents to increase the radiation-induced effects in the tumor volume, and to spare the healthy tissues surrounding tumor<sup>26,27</sup>. Charged particles, indeed, deposit little energy at the entrance to the body, and most at the end of their range in the tissue delivering conformal dose distribution in the tumor and minimizing the normal tissue exposed to radiation<sup>28</sup>.

Recently, nanotechnologies have paved the way to new approaches in local cancer therapy. Nanoparticles, with high electron density, offer the possibility to deposit high amounts of energy within the cancer cells, when activated by IR. To exploit the capability to increase the deposit of energy *via* secondary electron emission (photoelectric and/or Compton Effect) and atomic de-excitation processes (Auger electrons, X-Rays), the uptake of nanoparticles by cells is a very

important factor. **Developments of protocols addressed to quantify and localize these nanoparticles are needed.**

It is necessary to improve the knowledge about the fundamental mechanisms of cellular response to IR at both low and high doses. To this aim, different questions need to be answered: (i) which bio-molecular mechanisms induced *in cellulo* by IR have to be considered for a correct evaluation of radiation-induced effects? (ii) what are the effects of IR when the target is not the DNA? (iii) what is the mean 'dose' when radiobiological *in vitro* studies are conducted on cells and not on whole organs? (iv) which predictive methodologies can allow us to translate the results obtained *in vitro* to medical applications? (v) where nanoparticles accumulate in cells and how quantify the intracellular nanoparticles content? *etc, ...*

The aim of my PhD thesis is to decipher the biological effects of ionizing radiations from the molecular mechanisms to their applications in radiation therapy. Deciphering the radiation-induced effects, from molecular mechanisms in single cells to the behavior of a cell population, requires the development of original approaches using *in vitro* models and highly-controlled experimental conditions. Multidisciplinary knowledge is required, from physics to fundamental and medical biology to: (i) develop accurate irradiation setups where the dose is controlled in time, amount and space, (ii) study complex molecular and cellular regulation pathways activated after DNA damage at both low and high doses, (iii) explore the intricate radiobiological responses to IR and (iv) investigate the interaction of nanoparticles with cells.

Charged particle microbeams provide unique features to study *in vitro* the targeted and non-targeted radiation responses and have been shown to be powerful tools to localize and quantify chemical elements in cells. The "Centre d'Etudes Nucléaires de Bordeaux-Gradignan" (CENBG) is equipped with a Singletron™ particle accelerator that produces focalized charged particle microbeams. In particular during my work, I made use of two microbeam lines. One microbeam line is addressed to perform micro-irradiations of living cells and small organisms (*C. elegans*) where dose, target and time are highly controlled. Indeed, this set-up allows targeting energetic protons and helium ions in living biological specimens with micrometer precision. It is coupled with live cell imaging tools such as an epifluorescence microscopy for real time cell visualization and a laser photobleaching setup. The second beam line exploits the interactions of charged particles with matter for chemical element imaging and analytical techniques such as  $\mu$ -PIXE,  $\mu$ -RBS and  $\mu$ -STIM permit to obtain the spatial distribution and quantification of these chemical elements at the single cell level.



This manuscript is structured in three main parts.

**FIRST PART: BIOLOGICAL EFFECTS INDUCED BY IONIZING RADIATIONS. STUDY OF DOSE-EFFECT PROTEINS KINETICS AND NON-TARGETED EFFECTS**

After an introduction devoted to a general overview of IR, their effects on biological specimens and the description of the AIFIRA irradiation microbeam line, the experimental results obtained are summarized in three articles. These three manuscripts are then followed by a section where outcomes and impacts of the individual projects are discussed.

- The first result shows the development of a thin membrane for detection of single  $\alpha$ -particles minimizing beam scattering. These single particles were used to irradiate living cells and to study their impact on GFP-proteins accumulation at DNA damaged sites.
- The second result identifies a correlation between the number of delivered particles (starting from the “ultimate dose” of one single particle per cell), the Linear Energy Transfer of particles and the kinetics profile of proteins involved in the DNA damage signaling and repair. In particular, we chose to describe the kinetics profiles of different stable GFP-transfected cell lines, which are involved in the DNA signaling and repair mechanisms, such as XRCC1 (Single Strand Breaks and BER/NER pathways) and RNF8 (Double Strand Breaks ligase protein). These proteins accumulate at DNA damaged sites forming large nuclear aggregates that appear as ionizing radiation-induced nuclear foci (IRIF)<sup>21</sup>. DNA damage-induced foci are highly dynamic structures, subject to precise spatio-temporal regulation and the precise order and timing of recruitment is thought to provide the kinetics of how this lesion is processed and resolved after irradiations<sup>29</sup>.
- The third result, obtained thanks to the collaboration with my colleague Dietrich Walsh and the SNAKE microbeam facility (Bundeswehr University Munich), shows the radiation-induced effects after different doses of 3 MeV protons and 55 MeV carbon ions on mitochondria. The cytoplasm, which is the environment where the majority of processes involved in the maintenance of cellular integrity take place, has rarely been taken into account as a target of ionizing radiation. Mitochondria constitute a large volume of the cytoplasm in all cell types and they have been selected in this study to highlight the effect of targeted irradiation. We showed that targeted irradiations with both carbon ions and protons induce instant mitochondrial depolarization without changes the mitochondrial matrix.
- The fourth result describes the implementation of the microbeam line end-station with a 488 nm laser system. This intense light source can be focused into the object plane of our online fluorescence microscope and the focal point can be moved to selected positions to permanently bleach GFP molecules. These experiments enable us to measure the exchange and binding

behavior of repair proteins after bleaching and this validated system can now be coupled with targeted irradiations.

## **SECOND PART: *IN VITRO* EVALUATION OF RADIATION SENSITIVITY OF SARCOMA CELL LINES DERIVED FROM PATIENTS**

The second part of this PhD thesis starts with a general overview of sarcomas that are particularly radiation resistant types of tumor for which radiation therapy has to be improved.

The objective of this part is the development of protocols, ranging from dosimetry to biological assays, to describe the radiation sensitivity of patient's derived cell lines. Two cells lines, from a wide collection established by F. Chibon, are selected for their histology and genetic characteristics to study the influence of IR on the intrinsic radiation response. Working together with the Radiation Therapy Department of the Institut Bergonié, we developed and adapted an irradiation protocol to estimate the effectiveness of medical beams (9 MeV electrons and 6 MV photons), usually used in external radiotherapy, and the effectiveness of low energy protons (3 MeV). Electron and photon irradiations were carried out with a medical linear accelerator, and proton irradiations were carried out with the AIFIRA microbeam, which offers the possibility to study the effects of two different deposited energy distributions at the cellular level, such as the effects of focalized *versus* broad beam. The results obtained are described in the fourth manuscript that is followed by a discussion and perspectives opened by this work.

## **THIRD PART: *IN SITU* AND *IN CELLULO* DETECTION AND QUANTIFICATION OF METAL OXIDE NANOPARTICLES. TOWARD THE ELUCIDATION OF NANOTOXICITY MECHANISMS AND PERSPECTIVES FOR CANCER THERAPY**

Finally, the third part of this manuscript is devoted to the development of new protocols to combine nuclear microprobe analysis and microscopy techniques for quantification of chemical element distribution in single cells. After a general introduction of the microprobe present at the AIFIRA platform, its applications are presented. In particular, the quantification of nanoparticles at the single cell level is needed to understand the mechanisms involved in new emerging concepts of radiation therapy proposing to combine IR and nanoparticles to enhance the local dose deposition inside the tumors. We developed a procedure for the *in situ* detection and *in vitro* quantification of chemical elements present in human cells, as well as metal oxide nanoparticles and by using these methods we observed the effects of different nanoparticles in different cell types. These results are presented in two manuscripts which are followed by a discussion and perspectives for future works.

## Bibliography

1. Mullenders, L., Atkinson, M., Paretzke, H., Sabatier, L. & Bouffler, S. Assessing cancer risks of low-dose radiation. *Nat. Rev. Cancer* **9**, 596–604 (2009).
2. Muirhead, C. R. *et al.* Mortality and cancer incidence following occupational radiation exposure: third analysis of the National Registry for Radiation Workers. *Br. J. Cancer* **100**, 206–212 (2009).
3. Cardis, E. *et al.* The 15-Country Collaborative Study of Cancer Risk among Radiation Workers in the Nuclear Industry: Estimates of Radiation-Related Cancer Risks. *Radiat. Res.* **167**, 396–416 (2007).
4. Goodarzi, A. A. & Jeggo, P. A. Irradiation induced foci (IRIF) as a biomarker for radiosensitivity. *Mutat. Res. Mol. Mech. Mutagen.* **736**, 39–47 (2012).
5. Buonanno, M., de Toledo, S. M., Pain, D. & Azzam, E. I. Long-Term Consequences of Radiation-Induced Bystander Effects Depend on Radiation Quality and Dose and Correlate with Oxidative Stress. *Radiat. Res.* **175**, 405–415 (2011).
6. Smith, G. UNSCEAR 2013 Report. Volume I: Report to the General Assembly, Annex A: Levels and effects of radiation exposure due to the nuclear accident after the 2011 great east-Japan earthquake and tsunami. *J. Radiol. Prot.* **34**, 725–727 (2014).
7. Brenner, D. J. *et al.* Cancer risks attributable to low doses of ionizing radiation: assessing what we really know. *Proc. Natl. Acad. Sci. U. S. A.* **100**, 13761–6 (2003).
8. Preston, D. L. *et al.* Solid cancer incidence in atomic bomb survivors: 1958-1998. *Radiat. Res.* **168**, 1–64 (2007).
9. Preston, D. L. *et al.* Effect of Recent Changes in Atomic Bomb Survivor Dosimetry on Cancer Mortality Risk Estimates. *Radiat. Res.* **162**, 377–389 (2004).
10. UNSCEAR. Biological Mechanisms of Radiation Actions At Low Doses. *United Nations* 1–45 (2012).
11. UNSCEAR. Epidemiological Studies of Radiation and Cancer. *United Nations Annex A*, 13–322. (2006).
12. Doll, R. & Wakeford, R. Risk of childhood cancer from fetal irradiation. *Br. J. Radiol.* **70**, 130–139 (1997).
13. Mole, R. H. Childhood cancer after prenatal exposure to diagnostic X-ray examinations in Britain. *Br. J. Cancer* **62**, 152–68 (1990).
14. Wakeford, R. & Little, M. P. Risk coefficients for childhood cancer after intrauterine irradiation: a review. *Int. J. Radiat. Biol.* **79**, 293–309 (2003).
15. Waldren, C. A. Classical radiation biology dogma, bystander effects and paradigm shifts. *Hum Exp Toxicol* **23**, 95–100 (2004).
16. Tubiana, M., Feinendegen, L. E., Yang, C. & Kaminski, J. M. Linear No-Threshold Relationship Is Inconsistent with Radiation Biologic and Experimental Data. *Radiology* **251**, 13–22 (2009).
17. Kadhim, M. *et al.* Non-targeted effects of ionising radiation—Implications for low dose risk. *Mutat. Res. Mutat. Res.* **752**, 84–98 (2013).
18. Azzam, E. I., Jay-Gerin, J.-P. & Pain, D. Ionizing radiation-induced metabolic oxidative stress and prolonged cell injury. *Cancer Lett.* **31**, 48–60 (2012).
19. Mothersill, C. & Seymour, C. Low-dose radiation effects: Experimental hematology and the changing paradigm. *Exp. Hematol.* **31**, 437–445 (2003).
20. Mothersill, C. & Seymour, C. Implications for human and environmental health of low doses of ionising radiation. *J. Environ. Radioact.* **133**, 5–9 (2014).
21. Bekker-Jensen, S. & Mailand, N. Assembly and function of DNA double-strand break repair foci in mammalian cells. *DNA Repair (Amst.)* **9**, 1219–1228 (2010).
22. Brandes, D., Rundell, J. O. & Ueda, H. Radiation response of L1210 leukemia cells pretreated

- with vitamin A alcohol. *J. Natl. Cancer Inst.* **52**, 945–9 (1974).
23. Trougakos, I. P., Sesti, F., Tsakiri, E. & Gorgoulis, V. G. Non-enzymatic post-translational protein modifications and proteostasis network deregulation in carcinogenesis. *J. Proteomics* **92**, 274–298 (2013).
  24. Xing, L. *et al.* Overview of image-guided radiation therapy. *Med. Dosim.* **31**, 91–112 (2006).
  25. Durante, M. & Loeffler, J. S. Charged particles in radiation oncology. *Nat. Rev. Clin. Oncol.* **7**, 37–43 (2010).
  26. Kobayashi, K., Usami, N., Porcel, E., Lacombe, S. & Le Sech, C. Enhancement of radiation effect by heavy elements. *Mutat. Res.* **704**, 123–31 (2010).
  27. Wardman, P. Chemical radiosensitizers for use in radiotherapy. *Clin. Oncol. (R. Coll. Radiol.)* **19**, 397–417 (2007).
  28. Loeffler, J. S. & Durante, M. Charged particle therapy--optimization, challenges and future directions. *Nat. Rev. Clin. Oncol.* **10**, 411–424 (2013).
  29. Bekker-Jensen, S. *et al.* Spatial organization of the mammalian genome surveillance machinery in response to DNA strand breaks. *J. Cell Biol.* **173**, 195–206 (2006)



## **PART I**

**Biological effects induced by ionizing radiations. Study of dose-effects proteins kinetics and non-targeted effects**



When the integrity of the genetic material of cells, the DNA, is compromised, swift and efficient measures must be taken to restore it. Failures can lead to the occurrence and propagation of mutations and even cell death. An intricate cellular machinery has evolved to prevent the deleterious consequences of DNA damage. If successful repair cannot be achieved, the apoptotic suicide pathway may eliminate cells with compromised DNA to protect the organism against potential tumourigenesis. Collectively, the network of pathways that ensure the above objectives is called the DNA damage response. This network also affects cellular processes like transcription and replication of DNA and constitutes an important barrier against cancer development. The tight correlation between the DNA damage response and cancer development has solicited a massive effort to map the underlying molecular pathways and to understand their roles in human pathogenesis. Our understanding of the DNA damage response is already quite considerable and most of the central proteins and their functions have been described in details. Nevertheless, one key issue that remains somewhat under-represented in the field is how these important reactions are organized in time and space. The spatio-temporal aspects of the DNA damage response have been intensively conducted using a variety of tools including femto-second lasers and particle micorbeams. However, due to the nature of lasers, the energy deposited with these systems is not quantifiable. Charged particles micro-irradiation enables a quantification of deposited energy in a defined nuclear area by delivering a precise number of particles.

The aim of the first part of this project is to further develop our capabilities in detecting and irradiating cells with a highly controlled number of particles, and apply these techniques to investigate the spatio-temporal properties of the DNA damage response. In addition, the focusing capabilities of microbeams allow us to target single mitochondria and in collaboration with the University of Bunderswehr and the facility installed at SNAKE in Munich we studied the effects of charged particles on mitochondrial membrane.

The main body of this first part is divided into three sections: *Background*, *Experimental Results* and *Discussion*. The *Background* section deals with the micro-irradiation techniques, and outlines the theory and current status of the DNA damage response and DNA repair processes induced by IR. In *Experimental Results* section, I present three manuscripts produced during my PhD studies on which I appear as an author. Then, I discuss outcomes and impacts of these projects in the light of subsequent findings in this expanding fields.



# Background

## Chapter 1

### *Ionizing radiations and matter interactions*

Radiation can be defined as the propagation of energy through matter or space. We define a non-ionizing radiation, a radiation whose associated energy can excite an atom (raise an electron to a higher energy level) but not remove an electron from it. If the energy is sufficient to remove electrons from their orbits from atoms or molecules, then the radiation is called ionizing radiation (Figure 1).

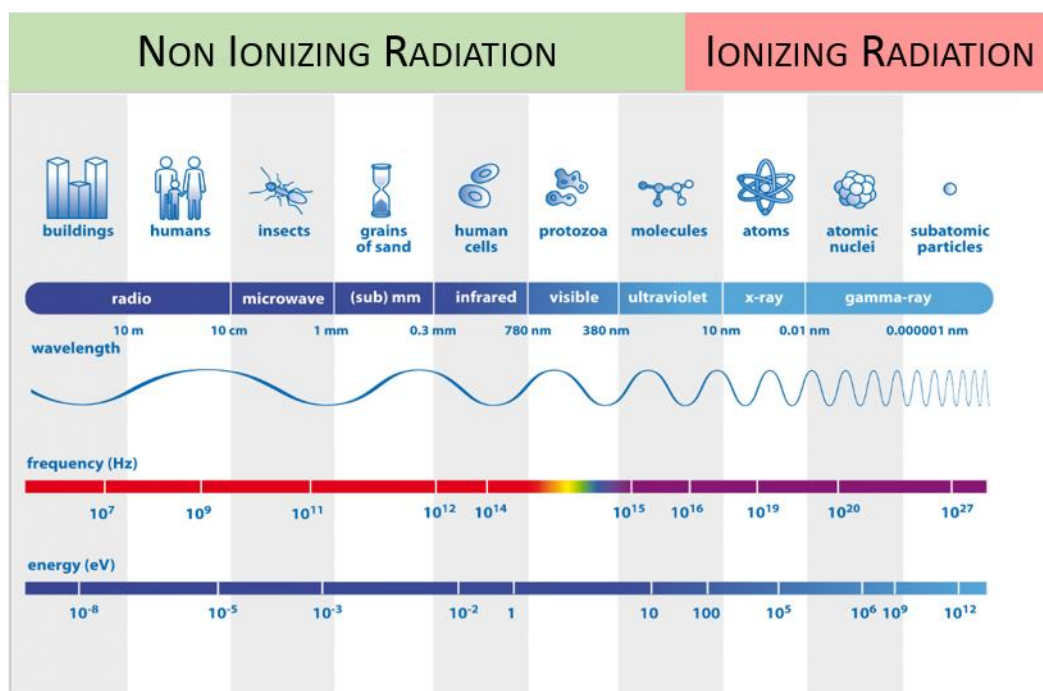


Figure 1. Ionizing radiations and non-ionizing radiations in the electromagnetic spectrum. When the energy of radiations is higher than 13.6 eV, it is considered as ionizing radiations. Adapted from [www.nasa.gov](http://www.nasa.gov)

The major types of IR are divided in four groups. (i) Charged particles, which include protons and  $\alpha$ -particles. Protons are positively charged particles, having a mass about 2000 times greater than that of an electron.  $\alpha$ -particles are nuclei of helium atoms, made up of two protons and two neutrons strongly bounded. They are the major source of natural background radiation because naturally

emitted during the decay of heavy radionuclides.  $\alpha$ -particles strongly interact with matter, but they have a very limited ability to penetrate. These particles can be blocked by a sheet of paper, skin, or even a few centimeters of air. Nonetheless, materials that emit  $\alpha$ -particles are potentially dangerous if they are inhaled or swallowed. (ii) Beta particles or electrons are light charged particles and are emitted from naturally occurring materials, such as strontium-90. In general beta particles have a great ability to penetrate few meters in the air, and can penetrate skin. Nonetheless, a thin sheet of metal, or plastic, or a block of wood can stop them. (iii)  $\gamma$ -Rays and X-Rays are two types of electromagnetic radiations with short wavelengths and high energies. X-Rays are produced by electrical devices accelerating electrons to high energy and stopping them in a target.  $\gamma$ -Rays are emitted by radioactive isotopes and are very similar to X-Rays in their effects on living organisms.  $\gamma$ -Rays are used in medical applications to treat cancer. Similarly, X-Rays are typically used to provide static images of body parts. Several meters of concrete, or a few meters of dense material, are able to block these types of radiations (Figure 2). (iv) Neutrons are high speed nuclear particles that have an exceptional ability to travel great distances in air and require very thick hydrogen-containing material to block them<sup>1</sup>.

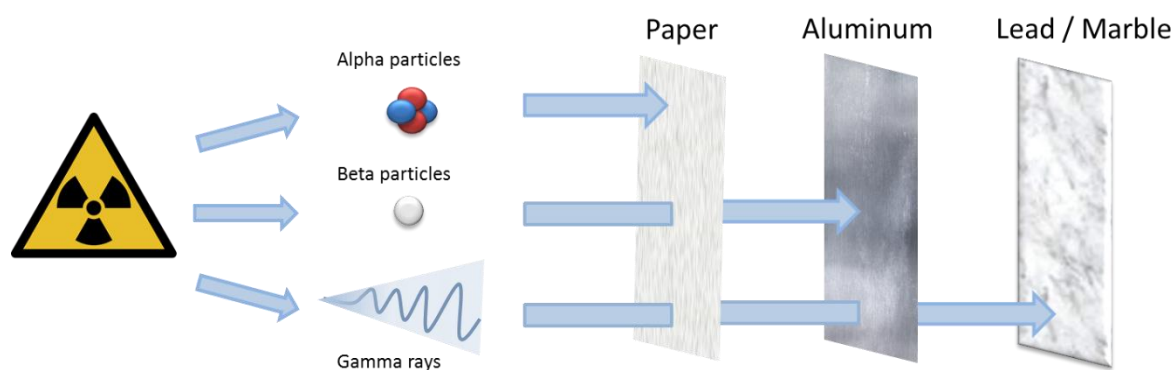


Figure 2. Penetration power of ionizing radiations in different materials.

*Linear Energy Transfer.* When IR traverse matter, they deposit energy along their tracks. Such energy is typically measured in electron volt (eV). The energy deposit along the track is strictly dependent on the type of incident radiation and it is described by the Linear Energy Transfer (LET). Indeed, the LET is the amount of energy transferred to matter per unit length of the track. The unit usually used for this quantity in radiation biology is kiloelectron volt per micrometer ( $\text{keV}\cdot\mu\text{m}^{-1}$ ) per density unit. For a given charged particle, the LET is influenced by its energy and its charge. On the basis of the LET, IR can be divided into sparsely ionizing radiations (X-Rays,  $\gamma$ -Rays and electrons with low LET) and densely ionizing radiations (particle radiations with high LET).  $10 \text{ keV}\cdot\mu\text{m}^{-1}$  is generally accepted as the threshold between low and high LET radiations. For example,  $\alpha$ -particles of few MeV are

classified as high LET radiations because they deposit their energy on a short linear range (20 to 100  $\mu\text{m}$ ), producing a dense ionization along their tracks. The energy lost by these particles during the interaction with matter rapidly increases after a small distance, generating the so-called Bragg peak, and particles are then stopped. While the energy deposition of protons and heavier charged particles is characterized by the presence of the Bragg peak, this is not the case for photons<sup>1,2</sup>.

*Absorbed Dose.* Some radiation damage causes permanent chemical change that can lead to harmful biological effects. Biological effects are found to be directly related to the amount of energy that is deposited by the radiation per unit of mass of tissue. The amount or quantity of absorbed radiation is expressed in terms of the absorbed dose, measured in Gray (Gy). One Gy corresponds to an energy deposition of 1 Joule per kilogram of irradiated matter. This unit is especially used when an organ is irradiated in a homogeneous manner, but this concept loses meaning when the dose is delivered in a small area such as cells. When single cells are irradiated it is more appropriate to speak about “deposited energy” instead of “dose”<sup>3</sup>.

*Relative Biological Effectiveness.* Equal doses of different types of radiation do not produce equal biological effects. The effectiveness of different types of IR is evaluated by the relative biological effectiveness (RBE). This parameter is obtained by comparing the dose of one type of radiation needed to cause a specific effect with the dose of another type of radiation needed to obtain an equal biological effect. The typical standard to define RBE of different radiations is X-rays. The RBE values for low LET radiations are close to 1 and increase as LET increases. The RBE generally increases as the dose is decreased, and it varies greatly according to the tissue or cell line studied<sup>4</sup>.

## Chapter 2

### *An original tool to observe ionizing radiation effects: Charged Particle Microbeam*

To study the effects of IR on living cells, methods and models which spanning from physics to biology are necessary. Synergy of various fields gives the possibility to explore livings and to understand the fundamental physiologic and pathologic mechanisms from original and complementary points of view.

From the end of 1990s, charged particle microbeams were developed as a specific tools to investigate the effects of IR on living samples<sup>5</sup>. The rationale for developing such devices was initially motivated by the necessity to study the cellular response to low doses. Using broad beam or radioactive sources, the delivering of an average of one particle per cells leads to a Poisson distribution of the number of particle traversals. This means that 37% of the cells receive no particle at all, 37% receive one particle and 26% receive more than one particle<sup>6</sup>. For this reason there was an increasing interest in the use of microbeam systems designed to deliver single particles with a position resolution of a few micrometers in biological targets. This allows the study of biological responses to charged particles at both single cell (nucleus) and subcellular (nucleolus or cytoplasm) levels. In addition, a large quantity of cells can be simultaneously irradiated within a relatively short time by moving the beam from cell to cell using fast electromagnetic scanning systems, which permit to study the effects on a cell population. Also, the dose that is delivered to cells can be accurately measured and controlled.

Nowadays, there are 11 microbeam facilities fully-operational or under-development worldwide and all of them contribute to the fundamental knowledge of cellular response to IR<sup>7</sup>. The feasible applications of microbeams are described below and schematized in Figure 3<sup>8,9</sup>:

- (i) *Study of biological effects of single charged particles in single cell.* The main advance of these facilities is to deliver single ion in single cell, and to measure the effect of a single particle track on mutagenic and oncogenic transformation<sup>10,11</sup>, cellular toxicity, micronuclei formation and genomic instability<sup>12-14</sup>.

- (ii) *Study of DNA damage response.* By their ability to target the cell nucleus in a highly-controlled way, microbeams are used to study DNA damage and repair machinery<sup>15</sup>. Indeed, DNA damage signaling and repair factors can accumulate around radiation induced lesions in microscopically discernible structures known as ionizing radiation-induced foci (IRIF). The protein accumulation can be visualized using immunofluorescence techniques or live cell imaging. For live cell imaging, the protein of interest need to be fluorescently tagged, e.g. by fusion to GFP. In this way the formation of IRIF can be followed before, during, and after irradiation by using microbeam lines equipped with advanced fluorescence microscopy end-stations<sup>16–20</sup>.
- (iii) *Cellular compartment targeting.* The micrometric resolution gives the possibility to target sub-nuclear compartments and allows studying the impact of IR on these structures. Initially, the sub-micrometer size of the beam was achieved at GSI Helmholtz Centre for Heavy Ion Research and nowadays this resolution permits to study the DNA repair response in heterochromatin centers<sup>21,22</sup>. Recently, at SNAKE (Superconducting Nanoscope for Applied nuclear physics Experiments) facility the ability to target larger structures such as nucleoli was shown<sup>23</sup>.
- (iv) *Study of non-targeted effects.* The possibility to irradiate the cytoplasm, without irradiate the nucleus gives the opportunity to study non-targeted effects, that also include effects on non-irradiated cells that respond to their neighbors irradiated cells<sup>5,24</sup>. Several reports even point to the involvement of mitochondria in the signaling pathways of the bystander response, induced by both nuclear and cytoplasmic irradiations<sup>25–28</sup>.
- (v) *Development of approaches for tumor therapy.* A series of reports have been addressed to study the effects of specially modified proton microbeams to irradiate cell systems and tissue models. As example, with microbeams is possible to study the dose-rate effects where similar doses can be delivered with different fluences (continuous or pulsed microbeams)<sup>29–31</sup>. Similar doses can also differently distributed on cell populations or on human skin models, as recently demonstrated at the SNAKE facility. These studies offer the possibility to analyze the effects of dose distributions in cancerous and healthy tissues<sup>32,33</sup>.

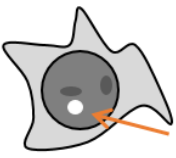
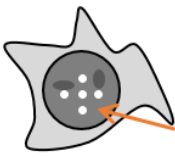
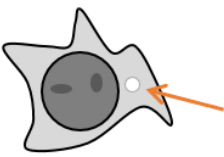
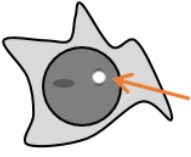
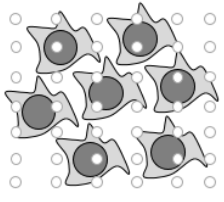
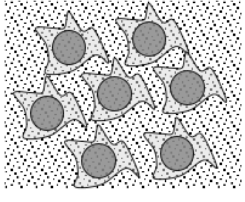
Single cells	Single spot 	Pattern 	Study the kinetics of DNA signaling and repair proteins tagged with GFP-protein.
	Cytoplasm or mitochondria 	Nucleolus 	
Cell population	Regular pattern 	Homogenous irradiation 	Study the effects of the same dose distributed in different ways

Figure 3. Microbeam irradiation applications. Using a microbeam it is possible to study the radiation-induced biological responses at the single cell level after targeted irradiations in the nucleus, in the cytoplasm or in sub-cellular compartments. In addition, thanks to the focalization and scanning system, is possible to study the effects of two dose distributions on a cell monolayer.

The major limitation of these devices is their restricted availability within the scientific community. This is due to the size requirement of these facilities and the costs of building and maintaining them in operation. Additionally, each charged particle microbeam facility is limited in the particle spectra and energies provided, and numerous technical problems had to be solved to perform radiobiological experiments<sup>9</sup>.

Besides these disadvantages, with respect to classical irradiation systems (random sources, X-Rays,  $\gamma$ -Rays and UV irradiations), microbeam target irradiation stands out for different characteristics:

- the spatial resolution, that determines the precision of the sample targeting
- the temporal resolution, which allows for fast samples irradiation within few seconds
- the dose resolution, that permits to deliver a controlled and precise number of particles at the cellular level.

A microbeam line with these characteristics is installed at the AIFIRA platform (*Applications Interdisciplinaires des Faisceaux d'Ions en Région Aquitaine*) situated in the CENBG (Centre d'Études Nucléaires de Bordeaux-Gradignan). This equipment, described in Bourret *et al.*<sup>20</sup>, represents a major resource to study the biological responses to protons and  $\alpha$ -particles in both single cell (at subcellular level, nucleus and cytoplasm) and cell population.

Briefly, the beam line is constituted by an accelerator (Singletron<sup>TM</sup>, High Voltage Engineering Europa, The Netherlands) that delivers protons and Helium ions with energies up to 3 MeV. To target single living cells, the beam is strongly collimated to reduce the particles flux to a few thousand ions per second on target and focused using a triplet of magnetic quadrupoles to achieve a sub-micron resolution under vacuum. The ion beam is extracted in air through a 200 nm thick Si<sub>3</sub>N<sub>4</sub> window (Silson Ltd., Northampton, England) and enters the sample through a 4- $\mu$ m thick polypropylene foil (Goodfellow) used as a cells support. The ion beam is positioned on target by means of electrostatic scanning plates situated downstream of the last quadrupole. In case of protons, the mean number of particles (N) hitting cells is linearly related to the opening time and the relative statistical fluctuation in the number of traversals delivered decreases as N increases. The exposure of targeted cells to charged particles is controlled using a fast electrostatic beam deflector allowing to open and close the beam within 1  $\mu$ s (DEI PVM-4210). In case of  $\alpha$ -particles, each particle is detected upstream with a BNCD (Boron-doped Nano-Crystalline Diamond) from which secondary electrons emitted are collected using a channeltron electron multiplier (These new achievements are obtained during my PhD and are presented in Manuscript 1).

The irradiation end-station is constituted of a motorized inverted fluorescence microscope (AxioObserver Z1, Carl Zeiss Micro-Imaging GmbH) equipped with a 14 bits Rolera EM-C<sup>2</sup><sup>TM</sup> Camera (QImaging) which is positioned horizontally at the end of the beam line. It can be equipped with up to 6 objectives and fluorescence filter sets. A good compromise between high numerical aperture (NA) and long working distance is obtained with a 63x objective (LD Plan-Neofluar 63x/0.75, Optical resolution of about 400 nm, Carl Zeiss MicroImaging GmbH). Fluorescence light is provided by Light Emitting Diode (LED) illuminating system (Colibri2<sup>TM</sup>, Zeiss) with negligible heat production.

Recently, to complete the imaging capabilities present on the beam line, we installed a commercially available laser diode (Roper Scientific, iLas2<sup>TM</sup>) coupled to a galvo-scanned mirror on our microscope. This set-up allows performing fluorescence recovery after photobleaching (FRAP) measurements in combination with charged particle irradiations (Figure 4). Some preliminary results obtained using this system are discussed in the *Experimental results* section.

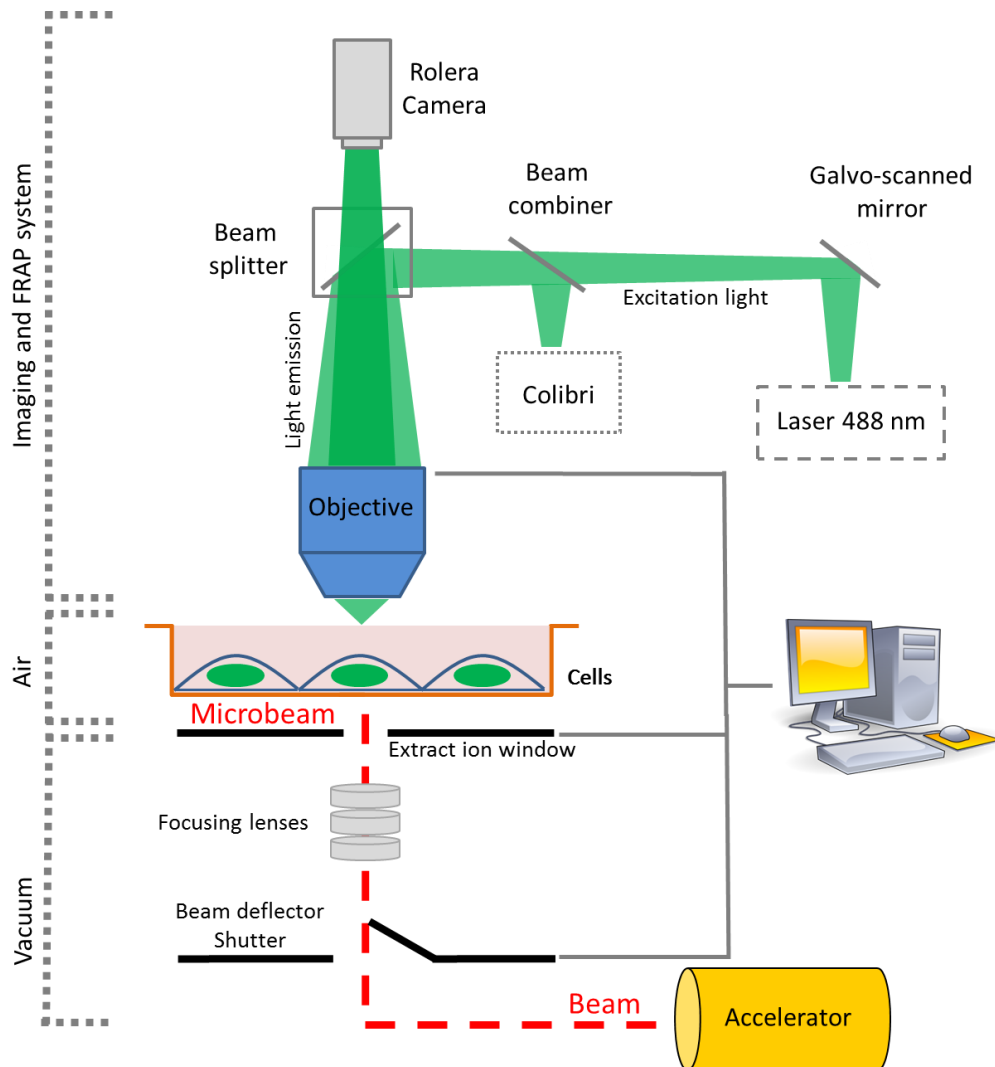


Figure 4. Scheme of the micro-irradiation set-up and imaging system. Charged particles are focused in a micrometer spot, using a triplet of magnetic lenses, and driven to the target cell under vacuum. The beam is extracted in air through a 200 nm thick extract window. A fluorescence microscope (Zeiss AxioObserver Z1) equipped with a 14-bits Rolera Camera is placed at the end of the beam line to visualize cells and perform online fast time-lapse imaging. A 488 nm Laser diode (iLas2™, Roper Scientific) coupled to a galvo-scanned mirror is installed on the microscope. The whole experiment is controlled by custom-made irradiation and acquisition software.



This micro-irradiation set-up allows the exposure of cells to 3 MeV protons and  $\alpha$ -particles presenting a Linear Energy Transfer of 12 and 148  $\text{keV}\cdot\mu\text{m}^{-1}$ , leading to a maximum range in liquid water of 148 and 18  $\mu\text{m}$ , respectively (Figure 5). These characteristics coupled with microscopic fluorescence techniques and a fast time-lapse imaging permit to obtain information on the protein dynamics as a function of their role, time, delivered dose and particles LET.

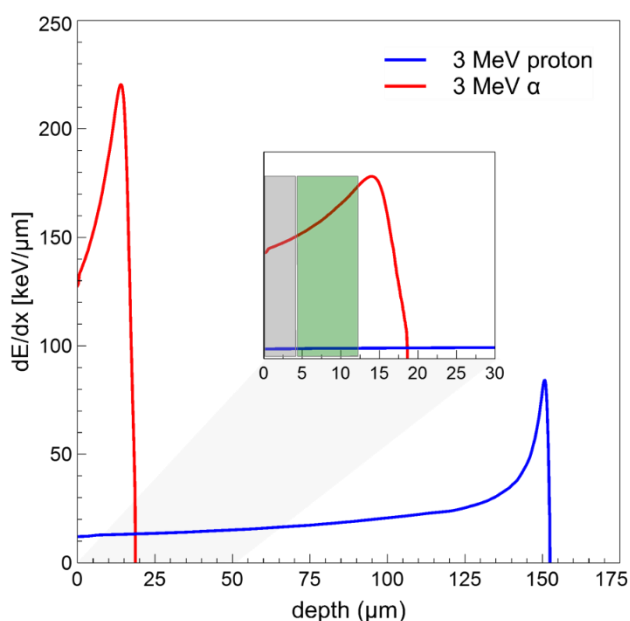


Figure 5. Simulations of 3 MeV protons and  $\alpha$ -particles in water. SRIM 2013 simulations<sup>34</sup> show that 3 MeV  $\alpha$ -particles pass through 18  $\mu\text{m}$  and 3 MeV protons pass through 148  $\mu\text{m}$  of water before to lose all their energy. The inset shows the position and thickness of polypropylene foil (grey square) and of cell (green square) with respect to the particle deposited energy.

It is important to mention that biological responses not only depend on the localization of irradiation, but also on the type of particle and on the deposited energy. Monte Carlo simulations allow the quantification of dose distributions at the microscopic level in well-defined conditions (beam focalization, extraction window, and cellular phantom). Modeling radiation-induced damages is today an active and intense field of research and more and more refined simulations are currently developed<sup>35</sup>. The Monte Carlo Geant4 toolkit has been widely adopted in the radiobiology community since it can reproduce the stochastic nature of interactions between elementary particles and matter<sup>36</sup>. Numerous specialized Monte Carlo codes, usually called “track structure codes”, have been developed for microdosimetry simulations and are able to simulate precisely particle-matter interactions, with (i) the “physics” stage, (ii) the “physico-chemical” and (iii) the “chemical” stages allowing in particular the simulation of oxidative radical species. To better understand the biological

effects of IR at the cellular scale, it is crucial to model the radiation energy deposit in cells and cellular responses.

The iRIBio (*ionizing Radiation interactions and Biology*) group has initiated a simulation activity based on the Geant4 simulation toolkit (an open-source and publicly available simulation platform) in order to develop models of track structure caused by IR traversals through living biological specimens and to compare predictions with experimental data<sup>37</sup>. The Geant4 tracking capabilities at the sub-micrometer scale were first extended and validated by the group, allowing to propose a complete simulation platform for the design of specific micron and sub-micron beam irradiation. These state-of-the-art setups allow for example a precise control of delivered ionizing doses to living organisms. Geant4 is further extended for the development of high-resolution 3D cellular “phantom” models obtained from confocal microscopy imaging and from ion beam analysis techniques available on the microbeam line facility. These “phantoms” allow high-resolution modeling of cell geometries and a more realistic estimation of deposited doses<sup>37,38</sup>. In this way the total energy distribution is calculated and early biological damage induced by IR at the DNA scale can be estimated. (All simulations presented in this work were carried out with the help and courtesy of Dr. P. Barberet).

## Chapter 3

### ***Ionizing radiations induce cluster of DNA lesions***

When IR interact with biological material, they cause a sequence of events. Complex events that accompany the absorption of IR can be divided into four consecutive, temporal stages (Figure 6). During the first or “physical” stage, the energy deposition is caused by the incident radiation and secondary electrons are generated. The resulting species are extremely unstable and undergo fast reorganization in the second or “physicochemical” stage. These processes produce radical and molecular products of radiolysis that are distributed in a highly non-homogeneous track structure. The initial ( $10^{-15}$  s) spatial distribution of reactants is then directly used as the starting point for the so-called third stage of “non-homogeneous chemistry”. During this stage, the various chemically reactive species diffuse and react with one another or with the environment, until all intra-track reactions are complete ( $10^{-6}$  s). Finally, in a physiological system, there is a “biological” stage in which cells respond to the damage resulting from the products formed in the previous stages. During this stage ( $10^{-3}$  s and longer), the biological responses affecting the long-term consequences of radiation exposure are induced<sup>39–44</sup>.

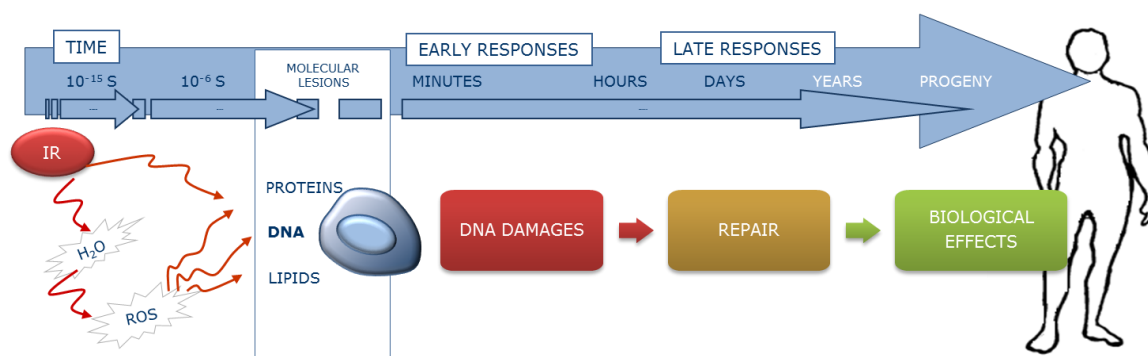


Figure 6. Representation of ionizing radiation effects. High and low doses of ionizing radiation can damage the DNA and other target in direct and indirect way. Cell response mechanisms act in a time scale from second to few minutes by signaling the damage and repairing it if possible. If misrepaired, the cell damage can lead to biological effects more or less important for the human life.

IR produces through direct and indirect effects a variety of DNA lesions, such as single strand breaks (SSBs), double strand breaks (DSBs), abasic sites (either apurinic or apyrimidinic), a variety of base modifications, sugar modifications, and DNA-DNA and DNA-protein cross-links<sup>45,46</sup>. The damage

spectrum is influenced by dose, dose-rate and type of radiation exposure. DSBs are the most lethal lesions since, if unrepaired, they can result in cell death and, if misrepaired, they can cause chromosomal translocation: an early step in the etiology of carcinogenesis<sup>47</sup>. Also, complex damages, defined by the proximity of DSB to other lesions such as DSB or SSB, could be induced by the high concentration of ionizing events along the particle track. Indeed, by using Monte Carlo track structure simulations, the increase of DSB complexity as a function of the LET has been shown (Figure 7)<sup>48-51</sup>.

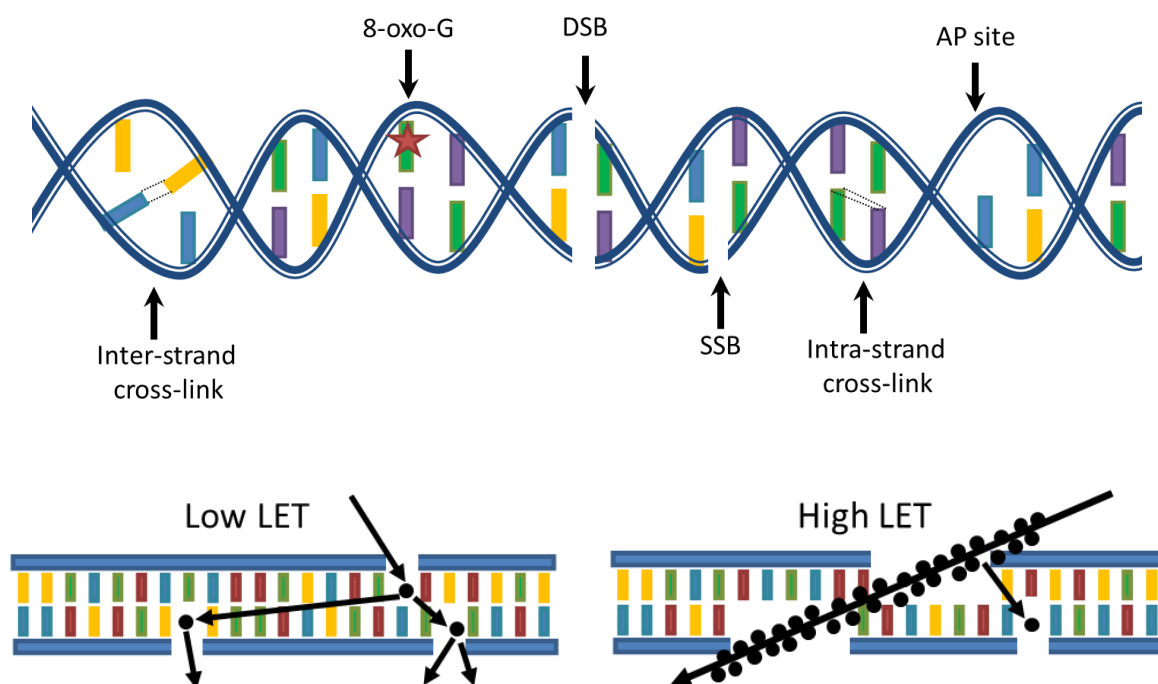


Figure 7. Radiation-induced spectra of DNA damages. The DNA damage can be of different entities, from a modification of bases to double strand breaks. Ionizing radiations produce clusters of DNA damage combining different types of damage depending on the particle LET used. Each dot represents event of ionization or excitation.

To protect their genome from the constant and severe assault from external and internal DNA damaging agents, cells have evolved elaborate defensive strategies, collectively termed the DNA damage response<sup>52</sup>. The choice of repair complex from the large panel of repair mechanisms depends on the type of damage occurred.

Mismatched DNA bases are replaced with correct bases by *mismatch repair* (MMR), and small chemical alterations of DNA bases are repaired by *base excision repair* (BER) through excision of the damaged base. More complex lesions, such as pyrimidine dimers and intra-strand crosslink, are corrected by *nucleotide excision repair* (NER), through the removal of an oligonucleotide of approximately 30 bp containing the damaged bases<sup>53-58</sup>. SSBs are repaired by *single-strand break repair* (SSBR), whereas

DSBs are processed either by *non-homologous end joining* (NHEJ) or *homologous recombination* (HR)<sup>59,60</sup>.

The various DNA repair pathways sometimes compete with each other for processing the same lesion, and each step in a multistep repair pathway creates an intermediate that constitutes another lesion, which may be susceptible to intervention by enzymes from another pathway. There are increasing evidences that the various DNA repair pathways are not separated, but well interlinked<sup>53</sup>. The *DNA damage response* (DDR) is a signal transduction pathway that senses DNA damage and replication stress and sets in motion a choreographed response to protect the cell and ameliorate the threat to the organism<sup>52,61</sup>.

Sometimes the first protein to access the lesion may be a transcription factor or another protein that is not directly involved in DNA repair. Also, the response to damage may require a threshold level of damage so that very low levels of lesions might be overlooked, whereas substantial amounts of damage or particular type of lesions may induce a robust response<sup>62</sup>.

*Base Excision and Single Strand Break Repair.* The base excision repair is designed to correct oxidized bases, abasic sites and SSBs. The sensory component of the repair system is made up by a large family of DNA glycosylases that continuously scan the genome for base modifications. Once bound to its target, the glycosylase separates the modified base from the sugar-phosphate backbone by enzymatic cleavage, leaving an abasic site<sup>63,64</sup>. Subsequently, other sensor proteins such as ATR, phosphorylate mediator proteins, which can amplify the DNA damage response by recruiting ATR substrates. The activation of poly(ADP-ribose) polymerase-1 (PARP-1), which binds the strand break site and reorganizes the chromatin, is one of the first event induced to repair SSBs. PARP-1 recruits DNA repair and chromatin modifying complexes at the DNA damage sites. In a PARP-dependent manner, XRCC1 is recruited and promotes SSB repair following DNA end-processing by XRCC1 interacting proteins, such as DNA polymerase  $\beta$ , polynucleotide kinase (PNK), and the nuclease APE1<sup>60,65-67</sup>. The reparation finished when ligase 3 (Lig III) ligates the broken DNA back together resolving the SSB with the correct insert. When damage is repaired all proteins dissociate from the SSB<sup>68</sup> (Figure 8).

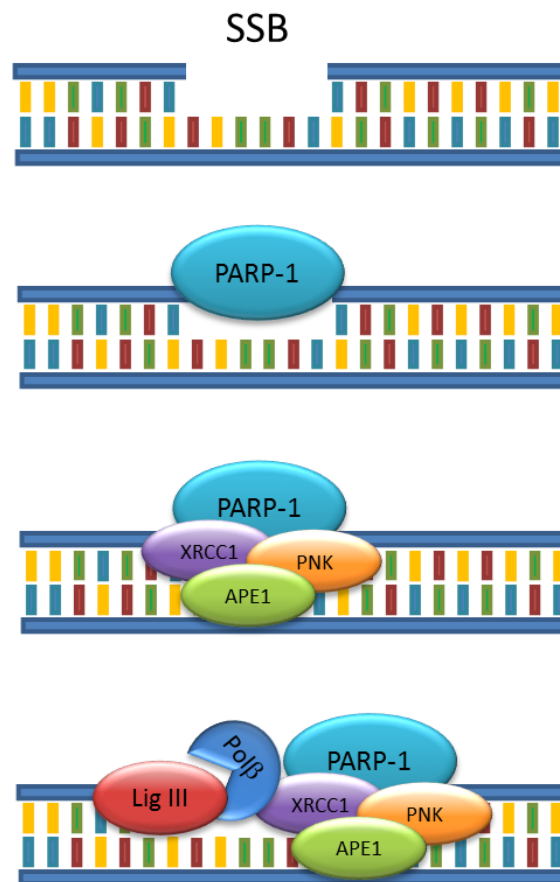


Figure 8. Simplified representation of SSB repair pathways and the actors involved in this repair mechanism.

*Double Strand Break Repair.* Double strand breaks (DSBs) are life threatening lesions, which repair is promoted by an intrinsic network of multiple DNA repair pathways. Repair of DSBs occur in two distinct kinetics. Approximately 85% of ionizing radiation-induced DSBs are rapidly repaired within 10-30 minutes, while 15% of the DSBs are repaired in a slower manner and it can take up to 24 hours. The observation of the fast and slow components of DSB repair by DNA fragmentation analysis, has suggested the role played by the chromatin compactness, in different cell types after irradiation to low and high LET radiations<sup>51,69,70</sup>. The DNA is packaged in a three-dimensional structure and chromatin is in a high-compacted state (heterochromatin), except when it is relaxed during active transcription (euchromatin). In response to DNA damage, chromatin undergoes to rapid local and global decondensation, a process that has been proposed to facilitate genome surveillance by enhancing access of DDR proteins to damaged sites<sup>71-73</sup>.

The ATM kinase plays a central role in chromatin relaxation, and it is responsible for recognition of DSBs, and the recruitment of repair factors to the break<sup>74,75</sup>. ATM phosphorylates itself and a specialized histone H2AX on Ser139 (named  $\gamma$ H2AX) and initiates a cascade of factor assembly<sup>76</sup>. ATM

also phosphorylates MDC1 that, through its fork head-associated (FHA) domain, further propagates  $\gamma$ H2AX spreading. The formation of extensive  $\gamma$ H2AX regions is important for sustaining the DNA damage response that is achieved through the recruitment of an intricate network of chromatin-modifying enzymes regulating ubiquitination, sumoylation, acetylation and methylation. It is worth noticing that the ubiquitin ligase RNF8 has emerged as key regulator of this molecular pathway with critical roles in early formation of DNA repair foci complex<sup>77</sup>. The ubiquitin ligase RNF8 protein belongs to the RING (Really Interesting New Gene) domain containing E3 ubiquitin ligase family, and thus, it is able to attach ubiquitin molecules to target proteins for propagation of molecular signal. Together with two more ubiquitin ligases, RNF168 and HERC2, RNF8 promotes the recruitment of the BRC1-A complex, a ligase that amplifies the cascade signal<sup>52,78,79</sup>.

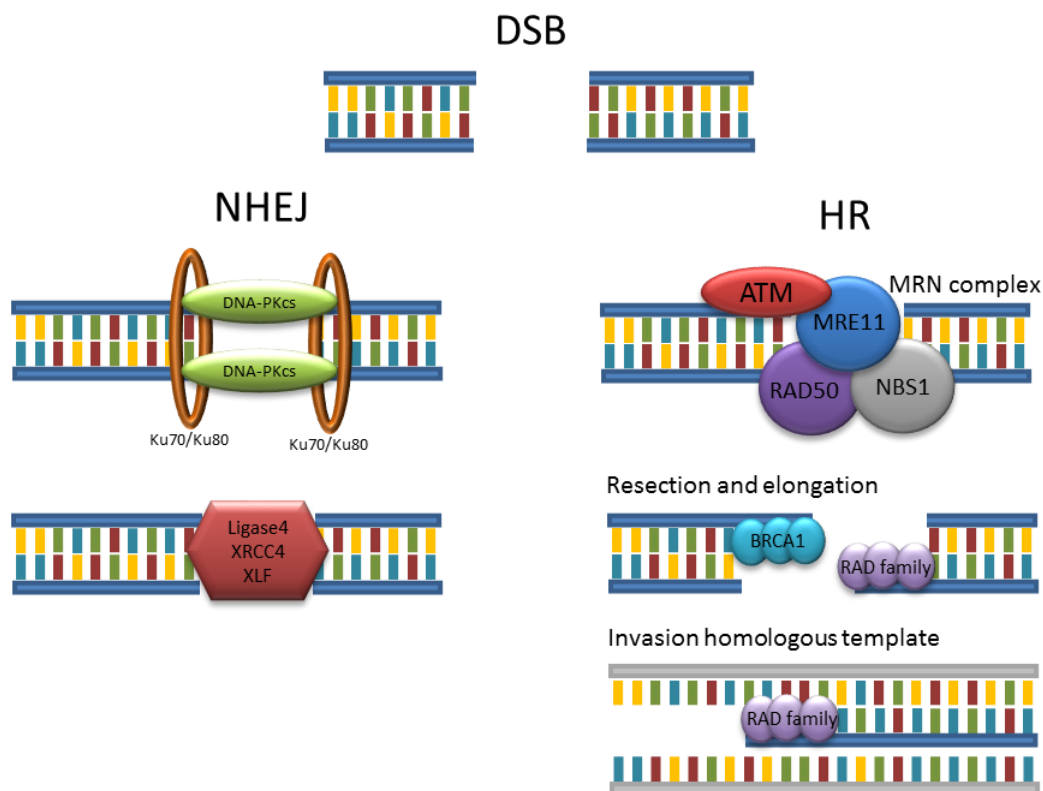


Figure 9. Schematization of NHEJ and HR mechanisms involved in DSBs repair.

Faced with a double strand break in the DNA, cells can employ two different pathways for its repair: *Non-Homologous End Joining* (NHEJ) and *Homologous Recombination* (HR) (Figure 9). Although NHEJ factors are recruited to DSB more rapidly than HR factors, and NHEJ and HR factors are independently recruited to DSB, there is a period of time when both sets of factors are present at the

damage sites<sup>80</sup>. This is consistent with the idea that the pathway choice may be regulated by one or more proteins acting in both pathways<sup>81</sup>.

NHEJ is fast and the simplest repair pathway, that is active during the whole cell cycle<sup>82</sup>. This DSB repair pathway, which binds DNA double strand breaks in juxtaposition and even incompatible ends, is mostly error prone. The NHEJ repair is executed by two core protein complexes: the DNA-dependent protein kinase (DNA-PKcs) complex, composed of the Ku70/Ku80 heterodimer (Ku) and catalytic subunit of the DNA-PKcs, and a second complex of ligase IV with its co-factors XRCC4 and XFL (also known as Cernunnos). The mechanism starts with the Ku complex activation that recognizes and binds the DSB ends of the damaged site<sup>83,84</sup>; then the DNA-dependent protein kinase catalytic subunit (DNA-PKcs) is recruited and it stabilizes the DSB ends, promoting the phosphorylation of several substrates including p53, Ku complex, DNA Ligase IV/XRCC4, all of which may facilitate end processing reactions<sup>85</sup>. End processing involves the removal of damaged or mismatched nucleotides by nucleases, such as PNK and Artemis, and/or synthesis of single strand DNA (ssDNA) by DNA polymerases<sup>86</sup>. For heterochromatic DSBs, ATM phosphorylation of Kap1 allows the localized chromatin relaxation, facilitating the repair by NHEJ. This process requires Artemis and mediator proteins in addition to ATM<sup>87</sup>.

HR is active during the S- and G2-phase of the cell cycle, when sister chromatids are available. This DSB-repair pathway is regarded as error-free, since HR uses an undamaged homologous sister chromatid as a template. During the first step of HR, the broken ends are resected to generate long stretches of single stranded DNA with 3' ends. The preparation of these single strands is mediated by the MRE11-RAD50-NBS1 (MRN) complex, which detects the lesion and promotes the activation of the key DDR signaling kinase ATM. Then, phosphorylation of H2AX, recruitment of MDC1, and association of 53BP1 and BRCA1 generate ssDNA overhangs around DSB<sup>88</sup>. The resulting ssDNA is recognized and coated by replication protein A (RPA) that protects and prevents the formation of higher order structures. At this point, RAD51, RAD52 and RAD54, after scanned the surroundings for a homologous sequence, promote the invasion into the homologous template provided by the sister chromatid<sup>71,73,89,90</sup>.



## Chapter 4

### *Ionizing radiation and non-targeted effects*

Accumulating evidences have shown that an energy deposition in the nuclear DNA is not only event which can trigger to cellular damage. There is an increasing evidence from a number of laboratories indicating that extra-nuclear target and or extra-cellular events may also play an important role in determining the biological responses to ionizing radiation<sup>91,92</sup>. A cellular reaction to radiations could derive from molecules other than DNA, such as lipids, proteins, and cytoplasm. These phenomena are termed as “non-targeted effects” (NTE) and include the responses to radiation exposure of non-targeted molecules or of molecules which have not directly interacted with radiation<sup>25,93</sup>. These effects include radiation-induced *bystander effects*, *genomic instability*, *adaptive response*, *low dose hyper radiosensitivity* (HRS) and radiation induction of genes expression/modulation<sup>25</sup>. Consideration of NTE is important because probably there is not a direct correlation between the number of cells exposed to radiation and the number of cells that are at risk of showing effects such as mutation, chromosomal damage or apoptosis<sup>41,94</sup>. NTE imply that radiation may affect targets other than directly irradiated cellular nuclear DNA, such as proteins, cell membranes, and sub-cellular compartments<sup>24,95-97</sup>. Mitochondria, as well as nucleoli, could be interesting targets and the understanding of their role in the cellular response to IR is nowadays a challenge.

Mitochondria may account for up to 30% of the total cell volume and they are the only sites where extra-nuclear DNA resides. Therefore, mitochondria are likely to be a major target of IR together with the cell nucleus<sup>26</sup>. Mitochondria dysfunction can lead to an increased release of reactive oxygen species (ROS), produced during normal oxidative respiration, which have been associated DNA lesions, increased levels of cell death, and cancer<sup>98,99</sup>. Today, more and more studies aim at studying the effect of mitochondria irradiations. Zhou *et al.* reported an increase mitochondrial mass 4 hours after X-Rays exposure and, more importantly, they showed a decrease in the mitochondrial membrane potential<sup>100</sup>. The mitochondrial polarization state is directly linked to the mitochondria function. When the membrane potential is maintained, mitochondria are considered polarized and fully functional. A loss of potential across the membrane is accompanied by a variety of cellular responses, such as apoptotic cell death<sup>101,102</sup>. Wu *et al.* found an increased level of cell mutations after cytoplasmic irradiation using  $\alpha$ -particle microbeam<sup>96</sup>. Moreover, several groups have reported an involvement of mitochondria in the signaling pathway involved in both cytoplasm irradiated and

bystander cells<sup>24,26</sup>. Understanding the impact of IR on mitochondrial functions (a major intracellular source of reactive oxygen) and the handling of free radicals is therefore likely to be useful.

## Questions addressed in this work

The knowledge of interaction between IR and living tissues has an important role in many fields, such as health risks associated to low dose exposure from natural or working environment, the appearance of radiation-induced tumors, and the new cancer therapeutic approaches.

Conventionally, the effects of IR have been explained using the “Target Theory”. Therefore, deleterious effects of IR, such as mutagenesis and carcinogenesis, can be attributed to the damage of a cellular target, usually identified as nuclear DNA *via* direct absorption of radiation energy. Therefore, numerous studies show the involvement of other cellular structure in response to ionizing radiations. The observation of early cellular responses activated to ionizing radiations requires highly controlled irradiation conditions. The AIFIRA charged particle microbeam allows us (i) to control the dose by delivering a precise number of particles, (ii) to irradiate a specific target with a micrometer precision, (iii) to visualize in real time living cells.

In this context, during the PhD my efforts were dedicated to:

- establish stable transfected cell lines expressing GFP-tagged proteins involved in different DNA damage signaling and repair pathways. In addition, stable transfected cell lines expressing GFP-tagged proteins involved in the structure of different cellular compartments permit to irradiate other targets than DNA.
- irradiate cells expressing GFP-proteins in highly controlled conditions and to visualize DNA damages induced by one  $\alpha$ -particle. To achieve this point a thin membrane which detects single  $\alpha$ -particles without interfering with beam lateral resolution and trajectory was developed.
- correlate protein responses with delivered doses and particles Linear Energy Transfer (LET). The mean recruitment time of proteins to the DNA damages gives the spatio-temporal organization of DNA damage response machinery.
- develop a system that allow the measurement of protein dynamics and binding ability in the damaged site. A 488 nm laser able to bleach GFP signal is installed and validated in order to perform FRAP experiments.
- participate in a project conducted by the Munich University where single mitochondria are irradiated with different particles.

## Experimental Results

The micro-irradiation beam line installed at AIFIRA routinely functions for micro-irradiation experiments. Micro-irradiation is a promising approach to provide more localized induction of DNA damage in highly controlled conditions. These highly controlled conditions consist in irradiating living cells with a precise number of particles in a precise area. The area can be chosen between nucleus and cytoplasm and successive analysis of cell responses can be performed. The microbeam line need continue technical improvements that I contribute to develop. Figure 10 shows in a simplified manner the main results that I obtained during my PhD. These results are discussed with more details in the following sections and in three manuscripts.

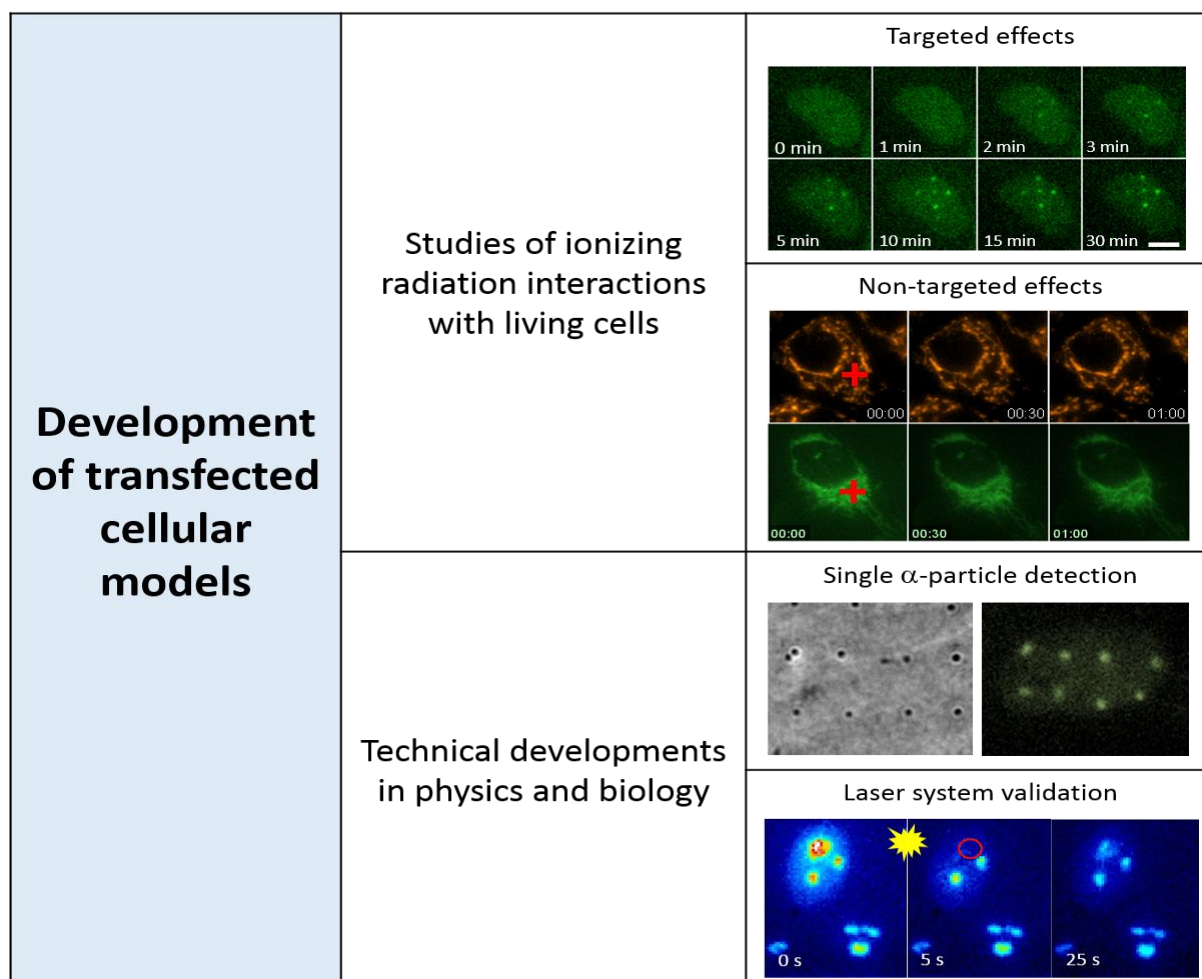


Figure 10. Main results obtained by using the micro-irradiation beam line.

## 1. Stable transfections of GFP-tagged proteins for DNA and sub-cellular structures visualization

Since its discovery, the use of GFP-expressing cells is hugely increased to monitor genes expression and proteins localization in living cells<sup>103</sup>. One of my principal efforts was to develop, establish and characterize stable transfected cell lines which enable to visualize, target and study different proteins involved or in the DNA repair pathways or in the structure of subcellular compartments. All along my PhD, I validated different stable transfected cell lines (HTB96-U2OS cells) and I established numerous transfected clones expressing several GFP-tagged proteins. The principal reason that lead to the choice of proteins involved in DNA repair pathways was the fact that despite the biochemical mechanisms of eukaryotic DNA damage repair have been largely studied, much remains to be elucidated regard the regulation of the DNA repair pathways and the connections between them. Another critical question that is worthwhile to answer is on roles played by subcellular organelles in response to ionizing radiations.

First, I focused on the generation of cell lines expressing GFP-tagged proteins involved in DNA repair pathways: GFP-XRCC1 (*BER/NER* pathways)<sup>104</sup>, GFP-OGG1 (*BER*, 8-oxo-guaanine)<sup>105</sup>, GFP-RNF8 (*Homologous recombination*)<sup>106</sup>, GFP-Ku70 and GFP-Ku80 (*Non-homologous End-joining*)<sup>107</sup>. These cell lines are established to study the dynamics and kinetics induced by 3 MeV charged particles (protons and  $\alpha$ -particles) as a function of the delivered dose and the particle LET.

Second, I defined stable transfected cell lines to visualize specific subcellular compartments, such as the nuclei (GFP-H2B)<sup>108</sup>, nucleoli (GFP-Nop52)<sup>109</sup> and mitochondria (Matrix-roGFP2)<sup>98</sup>. GFP-H2B and GFP-Nop52 were used to validate the 488 nm laser installed on the microbeam line end-station with which we are able to perform FRAP experiments. Matrix-roGFP2 triggers a good collaboration with the Bundeswehr University Munich which leads to mitochondria irradiations by ensuring the membrane integrity.

Third, I established stable transfected cells expressing GFP-polyQ peptides (23 and 74 repeats)<sup>110</sup> to test the radiation-induced effects on the proteostasis. Indeed, when exposed to different stressors, polyQ peptides could agglomerate and precipitate in cells and could be detected and quantified *in situ* and *in cellulo*.

The constructs containing GFP-tagged proteins have been recovered from different sources which are listed in Table 1.

<i>Protein</i>	<i>Source</i>	<i>Reference</i>
<i>XRCC1</i>	Kindly provided by Akira Yasui	Lan et al., PNAS, 2004
<i>OGG1</i>	Kindly provided by Anna Campalans and Pablo Radicella	Campalans et al., J Cell Sci, 2007
<i>RNF8</i>	Kindly provided by Jiri Lukas	Mailand et al., Cell, 2007
<i>Ku70</i>	Addgene #46957	Britton et al., Journal of Cell Biology, 2013
<i>Ku80</i>	Addgene #46958	Britton et al., Journal of Cell Biology, 2013
<i>H2B</i>	Addgene #11680	Kanda et al., Current Biology, 1998
<i>Nop52</i>	Kindly provided by Danièle Hernandez-Verdun	Savino et al., Journal of Cell Biology, 2001
<i>Matrix-ro</i>	Addgene #49437	Waypa et al., Circulation Research, 2010
<i>PolyQ-23</i>	Addgene #40261	Narain et al., Journal of medical genetics, 1999
<i>PolyQ-74</i>	Addgene #40262	Narain et al., Journal of medical genetics, 1999

Table 1. List of constructs used to produce stable transfected cell lines containing selected plasmids where the gene of interest is coupled with the GFP gene.

## 2. Validation of a thin membrane for single $\alpha$ -particles detection and irradiation of GFP-RNF8 transfected cells

A significant part of the natural background radiation exposure of humans is caused by  $\alpha$ -particles from the inhalation of radon gas<sup>3</sup>. In addition,  $\alpha$ -particles are increasingly considered in medical applications, such as targeted radiation therapy, where  $\alpha$ -emitting radionuclides are specifically localised to deliver a cytotoxic radiation dose to cancerous tissues, while sparing surrounding healthy tissues<sup>111–113</sup>. Therefore, potential health effects resulting from  $\alpha$ -particles exposure continue to be the focus of numerous studies<sup>10,11,114–118</sup>. Understanding cellular responses to complex DNA damages specifically induced by  $\alpha$ -particles is of particular importance and requires specific tools that allow the selective irradiation of single cells and follow-up observations of induced damage *via* dedicated biological markers (DNA damage signalling, DNA repair protein). By using a <sup>239</sup>Pu  $\alpha$ -particles emitting source, I irradiated GFP-RNF8 and GFP-XRCC1 cells. Using this irradiation method and combining it with  $\gamma$ H2AX *in situ* immunodetection assay, I observed that GFP-RNF8 relocalized to the DNA damage induced by one traversal and it persisted within the damaged site 30 min after irradiation. XRCC1 was difficult to visualize a posteriori because this protein dissociate from damaged site within 15 min<sup>119</sup>. Despite this source has extensive and of easier access with respect to the micro-irradiation beam line, the fluence of delivered particles is very low (30 min are necessary to obtain a mean number of hits per nucleus of  $7.6 \pm 3.3$ ), and the irradiation time and position are unknown<sup>37</sup>. Alternatively,

charged-particle microbeams can target living cells with single charged particles and can be used extensively to study various biological endpoints. Modern end-stations, equipped with fluorescence time-lapse imaging, provide the opportunity to visualize and quantify in real-time the early radiation-induced cellular response. However, due to the limited range of  $\alpha$ -particles in matter (a few tens of micrometres), it is difficult to detect single  $\alpha$ -particle without significantly altering the microbeam energy and size. For this reason was necessary to develop a system able to detect single  $\alpha$ -particles without interfering with the particle energy and trajectory and visualize the DNA effects in real time. Thanks to the collaboration with Michal Pomorski (CEA) and Philippe Barberet, we developed a Boron-doped Nano-Crystalline Diamond (BNCD) membrane that allows reliable single  $\alpha$ -particles detection and single cell irradiation with negligible beam scattering. The BNCD membranes give reproducible detection efficiency and are very homogeneous on millimetre surfaces. In addition to the detection capability, they are transparent and non-fluorescent, making them compatible with bright field and fluorescence imaging. The detection of single  $\alpha$ -particle traversals allows controlled irradiation of living cells. Post-irradiation analyses showed that GFP-RNF8 accumulates continuously at single  $\alpha$ -particle track during the first 30 minutes after irradiation. We observed that the intensity of irradiation-induced foci varies from one to another reflecting most probably the chromatin heterogeneity inside the nucleus. These achievements are detailed in the **Article 1** published in *Scientific Reports*.

### **3. GFP-RNF8 and GFP-XRCC1 proteins show different spatiotemporal kinetics after proton and $\alpha$ -particle microirradiations**

The AIFIRA microbeam therefore permits highly controlled irradiations with 3 MeV  $\alpha$ -particles and protons which have a Linear Energy Transfer (LET) of 148 and 12 keV. $\mu\text{m}^{-1}$ , respectively. It is known that DNA damage complexity and then formation of Single Strand Break (SSB) or Double Strand Break (DSB) increases with increasing LET<sup>48</sup>. For recognizing and repairing these damages, cells have evolved efficient defense system mechanisms in which several proteins are considered to be involved. *In vitro* studies aim to understand the role and the chronological recruitment order of these proteins. In recent years, several methods have been developed to introduce localized DNA lesions and subsequent real-time analysis of the DNA damage response in living cells starting immediately after irradiation. A variety of laser micro-irradiation setups have been described to induce DNA damages and to study the DNA damage response<sup>120-123</sup>. However, lasers (mono-energetic light photons) generate different types of DNA damages within the nucleus in a manner dependent on

wavelength, energy, exposure time, and on the setup itself<sup>9</sup>. With respect to laser micro-irradiation systems, charged particle-induced DNA damage is better defined and protein kinetics can be correlated with a measurable deposited energy<sup>19,124</sup>. Charged particle microbeams permit to vary particles and number of delivered particles per nucleus adjusting the deposited energy per cell and allowing the study of both particles LET and dose. Monte Carlo simulations and its extensions Geant4 and the Geant4-DNA<sup>125-127</sup> allow to measure the deposited energy per nucleus and particle track structures. By using the combination of charged particle microbeam and Monte Carlo simulations, it is possible to answer to challenging questions such as how fast is the recognition of various types of damaged DNA? Which proteins arrive first to the sites of DNA damage? What is the affinity of different repair proteins for clustered DNA lesions? How do distinct proteins recognize clustered DNA lesions?<sup>128</sup>

In particular, we studied the recruitment time to radiation-induced DNA damages of GFP-XRCC1 and GFP-RNF8 proteins, known to be involved in the recognition, signaling and repairing of DNA damages, as a function of the deposited energy and the particle LET which give the spatial distribution of ionizations. XRCC1 is an essential scaffold protein required for the coordination of different repair pathways and associated to Base Excision Repair (BER) and SSB Repair (SSBR) pathways<sup>65,119,129</sup>. RNF8 is an ubiquitin ligase that promotes DSB-associated chromatin ubiquitination, and it interacts directly with MDC1 which accumulates at DSB sites among the first proteins<sup>106,130-132</sup>. Performing targeted irradiation with increasing number of 3 MeV protons and  $\alpha$ -particles, for the first time, we showed the evidence that GFP-RNF8 recruitment time is 10 times slower with respect to GFP-XRCC1 recruitment time for the same deposited energy. In addition, the GFP-RNF8 recruitment time is primarily impacted by particle LET with respect to XRCC1 which recruitment time is mainly influenced by the deposited energy. Indeed, the recruitment of RNF8 takes place 4 times at higher speed after  $\alpha$ -particles (high LET irradiation) than after protons (lower LET). The recruitment time of GFP-XRCC1 does not depend on LET but mainly on the deposited energy. These results are detailed in the **Manuscript 2**.



This work opens other questions not only about the investigation of the recruitment time to the DNA damaged sites of other proteins but also on the time lapse image acquisition in case of an instantaneous protein recruitment.

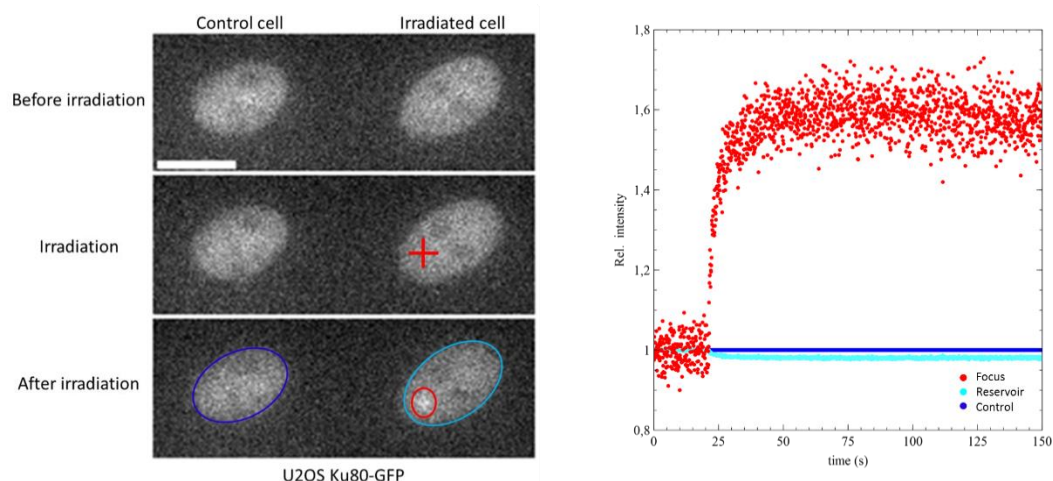


Figure 11. Visualization and targeting of cell nucleus containing the GFP-Ku80 protein before, during and after irradiation (left). Relocalization of the GFP-Ku80 protein in the irradiated area (right). The nucleus is irradiated in a micrometer spot (red cross) with  $10^5$  3 MeV protons 20 s after the images acquisition starts. Each image is taken every 100 ms with a new high-sensitivity camera (fast imaging). Scale bar: 10  $\mu$ m. Red: Measure of fluorescence intensity in the irradiated area; Cyan: fluorescence in the rest of nucleus; Blue: control nucleus used for normalization.

In particular, GFP-Ku80 occurred in very few seconds, as shown in Figure 11, when  $10^5$  3 MeV protons are delivered in a 2  $\mu$ m spot and this very rapid protein recruitment need to be monitored with a very fast image acquisition. To solve this issue and to perform fast imaging a new high-sensitivity camera was installed on the microbeam microscope. This new Rolera Camera EM-C<sup>2</sup><sup>TM</sup> is able to take images every 100 ms allowing a very fast imaging. Further studies are now necessary to study the response of this protein when different amount of protons or  $\alpha$ -particles are delivered.

#### 4. Photobleaching setup for the end-station of the AIFIRA charged particle microbeam

Local damage induced by charged particles delivered in a spot can be assessed by online fluorescence microscopy of GFP-tagged DNA repair proteins. These repair proteins are recruited in so called repair

foci around the damage and the local concentration of fluorescence intensities is monitored as a function of time after targeted irradiations. In this way protein kinetics and dynamics can be compared in different compartments of the same cell. Despite this type of fluorescence microscopy leads to measure the local concentration of the corresponding protein, the exchange processes between proteins in the damaged site cannot be measured. Fluorescence Recovery after Photobleaching (FRAP) experiments give information on the mobility fraction of the recruited proteins. This technique is based on the principle that fluorescent molecules lose their fluorescent capacity, i.e., they are photobleached, when they are irradiated with high-intensity light at their excitation wavelength. The redistribution of fluorescent and bleached molecules after photobleaching in a small area within a cell nucleus containing GFP-tagged proteins provides information on mobility of molecules under investigation<sup>133</sup>.

To perform these experiments, we installed a 488 nm Laser iLas2™ (Roper Scientific) coupled to a galvo-scanned mirror on the end-station of the micro-irradiation beam line. The validation of this new system is an essential step before to combine it with micro-irradiation experiments. With valuable contribution of Guillaume Devès two GFP-tagged proteins are photobleached and their mobile fraction are measured.

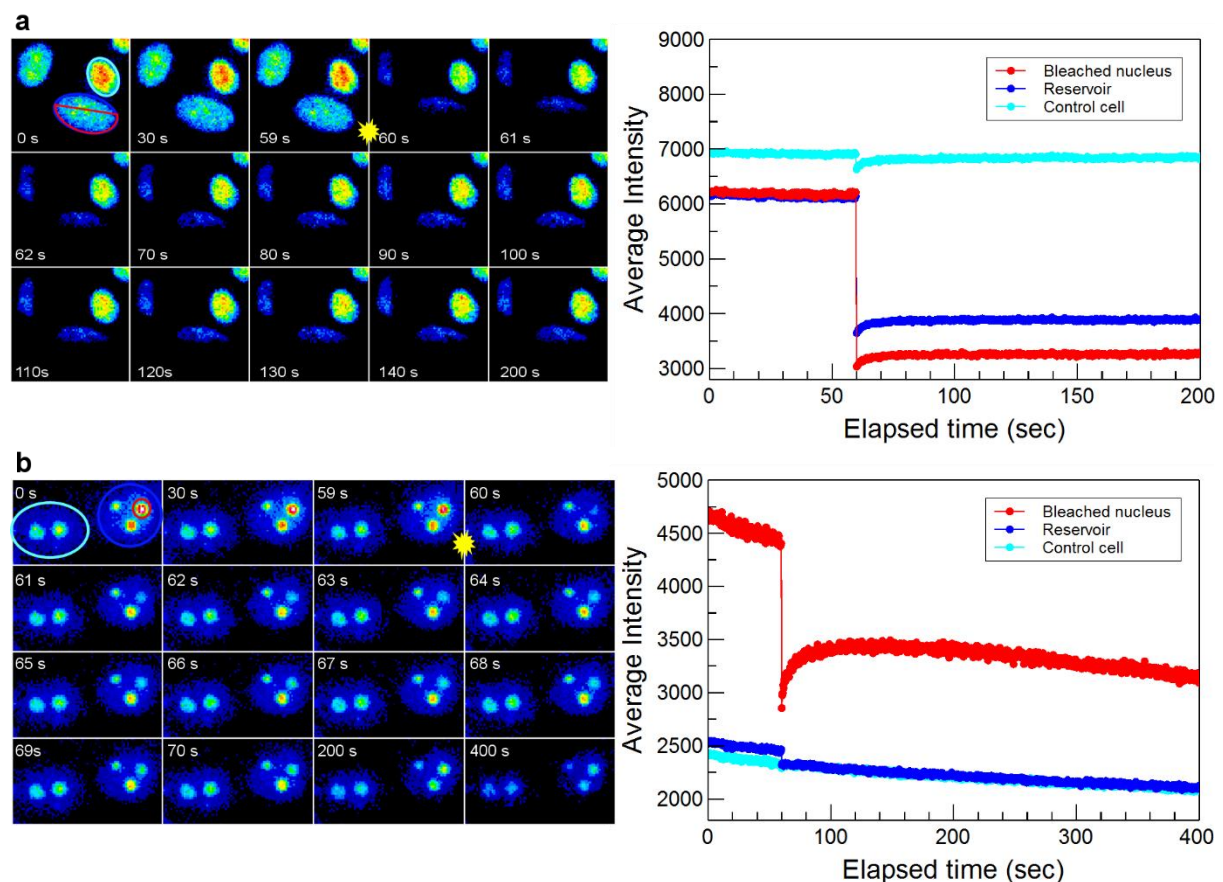


Figure 12. FRAP experiment on cells (a) GFP-H2B and (b) GFP-Nop52 (nucleolus protein). Left: Time-lapse

imaging every 400 ms. Photobleaching is done 60 s after images acquisition starting. Right: Measure of fluorescence intensity after photobleaching in the areas of interest. Cyan = control cell; blue = reservoir; red = photobleached nucleus.

The first protein, GFP-H2B, was selected because associated with the chromatin and then, fundamentally immobile<sup>134</sup>. The control software MetaMorph® was used for bleaching selected patterns (for example point, line, circle) with defined location, intensity and timing. GFP-H2B is an ideally target to calibrate the laser system because of its immobility. Figure 12a shows the first measurements of fluorescence intensity after photobleaching experiments of GFP-H2B protein. No recovery of fluorescence is observed during 3 min after bleach and the protein immobile fraction is calculated corresponding to 98%.

The second protein, GFP-Nop52, was selected because it represents a tiny target in the cell nucleus and allowed for the validation of targeting small areas<sup>135</sup>. Preliminary evaluation of the time-lapse images following methods reported in other studies<sup>134,136</sup> permits to obtain FRAP times of  $t_{1/2} = 43$  s (N = 18 cells). The immobile fraction of nucleolus expressing GFP-Nop52 calculated is 33% (Figure 12b).

The validation of this system allow us to move toward experiments combining micro-irradiation and photobleaching to study the proteins bond in the site of damage. Nowadays, micro-irradiation and laser diode for photobleaching experiments were available only at the GSI<sup>137</sup>.

## **5. Targeted irradiation of mitochondria with two microbeam facilities: the AIFIRA microbeam in Bordeaux and the SNAKE microbeam in Munich**

Finally, establishing Mito-roGFP2 cell line, I actively participated in a work realized in collaboration with the Bundeswehr University Munich and in particular with my colleague Dietrich Walsh. The main purpose of his project is to understand the role of cytoplasm and in particular the role of mitochondria in response to ionizing radiations. The prevailing dogma in radiation biology is that a high dose of energy deposited to the nucleus will lead to the destruction of cells<sup>93</sup>. However, the cytoplasm which is the cellular environment in which the majority of processes involved in the maintenance of cellular integrity take place has been rarely been taken into account. Despite cytoplasmic irradiation has been shown to be involved in inducing bystander effects and mutation induction<sup>96,138</sup> the question about the contribution of cytoplasmic components have in response to ionizing radiation remains open. Mitochondria constitute a large volume of cytoplasm and have been selected in this work to highlight the effect of targeted irradiation. The experiments of micro-

irradiation were carried out using the SNAKE facility in Munich and the AIFIRA facility in Bordeaux. These two facilities permitted mitochondria irradiations with both 55 MeV carbon ions and 3 MeV protons in a variety of patterns which allowed for irradiations with the same total deposited energy per unit area. In particular, I contributed to adapt the irradiation protocols between SNAKE and AIFIRA facilities.

The first result observed is the local depolarization of irradiated mitochondria, assessed by the loss of the accumulated tetramethyl rhodamine ester (TMRE), without effect on the rest of not-irradiated mitochondria of the targeted cell. These findings are confirmed repeating the experiments with different numbers of particles 5 times at SNAKE and then 2 times at AIFIRA. To test if the targeted irradiation causes mitochondrial membrane rupture, membrane integrity was tested. My contribution was to provide Mito-roGFP2 transfected cells to verify the integrity of membranes. The fluorescence signal of roGFP2 in the mitochondrial matrix stayed constant after irradiation excluding alterations of the mitochondrial matrix composition. Results obtained are detailed in the **Manuscript 3** which is submitted to *Scientific Reports*.

In addition, roGFP protein was created to be a reduction-oxidation-sensitive GFP protein with two fluorescence excitation maxima at about 400 and 490 nm. In response to changes in redox conditions, roGFP exhibits reciprocal changes in intensity at the two excitation maxima, and its ratiometric characteristics make it sensitive to expression levels<sup>139,140</sup>. These characteristics could be used in the future to measure the mitochondrial redox state in irradiated cells.

## Discussion and perspectives

The effects of ionizing radiations on the human body have been linked to the formation of DNA lesions, and have been classified as a risk factor for development of cancer. The “classical dogma” in radiation biology is that a high enough deposited energy in a cell nucleus will lead to the destruction of that cell. Numerous evidences showed that cytoplasm, in addition to DNA, can be also involved in bystander effects and mutations induction.

The observation of early cellular responses at charged particles damaged sites (at both nuclear and cytoplasmic levels) was achieved by using a microbeam set-up, which provides controlled irradiations of single cells with a determined number of charged particles.

The first development here presented demonstrates the ability to deliver single MeV  $\alpha$ -particles to the cell nuclei with a micrometric precision. Subsequently, the formation of ionizing radiation-induced foci of GFP-RNF8 protein was followed over time. Post-irradiation analysis shows that GFP-RNF8 accumulates at single  $\alpha$ -particle tracks during the first 30 minutes after irradiation. The intensity and the recruitment time varies from one IRIF to another reflecting most probably the chromatin heterogeneity inside the nucleus.

To investigate the influence of damage density and complexity on recruitment kinetics of GFP-RNF8 and GFP-XRCC1 proteins, we irradiated cells with 3 MeV protons and 3 MeV  $\alpha$ -particles. Delivering a precise number of particles having a LET well-identified (12 and 148 keV. $\mu\text{m}^{-1}$ , respectively) provides crucial insight into how DNA is damaged. In our study, we showed that the recruitment kinetics of GFP-RNF8 is dependent on the particles LET, indeed for the same deposited energy, GFP-RNF8 is recruited 5 times faster after  $\alpha$ -particles (higher LET) than after protons (lower LET). Then, we found that the GFP-XRCC1 recruitment time is dependent on the deposited energy for both  $\alpha$ -particles and protons and is not dependent on the LET. These different responses may be correlate with the molecular role of these proteins. RNF8 is recruited in a more specific manner to complex DNA damages (faster recruitment after high-LET particles) compare to XRCC1 that is a loading platform for other proteins and does not depend on damage complexity (recruitment faster when the deposited energy is increased independently on the particles LET). These data raise important questions about the mechanisms of DNA signaling and repair machinery and deserve more detailed studies.

As mentioned before, the DNA is not the only target of IR. Mitochondria constituting a large volume of the cytoplasm in all cell types are interesting targets to investigate. In the third presented study, mitochondria have been selected as the target of micro-irradiations. We showed that highly-localized

targeted mitochondrial irradiations using 55 MeV carbon ions and 3 MeV protons induce mitochondrial depolarization. Mitochondrial depolarization, as confirmed by the relocalization of TMRE from the mitochondria to the cytoplasm and then to the extracellular space, indicates a distinct change in mitochondrial membrane potential.

These studies underlined the importance of elucidating the biological mechanisms and responses activated by exposure to ionizing radiations in order to improve our knowledge and consequently the associated cancer risks. Further studies and several approaches are needed to completely understand the cellular mechanisms. The wide range of transfected cell lines developed during my PhD permits to study different DNA repair pathways (SSB and DSB Repair, 8-oxo guanine, BER, etc...) as a function of type of particle, deposited energy and track structure for which the Monte Carlo toolkit represents a fundamental tool. In addition modifications of chromatin and proteostasis induced by ionizing radiations and the epigenetic mechanisms can be a subject of future studies.

The investigation of radiation-induced effects on other cellular compartments different from DNA such as mitochondria and nucleoli is a point to clarify. Mitochondria depolarization were investigated during this work and more studies are necessary to explain the depolarization mechanisms that are not based on the membranes rupture but probably due to changes in the membrane structure and permeability.

The nucleolus, another interesting target, is a prominent non-membrane-bound nuclear substructure that organizes around chromosome segments containing nucleolar-organizing regions (NORs). It is the center of the rRNA transcription and ribosome biogenesis. Also additional functions, such as the cell cycle regulation, the telomerase activity, and the p53 metabolism have been attributed to the nucleolus itself<sup>135,141,142</sup>. In 1960 Montgomery *et al.* showed the first results of continuous ultraviolet microbeam irradiations of living cells nucleoli<sup>143</sup>. In 1971 Berns and colleagues irradiated with a laser microbeam the chromosome constriction and found a modified nucleolar organization<sup>144</sup>. Recently, Sorokin *et al.* investigated the movement and the morphology of nucleolar protein after gamma radiations<sup>145</sup>. From these studies an increasing interest in target nucleoli and in understanding their role in the radiation responses rose.



## Article 1

**“Single  $\alpha$ -particle irradiation permits real time visualisation of RNF8 accumulation at DNA damaged sites”**

Muggiolu, G. et al. Single  $\alpha$ -particle irradiation permits real time visualization of RNF8 accumulation at DNA damaged sites. *Sci. Rep.* 7, 41764; doi: 10.1038/srep41764 (2017)



# SCIENTIFIC REPORTS

OPEN

## Single $\alpha$ -particle irradiation permits real-time visualization of RNF8 accumulation at DNA damaged sites

Received: 26 October 2016  
Accepted: 22 December 2016  
Published: 31 January 2017

Giovanna Muggioli<sup>1,2</sup>, Michal Pomorski<sup>3</sup>, Gérard Claverie<sup>1,2</sup>, Guillaume Berthet<sup>3</sup>, Christine Mer-Calfati<sup>3</sup>, Samuel Saada<sup>3</sup>, Guillaume Devès<sup>1,2</sup>, Marina Simon<sup>1,2</sup>, Hervé Seznec<sup>1,2</sup> & Philippe Barberet<sup>1,2</sup>

As well as being a significant source of environmental radiation exposure,  $\alpha$ -particles are increasingly considered for use in targeted radiation therapy. A better understanding of  $\alpha$ -particle induced damage at the DNA scale can be achieved by following their tracks in real-time in targeted living cells. Focused  $\alpha$ -particle microbeams can facilitate this but, due to their low energy (up to a few MeV) and limited range,  $\alpha$ -particles detection, delivery, and follow-up observations of radiation-induced damage remain difficult. In this study, we developed a thin Boron-doped Nano-Crystalline Diamond membrane that allows reliable single  $\alpha$ -particles detection and single cell irradiation with negligible beam scattering. The radiation-induced responses of single 3 MeV  $\alpha$ -particles delivered with focused microbeam are visualized *in situ* over thirty minutes after irradiation by the accumulation of the GFP-tagged RNF8 protein at DNA damaged sites.

Every day humans are exposed to ionizing radiation from natural, industrial and medical sources. A significant part of the natural background radiation exposure is caused by  $\alpha$ -particles from the inhalation of radon gas<sup>1</sup>. In addition,  $\alpha$ -particles are increasingly considered in medical applications, such as targeted radiation therapy, where  $\alpha$ -emitting radionuclides are specifically localised to deliver a cytotoxic radiation dose to cancerous tissues, while sparing surrounding healthy tissues<sup>2–4</sup>. When traversing cells,  $\alpha$ -particles induce clustered molecular damages along their tracks as a function of their Linear Energy Transfer (LET) which is the energy transferred per unit length by ionizing radiation along its path. These clustered DNA damages, involving single and double strand breaks, occur when two or more lesions take place within one or two helical turns of the DNA strand. These can be designed as complex DNA damages and they are particularly deleterious because more difficult to repair<sup>5,6</sup>. Therefore, potential health effects resulting from  $\alpha$ -particles exposure continue to be the focus of numerous studies<sup>7–13</sup>. Understanding cellular responses to complex DNA damages specifically induced by  $\alpha$ -particles is of particular importance and requires specific tools that allow the selective irradiation of single cells and follow-up observations of induced damage *via* dedicated biological markers (DNA damage signalling, DNA repair protein...).

This can be achieved by exposing living cells to radioactive sources alongside immuno-detection<sup>8</sup> or fluorescence live cell imaging<sup>9</sup>. However using this approach, the number of traversals at the single cell level cannot be precisely controlled and the correlation of the particle traversals with observed biological responses relies on the retrospective observations made by nuclear track detectors<sup>14–19</sup>.

Alternatively, charged-particle microbeams can target living cells with single charged particles and have been used extensively to study various biological endpoints at low doses<sup>20,21</sup>. Modern end-stations, equipped with fluorescence time-lapse imaging, provide the opportunity to visualize and quantify in real-time the early radiation-induced cellular response. Using these techniques, studies of DNA damage and repair kinetics<sup>22–24</sup>, DNA double strand breaks diffusion characteristics<sup>25</sup>, and calcium alteration due to heavy-ions<sup>26</sup> have been

<sup>1</sup>Université de Bordeaux, Centre d'Etudes Nucléaires Bordeaux Gradignan (CENBG), Chemin du Solarium, 33175 Gradignan, France. <sup>2</sup>CNRS, UMR5797, Centre d'Etudes Nucléaires Bordeaux Gradignan (CENBG), Chemin du Solarium, 33175 Gradignan, France. <sup>3</sup>CEA-LIST, Diamond Sensors Laboratory, Gif-sur-Yvette F-91191, France. Correspondence and requests for materials should be addressed to P.B. (email: barberet@cenbg.in2p3.fr)

conducted. Up to now however, most studies have been performed using energetic heavy ions with high-LET, such as a carbon ions or heavier particles with LET ranging from a few hundred to several thousand keV/μm. Electrostatic accelerators delivering Helium ions allow to mimic perfectly the effects of α-particles (in the following, He ions will be designated as α-particles for clarity). Despite these accelerators are relatively common, investigations using MeV α-particles remain scarce. Indeed, delivering single α-particles requires the insertion of a thin detector in the beam path upstream of the sample. However, due to the limited range of α-particles in matter (a few tens of micrometres), this is difficult to accomplish without significantly altering the microbeam energy and size. The method used on several microbeam facilities, consisting of removing the cell nutrient medium and detecting the particles downstream the sample<sup>27,28</sup>, is not applicable when performing time-lapse imaging online over long periods during and after irradiation.

Several types of thin transmission detectors have been developed to achieve this goal: thin plastic scintillators coupled to photomultiplier tubes<sup>29,30</sup>, thin silicon detectors<sup>31,32</sup> and gas detectors<sup>33</sup>. More suitably, thin diamond membranes have shown very promising features for efficiently detecting single charged particles<sup>34–36</sup>. Nevertheless, all the detectors mentioned previously are usually a few micrometres thick and cannot be used to detect relatively low energy ions, such as MeV Helium ions delivered by conventional electrostatic accelerators.

In addition to the design of a specific detection system, visualizing and following the induced response of a single α-particle in living cells requires appropriate biological markers<sup>9</sup>. Several proteins are considered to be involved in the different steps of recognition, signalling and repair of DNA damages<sup>37</sup>. The activation of the MRN complex (including MRE11, RAD50 and NBS1 proteins), together with the recruitment to damaged areas of MDC1 and 53BP1 proteins, are the most studied mechanisms involved in DNA damage response<sup>38</sup>. These biomarkers tagged with fluorescent proteins, have allowed several laboratories to visualize the impact of single ion tracks in living cells<sup>9,23,24,39</sup>. However, a myriad of proteins acts during responses to DNA lesions, and most of them are primarily investigated with laser microbeams. Of particular importance, the discovery and characterization of the ubiquitin ligase RNF8 identify it as a key regulator of the rapid assembly of DNA repair complexes to DNA damage<sup>40–42</sup>. Several studies showed that RNF8 colocalizes with the DNA-damage marker γH2AX, and the strong collaboration with MDC1, NBS1 and 53BP1 proteins implies its critical role in the response to DNA damage<sup>40–42</sup>. More recently, its action mechanism and role in promoting DSB-associated chromatin ubiquitylation was shown<sup>43,44</sup> and the rapid dynamics was revealed with photo-bleaching experiments<sup>45,46</sup>.

Here, we report the development of a thin α-particle detector based on secondary electron emission. This method, initially developed for energetic heavy ions<sup>35</sup>, is presently not used in routine on microbeam irradiators. We revisited and improved this approach to provide efficient Helium ions detection (as these ions perfectly mimic the effect of α-particles). It relies on an ultra-thin free-standing Boron-doped Nano-Crystalline Diamond film (BNCD) of a few hundred nanometres in thickness. By collecting the secondary electrons (SE) emitted from the surface, this active vacuum window allows simultaneous extraction in air and detection of single α-particles with minimal alteration of the microbeam energy and without interfering considerably with the α-particle track trajectory. This technical development allows us to irradiate a stable cell line expressing the GFP-tagged RNF8 protein that accumulates at DNA damage sites, forming the so-called ionizing radiation induced-foci (IRIF). Combining detection and irradiation we can visualize, for the first time, one α-particle track within a few minutes after irradiation in living cells and follow in real-time the fluorescent signal evolution.

## Results

**Characterisation of the BNCD membranes.** The energy of α-particles transmitted through the BNCD membrane was measured using the experimental set-up depicted on Fig. 1a. It provides a simultaneous measurement of the electrons emitted from the BNCD surface and of the energy of the particles transmitted through the membrane. Figure 1b shows transmission spectra obtained with the silicon detector positioned downstream the BNCD samples. A mean energy loss of 200 keV through BNCD and its Si<sub>3</sub>N<sub>4</sub> supporting layer was measured on several membranes. Using the SRIM software (Stopping and Range of Ions in Matter)<sup>47</sup>, we estimated a mean thickness of 400 nm for the BNCD layer. Figure 1c shows channeltron pulse height spectra for two representative BNCD membranes. Compared to native Si<sub>3</sub>N<sub>4</sub> windows, the channeltron signal is clearly amplified indicating an enhanced SE yield. When using a BNCD layer, every single pulse can be unambiguously separated from the background. Dark counts, i.e. counts registered without the α-particle beam, were below 5 s<sup>-1</sup> in all cases. By comparing the number of counts registered in the spectra from Fig. 1b and c, the detection efficiency of the secondary electron detector was measured. In all cases, the difference in the number of counts on both detectors was lower than 0.2%. A detection efficiency of 100% was thus obtained and reproduced for several BNCD membranes.

The scanning capabilities of the microbeam allowed also maps to be created for both signals. The analysis of the transmitted energy shows that, in a scanned area of 400 × 400 μm, the maximum difference in energy loss from one beam position to the other is 30 keV (Supplementary Fig. S1). Maps obtained from the secondary electron detection over the same surface are also very homogeneous indicating a position-independent detection efficiency (Supplementary Fig. S2).

**Irradiations of track detectors.** Irradiating solid-state track detectors, such as CR39, is a reliable way to assess simultaneously the ability of the system to deliver single α-particles and the influence of the membrane on the beam spot size. Figure 2 shows the results obtained in CR39 track detectors irradiated with one or more α-particles delivered in regular patterns. In that case, the BNCD membrane was used as a vacuum window and the beam was extracted in air before reaching the CR39 (Fig. 2a). From these measurements, we confirm that one single α-particle can be delivered at every beam position (Fig. 2b) and that the beam spot size is not degraded due to the angular scattering in the BNCD membrane. Delivering 10 α-particles per spot, as shown in Fig. 2c, we estimated that all particles are delivered in a circle of 5 μm in diameter. This corresponds to a beam FWHM (Full Width at Half Maximum) of about 2 μm.

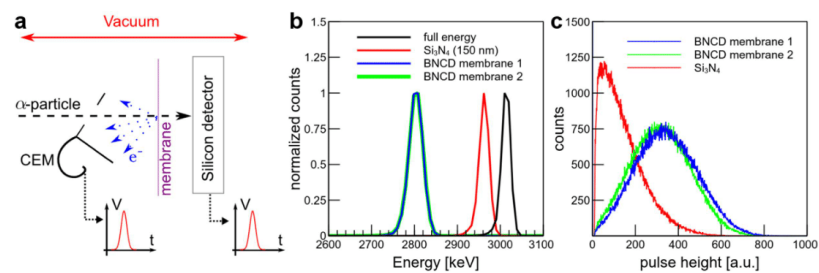


**Figure 1. Characterization of the BNCD membranes.** (a) Experimental set-up. The BNCD membranes were tested under vacuum for electron emission and thickness measurements. Electrical pulses induced by  $\alpha$ -particle hits were acquired simultaneously from both CEM (channel electron multiplier) and thick silicon detectors. (b) Impact of the BNCD membranes on the transmitted energy. The red spectrum shows the energy transmitted through a 150 nm thick commercially available  $\text{Si}_3\text{N}_4$  window. The two BNCD membranes (blue and green spectra) induce the same energy loss, thus the overlapped spectra. The black curve shows the beam energy without any material in its path. When passing through the BNCD membranes, an average energy loss of 200 keV is measured. (c) Channeltron pulse height spectra. The channeltron output signal is clearly separated from background for both BNCD membranes. The red curve shows the spectrum obtained on a  $\text{Si}_3\text{N}_4$  window without any coating.

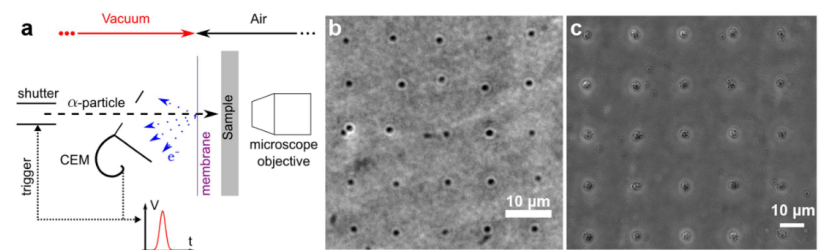


**Figure 2. CR39 track detectors irradiated with counted  $\alpha$ -particles.** (a) The BNCD membranes were validated as vacuum windows by irradiating track detectors or cells with single  $\alpha$ -particles in air. Pulses from the CEM were used to trigger the beam shutter when the required number of hits was reached. (b) Single particle irradiation in a regular pattern every 10  $\mu\text{m}$ . Black dots correspond to etched tracks. (c) 10 particles delivered every 20  $\mu\text{m}$ . All particles are delivered in a 5- $\mu\text{m}$  diameter circle.

**Induction of GFP-RNF8 recruitment to DNA damages induced by  $\alpha$ -particles.** Phosphorylation of the H2AX histone (serine 139), so called  $\gamma\text{H2AX}$ , is known to be associated with DNA damages<sup>48</sup>. Therefore, the capability of GFP-RNF8 to be recruited in distinct IRIF at DNA damaged sites induced by single  $\alpha$ -particles, was assessed by the colocalization with immuno-detected  $\gamma\text{H2AX}$ . Figure 3 shows cells exposed to a random  $\alpha$ -particles irradiation from  $^{239}\text{Pu}$  source.  $\gamma\text{H2AX}$  signal (Fig. 3b), obtained in cells fixed 30 min after irradiation is localized along  $\alpha$ -particles tracks. The accumulation of GFP-RNF8 is also observed at damaged sites within the first hour following irradiation (Fig. 3c). Co-localization of GFP-RNF8 and  $\gamma\text{H2AX}$  is depicted on the merged image confirming the presence of both proteins at damaged areas (Fig. 3d).

**RNF8 induction and accumulation dynamics at localized DNA damaged sites.** The main feature of microbeam is the ability to target and irradiate single cells with a precise number of  $\alpha$ -particles distributed in a regular pattern. Here we achieved the detection of single  $\alpha$ -particles using the BNCD membranes previously described. Figure 4 shows representative patterns illustrating the irradiation capabilities of the microbeam used. Single  $\alpha$ -particles induced-foci are clearly visible at the irradiated sites (Fig. 4a, b and d). Targeted points separated by 4  $\mu\text{m}$  are easily discernible confirming a beam resolution below 2  $\mu\text{m}$ . Figure 4c shows the focus induced by 10  $\alpha$ -particles, whose diameter corresponds to the beam size. The intensity profiles of example GFP-RNF8 IRIFs 30 minutes after irradiation are illustrated in Fig. 4e. Even if the three IRIFs, indicated by green peaks, are each induced by exactly one  $\alpha$ -particle, and thus by the same energy deposit, different fluorescence intensities are observed. These varying intensities could be explained by different chromatin configuration (hetero- and euchromatin) and densities, or by the presence of nucleolar compartments in the irradiated area. The brightest IRIF shows an increased fluorescence signal about two times greater than the background fluorescence intensity

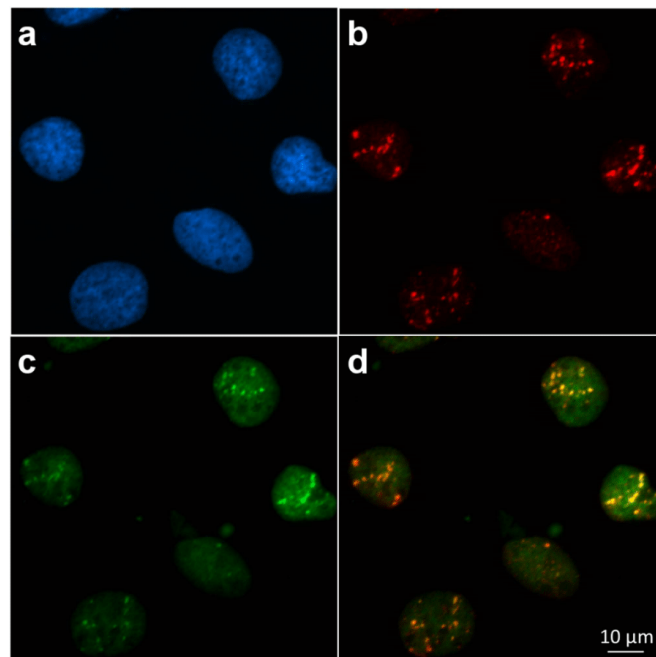


**Figure 3. Induction GFP-RNF8 and  $\gamma$ H2AX IRIF in cells irradiated with random  $\alpha$ -particles.** (a) Hoechst<sup>33342</sup> staining reveals the nuclear chromatin. (b) IRIF are visualized with  $\gamma$ H2AX immuno-detection in fixed cells exposed to <sup>239</sup>Pu source. (c) GFP-RNF8 is re-localized to the DNA damaged areas, and (d) the merged image shows the overlap of GFP-RNF8 and  $\gamma$ H2AX 30 minutes after irradiation.

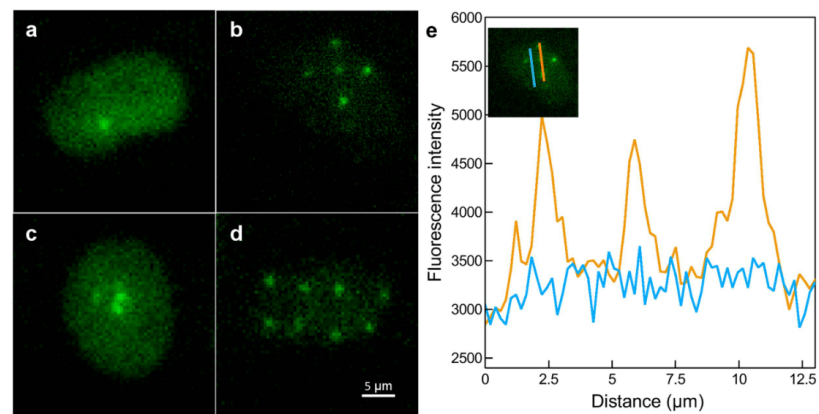


**Figure 4. Heterogeneity of GFP-RNF8 response in cell nuclei irradiated with different patterns.** Cells are irradiated with (a) one  $\alpha$ -particle, (b) 5  $\alpha$ -particles distributed on a cross pattern. The targeted positions are separated by 4  $\mu$ m. (c) 10  $\alpha$ -particles focalized on one position, and (d) regular pattern scanned over the whole microscope field of view. 8  $\alpha$ -particles induced-foci are distributed in the nucleus. (e) Fluorescence intensities measured along the two lines drawn in the inset plotted against their length. The blue line shows the constant nuclear fluorescence background; the orange line shows three peaks corresponding to the IRIF. Three different fluorescence intensities are observed suggesting an inhomogeneous chromatin density.

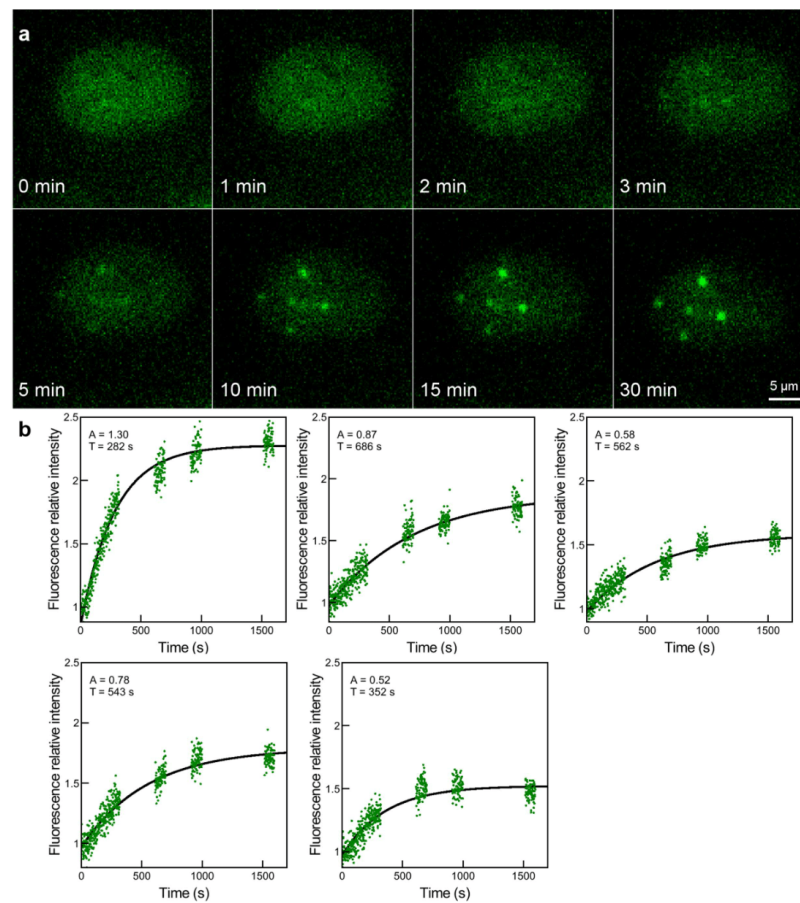


**Figure 5. Time-lapse imaging of GFP-RNF8 in a cell nucleus irradiated with single  $\alpha$ -particles.** (a) The cell nucleus is targeted and irradiated at time 0 with a single  $\alpha$ -particle per point on a cross pattern, each point separated by 4  $\mu\text{m}$ . The re-localization of GFP-RNF8 is observed over 30 min following irradiation and selected time points are shown. (b) Kinetics curves of GFP-RNF8 corresponding to each IRIF obtained from experimental data. Experimental curves (green points) are normalized and fit (black line) with a model for the first-order response. The intensity fluorescence of GFP-RNF8 protein in the damaged areas is highly variable, as described in each inset by the A parameter. The recruitment time (T) varies independently from the intensity fluorescence reached.

(Fig. 4e, blue line). The different IRIF distributed at various places in cell nucleus showed similar sizes of about 1  $\mu\text{m}$  FWHM.

Time-lapse imaging permits us to visualize and measure the time evolution of IRIF formation. At time 0, corresponding to the irradiation time, GFP-RNF8 is homogeneously distributed in the cell nucleus. Three minutes after irradiation, the protein starts to accumulate at the damaged areas to form visible IRIF. The fluorescence intensity increases with time over the 30 minutes following irradiation (Fig. 5a). The increase of IRIF fluorescence plotted against the time is illustrated in Fig. 5b for each focus. An exponential fit model permits to measure the IRIF intensity and the protein recruitment time (Supplementary Appendix S3). The IRIF fluorescence intensity varies from 1.3 to twice the fluorescent background value (insets Fig. 5b, parameters A). The recruitment time of the protein (insets Fig. 5b, parameters T) varies from 250 to 700 seconds independently from the A parameter. These results were reproduced in 28 cells during 3 independent experiments. Using the fit model (described in

Supplementary Appendix S3) we measured the GFP-RNF8 Mean  $\pm$  Standard Deviation recruitment halftime  $t_{1/2} = \frac{T}{\ln 2} = 652 \pm 302$  s.

### Discussion

We report here the development and validation of an experimental approach that permits, for the first time, the observation of early cellular responses at single  $\alpha$ -particle induced DNA damages. This is reached by the use of a microbeam which provides a controlled irradiation at the single-cell level (in time and dose) coupled to online fluorescence imaging.

In comparison to dynamic studies performed with radioactive sources, microbeams have several drawbacks: they are more complex to use and cannot irradiate cells at grazing angles that exploit the full track length. In addition, they require the use of specific dishes containing small volumes of medium restricting image acquisition time to less than an hour in order to avoid excessive cellular stress. Nevertheless, the results reported here demonstrate the ability to deliver single MeV  $\alpha$ -particles to cell nuclei with micrometre precision and then subsequently follow GFP-RNF8 IRIF formation over time. The difficulty of detecting MeV  $\alpha$ -particles without degrading the microbeam lateral resolution was overcome using thin BNCD membranes with sub-micrometre thicknesses. This solution is similar to that used at GSI Darmstadt for detecting heavy ions<sup>34,35</sup> and was optimized to provide a sufficient signal to count  $\alpha$ -particles, for which the electron emission yield is lower. In comparison to the earlier work reported by Fischer *et al.*<sup>34</sup>, BNCD membranes reported here are thinner (400 nm instead of 2  $\mu$ m) and grown on commercially available Si<sub>3</sub>N<sub>4</sub> windows facilitating the fabrication and handling. Diamond membranes were actually never used for irradiating living cells as Cesium Iodide (CsI) coated Si<sub>3</sub>N<sub>4</sub> windows showed more reproducible results<sup>35</sup>.

The BNCD membranes reported here give reproducible detection efficiency and are very homogeneous on millimetre surfaces, corresponding to typical field of views of our fluorescence microscope. In addition to the detection capability, they are also transparent and non-fluorescent, making them compatible with bright field and fluorescence imaging. Over the different experimental runs where these membranes were used, we observed that they were relatively radiation hard and could be used without significant degradation for several days at low beam intensities (i.e. a few thousands particles per second). Another interesting feature is that BNCD membrane can be stored in air without significant degradation. This constitutes a great advantage compared to CsI that showed to be very hygroscopic. Up to now, the fabricated membranes have thicknesses around 400 nm. Since electron emission is a surface phenomenon, thinner detectors could in principle be obtained while maintaining detection efficiency. Thickness reduction could allow smaller spot sizes to be achieved. Further tests to determine the minimum usable thicknesses of BNCD membranes are planned in the future.

The detection of single  $\alpha$ -particle traversals allows controlled irradiation of living cells. Post-irradiation analysis shows that GFP-RNF8 accumulates continuously at single  $\alpha$ -particle tracks during the first 30 minutes after irradiation. Even if physical interactions and ionizations are confined to less than 100 nm from the core of the tracks, IRIF of 1 to 2  $\mu$ m in diameter are formed. Their intensity varies from one IRIF to another reflecting most probably the chromatin heterogeneity inside the nucleus (as already reported in previous studies<sup>49–51</sup>). The brightest IRIF shows intensity about two times higher than the undamaged areas. Thus, GFP-RNF8 protein is a useful biological marker which permits to identify and follow over time the regions where DNA DSBs are induced by single  $\alpha$ -particles. The knowledge of the irradiation time, necessary for a precise measurement of the evolution of the IRIF over time, is also an important feature of microbeams. Here, irradiation can be achieved with a precision below one second. Finally, the ability to deliver single particles distributed in regular patterns is particularly interesting for the analysis of spatial dynamics of the damaged chromatin. Indeed, in the same cell, the protein recruitment time varies as a function of the hit position in the cell nucleus.

### Materials and Methods

**Membranes preparation.** Commercially available Si<sub>3</sub>N<sub>4</sub> vacuum windows on silicon frame of lateral dimensions 5  $\times$  5 mm, 1 mm squared opening and 150 nm thickness (Silson Ltd., England) were seeded with 5 nm diamond nanoparticles (average size, ADAMAS nano) using electrostatic grafting in PDDAC method (Poly(diallyldimethylammonium chloride))<sup>52</sup>. Boron doped nanocrystalline diamond (BNCD) film growth on nano-seeded Si<sub>3</sub>N<sub>4</sub> membranes was realized by MWCVD method (Microwave assisted chemical vapour deposition) in home-made ASTEX-type reactor employing trimethylborane gas (TMB) as a source of boron atoms. Following parameters were used during the growth: microwave power 1.2 kW; pressure 40 mbar; methane flow 33 sccm (standard cubic cm per minute); hydrogen flow 100 sccm; TMB flow 10 sccm; growth time 6 h. Synthesized BNCD membranes were employed as-grown with no additional treatment of surface in later experiments.

**Membrane characterisation.** The BNCD membranes were characterized using 3 MeV  $\alpha$ -particle beams on the AIFIRA facility (Applications Interdisciplinaires des Faisceaux d'Ions en Région Aquitaine)<sup>53</sup>.

**Electron yield and thickness measurements.** The secondary electron emission measurements were performed on the high resolution microbeam line (described previously<sup>54</sup>). The experimental set-up is shown in Fig. 1a. The beam was focused to 0.5  $\mu$ m FWHM and scanned over a 400  $\mu$ m  $\times$  400  $\mu$ m area to study the homogeneity of electron emission. The membrane was positioned in the beam path under vacuum and electrons emitted from their surface were collected using a channeltron electron multiplier (CEM, Sjuts™ model KBL15RS/90\_H). A 2 mm hole in the head of this particular CEM model was particularly well adapted to enhance the electron collection efficiency while letting the  $\alpha$ -particle beam pass through. The  $\alpha$ -particles passing through the membrane were detected using a 100  $\mu$ m thick silicon detector (C Canberra, partially depleted detector, 25 mm<sup>2</sup>, 12 keV resolution @ 4.5 MeV) providing a direct measurement of the transmitted energy. All measurements were performed at

beam rates between 1000 and 3000 particles per second. Pulse height spectra were obtained using the AIFIRA acquisition system based on a MPA-3 multichannel analyser (FAST ComTec GmbH)<sup>55</sup>.

**Use of BNCD membranes as a vacuum window and single-ion detector.** To validate the use of BNCD membranes as a thin detector for cell targeting experiments, they were fixed as usual vacuum windows on the cell irradiation microbeam line<sup>56</sup>. 3 MeV  $\alpha$ -particles were extracted in air through the membranes to irradiate either CR39 track detectors or living cells with single  $\alpha$ -particles. The distance between the vacuum window and the sample was approximately 60  $\mu\text{m}$ . The electrons emitted from the BNCD surface in vacuum were collected with the same CEM as the one described previously. Pulses generated by  $\alpha$ -particle traversals were counted using a dedicated stand-alone real-time system<sup>55</sup> triggering a fast electrostatic beam shutter when the required number of particles had been delivered. The *in-air* irradiation configuration is shown in Fig. 2a.

**Solid state track detectors.** To ensure the reliability of the dose control as well as the impact of the BNCD membranes on the beam spot size, CR39 solid state track detectors were irradiated in air with single ions. CR39 slabs were positioned at the position of the cell monolayer at a distance of 60  $\mu\text{m}$  from the beam exit window. After irradiation, CR39 were etched in concentrated KOH (12 M, at 80 °C) for 3 minutes. Irradiated patterns were imaged using phase contrast imaging with a Zeiss AxioObserver Z1 microscope (CarlZeiss MicroImaging, GmbH).

**Cell line culture and transfection.** HTB96 U2OS cells (from ATCC, CLS, Molsheim) were maintained in McCoy's 5 A medium (Dutscher) supplemented with 10% (v/v) Fetal Bovine Serum (FBS) and streptomycin/penicillin (100  $\mu\text{g}/\text{ml}$ ). Cells were kept in a humidified atmosphere at 37 °C and 5% (v/v)  $\text{CO}_2$ . A cDNA of human RNF8 inserted into pEGFP-C1 (kindly provided by Jiri Lukas) was used as construct for stable transfections<sup>41</sup>. Viromer Red transfection reagent (Lipocalyx GmbH, Germany) was used for transfections, in combination with the expression vector, according to the manufacturers' guidelines. Transfected cells were plated 48 h after transfection in presence of different geneticin/G418 dilutions (from 0.1 to 1 mg/ml, GIBCO) were added 72 h after transfection. After 10 days of drug selection, surviving colonies were checked under fluorescence microscopy and GFP-positive colonies were isolated. Several clones were selected and expanded into cell lines for further analysis. Stable expression of recombinant GFP-RNF8 with an exclusive nuclear localization was observed during cultivation for a period of several weeks, indicating a robust growth and reliable expression.

**Immuno-detection.** HTB96 U2OS cells were fixed within 1 h after irradiation with paraformaldehyde 4% (w/v) in phosphate-buffered saline (PBS 1X) medium for 15 minutes at room temperature and washed with PBS (pH 7.4, without  $\text{Ca}^{2+}$  and  $\text{Mg}^{2+}$ ). Then, cells permeabilization and saturation were performed using a blocking buffer containing 0.2% (v/v) Triton X-100, 10% (v/v) FBS in PBS for 30 min at room temperature. After three washes with PBS during 5 min, samples were incubated overnight, at 4 °C with anti-human  $\gamma\text{H2AX}$  rabbit monoclonal antibody (1:1000, 20E3, Cell Signaling). After three more washes with PBS, samples were incubated for 3 h at room temperature with goat anti-rabbit conjugated to Alexa Fluor<sup>488</sup> antibody (1:2000, Molecular Probes, Invitrogen). Cells were rinsed twice with PBS and nuclei stained with Hoechst<sup>33342</sup> (1  $\mu\text{M}$ ) for 10 min at room temperature. Polypropylene foils were cut and mounted using ProLong Gold Antifade Reagent (Molecular Probes, Invitrogen) overnight at room temperature, and visualized on Zeiss AxioObserver Z1 microscope (CarlZeiss MicroImaging, GmbH).

**Cell irradiations.** A custom made support dish is used as described by Bourret *et al.*<sup>56</sup>. This cell dish is adaptable for both <sup>239</sup>Pu  $\alpha$ -source and microbeam irradiation systems. Stably transfected GFP-RNF8 cells were plated on the polypropylene surface (Goodfellow) coated with CellTak (Biosciences) at a density of 14000 cells in 20  $\mu\text{l}$  drop, 24 h before irradiation.

**<sup>239</sup>Pu ( $\alpha$ -source) irradiation.** A charged-particle irradiation device, based on a 3.7 kBq <sup>239</sup>Pu  $\alpha$ -source, has been developed for experiments that do not require a precise targeting of individual cells. The  $\alpha$ -particles (5105 keV: 12%; 5143 keV: 15%; 5156 keV: 73%) randomly emitted go through 1 mm of air before reaching the polypropylene foil on which cells are attached. The set-up was designed to obtain a few traversals per nucleus for a few minutes of irradiation. During irradiation, cells are maintained in McCoy's medium. The source was characterized by Monte Carlo simulations, which showed a mean of one traversal per nucleus ( $1.4 \pm 1.1$ ) after 5 min of irradiation, and a mean number of  $7.6 \pm 3.4$  hits per nucleus after 30 min exposure<sup>57</sup>. Cells were exposed to random  $\alpha$ -particles irradiation over 30 min, and when the irradiation time was complete, cells were incubated for 30 min at 37 °C to ensure the protein recruitment had been completed in standard culture conditions.

**Microbeam irradiation.**  $\alpha$ -particles were accelerated by a 3.5 MV electrostatic accelerator (Singletron, High Voltage Engineering Europa, The Netherlands) present in the AIFIRA facility<sup>53</sup>. During microbeam irradiation and image acquisition, cells were maintained in FluoroBrite<sup>TM</sup> DMEM medium (GIBCO, TermoFisher Scientific) that ensures low background fluorescence. Cells were targeted and irradiated with single  $\alpha$ -particles or following different irradiation patterns. Time-lapse imaging was performed online using a 63x objective (LD Plan-Neofluar, NA 0.75, no immersion). Protein re-localization to the damaged area was followed over 30 min. Images were taken every second for the firsts 5 min, then 100 images were taken at 10, 15 and 25 min with a high sensitivity Rolera EM-C<sup>2</sup><sup>TM</sup> Camera (QImaging) using the MicroManager software<sup>58</sup>. Obtained data are corrected for non specific fluorescence bleaching and normalized for the fluorescence intensity measured before irradiation. The accumulation of GFP-RNF8 protein at DSB sites follows a model for a first order step response, previously described by Lukas *et al.*<sup>59</sup> and illustrated in Supplementary Appendix 3.

## References

- Morgan, W. F. & Bair, W. J. Issues in low dose radiation biology: the controversy continues. A perspective. *Radiat. Res.* **179**, 501–10 (2013).
- Dadachova, E. Cancer therapy with alpha-emitters labeled peptides. *Semin. Nucl. Med.* **40**, 204–8 (2010).
- Kelly, M. P. *et al.* Radioimmunotherapy with alpha-particle emitting <sup>213</sup>Bi-C-functionalized trans-cyclohexyl-diethylenetriaminepentaacetic acid-humanized 3S193 is enhanced by combination with paclitaxel chemotherapy. *Clin. Cancer Res.* **13**, 5604s–5612s (2007).
- Dekempeneer, Y. *et al.* Targeted alpha therapy using short-lived alpha-particles and the promise of nanobodies as targeting vehicle. *Expert Opin. Biol. Ther.* **16**, 1035–1047 (2016).
- Lorat, Y. *et al.* Nanoscale analysis of clustered DNA damage after high-LET irradiation by quantitative electron microscopy - The heavy burden to repair. *DNA Repair (Amst)*. **28**, 93–106 (2015).
- dos Santos, M. *et al.* Influence of chromatin condensation on the number of direct dsb damages induced by ions studied using a monte carlo code. *Radiat. Prot. Dosimetry* **161**, 469–473 (2014).
- Pugliese, M. *et al.* Inactivation of individual mammalian cells by single alpha-particles. *Int. J. Radiat. Biol.* **72**, 397–407 (1997).
- Aten, J. *et al.* Dynamics of DNA double-strand breaks revealed by clustering of damaged chromosome domains. *Science* **303**, 92–5 (2004).
- Stap, J. *et al.* Induction of linear tracks of DNA double-strand breaks by  $\alpha$ -particle irradiation of cells. *Nat. Methods* **5**, 261–266 (2008).
- Miller, R. C., Randers-Pehrson, G., Geard, C. R., Hall, E. J. & Brenner, D. J. The oncogenic transforming potential of the passage of single particles through mammalian cell nuclei. *Proc. Natl. Acad. Sci.* **96**, 19–22 (1999).
- Hei, T. K. *et al.* Mutagenic effects of a single and an exact number of particles in mammalian cells. *Proc. Natl. Acad. Sci.* **94**, 3765–3770 (1997).
- Lyckesvärd, M. N. *et al.* Alpha particle induced DNA damage and repair in normal cultured thyrocytes of different proliferation status. *Mutat. Res. - Fundam. Mol. Mech. Mutagen.* **765**, 48–56 (2014).
- Chauhan, V. & Howland, M. Gene expression responses in human lung fibroblasts exposed to alpha particle radiation. *Toxicol. Vitro*. **28**, 1222–1229 (2014).
- Chan, K. F., Yum, E. H. W., Wan, C. K., Fong, W. F. & Yu, K. N. Study of DNA integrity in alpha-particle radiobiological experiments using thin CR-39 detectors. *Radiat. Meas.* **43**, S541–S545 (2008).
- Chan, K. F. *et al.* Alpha-particle radiobiological experiments using thin CR-39 detectors. *Radiat. Prot. Dosimetry* **122**, 160–162 (2006).
- Tobias, F., Durante, M., Taucher-Scholz, G. & Jakob, B. Spatiotemporal analysis of DNA repair using charged particle radiation. *Mutat. Res. Mutat. Res.* **704**, 54–60 (2010).
- Kodaira, S. *et al.* Co-visualization of DNA damage and ion traversals in live mammalian cells using a fluorescent nuclear track detector. *J. Radiat. Res.* **56**, 360–365 (2015).
- Niklas, M. *et al.* Subcellular spatial correlation of particle traversal and biological response in clinical ion beams. *Int. J. Radiat. Oncol. Biol. Phys.* **87**, 1141–7 (2013).
- Niklas, M. *et al.* Registration procedure for spatial correlation of physical energy deposition of particle irradiation and cellular response utilizing cell-fluorescent ion track hybrid detectors. *Phys. Med. Biol.* **61**, N441–N460 (2016).
- Schettino, G., Al-Rashid, S. & Prise, K. Radiation microbeams as spatial and temporal probes of subcellular and tissue response. *Mutat. Res.* **704**, 68–77 (2011).
- Barberet, P. & Seznec, H. Advances in microbeam technologies and applications to radiation biology. *Radiat. Prot. Dosimetry* **166**, 182–187 (2015).
- Müller, I. *et al.* Species conserved DNA damage response at the inactive human X chromosome. *Mutat. Res. Toxicol. Environ. Mutagen.* **756**, 30–36 (2013).
- Mosconi, M. *et al.* 53BP1 and MDC1 foci formation in HT-1080 cells for low- and high-LET microbeam irradiations. *Radiat. Environ. Biophys.* **50**, 345–352 (2011).
- Hable, V. *et al.* Recruitment kinetics of DNA repair proteins Mdc1 and Rad52 but not 53BP1 depend on damage complexity. *PLoS One* **7**, e41943 (2012).
- Girst, S. *et al.* Subdiffusion supports joining of correct ends during repair of DNA double-strand breaks. *Sci. Rep.* **3**, 2511 (2013).
- Du, G. *et al.* The absence of an early calcium response to heavy-ion radiation in mammalian cells. *Radiat. Res.* **170**, 316–26 (2008).
- Randers-Pehrson, G., Geard, C. R., Johnson, G., Elliston, C. D. & Brenner, D. J. The Columbia University single-ion microbeam. *Radiat. Res.* **156**, 210–4 (2001).
- Konishi, T. *et al.* SPICE-NIRS Microbeam: a focused vertical system for proton irradiation of a single cell for radiobiological research. *J. Radiat. Res.* **54**, 736–747 (2013).
- Folkard, M. *et al.* A charged-particle microbeam: II. A single-particle micro-collimation and detection system. *Int. J. Radiat. Biol.* **72**, 387–95 (1997).
- Greif, K.-D., Brede, H. J., Frankenberg, D. & Giesen, U. The PTB single ion microbeam for irradiation of living cells. *Nucl. Instruments Methods Phys. Res. Sect. B Beam Interact. with Mater. Atoms* **217**, 505–512 (2004).
- Nilsson, C. *et al.* Evaluation of a pre-cell hit detector for the future single ion hit facility in Lund. *Nucl. Instruments Methods Phys. Res. Sect. B Beam Interact. with Mater. Atoms* **249**, 924–927 (2006).
- Grad, M., Harken, A., Randers-Pehrson, G., Attinger, D. & Brenner, D. J. An ultra-thin Schottky diode as a transmission particle detector for biological microbeams. *J. Instrum.* **7**, P12001–P12001 (2012).
- Barberet, P. *et al.* Development of a focused charged particle microbeam for the irradiation of individual cells. *Rev. Sci. Instrum.* **76**, 1–6 (2005).
- Fischer, B. E., Cholewa, M. & Noguchi, H. Some experiences on the way to biological single ion experiments. *Nucl. Instruments Methods Phys. Res. Sect. B Beam Interact. with Mater. Atoms* **181**, 60–65 (2001).
- Fischer, B. E., Heiß, M. & Cholewa, M. About the art to shoot with single ions. *Nucl. Instruments Methods Phys. Res. Sect. B Beam Interact. with Mater. Atoms* **210**, 285–291 (2003).
- Grilj, V. *et al.* An ultra-thin diamond membrane as a transmission particle detector and vacuum window for external microbeams. *Appl. Phys. Lett.* **103**, 243106 (2013).
- Polo, S. & Jackson, S. Dynamics of DNA damage response proteins at DNA breaks: a focus on protein modifications. *Genes Dev.* **25**, 409–33 (2011).
- Bakkenist, C. J. & Kastan, M. B. Chromatin perturbations during the DNA damage response in higher eukaryotes. *DNA Repair (Amst)*. **36**, 8–12 (2015).
- Tobias, F. *et al.* Spatiotemporal dynamics of early DNA damage response proteins on complex DNA lesions. *PLoS One* **8**, e57953 (2013).
- Huen, M. S. Y. *et al.* RNF8 transduces the DNA-damage signal via histone ubiquitylation and checkpoint protein assembly. *Cell* **131**, 901–14 (2007).
- Mailand, N. *et al.* RNF8 Ubiquitylates Histones at DNA Double-Strand Breaks and Promotes Assembly of Repair Proteins. *Cell* **131**, 887–900 (2007).
- Kolas, N. K. *et al.* Orchestration of the DNA-Damage Response by the RNF8 Ubiquitin Ligase. *Science (80-)*. **318**, 1637–1640 (2007).
- Bartocci, C. & Denchi, E. L. Put a RING on it: regulation and inhibition of RNF8 and RNF168 RING finger E3 ligases at DNA damage sites. *Front. Genet.* **4**, 128 (2013).
- Thorslund, T. *et al.* Histone H1 couples initiation and amplification of ubiquitin signalling after DNA damage. *Nature* **527**, 389–93 (2015).



45. Mok, M. T. S., Cheng, A. S. L. & Henderson, B. R. The ubiquitin ligases RNF8 and RNF168 display rapid but distinct dynamics at DNA repair foci in living cells. *Int. J. Biochem. Cell Biol.* **57**, 27–34 (2014).
46. Doil, C. *et al.* RNF168 Binds and Amplifies Ubiquitin Conjugates on Damaged Chromosomes to Allow Accumulation of Repair Proteins. *Cell* **136**, 435–446 (2009).
47. Ziegler, J. F., Ziegler, M. D. & Biersack, J. P. SRIM – The stopping and range of ions in matter (2010). *Nucl. Instruments Methods Phys. Res. Sect. B Beam Interact. with Mater. Atoms* **268**, 1818–1823 (2010).
48. Rogakou, E. P., Pilch, D. R., Orr, A. H., Ivanova, V. S. & Bonner, W. M. DNA double-stranded breaks induce histone H2AX phosphorylation on serine 139. *J. Biol. Chem.* **273**, 5858–68 (1998).
49. Jakob, B. *et al.* DNA double-strand breaks in heterochromatin elicit fast repair protein recruitment, histone H2AX phosphorylation and relocation to euchromatin. *Nucleic Acids Res.* **39**, 6489–99 (2011).
50. Chiolo, I. *et al.* Double-strand breaks in heterochromatin move outside of a dynamic HP1a domain to complete recombinational repair. *Cell* **144**, 732–744 (2011).
51. Chiolo, I., Tang, J., Georgescu, W. & Costes, S. V. Nuclear dynamics of radiation-induced foci in euchromatin and heterochromatin. *Mutat. Res. - Fundam. Mol. Mech. Mutagen.* **750**, 56–66 (2013).
52. Girard, H. A. *et al.* Electrostatic Grafting of Diamond Nanoparticles: A Versatile Route to Nanocrystalline Diamond Thin Films. *ACS Appl. Mater. Interfaces* **1**, 2738–2746 (2009).
53. Sorieul, S., Alfaut, P., Daudin, L., Serani, L. & Moretto, P. Aifira: an ion beam facility for multidisciplinary research. *Nucl. Instruments Methods Phys. Res. Sect. B Beam Interact. with Mater. Atoms* **332**, 68–73 (2014).
54. Barberet, P. *et al.* First results obtained using the CENBG nanobeam line: Performances and applications. *Nucl. Instruments Methods Phys. Res. Sect. B Beam Interact. with Mater. Atoms* **269**, 2163–2167 (2011).
55. Daudin, L., Barberet, P., Serani, L. & Moretto, P. CRionScan: A stand-alone real time controller designed to perform ion beam imaging, dose controlled irradiation and proton beam writing. *Nucl. Instruments Methods Phys. Res. Sect. B Beam Interact. with Mater. Atoms* **306**, 64–70 (2013).
56. Bourret, S. *et al.* Fluorescence time-lapse imaging of single cells targeted with a focused scanning charged-particle microbeam. *Nucl. Instruments Methods Phys. Res. Sect. B Beam Interact. with Mater. Atoms* **325**, 27–34 (2014).
57. Barberet, P. *et al.* Monte-Carlo dosimetry on a realistic cell monolayer geometry exposed to alpha particles. *Phys. Med. Biol.* **57**, 2189–2207 (2012).
58. Edelstein, A. D. *et al.* Advanced methods of microscope control using  $\mu$ Manager software. *J. Biol. Methods* **1**, 10 (2014).
59. Lukas, J., Lukas, C. & Bartek, J. Mammalian cell cycle checkpoints: Signalling pathways and their organization in space and time. *DNA Repair (Amst.)* **3**, 997–1007 (2004).

#### Acknowledgements

The AIFIRA facility and the microbeam line have been financially supported by the Region Aquitaine (IOPRA, POPRA). MS is supported by the Region Aquitaine (POPRA). Merete Grofte and Jiri Lukas from Novo Nordisk Foundation Center for Protein Research for their generous gift (plasmids GFP-RNF8). This work has been partly supported by the European Community as an Integrating Activity “Support of Public and Industrial Research Using Ion Beam Technology” (SPIRIT) under the EC contract n° 227012. GM is supported by the European Community as an “Integrating Activity Supporting Postgraduate Research with Internships in Industry and Training Excellence” (SPRITE) under EC contract no. 317169. BNCD membrane development was supported by the French national centre for scientific research (CNRS, Mission Interdisciplinaire). We thank Nathanael Lampe for valuable help with the manuscript.

#### Author Contributions

M.P., G.B., C.M.C. and S.S. designed and produced the BNCD detectors; P.B., G.C. and M.P. characterized the BNCD detectors; G.M. and H.S. established the GFP-RNF8 cell lines; G.M., P.B., M.S., G.D. and H.S. designed and performed the radiation biology experiments; G.M. and P.B. wrote the paper; all authors reviewed the manuscript.

#### Additional Information

**Supplementary information** accompanies this paper at <http://www.nature.com/srep>

**Competing financial interests:** The authors declare no competing financial interests.

**How to cite this article:** Muggioli, G. *et al.* Single  $\alpha$ -particle irradiation permits real time visualization of RNF8 accumulation at DNA damaged sites. *Sci. Rep.* **7**, 41764; doi: 10.1038/srep41764 (2017).

**Publisher's note:** Springer Nature remains neutral with regard to jurisdictional claims in published maps and institutional affiliations.



This work is licensed under a Creative Commons Attribution 4.0 International License. The images or other third party material in this article are included in the article's Creative Commons license, unless indicated otherwise in the credit line; if the material is not included under the Creative Commons license, users will need to obtain permission from the license holder to reproduce the material. To view a copy of this license, visit <http://creativecommons.org/licenses/by/4.0/>

© The Author(s) 2017

## Supplementary material

### Results

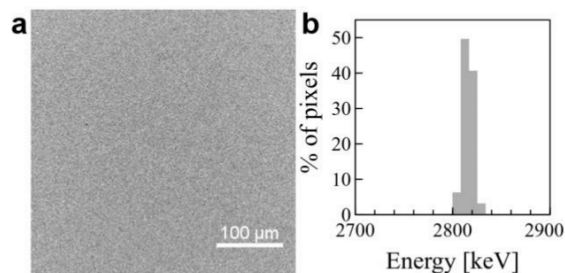


**Figure S1. Energy loss mapping.** Transmitted energy maps obtained using STIM (Scanning Transmission Ion Microscopy). (a) Map of median energy transmitted through the BNCD membrane. The median energy for each pixel is represented by a grey level showing a good homogeneity of the BNCD thickness. (b) Histogram of the left image showing the dispersion of the transmitted energy on a 400 x 400 μm<sup>2</sup> area.

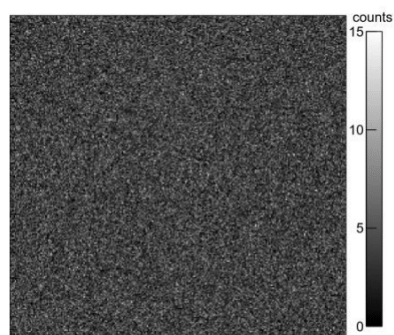


**Figure S2. Secondary electron map.** Grey levels represent the number of counts registered by the channeltron at different beam position. The detection efficiency is shown to be very homogeneous on 400 x 400 μm area.

### Appendix S3

The fit of experimental curves are obtained as follow:

$$Int = 1 + A \cdot \left( 1 - e^{-\frac{t-t_0}{T}} \right)$$

Where A is the highest intensity value reached; t represents the time, and  $t_0$  is the irradiation time fixed to 0 sec; the most relevant parameter is T, which represents the recruitment time expressed in seconds.



## **Manuscript 2**

**“Microdosimetric simulations razionalize *in cellulo* radiation-induced spatiotemporal dynamics of GFP-tagged DNA repair proteins at the cellular scale”**

Muggiolu G, Torfeh E, Simon M, Devès G, Incerti S, Lampe N,  
Seznec H and Barberet P

## Microdosimetric simulations rationalize *in cellulo* radiation-induced spatiotemporal dynamics of GFP-tagged DNA repair proteins at the cellular scale

Giovanna Muggioli<sup>(1,2)</sup>, Eva Torfeh<sup>(1,2)</sup>, Marina Simon<sup>(1,2)</sup>, Guillaume Devès<sup>(1,2)</sup>, Sébastien Incerti<sup>(1,2)</sup>, Nathanael Lampe<sup>(1,2)</sup>, Philippe Barberet<sup>(1,2)</sup> and Hervé Seznec<sup>(1,2)</sup>

(1) Université de Bordeaux, Centre d'Etudes Nucléaires Bordeaux Gradignan (CENBG), Chemin du Solarium, 33175 Gradignan, France

(2) CNRS, UMR5797, Centre d'Etudes Nucléaires Bordeaux Gradignan (CENBG), Chemin du Solarium, 33175 Gradignan, France

Corresponding author: [barberet@cenbg.in2p3.fr](mailto:barberet@cenbg.in2p3.fr), [herve.seznec@cenbg.in2p3.fr](mailto:herve.seznec@cenbg.in2p3.fr)

### Abstract (150 words)

Using charged particles microbeam to precisely control cellular irradiation, the *in cellulo* kinetics of individual response factors in DNA repair, and the mechanisms that select different DNA repair pathways may be better studied. Precise control over the irradiating particles allows the impact of the density of damaged DNA sites and their complexity to be studied using a precise number of ionizing particles with a well-defined linear energy transfer. In this study, we investigated the impact of both linear energy transfer and the number of irradiating particles on repair protein recruitment time. Using protons and  $\alpha$ -particles, we irradiated cell nucleus with between 10 and 1000 particles, and measured the *in situ* recruitment kinetics of GFP-tagged proteins, such as RNF8 and XRCC1, respectively. We observed a close relationship between the protein behavior and the proton and  $\alpha$ -particle track structures simulated using the Geant4 Monte Carlo particle transport toolkit. From this, we can infer that GFP-XRCC1 recruitment occurs a few seconds after irradiation and is highly related to the amount of energy deposited, while GFP-RNF8 recruitment depends on both the energy deposited in the cell, and the density of ionizations produced by the particle. These results show the importance of combining a microdosimetry with *in situ* and quantitative DNA damage response and signaling analyses to fully explain biological outcomes.

### Introduction

The harmful effects of ionizing radiations can be attributed to the damage of a cellular target, usually identified as nuclear DNA, *via* direct absorption of radiation energy<sup>1,2</sup>. This leads to complex lesions consisting of damaged bases, single strand breaks (SSBs) and double strand breaks (DSBs)<sup>3</sup>. Cells have developed efficient defense mechanisms to repair these lesions, using dedicated and specialized pathways. *In vitro* studies of these mechanisms can be performed to understand the role and recruitment of these proteins by visualizing radiation-induced foci (IRIF). Time lapse imaging allows

the kinetics of protein accumulation to be studied, from a few seconds to several minutes after irradiation.

Several methods have been developed to trigger localized DNA lesions and analyze subsequent cellular responses in real-time in living cells, immediately after irradiation. These include laser-based micro-irradiation setups<sup>4-8</sup> and charged particle microbeam<sup>9-15</sup>. In contrast with the photon irradiation offered by lasers, which can generate a wide variety of lesions depending on photon wavelength, energy and exposure time<sup>16</sup>, charged particle microbeams provide more well-behaved energy deposition equally distributed over all molecular species, better linking induced DNA damage and protein kinetics<sup>17,18</sup>.

Charged particle microbeams allow different incident particle types as well as the number of delivered particles to be selected, enabling the precise study of the effects of a total deposited energy per nucleus as a function of the deposited energy per track on biological responses. The linear energy transfer (LET) is a consequence of the track structure of a given radiation type and energy, and determines the damage complexity. Densely ionizing radiation, with a high LET (*e.g.*  $\alpha$ -particles), produce more complex lesions than those produced by radiations with a lower LET<sup>19</sup>, which causes significantly sparser damage. The micrometre and nanometer-scale distributions of the energy deposited by ionizing radiations allow one to predict the heterogeneity and density of DNA damage. The spatial distribution of ionization radiation events in the target can be calculated using track structure codes such as Geant4-DNA<sup>20</sup>, which model the all physical processes that occur when ionizing radiation interacts with matter, enabling the number of radiation-induced DNA lesions to be predicted<sup>21</sup>. Through such microdosimetric simulations the variations in energy depositions on micrometer scales can be measured for a given macroscopic adsorbed dose<sup>22</sup>.

We developed stable transfected GFP-tagged cell lines for the proteins XRCC1 and RNF8, known to be involved in the recognition, signaling and repair of DNA damages. XRCC1 is an essential scaffold protein with an unknown enzymatic activity, required for the coordination of different repair pathways and associated with Base Excision Repair (BER) and SSB Repair (SSBR) pathways<sup>23-25</sup>. RNF8 is an ubiquitin ligase that promotes DSB-associated chromatin ubiquitination; it interacts directly with MDC1 which is among the first proteins which accumulate at DSB sites<sup>8,26-28</sup>.

We performed targeted irradiations of these cell lines using the microbeam line installed at the AIFIRA ion accelerator facility<sup>14,15</sup> (*Applications Interdisciplinaires des Faisceaux d'Ions en Région Aquitaine*). Increasing numbers of 3 MeV protons or  $\alpha$ -particles, for which the deposited energy per beam spot and track structures are estimated using Monte Carlo simulations (Geant4 and the Geant4-DNA extension<sup>20,29,30</sup>), were delivered to single cells. We measured the corresponding protein responses and compared these responses with particle track structures. We show that XRCC1 is recruited to DNA damage sites a few seconds after irradiation as a function of the total deposited energy, while RNF8 is recruited to DNA damage sites few minutes after irradiation, though LET, as a

proxy for lesion complexity plays a primary role in driving RNF8 recruitment firstly as a function of the LET and secondly as a function of the total deposited energy.

This study seeks to find the biological consequences of different microdosimetric energy depositions arising from exposing cells to different charged particles, helping us to answer challenging questions such as which is the affinity of different repair proteins to clustered DNA lesions and how do different DNA repair systems recognize clustered DNA lesions<sup>31</sup>.

## Results

### Monte Carlo simulations to estimate the deposited energy and particle track structures.

Charged particles are delivered in a Gaussian distribution of about 1.5  $\mu\text{m}$  full width at half maximum (FWHM)<sup>15,32</sup>. Varying the number and type of incident particles allows one to adjust both the energy deposited and its structure, highlighting the effects of both LET and absorbed dose. Experimentally, we changed the total deposited energy and the density of DNA lesions by irradiating cells with increasing numbers of 3 MeV  $\alpha$ -particles (LET = 148  $\text{keV}\cdot\mu\text{m}^{-1}$ ) and 3 MeV protons (LET = 12  $\text{keV}\cdot\mu\text{m}^{-1}$ ). The mean absorbed dose per nucleus corresponds to 0.135 Gy when one  $\alpha$ -particle is delivered<sup>32</sup>. A similar mean absorbed dose per nucleus is obtained when ten protons are delivered. We note though that the mean absorbed dose is estimated by considering the cellular volume, which varies from cell to cell. As the irradiation is not uniform within the cellular volume we discuss the *mean deposited energy* per spot (roughly a surface density per 0.04  $\mu\text{m}^2$ ), rather than *absorbed dose*, as it better defines our independent variable. We generated track structures for incident particles using Monte Carlo simulations in Geant4-DNA (using the default Geant4-DNA physics constructor), calculating the deposited energy per spot and the distribution of ionizations within the irradiated area. Figure 1a shows a schematic representation of the beam direction and the method used to calculate the deposited energy by different numbers of charged particles. The deposited energy was calculated for each pixel constituting the target; the pixel size was fixed at 0.2 x 0.2  $\mu\text{m}$  to be similar to the pixel dimension of microscope fluorescent images. The 6  $\mu\text{m}$ -depth corresponds to the mean depth of a cell nucleus. Similar mean total deposited energies per beam spot calculated using Geant4 standardED models (Livermore) were reached after 10  $\alpha$ -particles or 100 protons and after 100  $\alpha$ -particles or 1000 protons.

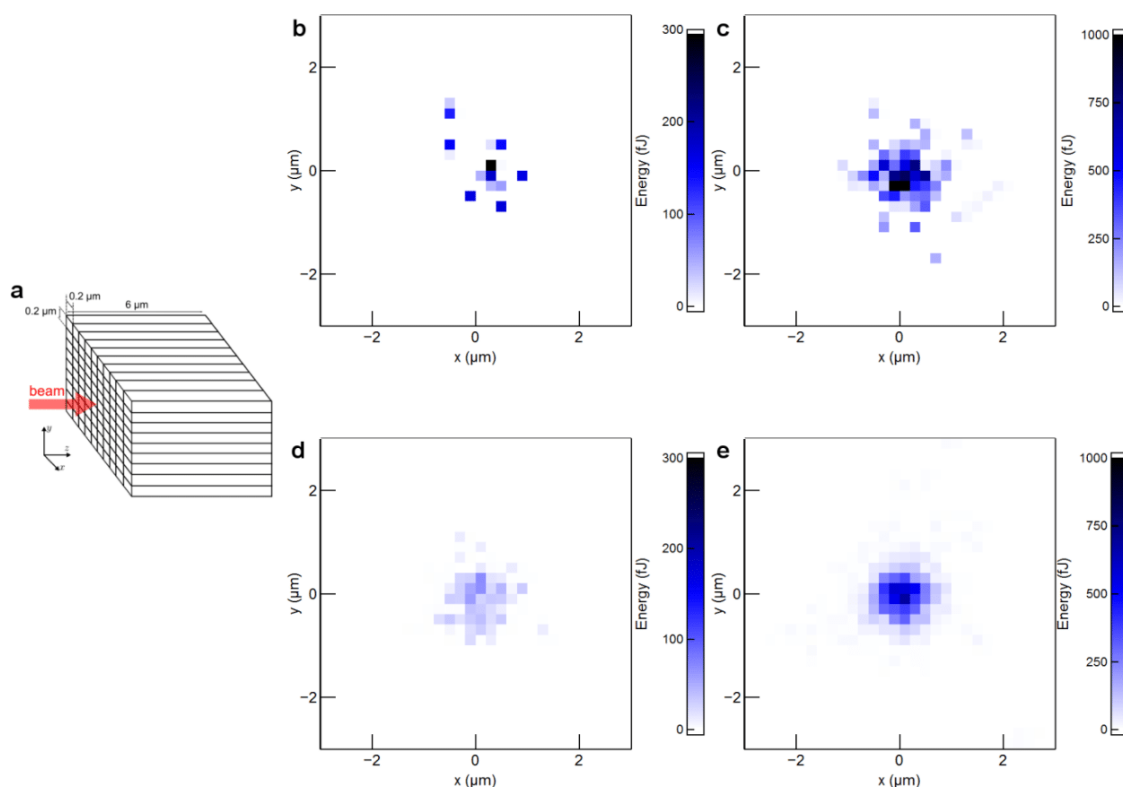


**Figure 1. Geant4 simulations estimated the deposited energy in a simplified cell nucleus.** (a) Schematic representation of the beam direction (red arrow) and the target (cell nucleus), which is divided into rectangular prisms with size  $0.2 \times 0.2 \times 6 \mu\text{m}$ . The deposited energy is calculated within these volumes. The total deposited energy is similar when (b) 10  $\alpha$ -particles and (d) 100 protons are delivered, and when (c) 100  $\alpha$ -particles and (e) 1000 protons are delivered.

Despite the similar mean total deposited energy per spot by 10  $\alpha$ -particles or 100 protons, the distribution of ionizations along the particle path and thus the subsequent induced-DNA damages distribution are different. We estimated the number and the distribution of ionizations at the nanometric scale induced by both one 3 MeV  $\alpha$ -particle and of one 3 MeV proton through  $1 \mu\text{m}$  of water (Supplementary Fig.S1) and by increasing numbers of charged particles in Geant4-DNA simulations. Figure 2 shows the tracks of 10  $\alpha$ -particles and 100 protons delivered in  $1.5 \mu\text{m}$  FWHM beam along  $30 \text{ nm}$  of water and the respective projections of ionizations distribution. When 10  $\alpha$ -particles are delivered within  $1.5 \mu\text{m}$  (FWHM) beam, 10 distinct dense ionization tracks are visible; by contrast, when 100 protons are delivered, the tracks are so dispersed that the induced ionizations are almost evenly distributed in the irradiated area. The high density of ionizations induced along  $\alpha$ -particle tracks strongly suggests the formation of significantly more complex DNA damaged area than the sparse ionizations induced by protons.



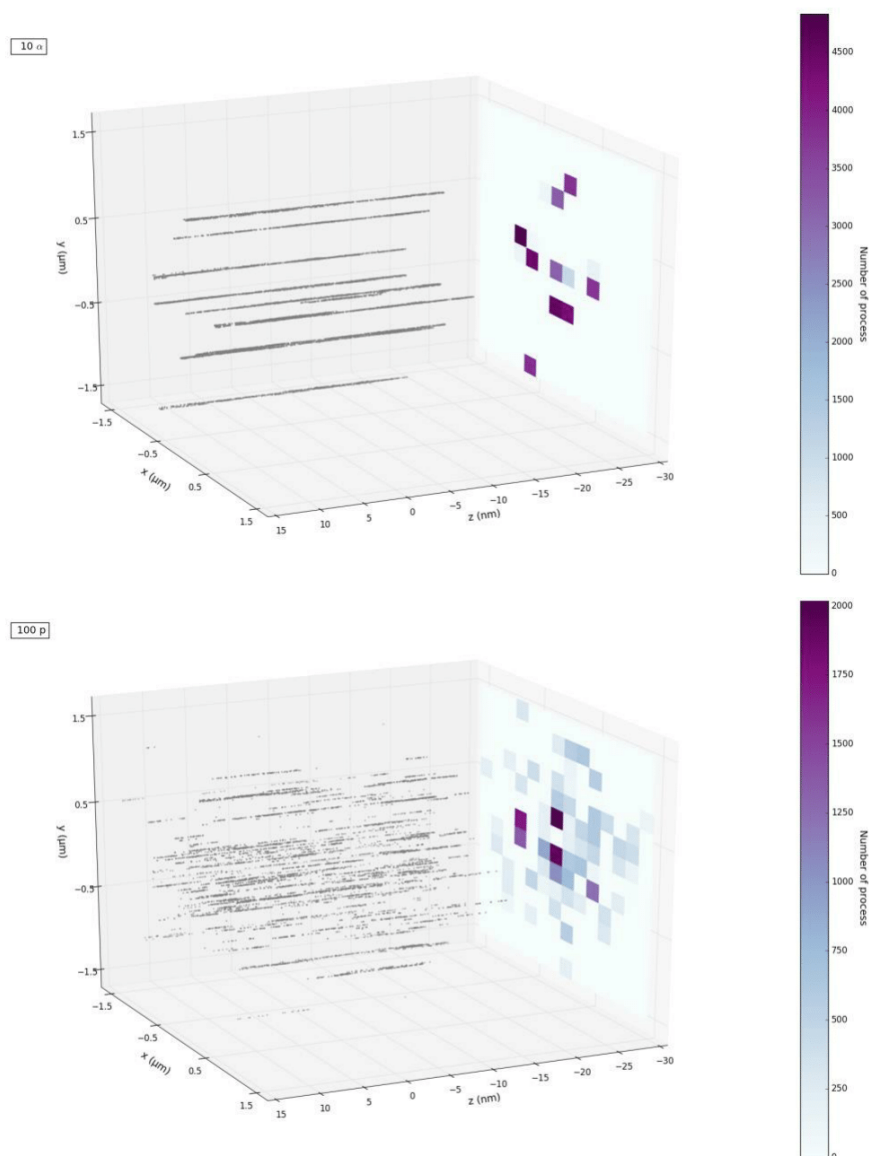


**Figure 2. Track structures of 3 MeV  $\alpha$ -particles and protons in liquid water obtained with Geant4-DNA.** Each dot represents one ionization induced by increasing number of charged particles through 30 nm of water. Despite the deposited energy in the cell nucleus is similar when 10  $\alpha$ -particles and 100 protons are delivered, the distribution of ionizations in the irradiated medium is completely different.

The distribution of ionizations along the particle track can be associated with the formation of cluster of damages where SSBs or DSBs are prevalent. Indeed, it has been suggested that a DSB can occur when two or more ionization events occur within a distance of 20 base pairs (bp) of each other<sup>33</sup>, which corresponds to a linear distance of 6.8 nm. The distribution of ionizations present in a 30 nm wide cylinder (the size of a chromatin fiber<sup>34</sup>) were visualized after irradiation with 100  $\alpha$ -particles and 1000 protons (Supplementary Fig. S2).

**Recruitment kinetics of GFP-tagged proteins to DNA damage sites after irradiations.**

It is important to mention that in this work, two proteins were selected for their known function in response to ionizing radiation, but we did not consider their respective recruitment time (which could be affected by the presence of the endogenous proteins) to explain the organization of the DNA repair machinery. Nevertheless, we used these two GFP-tagged proteins as biological indicators to estimate the relation between physical interactions and biological responses.

The ability of GFP-RNF8 protein to accumulate at distinct DNA damage sites was assessed by co-localization of the protein with immuno-detected  $\gamma$ H2AX (Supplementary Fig. S3) and with online live cell microscopy after both proton and  $\alpha$ -particle irradiation<sup>27,35</sup>. To monitor the recruitment of GFP-RNF8 at radiation-induced DNA damage sites, images were taken before, during and up to 30 min after irradiation. To quantify the protein recruitment time, the normalized mean fluorescence intensity of IRIF was plotted as function of time after irradiation. The protein accumulation follow a curve (Fig. 3) characterized by a single time constant (T), obtained using Eq. 2, described in the Materials and Methods. The formation of GFP-RNF8 radiation-induced foci became visible within 2 min. The protein reached a steady-state equilibrium 30 min after irradiation. The kinetic parameter T was calculated after integrating at least 16 cells irradiated over three independent beam times with increasing numbers of protons and  $\alpha$ -particles (Supplementary Table S1).

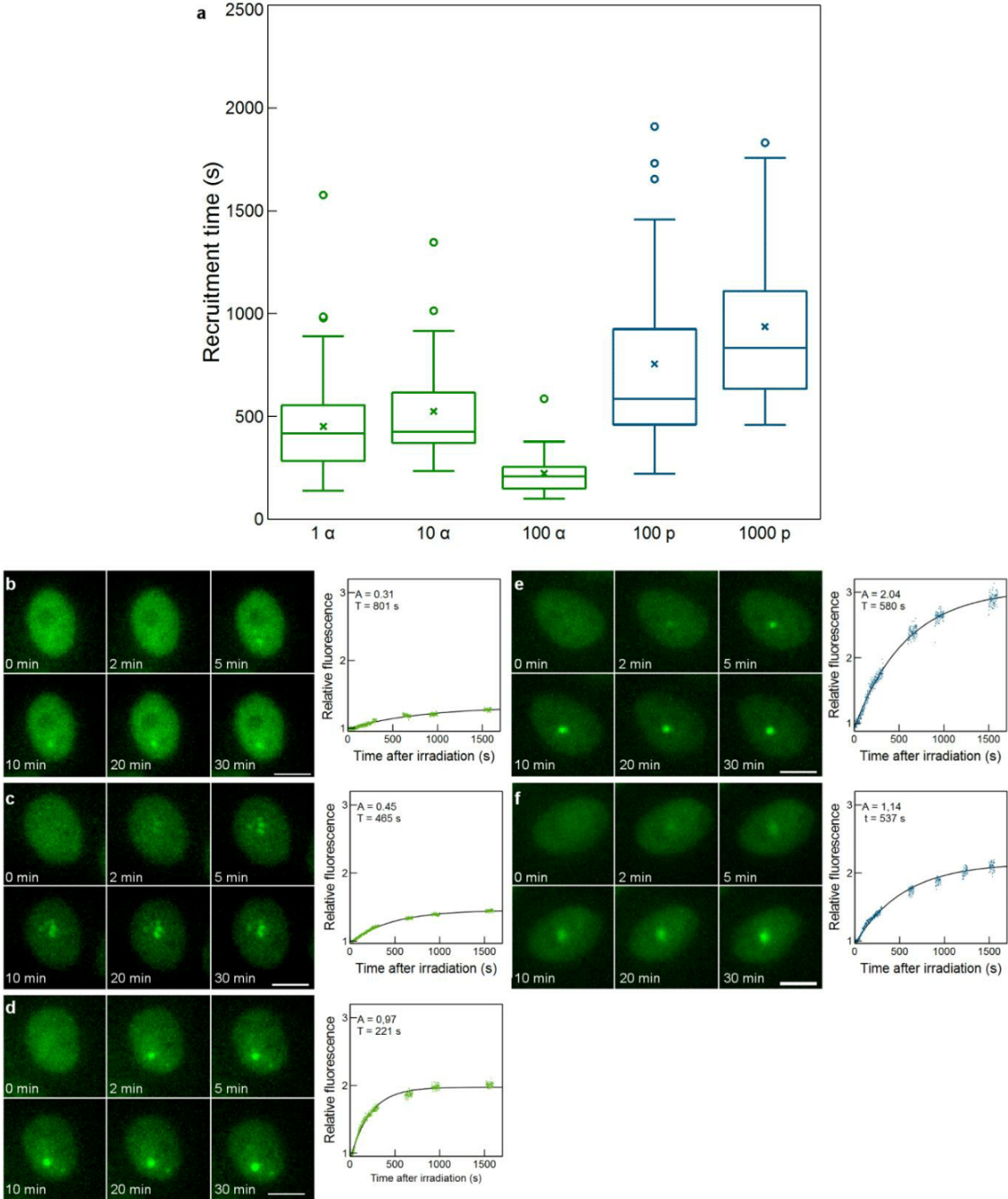


**Figure 3. GFP-RNF8 mean recruitment time (T) after proton and  $\alpha$ -particle irradiations.** (a) Cells are irradiated with increasing numbers of  $\alpha$ -particles (green) and protons (blue). The mean recruitment time is much faster when cells are irradiated with  $\alpha$ -particles with respect to protons suggesting a LET-dependent protein recruitment. T changes as a function of the deposited energy when  $\alpha$ -particles are increased from 10 to 100; it does not significantly change when the number of protons is increased. (b) 1, (c) 10 and (d) 100  $\alpha$ -particles and (e) 100 and (f) 1000 protons are delivered in a spot and one cell nucleus is shown together with the corresponding kinetic curve as an example.

By increasing the number from 1 to 10  $\alpha$ -particles, the recruitment time does not significantly change. These measurements can be influenced by the particles distribution due to their scattering in air and traversed materials. When 10  $\alpha$ -particles are delivered in 1.5  $\mu\text{m}$  FWHM, they are distributed in a way that are considered as 10 “single” impacts (Fig. 2). The recruitment time calculated corresponds to an irradiation with 10 individual particles in close vicinity ( $\mu\text{m}$  area) and not to a beam path composed of 10 particles. By contrast, when 100  $\alpha$ -particles are delivered the recruitment time decreases significantly compared to that obtained after 10  $\alpha$ -particles. When 100 and 1000 protons are delivered, the mean time does not change significantly, likely because protons generate sparse, simple damage events for which the GFP-RNF8 protein is recruited with the same velocity. Comparing different particles, but the same deposited energy (*i.e.* 100  $\alpha$ -particles and 1000 protons) the mean recruitment time is shorter when cells are irradiated with  $\alpha$ -particles with respect to the mean recruitment time of cells irradiated with protons. This tendency is also observed when cells are irradiated with 10  $\alpha$ -particles and 100 protons. The faster accumulation of the GFP-RNF8 protein when cells are irradiated with  $\alpha$ -particles rather than protons suggests that this protein is mainly dependent on the LET of particles and thus on the complexity and density of DNA damage.

The ability of GFP-XRCC1 to accumulate in distinct DNA damaged sites was also assessed by colocalization of the protein with immuno-detected  $\gamma\text{H2AX}$  (Supplementary Fig. S3). To study the accumulation of GFP-XRCC1 at DNA damage sites, we irradiated GFP-XRCC1 cells with increasing numbers of protons (100, 500 and 1000) and  $\alpha$ -particles (10, 50, 100 and 1000) and we performed online live cell microscopy. The course of protein kinetics can be described by curve characterized by a recruitment time ( $T$ ) and a decay time ( $T_2$ ), obtained using Eq. 3 in the Materials and Methods. The fluctuations of  $T$  are irrelevant between different cells. Instead, the intensity of fluorescence reached after irradiation ( $A$ ) and the mean decay time ( $T_2$ ) deviate extensively from cell to cell (Supplementary Table S2). These differences for  $A$  and  $T_2$  parameters can be due to several causes such as the individual capacity of cells to repair damages, the cell cycle position, the amount of DNA damaged or the GFP-level expression<sup>36</sup>. For these reasons the  $A$  and  $T_2$  obtained are not discussed in this study, but they are used for correctly fitting the model function, as already done in other studies<sup>36,37</sup>. We focused on the mean recruitment time  $T$ , which is calculated for at least 16 cells irradiated during three independent beam times.

Figure 4 shows that  $T$  does not vary significantly between 10 and 50  $\alpha$ -particles. When 10  $\alpha$ -particles were delivered, the fluorescent signal was weak and the detection limit of our system was reached. Following irradiation with 50, 100 and 1000  $\alpha$ -particles the recruitment time decreased as a function of the number of delivered particles. In the same manner, a decrease in the mean recruitment time is observed when the number of delivered protons is increased from 100 to 1000. Considering the LET,  $T$  is similar when the energy deposited by  $\alpha$ -particles and protons is the same. Indeed, the recruitment

time after 50  $\alpha$ -particles and 500 protons is the same (the deposited energy per spot is in the same order of magnitude), as the same recruitment time is observed after 100  $\alpha$ -particles and 1000 protons (similar deposited energy).

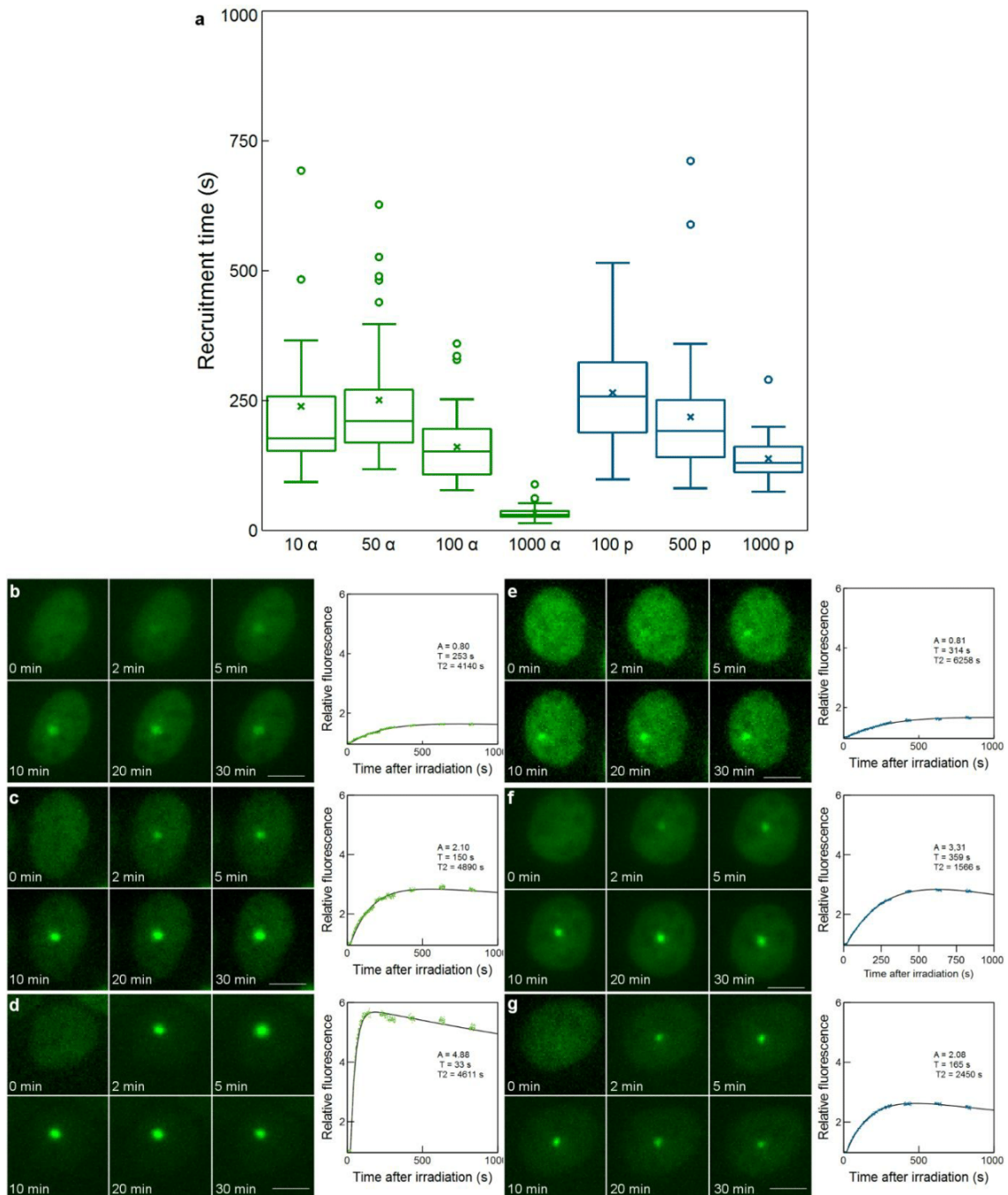


**Figure 4. GFP-XRCC1 mean recruitment time (T) after  $\alpha$ -particle and proton irradiations.** (a) Box plots representing the mean recruitment times of GFP-XRCC1 proteins after different deposited energy of  $\alpha$ -particles (green) and protons (blue) delivered in a single spots within cell nuclei. GFP-XRCC1 accumulates faster as a function of the deposited energy but not as a function of the particle LET. (b) 50, (c) 100, (d) 1000  $\alpha$ -particles and (e) 100, (f) 500 and (g) 1000 protons are delivered in a

spot and time-lapse imaging are shown for one sample nucleus per condition. Kinetics curves of GFP-XRCC1 are obtained by fitting experimental data (green and blue points) with a double-exponential curve. A: fluorescence increase after irradiation, T: protein recruitment time and  $T_2$ : protein decay time.

Summarizing these results, we first observe that immediately after irradiation the fluorescence intensity increases in irradiated areas as a function of the number of delivered particles. Secondly, the type of particles does not noticeably influence the recruitment time of GFP-XRCC1, which is for the same energy deposited by protons or  $\alpha$ -particles. We observe also that the fluorescence intensity decreased as a function of the type of the incident particles, the deposited energy and probably the chromatin density (as previously described<sup>25,38</sup>). These observations all suggest that the recruitment of GFP-XRCC1 is mainly dependent on deposited energy, rather than the LET of the radiation chosen.

## Discussion

Charged particle microbeam enables the uninterrupted monitoring and direct comparison of GFP-tagged proteins at a single cell level, starting from a few seconds after DNA damage generation. Monte Carlo simulations allow the estimation of the particle track structures and the calculation of the mean delivered energy per spot. By combining experimental and simulation methods from realistic conditions at the micrometric level, we present for the first time the evidence that the *in cellulo* kinetics of GFP-tagged proteins exhibits dependence on LET, and thus on the distribution of ionizations in irradiated cell nuclei.

A detailed picture of the protein migrations and post-translational modifications occurring within the first seconds to minutes after DNA damage induction has emerged largely based on data obtained after localized irradiation with laser microbeams<sup>39,40</sup>. However, the damage types induced by laser micro-irradiation still remain unclear<sup>41-44</sup> while charged particle irradiations allow for a calculation of the deposited energy at any point along the particle's track. This allows for a more accurate assessment of the energy required to induce a biological effect. Charged particle microbeam irradiation, Monte Carlo simulations and modern track structure codes providing a detailed description of physical interactions, and live cell imaging allow complementary investigations of the influence of damage density and complexity on recruitment kinetics by means track structures identification, which provides crucial insight into how DNA insults are generated and considered by the different cellular repair systems<sup>45,46</sup>. We investigated the radiation-induced behavior of two proteins that respond to DNA damage, while belonging to different DNA damage signaling pathways, and we correlated these responses with microdosimetry at a cellular scale. RNF8 has recently been shown, from the RNF8-RNF168-BRCA molecular complex, to be a key regulator of DNA repair foci complexes and is mainly involved in the

DNA ubiquitination of DSBs<sup>35,47-49</sup>. XRCC1 is considered to act as a central loading platform in SSB repair and BER<sup>4,50</sup>.

Increasing numbers of 3 MeV protons and  $\alpha$ -particles were delivered in a 1.5  $\mu\text{m}$  spot to create different densities of DNA damages and to increase the *total deposited energy*. To characterize this, we observed the track structures and spatial distribution of ionizations induced by  $\alpha$ -particles and protons. For similar deposited energies, the ionizations induced by 10  $\alpha$ -particle traversals are more densely distributed than those of 100 protons, which induce more dispersed ionizations. This spatial distribution of ionizations reflects the more complex damage induced by  $\alpha$ -particles compared to protons for the same deposited energy.

We observed that the recruitment of GFP-RNF8 to radiation-induced DNA damages is dependent firstly on the distribution of ionizations, and secondly on the total deposited energy. GFP-RNF8 recruitment takes place 1.5 to 4.5 times quicker after  $\alpha$ -particles than protons, when the deposited energy per spot is similar (Fig. 3). RNF8 behavior induced by charged particles has not been studied yet but studies conducted with laser systems described a strong interaction of RNF8 with MDC1 and NBS1, showing the same recruitment time at DSBs by these proteins<sup>47,49</sup>. This was echoed in a study of MDC1 recruitment time following carbon ion and proton irradiations, which indicated that its recruitment is LET- and absorbed dose-dependent<sup>36</sup>.

When 1 or 10  $\alpha$ -particles are delivered the GFP-RNF8 recruitment time does not change but a decrease was observed after 100  $\alpha$ -particles. These responses can be influenced by the microscopic spatial distributions of ionizations<sup>51</sup>. Figure 2 shows clearly that 10  $\alpha$ -particles are distributed as discrete events and can be considered as *single* impacts with respect to 100  $\alpha$ -particles that involve almost all the irradiated area (Supplementary Fig. S2). We did not observe changes of GFP-RNF8 recruitment time after increasing the deposited energy with increasing the number of delivered protons. A possible hypothesis to explain this behavior is the role of RNF8 mainly involved in complex DSBs repair. At high LETs, approximately 30% of DSBs induced are simple and 70% are complex, while at low LETs, only around 30% DSBs are complex<sup>52</sup>. Due to the increased complexity of damages induced by  $\alpha$ -particles, RNF8 is recruited faster to damage sites when  $\alpha$ -particles, rather than protons are used to irradiate cells for the same energy deposited.

Considering the GFP-XRCC1 recruitment time after irradiation by  $\alpha$ -particles and protons, different dynamics have been reported for its recruitment and retention at damaged sites following laser induced damage, depending upon the different in the wavelengths of the laser light used<sup>25,38,53,54</sup>. Following 365 nm and 405 nm laser irradiation, XRCC1 persists at damage sites. On the contrary, others studies showed that the loss of XRCC1 after irradiation with heavy ions is inconsistent with this data<sup>11,17</sup>. To explain these differences, the authors speculate that the damage produced by 365 nm and 405 nm laser light is highly complex, possibly reflecting a high density of lesions induced. As a consequence, the reparability of such complex DNA damage is reduced, leading to persistence of XRCC1 at damage

sites<sup>5</sup>. Immediate and fast recruitment of XRCC1 is however observed by all authors<sup>17,31,37</sup>. We focused on the recruitment time of XRCC1, and we found that the GFP-XRCC1 recruitment time is dependent mainly on the deposited energy for both  $\alpha$ -particles and protons, with a minimum value of  $34 \pm 14$  s following irradiation by 1000  $\alpha$ -particles (Supplementary Table 2).

The recruitment time seems to be independent of the spatial distribution of ionizations, showing the same recruitment time when the same energy is deposited by  $\alpha$ -particles or protons. This is in accordance with the role of XRCC1 as a loading platform for other proteins after DNA damage, suggesting it is independent of damage complexity. In addition, we observed that the recruitment of XRCC1 can be up to 7 times faster than the RNF8 recruitment time. This probably means that cells recognize DNA damage independently of its complexity, and recruit XRCC1, and then cells recruit specific proteins, such as RNF8, that act to repair complex DNA damage, as underlined by its dependency on particle LET.

## Materials and Methods

### Beam line characteristics

The micro-irradiation setup is installed on the AIFIRA facility (*Applications Interdisciplinaires des Faisceaux d'Ions en Région Aquitaine*). The accelerator (Singletron<sup>TM</sup>, High Voltage Engineering Europa, The Netherlands) delivers protons and helium ions ( $\text{He}^+$ ) with energies up to 3 MeV. This allows cells to be exposed to 3 MeV protons ( $\text{H}^+$ ) and  $\alpha$ -particles ( $\text{He}^+$ ) presenting a linear energy transfer of 12 and 148  $\text{keV}\cdot\mu\text{m}^{-1}$ , respectively. As already described<sup>14</sup>, to target single living cells, the beam was strongly collimated to reduce the particles flux to a few thousand ions per second on target and focused using a triplet of magnetic quadrupoles to achieve a sub-micron resolution under vacuum. The ion beam was extracted in air through a 200-nm thick  $\text{Si}_3\text{N}_4$  window (Silson Ltd., Northampton, England) and enters the sample through a 4- $\mu\text{m}$  thick polypropylene foil (Goodfellow) used as a cell support. The ion beam was positioned on the target by means of electrostatic scanning plates situated downstream of the last quadrupole. In the case of protons, the mean number of particles (N) hitting the cells was linearly related to the opening time and the relative statistical fluctuation in the number of traversals delivered to the cells decreases as N increases. Considering the mean number of traversals used in this work, this leads to an uncertainty of  $100 \pm 10$  and  $1000 \pm 33$  protons per spot. The exposure of the target cells to the charged particles was controlled using a fast electrostatic beam deflector allowing to open and close the beam within 1  $\mu\text{s}$  (DEI PVM-4210)<sup>14</sup>. In case of  $\alpha$ -particles, each particle was detected upstream with a BNCD (Boron-doped Nano-Crystalline Diamond) from which secondary electrons emitted were collected using a channeltron electron multiplier<sup>15</sup>.

The irradiation end-station consists of a motorized inverted fluorescence microscope (AxioObserver Z1, Carl Zeiss Micro-Imaging GmbH) equipped with a 14 bits Rolera EM-C<sup>2TM</sup> Camera (QImaging)



which was positioned horizontally at the end of the beam line. It can be equipped with up to 6 objectives and fluorescence filter sets. A good compromise between high numerical aperture (NA) and long working distance was obtained with a 63x objective (LD Plan-Neofluar 63x/0.75, Optical resolution of about 400 nm, Carl Zeiss MicroImaging GmbH). Fluorescence light was provided by a Light Emitting Diode (LED) illuminating system (Colibri2™, Zeiss) with negligible heat production.

### **Simulation using the Geant4 Monte Carlo toolkit**

Deposited energies from  $\alpha$ -particles and protons were simulated using the Geant4 Monte Carlo toolkit<sup>55</sup>. Simulations were carried out by setting the distance from beam exit window at 80  $\mu\text{m}$  for  $\alpha$ -particles and 250  $\mu\text{m}$  for protons, and the beam FWHM in vacuum before extraction was set to 0.5  $\mu\text{m}$ . In the simulation, the extraction window (150 nm  $\text{Si}_3\text{N}_4$ ), the air gap (80 or 250  $\mu\text{m}$ ) and the polypropylene foil (4  $\mu\text{m}$ ) were also considered. The energy deposition and the absorbed dose deposited were calculated for a thickness of 6  $\mu\text{m}$  (approximate thickness of a cell nucleus) in liquid water.

For the simulation of  $\alpha$ -particles and protons track structures, Geant4-DNA processes and models<sup>20,29</sup> available in Geant4 version 10.2.p02 were used. Geant4-DNA discrete Physics processes such as ionizations for electrons, protons and  $\alpha$ -particles were simulated. The track structures of single particles were simulated for a thickness of 1  $\mu\text{m}$  in water, while the track structures of 10 and 100  $\alpha$ -particles, 100 and 1000 protons were obtained for a thickness of 20 nm in water. Protons and  $\alpha$ -particles were shot with a Gaussian beam having a FWHM of 1.5  $\mu\text{m}$  at the inlet of the water volume. We used a Geant4-DNA Physics list based on the “G4EmDNAPhysics” physics constructor.

### **Cell line cultures and transfections**

HTB96 U2OS cells (ATCC) were maintained in McCoy's 5A medium (Dutscher) supplemented with 10% (v/v) Fetal Bovine Serum (FBS, Dutscher) and 100  $\mu\text{g}/\text{ml}$  streptomycin/penicillin (Pen-Strep 15140, GIBCO). All cell lines were kept in an incubator at 37 °C under 5%  $\text{CO}_2$  humidified atmosphere. A cDNA of human RNF8 inserted into pEGFP-C1 (kindly provided by Jiri Lukas) was used as a construct for stable transfection of GFP-RNF8<sup>8</sup>. The XRCC1 human cDNA inserted in pEGFP-N1 vectors (kindly provided from Akira Yasui) was used as a construct for stable transfection of GFP-XRCC1<sup>54</sup>. Viromer Red transfection reagent (Lipocalyx GmbH, Germany) was used for all transfections, in combination with various expression vectors which were used according to the manufacturers' guidelines. Transfected cells were plated 48 h after transfection and different geneticin/G418 dilutions (from 0.1 mg/ml to 1 mg/ml, GIBCO) were added 72 h after transfection. After 10 days of drug selection, surviving colonies were checked under fluorescence microscopy and GFP-positive colonies were isolated. Several clones were selected and expanded into cell lines for further analysis.

### Cell irradiation

Stably transfected GFP-RNF8 and GFP-XRCC1 cells were plated on the polypropylene surface (Goodfellow) coated with CellTak (Biosciences) at a density of 14000 cells per 20  $\mu$ l drop, 24 h before irradiation. During microbeam irradiation cells were maintained in FluoroBrite™ DMEM medium (GIBCO, ThermoFisher Scientific) that ensures a low background fluorescence during images acquisition. Cells were targeted and irradiated with different absorbed doses of protons or  $\alpha$ -particles from 1 to several thousand of particles per cell. The proteins re-localization to the damaged area was followed for 15 and 30 min for GFP-XRCC1 and GFP-RNF8 proteins, respectively.

### Immuno-detection

HTB96 U2OS cells were fixed within 1 h with paraformaldehyde 4% (w/v) in phosphate-buffered saline (PBS, pH 7.4, without  $\text{Ca}^{2+}$  and  $\text{Mg}^{2+}$ ) medium for 15 min at room temperature and washed with PBS. Then, cells permeabilization and saturation were performed using a blocking buffer containing 0.2% (v/v) Triton X-100 (Sigma, St Quentin Fallavier, France), 10% FBS (Dutscher) in PBS for 30 min at room temperature. After three washes with PBS during 5 min, samples were incubated overnight, at 4 °C with anti-human  $\gamma$ H2AX rabbit monoclonal antibody (20E3, Cell signaling) at 1:1000 in blocking buffer. After three more washes with PBS, samples were incubated for 3 h at room temperature with Goat anti-rabbit conjugated to Alexa Fluor<sup>488</sup> antibody (Molecular Probes, Invitrogen) at 1:2000 in blocking buffer. Cells were rinsed twice with PBS and nuclei stained with 1  $\mu$ M Hoechst<sup>33342</sup> in PBS for 10 min at room temperature. Polypropylene foils were cut and mounted using ProLong Gold Antifade Reagent (Molecular Probes) overnight at room temperature, and visualized on Zeiss AxioObserver Z1 microscope (CarlZeiss MicroImaging, GmbH).

### Time lapse imaging treatment and fitting models

Images, obtained using the MicroManager software<sup>56</sup>, were treated in ImageJ. Only cells that were not moving during video were analyzed. The kinetics of GFP-tagged proteins redistribution were measured by recording the specific fluorescence in irradiated areas (ROI). The measured values were corrected for non-specific fluorescence bleaching during the repeated image acquisition and were processed as follows:

$$Rel. Int = \frac{(I_{foci} - I_{back}) / (I_{res} - I_{back})}{I_{preIR}} \quad (1)$$

Where  $I_{foci}$  is the intensity of foci (selected ROI),  $I_{back}$  is the background mean fluorescence intensity,  $I_{res}$  is the mean fluorescence intensity of irradiated cell nucleus (protein reservoir), and  $I_{preIR}$  is the mean of irradiated nucleus fluorescence intensity measured before irradiation.

The redistribution of fluorescence in GFP-RNF8 cells was fitted with a mathematical model for a first order step response as already described<sup>57</sup>. Data from individual cells are treated as individual experiments and fitted to the model:

$$Rel\ Int = 1 + A \left( 1 - e^{-\frac{(t-t_0)}{T}} \right) \quad (2)$$

The distribution of fluorescence in GFP-XRCC1 cells was fitted to a mathematical model used for the first time by Hable *et al.*<sup>9</sup>.

$$Rel\ Int = 1 + A \left( 1 - e^{-\frac{(t-t_0)}{T}} \right) * e^{-\frac{(t-t_0)}{T_2}} \quad (3)$$

The first part of the model function is the same used previously and describes the IRIF formation, in which T representing the mean recruitment time. At the same time the intensity decreases and it is described by a mean decay time  $T_2$ . A is the highest intensity value reached if a decrease in intensity did not appear.  $t_0$  is the time when focus formation starts. The relevant parameters are T and  $T_2$ . These parameters are determined for each cell separately, and then a mean value is calculated.

## Bibliography

1. Maxwell, C. A. *et al.* Targeted and nontargeted effects of ionizing radiation that impact genomic instability. *Cancer Res.* **68**, 8304–8311 (2008).
2. Desouky, O., Ding, N. & Zhou, G. Targeted and non-targeted effects of ionizing radiation. *J. Radiat. Res. Appl. Sci.* **8**, 247–254 (2015).
3. Sage, E. & Shikazono, N. Radiation-induced clustered DNA lesions: repair and mutagenesis. *Free Radic. Biol. Med.* 1–11 (2016). doi:10.1016/j.freeradbiomed.2016.12.008
4. Mortusewicz, O., Leonhardt, H. & Cardoso, M. C. Spatiotemporal dynamics of regulatory protein recruitment at DNA damage sites. *J. Cell. Biochem.* **104**, 1562–1569 (2008).
5. Gassman, N. R. & Wilson, S. H. Micro-irradiation tools to visualize base excision repair and single-strand break repair. *DNA Repair (Amst)*. **31**, 52–63 (2015).
6. Solarczyk, K. J., Kordon, M., Berniak, K. & Dobrucki, J. W. Two stages of XRCC1 recruitment and two classes of XRCC1 foci formed in response to low level DNA damage induced by visible light, or stress triggered by heat shock. *DNA Repair (Amst)*. **37**, 12–21 (2016).
7. Feng, L. & Chen, J. The E3 ligase RNF8 regulates KU80 removal and NHEJ repair. *Nat. Struct. Mol. Biol.* **19**, 201–206 (2012).
8. Mailand, N. *et al.* RNF8 Ubiquitylates Histones at DNA Double-Strand Breaks and Promotes Assembly of Repair Proteins. *Cell* **131**, 887–900 (2007).
9. Hable, V. *et al.* Recruitment kinetics of DNA repair proteins Mdc1 and Rad52 but not 53BP1 depend on damage complexity. *PLoS One* **7**, e41943 (2012).
10. Mosconi, M. *et al.* 53BP1 and MDC1 foci formation in HT-1080 cells for low- and high-LET microbeam irradiations. *Radiat. Environ. Biophys.* **50**, 345–352 (2011).
11. Guo, N. *et al.* Live cell imaging combined with high-energy single-ion microbeam. *Rev. Sci. Instrum.* **87**, (2016).
12. Schettino, G., Ghita, M., Richard, D. J. & Prise, K. M. Spatiotemporal investigations of DNA damage repair using microbeams. *Radiat. Prot. Dosimetry* **143**, 340–343 (2011).
13. Van Oven, C. *et al.* An ultrasoft X-ray multi-microbeam irradiation system for studies of DNA damage responses by fixed- and live-cell fluorescence microscopy. *Eur. Biophys. J.* **38**, 721–728 (2009).
14. Bourret, S. *et al.* Fluorescence time-lapse imaging of single cells targeted with a focused

- scanning charged-particle microbeam. *Nucl. Instruments Methods Phys. Res. Sect. B Beam Interact. with Mater. Atoms* **325**, 27–34 (2014).
15. Muggioli, G. *et al.* Single  $\alpha$ -particle irradiation permits real-time visualization of RNF8 accumulation at DNA damaged sites. *Sci. Rep.* **7**, 41764 (2017).
  16. Drexler, G. A. & Ruiz-Gómez, M. J. Microirradiation techniques in radiobiological research. *J. Biosci.* **40**, 629–643 (2015).
  17. Tobias, F., Durante, M., Taucher-Scholz, G. & Jakob, B. Spatiotemporal analysis of DNA repair using charged particle radiation. *Mutat. Res. Mutat. Res.* **704**, 54–60 (2010).
  18. Tobias, F. *et al.* Spatiotemporal dynamics of early DNA damage response proteins on complex DNA lesions. *PLoS One* **8**, e57953 (2013).
  19. Vadhavkar, N. *et al.* Combinatorial DNA Damage Pairing Model Based on X-Ray-Induced Foci Predicts the Dose and LET Dependence of Cell Death in Human Breast Cells. *Radiat. Res.* **000**, 273–281 (2014).
  20. Bernal, M. A. *et al.* Track structure modeling in liquid water: A review of the Geant4-DNA very low energy extension of the Geant4 Monte Carlo simulation toolkit. *Phys. Medica* **31**, 861–874 (2015).
  21. Douglass, M., Bezak, E. & Penfold, S. Development of a radiation track structure clustering algorithm for the prediction of DNA DSB yields and radiation induced cell death in Eukaryotic cells. *Phys. Med. Biol.* **60**, 3217–3236 (2015).
  22. Gruel, G. *et al.* Cell to cell variability of radiation-induced foci: Relation between observed damage and energy deposition. *PLoS One* **11**, 1–20 (2016).
  23. Campalans, A. *et al.* Distinct spatiotemporal patterns and PARP dependence of XRCC1 recruitment to single-strand break and base excision repair. *Nucleic Acids Res.* **41**, 3115–3129 (2013).
  24. Solarczyk, K. J., Kordon, M., Berniak, K. & Dobrucki, J. W. Two stages of XRCC1 recruitment and two classes of XRCC1 foci formed in response to low level DNA damage induced by visible light, or stress triggered by heat shock. *DNA Repair (Amst)*. **37**, 12–21 (2016).
  25. Wei, L. *et al.* Damage response of XRCC1 at sites of DNA single strand breaks is regulated by phosphorylation and ubiquitylation after degradation of poly(ADP-ribose). *J. Cell Sci.* **126**, 4414–4423 (2013).
  26. Yan, J. & Jetten, A. M. RAP80 and RNF8, key players in the recruitment of repair proteins to DNA damage sites. *Cancer Lett.* **271**, 179–90 (2008).
  27. Thorslund, T. *et al.* Histone H1 couples initiation and amplification of ubiquitin signalling after DNA damage. *Nature* **527**, 389–93 (2015).
  28. Doil, C. *et al.* RNF168 Binds and Amplifies Ubiquitin Conjugates on Damaged Chromosomes to Allow Accumulation of Repair Proteins. *Cell* **136**, 435–446 (2009).
  29. Incerti, S. *et al.* Comparison of GEANT4 very low energy cross section models with experimental data in water. *Med. Phys.* **37**, 4692–4708 (2010).
  30. Allison, J. *et al.* Recent developments in Geant4. *Nucl. Instruments Methods Phys. Res. Sect. A Accel. Spectrometers, Detect. Assoc. Equip.* **835**, 186–225 (2016).
  31. Asaithamby, A. & Chen, D. J. Mechanism of cluster DNA damage repair in response to high-atomic number and energy particles radiation. *Mutat. Res. Mol. Mech. Mutagen.* **711**, 87–99 (2011).
  32. Barberet, P. *et al.* Monte-Carlo dosimetry on a realistic cell monolayer geometry exposed to alpha particles. *Phys. Med. Biol.* **57**, 2189–2207 (2012).
  33. Stewart, R. D. Two-Lesion Kinetic Model of Double-Strand Break Rejoining and Cell Killing. *Radiat. Res.* **156**, 365–378 (2001).
  34. Friedland, W., Dingfelder, M., Kunderát, P. & Jacob, P. Track structures, DNA targets and radiation effects in the biophysical Monte Carlo simulation code PARTRAC. *Mutat. Res. - Fundam. Mol. Mech. Mutagen.* **711**, 28–40 (2011).
  35. Huen, M. S. Y. *et al.* RNF8 transduces the DNA-damage signal via histone ubiquitylation and checkpoint protein assembly. *Cell* **131**, 901–14 (2007).
  36. Hable, V. *et al.* Recruitment kinetics of DNA repair proteins Mdc1 and Rad52 but not 53BP1 depend on damage complexity. *PLoS One* **7**, e41943 (2012).

37. Jakob, B. *et al.* DNA double-strand breaks in heterochromatin elicit fast repair protein recruitment, histone H2AX phosphorylation and relocation to euchromatin. *Nucleic Acids Res.* **39**, 6489–99 (2011).
38. Mortusewicz, O. & Leonhardt, H. XRCC1 and PCNA are loading platforms with distinct kinetic properties and different capacities to respond to multiple DNA lesions. *BMC Mol. Biol.* **8**, 81 (2007).
39. Bekker-Jensen, S. & Mailand, N. Assembly and function of DNA double-strand break repair foci in mammalian cells. *DNA Repair (Amst)*. **9**, 1219–1228 (2010).
40. Jungmichel, S. & Stucki, M. MDC1: The art of keeping things in focus. *Chromosoma* **119**, 337–349 (2010).
41. Drexler, G. A. *et al.* Live cell imaging at the Munich ion microbeam SNAKE - a status report. *Radiat. Oncol.* **10**, 42 (2015).
42. Suzuki, K., Yamauchi, M., Oka, Y., Suzuki, M. & Yamashita, S. Creating localized DNA double-strand breaks with microirradiation. *Nat. Protoc.* **6**, 134–139 (2011).
43. Nagy, Z. & Soutoglou, E. DNA repair: easy to visualize, difficult to elucidate. *Trends Cell Biol.* **19**, 617–629 (2009).
44. Splinter, J. *et al.* Biological dose estimation of UVA laser microirradiation utilizing charged particle-induced protein foci. *Mutagenesis* **25**, 289–297 (2010).
45. Kramer, M. & Kraft, G. Track structure and DNA damage. *Adv. Space Res.* **14**, 151–9 (1994).
46. Averbeck, N. B. *et al.* Efficient Rejoining of DNA Double-Strand Breaks despite Increased Cell-Killing Effectiveness following Spread-Out Bragg Peak Carbon-Ion Irradiation. *Front. Oncol.* **6**, 1–8 (2016).
47. Kolas, N. K. *et al.* Orchestration of the DNA-Damage Response by the RNF8 Ubiquitin Ligase. *Science (80-. )*. **318**, 1637–1640 (2007).
48. Bartocci, C. & Denchi, E. L. Put a RING on it: regulation and inhibition of RNF8 and RNF168 RING finger E3 ligases at DNA damage sites. *Front. Genet.* **4**, 128 (2013).
49. Mok, M. T. S., Cheng, A. S. L. & Henderson, B. R. The ubiquitin ligases RNF8 and RNF168 display rapid but distinct dynamics at DNA repair foci in living cells. *Int. J. Biochem. Cell Biol.* **57**, 27–34 (2014).
50. Campalans, A. *et al.* Interaction with OGG1 Is Required for Efficient Recruitment of XRCC1 to Base Excision Repair and Maintenance of Genetic Stability after Exposure to Oxidative Stress. *Mol. Cell. Biol.* **35**, 1648–1658 (2015).
51. Goodhead, D. T. Mechanisms for the biological effectiveness of high-LET radiations. *J. Radiat. Res.* **40 Suppl**, 1–13 (1999).
52. Nikjoo, H., Neill, P. O., Wilson, W. E. & Goodhead, D. T. Computational Approach for Determining the Spectrum of DNA Damage Induced by Ionizing Radiation. **583**, 577–583 (2001).
53. Reynolds, P., Botchway, S. W., Parker, A. W. & O'Neill, P. Spatiotemporal dynamics of DNA repair proteins following laser microbeam induced DNA damage - When is a DSB not a DSB? *Mutat. Res. - Genet. Toxicol. Environ. Mutagen.* **756**, 14–20 (2013).
54. Lan, L. *et al.* In situ analysis of repair processes for oxidative DNA damage in mammalian cells. *Proc. Natl. Acad. Sci. U. S. A.* **101**, 13738–43 (2004).
55. Agostinelli, S. *et al.* GEANT4 - A simulation toolkit. *Nucl. Instruments Methods Phys. Res. Sect. A Accel. Spectrometers, Detect. Assoc. Equip.* **506**, 250–303 (2003).
56. Edelstein, A. D. *et al.* Advanced methods of microscope control using µManager software. *J. Biol. Methods* **1**, 10 (2014).
57. Lukas, C. *et al.* Mdc1 couples DNA double-strand break recognition by Nbs1 with its H2AX-dependent chromatin retention. *EMBO J.* **23**, 2674–2683 (2004).

## Acknowledgments

The AIFIRA facility and the microbeam line have been financially supported by the Region Aquitaine (IOPRA, POPRA). MS is supported by the Region Aquitaine (POPRA). Merete Grofte and Jiri Lukas from Novo Nordisk Foundation Center for Protein Research for their generous gift (plasmids GFP-

RNF8), and Akira Yasui from Tohoku University, Institute of Development, Aging and Cancer for his generous gift (plasmids GFP-XRCC1). This work has been partly supported by the European Community as an Integrating Activity “*Support of Public and Industrial Research Using Ion Beam Technology*” (SPIRIT) under the EC contract n° 227012. GM is supported by the European Community as an “*Integrating Activity Supporting Postgraduate Research with Internships in Industry and Training Excellence*” (SPRITE) under EC contract no. 317169.

#### **Author contributions statement**

GM and HS established the GFP-RNF8 and GFP-XRCC1 cell lines; GM, PB, MS, GD and HS designed and performed the radiation biology experiments; PB, ET, SI and NL performed Monte Carlo simulations; all authors contributed to data analyses and reviewed the manuscript.

#### **Additional information**

Supplementary information accompanies this paper.

**Competing financial interests.** The authors declare no competing financial interests.

## Microdosimetric simulations explain radiation-induced spatiotemporal dynamics of GFP-tagged DNA repair proteins at the cellular scale

Giovanna Muggioli<sup>(1,2)</sup>, Eva Torfeh<sup>(1,2)</sup>, Marina Simon<sup>(1,2)</sup>, Guillaume Devès<sup>(1,2)</sup>, Sébastien Incerti<sup>(1,2)</sup>, Nathanael Lampe<sup>(1,2)</sup>, Hervé Seznec<sup>(1,2)</sup> and Philippe Barberet<sup>(1,2)</sup>

(1) Université de Bordeaux, Centre d'Etudes Nucléaires Bordeaux Gradignan (CENBG), Chemin du Solarium, 33175 Gradignan, France

(2) CNRS, UMR5797, Centre d'Etudes Nucléaires Bordeaux Gradignan (CENBG), Chemin du Solarium, 33175 Gradignan, France

### Supplementary Data

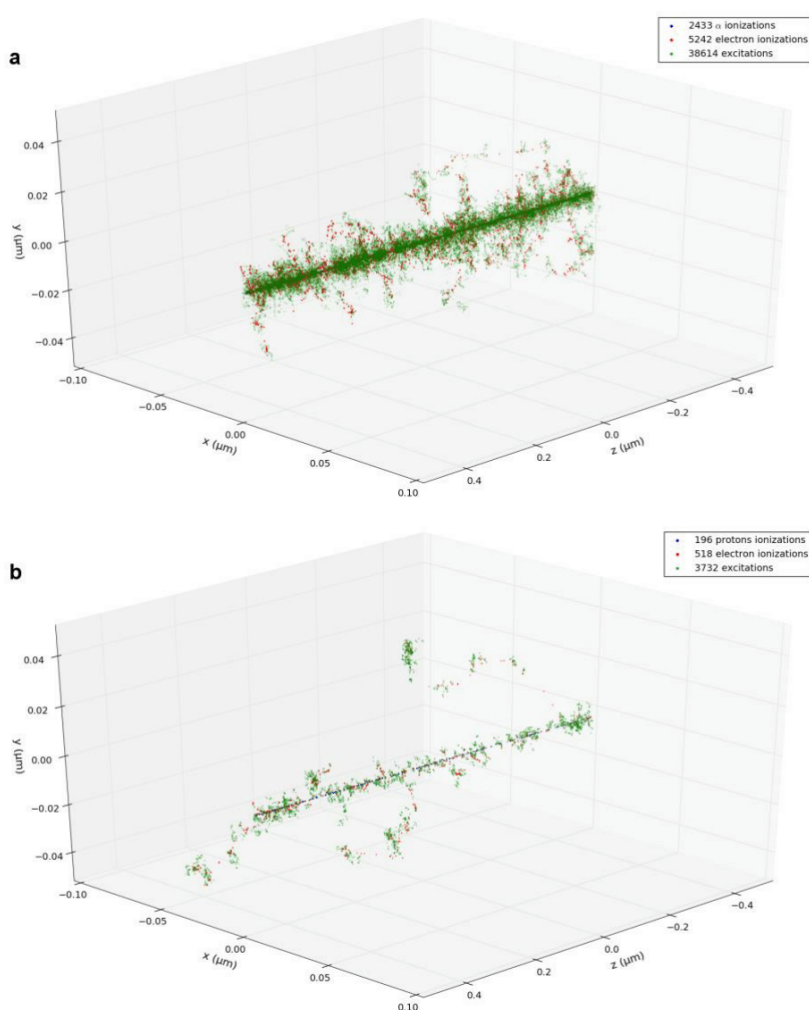


**Fig. S1. Track structures and number of ionizations of a single 3 MeV  $\alpha$ -particle/proton in water.** When (a) one  $\alpha$ -particle and (b) one proton traverse 1  $\mu\text{m}$  of liquid water, the total number of counted processes and the deposited energy (149.54 and 13.94 keV for  $\alpha$ -particle and proton, respectively) is ten times higher for  $\alpha$ -particles than for protons, due to the higher LET of  $\alpha$ -particle. The blue dots indicate the position of ionization events produced by the primary charged particles, red dots indicate the position of the ionization events produced by secondary electrons and green dots represent the excitations produced.

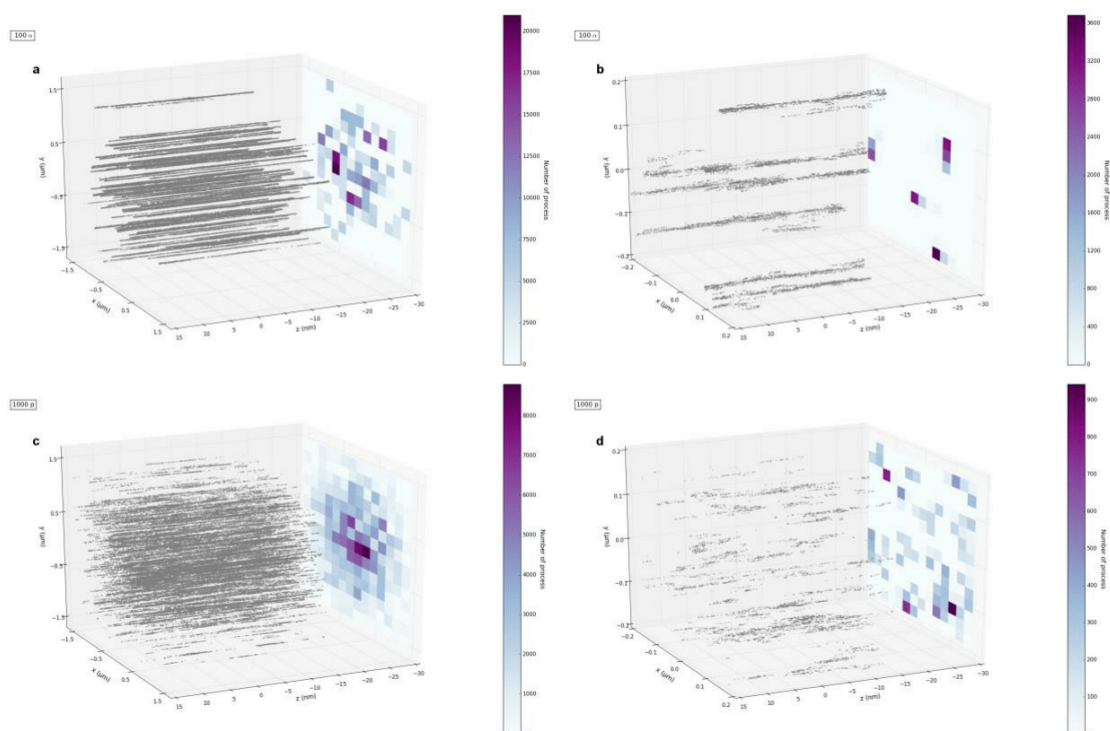


**Fig. S2. Track structures of 3 MeV  $\alpha$ -particles and protons in liquid water obtained with Geant4-DNA.** Each dot represents one ionization induced by (a) 100  $\alpha$ -particles and (c) 1000 protons through 30 nm of water with a 1,5  $\mu\text{m}$  FWHM beam and the respective projections of ionizations induced. (b) and (d) represent the distribution of ionizations induced by 100  $\alpha$ -particles and 1000 protons through 30 nm wide cylinder (the size of a chromatin fiber).



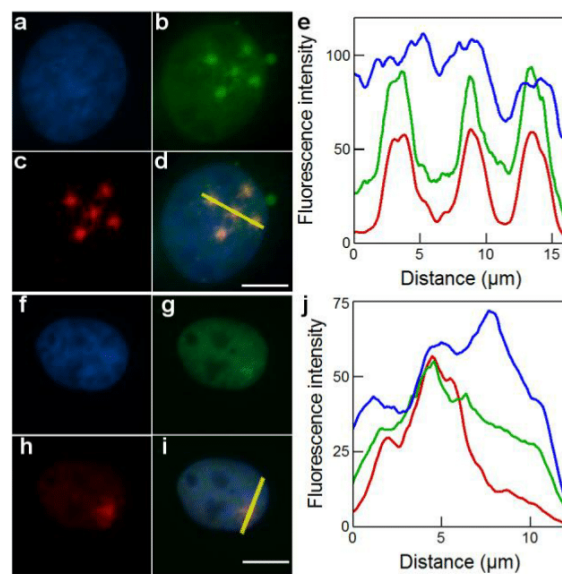


**Fig. S3. Colocalization of both GFP-RNF8 and GFP-XRCC1 with  $\gamma$ H2AX foci.** (a) GFP-RNF8 and (f) GFP-XRCC1 paraformaldehyde fixed cell nuclei counterstained with Hoechst<sup>33342</sup>. Targeted irradiation with 1000 protons on 5 spots distributed on a 10  $\mu$ m wide cross pattern or with 100  $\alpha$ -particles in 1 spot. (b and g) GFP-RNF8 and GFP-XRCC1 proteins accumulated at radiation-induced DNA damages. (c and h)  $\gamma$ H2AX signal observed at IRIF and (d and i) respectively colocalization confirming the presence of induced DNA damages. (e and j) Blue lines represent the nuclear chromatin. Peaks showed  $\gamma$ H2AX (red line) and GFP-RNF8 or GFP-XRCC1 (green line) signal colocalization plotted with the length of the yellow lines, in paraformaldehyde fixed cell 1 h after irradiation. The beam size observed is about 2  $\mu$ m FWHM. Scale bars: 10  $\mu$ m.

Ion	Ions per point/nucleus	Dose (Gy)	Number of cells analyzed	Mean recruitment time (s) $\pm$ SD
3 MeV $\alpha$	1	0.1	28	452 $\pm$ 210
3 MeV $\alpha$	10	1	27	524 $\pm$ 254
3 MeV $\alpha$	100	10	26	223 $\pm$ 105
3 MeV H+	100	1	31	755 $\pm$ 445
3 MeV H+	1000	10	16	937 $\pm$ 425

**Table S1. GFP-RNF8 kinetics after proton and  $\alpha$ -particle irradiations.**

Ion	Ions per point/nucleus	Dose (Gy)	Number of cells analyzed	Intensity of fluorescence $\pm$ SD	Mean recruitment time (s) $\pm$ SD	Mean decay time (s) $\pm$ SD
3 MeV $\alpha$	10	1	8	0,4 $\pm$ 0,3	117 $\pm$ 93	3102 $\pm$ 179 <sup>(a)</sup>
3 MeV $\alpha$	10	1	8	0,3 $\pm$ 0,01	307 $\pm$ 187	1,0E+05 $\pm$ 9,7E+04 <sup>(b)</sup>
3 MeV $\alpha$	50	5	36	1,5 $\pm$ 0,4	259 $\pm$ 127	3678 $\pm$ 1819
3 MeV $\alpha$	100	10	29	1,5 $\pm$ 0,7	160 $\pm$ 29	4200 $\pm$ 2507
3 MeV $\alpha$	1000	100	34	3,8 $\pm$ 1,4	34 $\pm$ 14	5343 $\pm$ 2155
3 MeV H+	100	1	28	0,4 $\pm$ 0,2	233 $\pm$ 83	5336 $\pm$ 7639 <sup>(a)</sup>
3 MeV H+	100	1	18	0,5 $\pm$ 0,3	315 $\pm$ 113	1,7E+05 $\pm$ 5,2E+05 <sup>(b)</sup>
3 MeV H+	500	5	28	1,9 $\pm$ 1,1	221 $\pm$ 142	1697 $\pm$ 2300 <sup>(a)</sup>
3 MeV H+	500	5	10	1,2 $\pm$ 0,5	210 $\pm$ 51	2,0E+05 $\pm$ 2,9E+05 <sup>(b)</sup>
3 MeV H+	1000	10	25	2,4 $\pm$ 0,7	138 $\pm$ 44	11120 $\pm$ 28607

**Table S2. GFP-XRCC1 kinetics after proton and  $\alpha$ -particle micro-irradiations.** The variations of  $T_2$  parameter allowed to separate the cells behavior in two main groups: in the first one <sup>(a)</sup> the fluorescence intensity decreases after reaching the maximum value; in the second one <sup>(b)</sup> the fluorescence intensity does not decrease. The recruitment time is not influenced by these variations.



## Article 3

**“Live cell imaging of mitochondria following targeted irradiation *in situ* reveals rapid and highly localized loss of membrane potential”**

Walsh, D.W.M. et al. Live cell imaging of mitochondria following targeted irradiation *in situ* reveals rapid and highly localized loss of membrane potential. *Sci. Rep.* 7, 46648; doi:10.1038/srep46684 (2017).

SCIENTIFIC REPORTS 

OPEN

# Live cell imaging of mitochondria following targeted irradiation *in situ* reveals rapid and highly localized loss of membrane potential

Received: 04 October 2016

Accepted: 24 March 2017

Published: 25 April 2017

Dietrich W. M. Walsh<sup>1,2</sup>, Christian Siebenwirth<sup>1,2</sup>, Christoph Greubel<sup>1</sup>, Katarina Ilicic<sup>2</sup>, Judith Reindl<sup>1</sup>, Stefanie Girst<sup>1</sup>, Giovanna Muggioli<sup>3,4</sup>, Marina Simon<sup>3,4</sup>, Philippe Barberet<sup>3,4</sup>, Hervé Sezec<sup>3,4</sup>, Hans Zischka<sup>5</sup>, Gabriele Multhoff<sup>2</sup>, Thomas E. Schmid<sup>2</sup> & Guenther Dollinger<sup>1</sup>

The reliance of all cell types on the mitochondrial function for survival makes mitochondria an interesting target when trying to understand their role in the cellular response to ionizing radiation. By harnessing highly focused carbon ions and protons using microbeams, we have performed *in situ* live cell imaging of the targeted irradiation of individual mitochondria stained with Tetramethyl rhodamine ethyl ester (TMRE), a cationic fluorophore which accumulates electrophoretically in polarized mitochondria. Targeted irradiation with both carbon ions and protons down to beam spots of  $<1\ \mu\text{m}$  induced a near instant loss of mitochondrial TMRE fluorescence signal in the targeted area. The loss of TMRE after targeted irradiation represents a radiation induced change in mitochondrial membrane potential. This is the first time such mitochondrial responses have been documented *in situ* after targeted microbeam irradiation. The methods developed and the results obtained have the ability to shed new light on not just mitochondria's response to radiation but to further elucidate a putative mechanism of radiation induced depolarization and mitochondrial response.

The detrimental effects of ionizing radiation on the human body as a whole have been studied since 1896<sup>1</sup> and, after decades of work, have been linked to the formation of DNA lesions, and classified as a risk factor for the development of cancer. Ionizing radiation has also been harnessed very successfully as a tool in the treatment of cancers. However, many key questions regarding the effects of ionizing radiation on cells, cancerous and non-cancerous, still remain unanswered. The main focus of research conducted into the effects of ionizing irradiation on cells has focused on the damage to the cell nucleus and the detrimental effects this has upon the cell<sup>2</sup>. The prevailing dogma in radiation biology and radiotherapy is that a high enough dose of energy deposited to the nucleus will ultimately lead to the destruction of that cell. Within this "classical dogma", the cytoplasm, the cellular environment in which the majority of cellular processes involved in the maintenance of cellular integrity take place and which makes up a large part of each cell by volume, have rarely been taken into account as the cytoplasm has been assumed to be less sensitive to radiation.

The first cytoplasmic irradiation experiments were documented in 1953 by Zirkle and Bloom<sup>3</sup> and have more recently been intensively conducted using a variety of tools, including femto-second lasers<sup>4-7</sup> and particle micro beams<sup>8</sup>. The overall consensus, since 1953, is still that the cytoplasm as a whole is less radio-sensitive than the nucleus<sup>9</sup>. Cytoplasmic irradiation has been shown to be involved in inducing bystander effects<sup>10</sup> and mutation

<sup>1</sup>Universität der Bundeswehr München, Institut für Angewandte Physik und Messtechnik, D-85577 Neubiberg, Germany. <sup>2</sup>Klinikum rechts der Isar, Technische Universität München, D-81675 München, Germany. <sup>3</sup>Université de Bordeaux, Centre d'Etudes Nucléaires de Bordeaux Gradignan (CENBG), Chemin du Solarium, 33175 Gradignan, France. <sup>4</sup>IN2P3, CNRS, UMR5797, Centre d'Etudes Nucléaires de Bordeaux Gradignan (CENBG), Chemin du Solarium, 33175 Gradignan, France. <sup>5</sup>Institute of Molecular Toxicology and Pharmacology, Helmholtz Center Munich, German Research Center for Environmental Health, D-85764 Neuherberg, Germany. Correspondence and requests for materials should be addressed to D.W.M.W. (email: dietrich.walsh@unibw.de)

induction<sup>11</sup>. The question therefore remains what contribution the cytoplasmic components have in damage induction and cellular survival.

Owing to the number of constituents and the high density of proteins, the cytoplasm is a highly complicated environment to study. In the majority of mammalian, cells the cytoplasm makes up the largest volume of the cell and to investigate the cytoplasm means to investigate the response to radiation of a variety of individual organelles and biological components. In this study mitochondria have been selected to highlight the effect of targeted irradiation. Mitochondria constitute a large volume of the cytoplasm in all cell types found in the body as they are the main site of cellular energy homeostasis in normal and cancer cells.

Mitochondrial function is directly linked to mitochondrial polarization state. Intact mitochondria are polarized, i.e. they sustain a highly charged (negative inside) membrane potential for full functionality<sup>12</sup>. Membrane potential is a key feature of mitochondria, as the loss of the potential across the membrane is accompanied by a variety of cellular responses, including cytochrome c release, and is involved in apoptotic cell death<sup>13</sup>.

The majority of previous work on the response of mitochondria to radiation has been performed using lasers<sup>4-7</sup>. However, due to the nature of energy deposition of lasers, such experiments do not enable a quantification of the energy deposited in individual mitochondria and only a minor fraction of molecular species may be affected. This is where particle radiation and ion beams become invaluable radiation techniques. Focused ion beam irradiation allows for the quantification of deposited energy equally distributed over all molecular species and consequently can be linked to the effect on the mitochondria. The heavy ion microbeam SNAKE (Super conducting Nanoprobe for Applied Nuclear (Kern) physics Experiments) based in Munich and the Proton Microbeam AIFIRA (Applications Interdisciplinaires de Faisceaux d'Ions en Région Aquitaine) in Bordeaux are ideal tools to probe the radiation response to minute cellular constituents, such as mitochondria.

Tetramethyl rhodamine ethyl ester (TMRE) a cationic fluorophore, which accumulates electrophoretically in polarized mitochondria<sup>14</sup> enables the assessment of mitochondrial membrane potential, and therefore mitochondrial function, allowing for changes in membrane potential to be visualized very rapidly<sup>15</sup>. This membrane permeable dye allows for a simple "on/off" readout of fluorescent signal accumulation in mitochondria in direct relation to the mitochondrial membrane potential  $\Delta\Psi_m$ . In functional and polarized mitochondria,  $\Delta\Psi_m$  ranges between  $-120$  to  $-200$  mV and mitochondria accumulate the positively charged TMRE in direct relation to the negative membrane potential within the mitochondria. If  $\Delta\Psi_m$  is increasingly lost, the fluorescence signal dissipates as the mitochondrial  $\Delta\Psi_m$  increases. Live cell irradiation combined with fast online fluorescence microscopy therefore enables irradiation and imaging, with a delay of only a few seconds, for live cells under controlled cell culture conditions (temperature, medium, pH, humidity). Mitochondria vary between  $\sim 0.2$ – $0.5$   $\mu\text{m}$  in width and  $\sim 0.5$ – $10$   $\mu\text{m}$  in length. They are highly dynamic and, in many cases, strongly networked organelles that are in constant movement. Therefore irradiation and imaging must be performed in fast succession for any usable data to be obtained. Both SNAKE and AIFIRA beamlines enable fast and accurate data acquisition using Zeiss epifluorescence microscopes in line with the beam exit windows. The techniques enable the exploration of the response of mitochondria to highly specific energy deposition with beam spot sizes which are in the size range of the mitochondria themselves.

## Results

TMRE accumulates electrophoretically within the cell in a concentration dependent manner that is directly related to the  $\Delta\Psi_m$  of each individual mitochondria, yielding a bright mitochondrial fluorescence signal and a less pronounced cytoplasmic background<sup>12</sup>. The accumulation of TMRE fluorescence in the cytoplasm and in the mitochondria is in direct relation to the membrane potential, which is maintained across the cellular and mitochondrial membranes respectively. Polarized mitochondria labelled with TMRE were visualized in both A549 and MCF7 cell lines and consequently irradiated with either arrays of irradiation points targeted to single (Fig. 1a) or clusters of mitochondria (Fig. 1b) using both 55 MeV carbon ions (SNAKE) or 3 MeV protons (AIFIRA). Each beam spot represents a counted number of carbon ions ranging from 1–100 55 MeV carbon ions (LET = 350 keV/ $\mu\text{m}$ ) focused to  $< 1$   $\mu\text{m}$  per point or, in the case of protons, 700 to 14000 protons (LET = 10 keV/ $\mu\text{m}$ ) per point focused to  $< 1.5$   $\mu\text{m}$ . To deposit the same amount of energy as 1 carbon ion applied at SNAKE, 35 protons were used at AIFIRA. The dose rate was adjusted so that the same amount of energy was deposited per second; to ensure this was the case, carbon ions were applied at a count rate of 1 kHz and protons at 35 kHz.

Live cell imaging of mitochondria during irradiation showed a near instant induction of depolarization in mitochondria after targeted application of either protons or carbon ions. The depolarization manifested itself as a highly localized loss of TMRE in the irradiated area only, with no perceptible effect on the rest of the mitochondria in the targeted cell. The induction of depolarization was less than the temporal resolution of the imaging system. When control experiments with the mitochondrial membrane uncoupler FCCP were performed (Fig. 1i) a similar loss of mitochondria specific TMRE signal was seen as after irradiation. A quantification of mitochondrial areas irradiated with 80 carbon ions per point using the standard  $6 \times 6$  matrix shows a highly significant difference between the irradiated and the control mitochondria (Fig. 2). The results show a mean change in fluorescence signal intensity of  $-87.5$  for the irradiated areas and  $2.2$  in the unirradiated control mitochondria in 20 independently irradiated cells. A loss of fluorescence was not seen when a mitochondrial stain not dependent on  $\Delta\Psi_m$ , such as Mitotracker green (MTG) (Life Technologies), was used (Fig. 1f). Mitochondrial fluorescence intensity was imaged using time-lapse fluorescent microscopy. When the majority of cells in the field of view were irradiated with counted ions, no more than 10 seconds elapsed between irradiation start and imaging. On the other hand, when imaging and irradiation were performed concurrently (Fig. 3) the time interval between images (300ms) was the limiting factor. The short time interval between initial image acquisition and post irradiation follow-up images ensures minimal movement of mitochondria within the captured frame and allows for the tracking of the irradiated mitochondrial area. The time series acquired from before/after irradiation (Fig. 1) depicted mitochondria just before and 5–10 seconds after targeted irradiation was completed. The micrographs

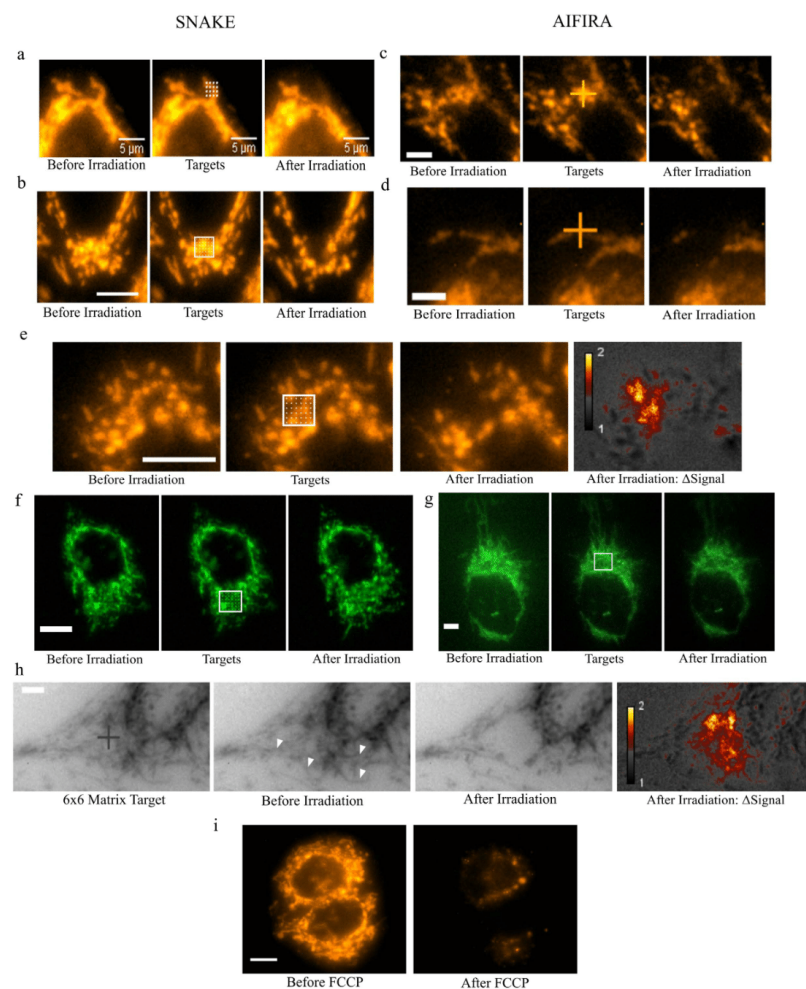


**Figure 1.** Micrographs of irradiated MCF7 and A549 cells from experiments at SNAKE (a,b,e) and AIFIRA (c,d,g,h); unless specifically stated scale bars represent  $10\mu\text{m}$ . Successive images (left to right) show pre-irradiation, target placement on pre-irradiation image and post irradiation. (a,b) TMRE stained cells irradiated with 100 carbon ions per point show mitochondrial depolarization (localized loss of signal) of targeted and consequently irradiated mitochondria with  $4 \times 4$  irradiation points for MCF7 (a),  $6 \times 6$  points with A549 (b). (e) Targeted irradiation performed at SNAKE. Images show pre and post irradiation with  $6 \times 6$  matrix and 100 carbon ions per point. The pseudocolour images (e,h) depict the changes in signal between pre and post irradiation. Before images were divided by after images to obtain a 32 bit float image, the changes were represented in a pseudocolour look up table (Smart, Fiji). A value of 1 (gray) equates to no difference between before and after and a value of up to 2 (yellow) equates to a drop in signal intensity. (f) MTG stained cells do not show localized loss of signal after irradiation with 100 carbon ions per point. (c,d) Experiments performed at AIFIRA show the same loss of TMRE after irradiation with an equivalent number of protons. (g) HTB U2OS mito-RoGFP2 tagged cells irradiated with  $3 \times 3$  target matrix do not show any change of mitochondria staining after irradiation with 6800 protons per point (equivalent to 200 carbon ions). (h) Inverted greyscale representation used to depict the irradiation ( $6 \times 6$  point matrix) and depolarization of a whole interconnected network of mitochondria up to  $18\mu\text{m}$  away from the irradiation site. Pseudocolour image ( $\Delta\text{Signal}$ ) represents change in signal between before and after irradiation. (i) Control experiment depicting mitochondria stained with TMRE before treatment with  $1\mu\text{M}$  FCCP and 10s after. Images depict the loss of specific, TMRE signal after uncoupling of mitochondrial membrane potential and are comparable to that induced by irradiation induced damage.

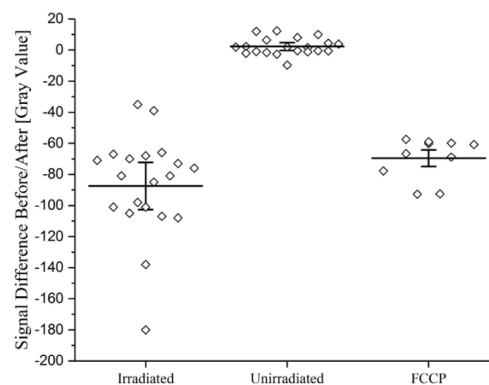


**Figure 2. Quantification of TMRE signal before and after irradiation with carbon ions of 20 individually irradiated and unirradiated areas in 20 separate cells as well as 10 areas for FCCP control experiments.** The individual points represent measurements, the horizontal lines represent the means and the error bars represent 95% CI. FCCP control experiments and the irradiated values overlap, and fall within a region normal for depolarization. The irradiation was performed using 80 ions per point in a  $6 \times 6$  matrix. The irradiation areas were analyzed before and after irradiation by quantifying the background subtracted gray values in the micrographs before and after irradiation. The unirradiated controls consisted of mitochondria in the same irradiated cell but more than  $10 \mu\text{m}$  away from the irradiated area. A paired two tailed t-test indicates a highly significant result ( $P < 0.001$ ) between non-irradiated and irradiated samples, and the effect size as calculated by Cohen's  $d$  is 3.85, making the results highly significant.

obtained indicate that given a high enough local application of carbon ions or protons, to individual (Fig. 1a,d) or clusters (Fig. 1b,c,e) of mitochondria will induce near instant depolarization under the temporal resolution of the imaging method. The difference in signal intensity of targeted mitochondria is also depicted in pseudocolour images (Fig. 1e,h). The figures show that only the targeted mitochondrial clusters and connected mitochondria undergo a decrease in signal (yellow) after irradiation, compared to rest of the mitochondria and cell (gray). The mitochondria in the irradiated area are depolarized without affecting the overall polarization state of the remaining, unirradiated, mitochondria in the cell during short-term follow-up of up to 30 min.

Given such a pronounced effect, the reproducibility of the depolarization events required a rigorous verification process. To confirm the findings, the experiments were repeated 5 times over the span of two years at SNAKE and then a further two times at the AIFIRA facility. Given the results seen at both SNAKE and AIFIRA using different ions with different LET and that the depolarization was seen with every independent beam setup, the results cannot be classified as an experimental artifact.

**TMRE fluorescence signal and  $\Psi_m$ .** To verify that the TMRE molecules accumulated within the mitochondria were not destroyed by the energy deposited by the protons and carbon ions, but relocated within the cell after the highly localized loss of  $\Psi_m$ , an auto targeting routine for all mitochondria was developed. The macro "AutoTarget" detected and applied a radiation spot matrix over all mitochondria in cells exhibiting bright TMRE fluorescence, which then enabled the irradiation of all mitochondria (Fig. 3a). This irradiation point matrix allowed for the targeting of the mitochondria in a cell while sparing the nucleus from damage. The application of  $\geq 80$  carbon ions per point yielded total depolarization of all targeted mitochondria and a consequent re-localization of TMRE from a point like mitochondrial staining pattern to a homogeneous whole cell distribution of fluorescence staining (Fig. 3b). When monitoring individual mitochondria over time (Fig. 3c), the fluorescence intensity plot reveals a small dip in fluorescence intensity followed by a peak of hyperpolarization and the final drop of signal indicative of depolarization. After depolarization, the now homogenous cytoplasmic TMRE signal slowly decreased due to the plasma membrane potential of the cell being unchanged and the overall charge of the released TMRE far outweighed that of  $\Delta\Psi$  of the plasma membrane. The plasma membrane potential limits the amount of TMRE which can be present in the cytoplasm due to the fixed membrane potential. Positively charged TMRE dye molecules, whose collective charge is above that of the plasma membrane potential, will be removed to restore charge equilibrium. Therefore, the non-specific, superfluous, positively charged dye from the depolarized mitochondria flows out of the cell again yielding an increased extracellular background signal as measured in a coronal region around the plasma membrane (Fig. 3c). These results clearly indicated that the loss of mitochondrial specific TMRE signal was due to mitochondrial depolarization and not a destruction or bleaching of the TMRE molecules. Further verification of this hypothesis came from experiments at AIFIRA where highly interconnected mitochondria were irradiated. In this case, irradiation of a single interconnected mitochondrial cluster caused all the connected mitochondria in the network to depolarize at the same time (Fig. 1h). Connected mitochondrial signal as far as  $18 \mu\text{m}$  from the edge of the irradiated area showed depolarization within the connected network, again strongly arguing against direct destruction of the TMRE molecules. Thus, the loss



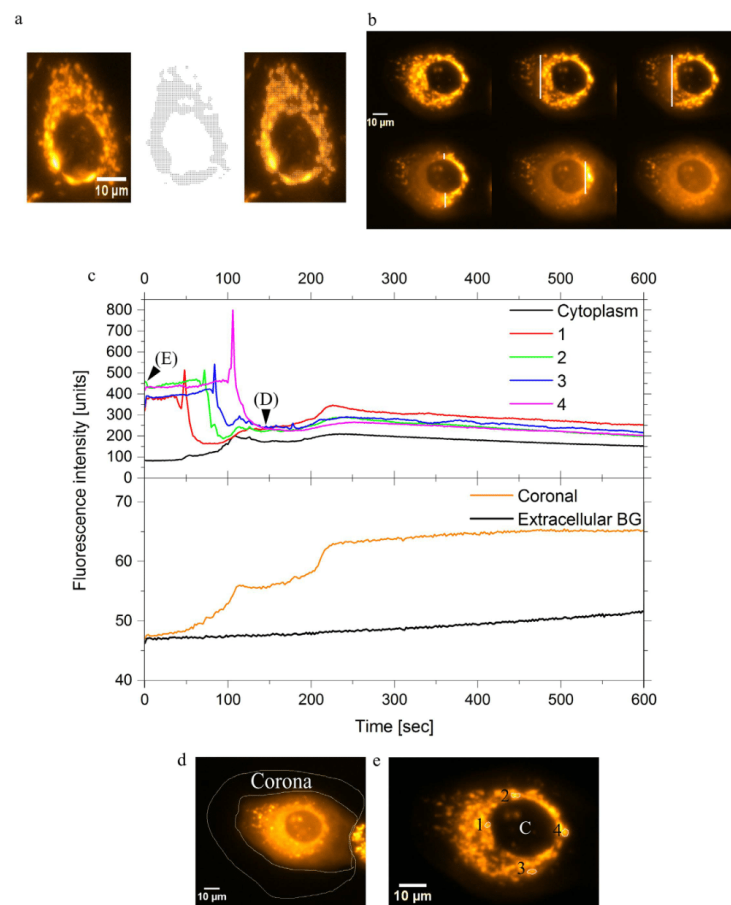


**Figure 3. Results for MCF7 cells stained with TMRE during irradiation experiments at SNAKE are shown.** (a) Automatic targeting macro “AutoTarget” as used for recognition and irradiation of mitochondria. The images show cells before irradiation (left), targets (black points, centre) and the overlay after target acquisition (right) for a representative living cell. Each target point represents a counted number of carbon ions. (b) Overview of live irradiation shows snapshots taken from the timelapse video (Video File 1 of the irradiation at SNAKE), whereby irradiation and imaging were performed simultaneously. The micrographs show loss of highly localized mitochondrial signal and a relocation of TMRE to the cytoplasm (File 1). The white line represents the position of the scanning beam. (c) The mitochondrial membrane potential plotted for four selected mitochondria in the representative cell during irradiation with 80 carbon ions per point over time. Four mitochondria were chosen as shown in (e) and measured for 10 minutes from start of irradiation. The peaks represent hyperpolarization before depolarization as seen after irradiation. The markers on the graph (E and D) depict the times corresponding to the starting image before irradiation (e) and the image after irradiation is complete (d). The cytoplasmic background value was measured over the nucleus as labelled with “C” and the coronal measurement area and cell membrane outline are represented in (d). The coronal measurement (c, lower segment) measured the area around the cell and the increases in signal intensity during and after irradiation as compared to background signal in the same micrograph.

of fluorescence intensity is not related to dye destruction or bleaching but to radiation induced mitochondrial depolarization.

**Mitochondrial membrane integrity.** At present, the mechanism of the mitochondrial depolarization remains unclear. To test if the targeted irradiation causes mitochondrial membrane rupture, mimicking biological

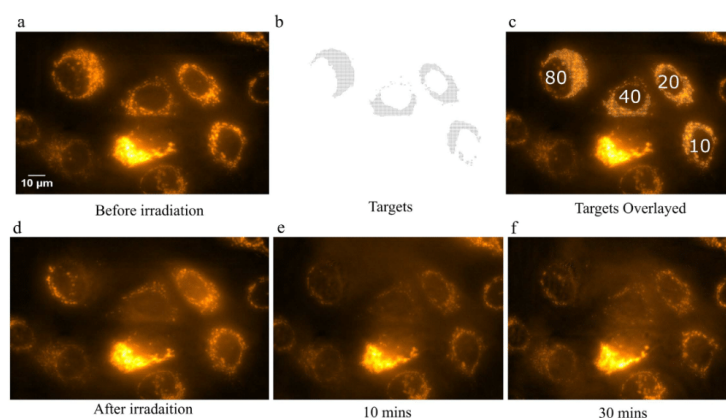


**Figure 4.** Images from a timelapse imaging sequence performed at SNAKE. (a) TMRE (500 nM) stained MCF7 cells in 1  $\mu$ M PI containing medium for the detection of membrane rupture. (b) Targets acquired with “AutoTarget”. (c) Cells were sequentially irradiated with 80, 40, 20 and 10 carbon ions per point as labelled. (d) Image after irradiation showing TMRE relocation in the form of intracellular background signal increase is visible, however no PI specific nuclear staining is visible. At 10 min post irradiation (e) and 30 min (f) there was still no sign of PI specific staining.

depolarization, membrane integrity was tested. MTG staining was used for non-depolarization related mitochondrial membrane staining. Targeted irradiation of clusters of MTG stained mitochondria showed no significant change in fluorescence signal intensity as was previously seen in the irradiated TMRE labelled cells (Fig. 1f). The lack of change in MTG fluorescence also indicated that the dye was not destroyed in the targeted area by the energy deposited. The MTG experiments were also performed at AIFIRA with the same outcome. To further verify this integrity of the membranes, an additional, non-dye based marker for mitochondrial membrane integrity was used. U2OS cells tagged with RoGFP2 in the mitochondrial matrix were irradiated to test for mitochondrial matrix integrity. As seen in the MTG experiments, the fluorescence signal intensity and localization of RoGFP2 in the mitochondrial matrix stayed constant after irradiation (Fig. 1g). HTB96 U2OS Mito-roGFP2 cells were irradiated at AIFIRA with 6800 protons per point with a matrix of  $3 \times 3$  points. RoGFP2 tagged mitochondria do not show change in fluorescence signal intensity, thus excluding alterations of the mitochondrial matrix composition after irradiation for molecules in the same molecular weight range as roGFP2.

As an additional verification of the cellular membrane integrity, 1  $\mu$ M of propidium iodide (PI) was added to the imaging media during irradiation of A549 and MCF7 cells at AIFIRA and during experiments at SNAKE to check the integrity of the cell membrane after irradiation. Even during irradiation of all mitochondria using the AutoTarget routine in a cell with 80, 40, 20 and 10 carbon ions per point, there was no PI typical nuclear staining (Fig. 4). The lack of PI nuclear staining indicated that the dose of radiation applied was not high enough to rupture the plasma membrane sufficiently to allow PI to enter the cells and stain the DNA up to 30 min after irradiation. The mitochondrial membranes (inner and outer) are estimated to be 22 nm wide<sup>16</sup>; in comparison the cell membrane is estimated to be  $\sim 4$  nm thick. However the total energy deposited per nanometer of membrane is the same in both cases. The rate of opening and closing of the plasma membrane may however differ from that of the mitochondria which could explain the lack of PI positive cell staining after irradiation.

**Mitochondrial depolarization and dose threshold.** A small matrix of irradiation spots ( $6 \times 6$  points, 1  $\mu$ m between each point), or a whole cell irradiation matrix, showed that given a high enough number of ions (carbon or equivalent number of protons) per point, the dose deposition yielded a total depolarization in the targeted mitochondria. A  $6 \times 6$  irradiation point matrix was used to compare the effects of varying ion numbers on mitochondrial depolarization. Between 100 and 80 carbon ions per point, total depolarization of the targeted area was observed for carbon ions. One hundred carbon ions or equivalent protons caused total depolarization in 100% of the irradiated areas. When 80 carbon ions were applied, total depolarization was seen in 100% of the targeted areas and in 95% of the irradiated areas for protons (Fig. 5B). Below 80 ions, a larger range of responses were observed in the  $\Psi_m$ . A threshold below which total mitochondrial depolarization was not seen was determined to be  $\sim 10$  carbon ions per point or equivalent protons. Between 20 and 100 carbon ions the degree of depolarization varied from a partial effect (flickering or short term loss of potential) to total depolarization. The most interesting depolarization phenomena were seen in the intermediate range, some mitochondria only partially depolarized, flashed or depolarized totally and reappeared with less intensity within seconds of the targeted irradiation. These effects were labelled as “partial depolarization” and along with total and absence of depolarization are summarized for both carbon ions and protons in Fig. 5.

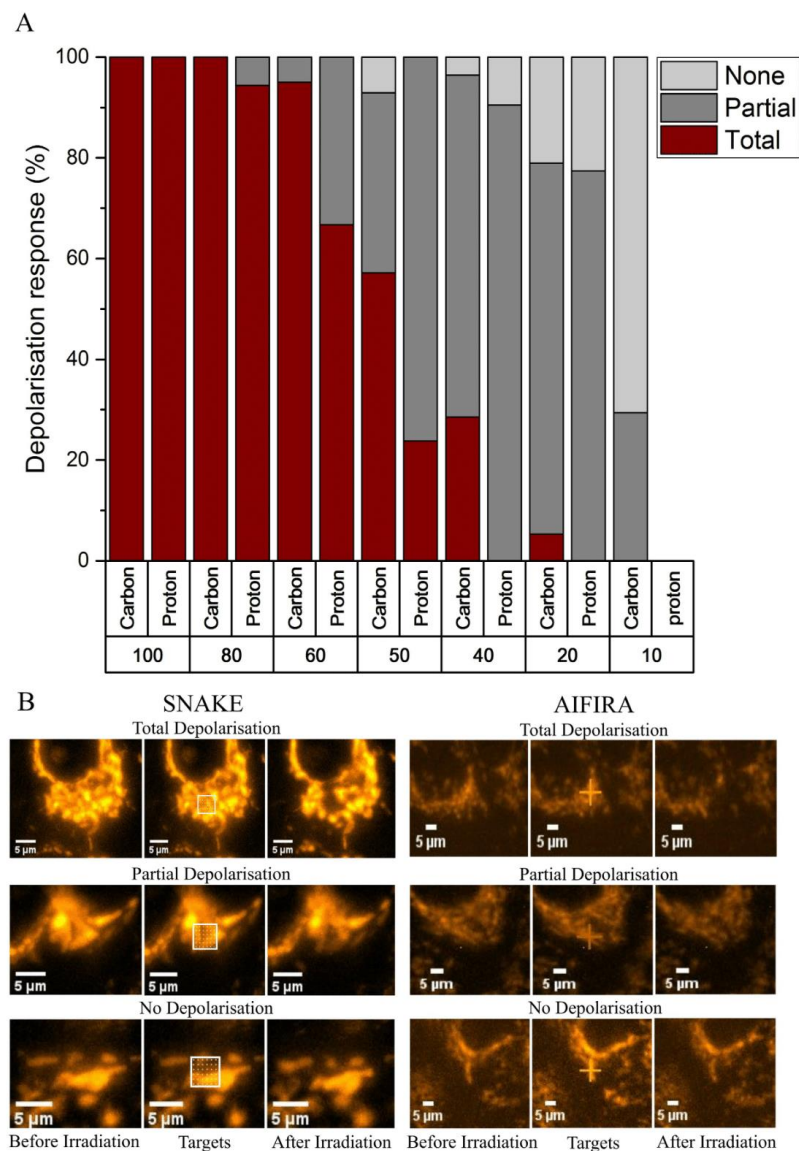


**Figure 5.** (A) Histogram depicting the quantification of polarization state of irradiated mitochondria for experiments performed at SNAKE (carbon ions) and AIFIRA (protons). The percentage of cells featuring Total, Partial or no (None) depolarization are plotted above the number of carbon ions per point (100–10) and equivalent number of protons (3500–350), both decreasing to the right, required to deposit the same amount of energy in a  $6 \times 6$  irradiation point matrix. The number of cells analyzed for each ion application in the order shown are: for carbon 4, 20, 20, 28, 28, 19, 17, and for protons, 19, 18, 12, 21, 21, 30. (B) Representative micrographs of total, partial and no depolarization are included for experiments at SNAKE and AIFIRA. Images in the first column depict the cell before irradiation, in the second column, the targets are shown, ( $6 \times 6$ ), and the third column shows the result after irradiation. For total depolarization, micrographs with 100 carbon ions and 3500 protons are depicted; for partial depolarization 40 carbon ions and 1500 protons; and for no depolarization 20 carbon and 700 protons are depicted.

The lower the dose per point, the more likely it was that the mitochondria would not totally depolarize or in fact show no overall loss of signal at all, indicating that the energy deposited was not sufficient to induce depolarization. The differences between the responses of the mitochondria to carbon ions and the equivalent number of protons (Fig. 5A,B) required for the same energy deposition showed the same overall trend but differ slightly in their overall effect, which may be due to differences in beam spot size and the manner and precision in which the ions are counted and applied. In addition, the LET of the particles must be taken into account, as the LET of the particles is not the same and therefore the relative biological effect cannot automatically be assumed to be the same either.

### Discussion

For the first time we have shown that highly localized targeted mitochondrial irradiation using 55 MeV carbon ions and 3 MeV protons induces mitochondrial membrane potential loss. The number of ions required to induce instant mitochondrial membrane depolarization is rather high: the results indicate that 80 carbon ions or the equivalent number of protons per point (same equivalent energy) focused to a single point or in a matrix of points are required for near instant and total depolarization of all targeted mitochondria. Below this applied dose of ions, mitochondrial depolarization is not binary in its nature since a partial reduction in the TMRE signal is observed, as well as mitochondrial flashes. When the mitochondrial loss of TMRE was quantified (Fig. 2) a large and significant ( $p < 0.001$ ) difference was seen between unirradiated and irradiated samples. The effect size, as calculated by Cohen's  $d$  produced a value of 3.85, further verifying the highly significant difference between control and irradiated groups means. The total changes of gray values depicted are also within the same region as the results from the FCCP control experiments (Fig. 2) performed using the same microscope setup and parameters. The time required for application of 80 ions is well below that of the imaging setup, so a progressive loss of  $\Psi_m$  stepwise as each ion traverses the mitochondria is not observable. At the threshold of 10 carbon ions per point there is little to no visible effect of any of the above mentioned phenomena anymore. In comparison to previous experiments using lasers, heavy ion irradiation allows for a calculation of deposited energy at any point along the particle's track. This is a great advantage over laser irradiation as it allows for a far more accurate assessment of the energy required to induce a biological effect. Laser irradiations performed by Yoon *et al.* show plasma membrane rupture (PI, DAPI) and apoptosis between 6–25  $\mu\text{J}$  within minutes<sup>5</sup>. In comparison, the results shown here enable a precise deposition of energy within the range of *pico* to *femto* Joule, depending on size of mitochondria targeted, which is evidently sufficient to depolarize individual mitochondria without disrupting the plasma membrane, as has been confirmed by lack of PI signal up to 30 minutes after irradiation (Fig. 4).

The differences in the mitochondrial responses between carbon ions and protons seen in Fig. 5A may well be attributed to a difference in the accuracy of counting of the ions. The proton irradiation at AIFIRA relies on the count rate of the ions coming out of the accelerator and is checked multiple times per experiment. In comparison carbon ions at SNAKE are individually counted, ensuring a highly accurate number of ions applied. A drop in count rate of protons during the irradiation could therefore be the explanation for the difference in the responses seen in Fig. 5 for protons compared to carbon ions. The overall mitochondrial response to protons and carbons, however, seems to be very similar and the total energy deposited seems to be a good guideline for mitochondrial depolarization as the effect is seen after irradiation with both ion types.

Loss of mitochondrial membrane potential, as confirmed by the relocalization of TMRE from the mitochondria to the cytoplasm (Fig. 3b and Video File 1) and then to the extracellular space, as measured in the coronal region (Fig. 3c), indicates a distinct change in mitochondrial membrane potential. In detail, a small dip in fluorescence signal followed by a spike in intensity, again followed by the strong depolarization reaction, shows an interesting dynamic in mitochondrial depolarization-polarization and demonstrates a state of complete depolarization that cannot yet be modelled. When looking at a longer time scale of up to 600 s after irradiation, there is an additional dynamic in repolarization and depolarization of the individual irradiated mitochondria, but also within the cytoplasm and even in the coronal region. The correlated increase of cytoplasmic signal with the depolarization of the mitochondria reveals the redistribution of TMRE and thus the changes within the cell. Furthermore the TMRE released from the irradiated mitochondria is taken up by the surrounding mitochondria, leading to an increased peak before the radiation induced loss of TMRE (Fig. 3c and Video File 1). If TMRE would have been destroyed or inactivated by the irradiation, such a relocalization and uptake by neighboring mitochondria would not occur as shown in mitochondria labelled 4 (Fig. 3c). This dynamic relocalization of the TMRE from the irradiated mitochondria indicates that TMRE is not destroyed or inactivated by the irradiation.

The mechanism of this membrane potential change is currently unclear, however the MTG (Fig. 1f) and PI results (Fig. 4) are an initial indication that the TMRE relocalization may not necessarily be based on irreversible physical membrane rupture. Although indicative, the lack of change in roGFP2 and MTG fluorescence intensity cannot completely rule out subtle changes in membrane integrity. Carbon ion and proton irradiation with up to 100 ions per point would deposit 1.5 keV ( $\sim 0.24$  fJ) into the plasma membrane, after which the plasma membrane permeability remained unchanged in relation to PI uptake. The mitochondrial membrane structure (inner, inter membrane space and outer) are 5.5x thicker than the cell membrane but absorb the same amount of energy per nanometer of membrane. So the closing and opening of the membranes may well play a more crucial role than the thickness alone. After irradiation, a distinct and total change in membrane potential was observed, which in the cases of higher ion/point applications remained depolarized. The indication here could be that changes in the membrane structure, such as lipid peroxidation, may have occurred which has in the past been shown to cause changes in membrane permeability<sup>17</sup>. The structural changes induced by these types of radiation may also be so small and distinct that they are not large enough to allow PI to traverse the membrane. The formation of radiation induced transient nanopores cannot be ruled out at this stage either. Mitochondrial membrane transition pore opening is also an unlikely cause of the depolarization, as initial experiments with a transition pore inhibitor CyclosporinA show the same instant and total depolarization of irradiated mitochondria. In addition to

the structural changes induced by direct interaction, radiation induced reactive oxygen species which are formed after the ions interact and ionize water molecules, may play a role in the process of depolarization. Radiation induced reactive oxygen species (ROS) are known to cause changes in mitochondrial membrane potential, however further work is required to directly link radiation induced ROS at the site of targeted irradiation to the depolarization seen in this work. The damage to membranes induced by transient ROS formation could be a cause for this depolarization. Furthermore, the secondary electrons created in the path of the ions by ionizations may lead to a highly localized disruption of the electron transport chain within the mitochondria, which, in turn could also be the cause of the loss of the membrane potential.

This body of work describes a novel method for single mitochondrial manipulation and monitoring *in situ* by precisely controlled energy deposition, and opens up the field for further in-depth analysis. The results show a previously unseen change in mitochondrial membrane potential as indicated by loss of mitochondrial TMRE fluorescence, the mechanism of which still remains to be elucidated. To further assess this radiation induced loss of membrane potential, new methods will have to be devised and their limitations will have to be overcome, but the results will have the ability to shed new light not only on mitochondria's response to radiation but also a mechanism of radiation induced depolarization.

## Materials and Methods

**Cell culture and mitochondrial staining.** MCF-7 breast adenocarcinoma cells (ATCC HTB22) and A549 lung carcinoma cells (ATCC CCL-185) were grown in DMEM (D6429, Sigma Aldrich) completed with 10% v/v FCS (Sigma) and 100 mg.mL<sup>-1</sup> penicillin/streptomycin (Sigma Aldrich) at 37 °C, 95% humidity and 5% CO<sub>2</sub> saturated atmosphere. HTB U2OS were grown in McCoy's medium (Dutscher, L0211-500) completed with 2 mM L-glutamine, 100 mg.mL<sup>-1</sup> penicillin/streptomycin (Thermo Fischer) and with 10% v/v FCS (Dutscher). HTB96 U2OS cells were stable transfected with the Matrix-roGFP2 constructs (Plasmid #49437, Addgene). This plasmid expresses the thiol redox-sensitive ratiometric fluorescent sensor roGFP2 in the mitochondrial matrix, under the control of the CMV promoter. Viromer Red transfection reagent was used for transfections in accordance with the manufacturer's protocols. The transfection efficiency was 80–90% in all experiments.

Twelve hours before irradiation, cells were plated into the custom designed live cell imaging containers<sup>18</sup> and allowed to adhere to the scintillator surface (SNAKE) or polypropylene foil<sup>19</sup> (AIFIRA), which had previously been treated with Corning CellTak (as per manufacturer's instructions). Thirty minutes before irradiation, pre-warmed DMEM medium containing 25 mM HEPES buffer and 250 nM TMRE (Enzo Lifesciences), or 200 nM Mitotracker green FM (Life Technologies) for the control experiments, were added to the cells in the dark and incubated as above. The TMRE in medium was left on the cells for 30 min so that the mitochondria could reach an equilibrium of TMRE uptake. The media containing TMRE was then removed and pre-warmed media with an additional 25 mM HEPES was added to the sample before being placed into the heated microscope table at SNAKE and AIFIRA. To verify plasma membrane integrity during experiments, 1 μM Propidium iodide (PI) was added to the medium during imaging and irradiation. As a control for PI staining upon membrane rupture, 10% (v/v) Triton X-100 (Sigma Aldrich) was added to cells in PI containing medium to disrupt the plasma membrane. As a control for depolarization level, 1 μM FCCP (Enzo Lifesciences) was added to MCF7 cells incubated with TMRE to show the effect of total uncoupling of the mitochondrial membrane potential under the same imaging conditions.

**Microbeam irradiation and live cell imaging at SNAKE.** Irradiation was performed by spot application of counted, individual carbon ions with initial beam energy in vacuum of 55 MeV, as previously described by Siebenwirth *et al.*<sup>20</sup>. After leaving the vacuum, the ions lost about 10 MeV of energy by penetrating the beam exit window and approximately 20 μm of culture medium resulting in an LET in water of 350 keV/μm at the cells. Samples were imaged using a Zeiss Axiovert 200 M with a 63x Objective (LCI Plan-Neofluar 63x/1.3 Ph3 Imm Corr M27, Zeiss) and a Colibri LED light source (Zeiss). The microscope is tilted by 90° so that it is in line with the beam exit nozzle as described by Hable *et al.*<sup>18</sup>. For excitation of the TMRE, a 555 nm LED was used at 2–4% intensity and an appropriate filter cube (43 HE Zeiss) with varying exposure times depending on the overall fluorescence of the given area being imaged. A maximum exposure time of 500 ms was never exceeded. The images were captured using a Zeiss MRm rev. 3 CCD.

To detect and irradiate all mitochondria in the targeted cell a Visual Basic macro "AutoTarget" was written and integrated into Axiovision. The macro overlaid an irradiation target matrix with a defined distance of 0.5 μm between irradiation points over mitochondria exhibiting bright fluorescent signal. The mitochondria were automatically selected by thresholding, leaving the nucleus, which was lacking fluorescence signal, devoid of targets and therefore spared of dose. The density of irradiation points was therefore 4 per μm<sup>2</sup>.

**Microbeam irradiation and live cell imaging at AIFIRA.** Irradiation was performed by spot application of 3 MeV protons (LET in water of 10 keV/μm), as previously described by Bourret *et al.*<sup>19</sup>. Sample irradiation/imaging was performed at 37 °C and was limited to a maximum of 2 hours per sample to ensure constant conditions for the cells within the sample holder. Samples were imaged using a Zeiss AxioObserver Z1 with a 63x lens (LD Plan-Neofluar, NA 0.75). For excitation the same 555 nm LED and 43 HE filter cube were used as in Munich and for image acquisition a Zeiss CCD (AxioCam Mrm rev 03) was used. Similar imaging conditions and equivalent CCD settings were maintained as closely as possible between both institutions apart from binning which was adjusted to 2 × 2.

All analysis of micrographs was performed using FIJI (Fiji Is Just ImageJ) and plotted with Origin pro plotting software.

**Statistical analysis.** To analyze the statistical significance of the quantification of the micrographs a two-tailed students T-test for paired samples was performed. In addition, the equation to calculate Cohens d (Eq. 1) was used to determine effect size for the sample set.

$d$  is the Cohens d value,  $\mu_1$  is the mean of the irradiated population,  $\mu_2$  is the mean of the control (unirradiated) population and  $\sigma_{pooled}$  is the pooled standard deviation of both of the samples and is calculated by Eq. 2

$$d = \frac{\mu_1 - \mu_2}{\sigma_{pooled}} \quad (1)$$

$$\sigma_{pooled} = \sqrt{\frac{(\sigma_1^2 + \sigma_2^2)}{2}} \quad (2)$$

## References

1. Clarke, R. H. & Valentin, J. The History of ICRP and the Evolution of its Policies. *Annals of the ICRP* **39**, 75–110, doi: 10.1016/j.icrp.2009.07.009 (2009).
2. Waldren, C. A. Classical radiation biology dogma, bystander effects and paradigm shifts. *Human & experimental toxicology*, doi: 10.1191/0960327104ht425oa (2004).
3. Zirkle, R. E. & Bloom, W. Irradiation of parts of individual cells. *Science* **117**, 487–493, doi: 10.1126/science.117.3045.487 (1953).
4. Watanabe, W. *et al.* Femtosecond laser disruption of mitochondria in living cells. *Medical Laser Application* **20**, 185–191, doi: 10.1016/j.mla.2005.07.004 (2005).
5. Jonghee, Y., Seung-wook, R., Seunghee, L. & Chulhee, C. Cytosolic Irradiation of Femtosecond Laser Induces Mitochondria-dependent Apoptosis-like Cell Death via Intrinsic Reactive Oxygen Cascades. *Scientific Reports* **5**, doi: 10.1038/srep08231 (2015).
6. Tanaka, Y. Effect of the ruby laser microbeam on mitochondria of KB cells supravivally stained by pinacyanol. *The Journal of cell biology*, doi: 10.1083/jcb.41.2.424 (1969).
7. Watanabe, W., Arakawa, N. & Matsunaga, S. Femtosecond laser disruption of subcellular organelles in a living cell. *Optics Express*, doi: 10.1364/OPEX.12.004203 (2004).
8. Hongning, Z., Mei, H., Yunfei, C. & Tom, K. H. Consequences of Cytoplasmic Irradiation: Studies from Microbeam. *Journal of Radiation Research* **50**, doi: 10.1269/jrr.08120S (2009).
9. Munro, T. R. The Relative Radiosensitivity of the Nucleus and Cytoplasm of Chinese Hamster Fibroblasts. *Radiation Research* **42**, 451–470, doi: 10.2307/3572962 (1970).
10. Shao, C., Folkard, M. & Michael, B. D. Targeted cytoplasmic irradiation induces bystander responses. *PNAS*, doi: 10.1073/pnas.0404930101 (2004).
11. Wu, L. J., Randers-Pehrson, G. & Xu, A. Targeted cytoplasmic irradiation with alpha particles induces mutations in mammalian cells. *PNAS*, doi: 10.1073/pnas.96.9.4959 (1999).
12. Scaduto, R. C. & Grotyohann, L. W. Measurement of mitochondrial membrane potential using fluorescent rhodamine derivatives. *Biophysical Journal* **76**, 469–477, doi: 10.1016/S0006-3495(99)77214-0 (1999).
13. Kroemer, G., Galluzzi, L. & Brenner, C. Mitochondrial membrane permeabilization in cell death. *Physiological reviews*, doi: 10.1152/physrev.00013.2006 (2007).
14. Ehrenberg, B., Montana, V., Wei, M. D., Wuskell, J. P. & Loew, L. M. Membrane potential can be determined in individual cells from the nernstian distribution of cationic dyes. *Biophysical Journal* **53**, 785–794, doi: 10.1016/S0006-3495(88)83158-8 (1988).
15. Mitra, K. & Lippincott-Schwartz, J. Analysis of mitochondrial dynamics and functions using imaging approaches. *Current protocols in cell biology/editorial board, Juan S. Bonifacio ... [et al.]* Chapter 4, 21, doi: 10.1002/0471143030.cb0425s46 (2010).
16. Perkins, G. *et al.* Electron tomography of neuronal mitochondria: three-dimensional structure and organization of cristae and membrane contacts. *Journal of structural biology* **119**, 260–272, doi: 10.1006/jsbi.1997.3885 (1997).
17. Kam, W. W. & Banati, R. B. Effects of ionizing radiation on mitochondria. *Free radical biology & medicine* **65C**, 607–619, doi: 10.1016/j.freeradbiomed.2013.07.024 (2013).
18. Hable, V. *et al.* The live cell irradiation and observation setup at SNAKE. *Nuclear Instruments and Methods in Physics Research Section B: Beam Interactions with Materials and Atoms* **267**, 2090–2097, doi: 10.1016/j.nimb.2009.03.071 (2009).
19. Bourret, S. *et al.* Fluorescence time-lapse imaging of single cells targeted with a focused scanning charged-particle microbeam. *Nuclear Instruments and Methods in Physics Research Section B: Beam Interactions with Materials and Atoms* **325**, 27–34, doi: 10.1016/j.nimb.2014.02.004 (2014).
20. Siebenwirth, C. *et al.* Determination of the accuracy for targeted irradiations of cellular substructures at SNAKE. *Nuclear Instruments and Methods in Physics Research Section B: Beam Interactions with Materials and Atoms* **348**, 137–142, doi: 10.1016/j.nimb.2015.01.064 (2015).

## Acknowledgements

This work has been supported by Marie Curie Actions–Initial Training Networks (ITN) as an Integrating Activity Supporting Postgraduate Research with Internships in Industry and Training Excellence (SPRITE) under EC contract no. 317169 and by the project LET-Verbund (funding no. 02NUK031A and 02NUK031B) of the German Federal Ministry of Education and Research, by the DFG-Cluster of Excellence Munich-Centre for Advanced Photonics and by the Maier Leibnitz Laboratory Munich.

## Author Contributions

D.W. planned and performed the experiments, wrote the manuscript, analyzed data and created figures. C.S., C.G., K.I., J.R. and S.G. all performed the experiments at SNAKE. Gi. M., M.S., P.B. and H.S. planned and performed experiments at AIFIRA. T.S., G.D., H.Z. and Ga. M. worked on experimental planning, advised on data analysis as well as working on the manuscript. All authors reviewed the manuscript.

## Additional Information

**Supplementary information** accompanies this paper at <http://www.nature.com/srep>

**Competing Interests:** The authors declare no competing financial interests.

www.nature.com/scientificreports/

**How to cite this article:** Walsh, D. W. M. *et al.* Live cell imaging of mitochondria following targeted irradiation *in situ* reveals rapid and highly localized loss of membrane potential. *Sci. Rep.* 7, 46684; doi: 10.1038/srep46684 (2017).

**Publisher's note:** Springer Nature remains neutral with regard to jurisdictional claims in published maps and institutional affiliations.



This work is licensed under a Creative Commons Attribution 4.0 International License. The images or other third party material in this article are included in the article's Creative Commons license, unless indicated otherwise in the credit line; if the material is not included under the Creative Commons license, users will need to obtain permission from the license holder to reproduce the material. To view a copy of this license, visit <http://creativecommons.org/licenses/by/4.0/>

© The Author(s) 2017

## Bibliography

1. Fleet, A. Radiobiology for the Radiologist: 6th edition, Eric J. Hall, Amato J. Giaccia, Lippincott Williams and Wilkins Publishing; ISBN 0-7817-4151-3; 656 pages; 2006; Hardback; £53. *J. Radiother. Pract.* **5**, 237 (2006).
2. Lorat, Y. *et al.* Nanoscale analysis of clustered DNA damage after high-LET irradiation by quantitative electron microscopy - The heavy burden to repair. *DNA Repair (Amst)*. **28**, 93–106 (2015).
3. Morgan, W. F. & Bair, W. J. Issues in low dose radiation biology: the controversy continues. A perspective. *Radiat. Res.* **179**, 501–10 (2013).
4. Sørensen, B. S., Overgaard, J. & Bassler, N. In vitro RBE-LET dependence for multiple particle types. *Acta Oncol.* **50**, 757–62 (2011).
5. Prise, K. M. & Schettino, G. Microbeams in radiation biology: review and critical comparison. *Radiat. Prot. Dosimetry* **143**, 335–339 (2011).
6. Prise, K. M., Schettino, G., Vojnovic, B., Belyakov, O. & Shao, C. Microbeam studies of the bystander response. *J. Radiat. Res.* **50 Suppl A**, A1–6 (2009).
7. Azaiez, F. *et al.* *Nuclear Physics for Medicine. Nuclear Physics News* (2014). doi:10.1080/10619127.2014.912054
8. Barberet, P. & Seznec, H. Advances in microbeam technologies and applications to radiation biology. *Radiat. Prot. Dosimetry* **166**, 182–187 (2015).
9. Drexler, G. A. & Ruiz-Gómez, M. J. Microirradiation techniques in radiobiological research. *J. Biosci.* **40**, 629–643 (2015).
10. Miller, R. C., Randers-Pehrson, G., Geard, C. R., Hall, E. J. & Brenner, D. J. The oncogenic transforming potential of the passage of single particles through mammalian cell nuclei. *Proc. Natl. Acad. Sci.* **96**, 19–22 (1999).
11. Hei, T. K. *et al.* Mutagenic effects of a single and an exact number of particles in mammalian cells. *Proc. Natl. Acad. Sci.* **94**, 3765–3770 (1997).
12. Fournier, C. *et al.* The Fate of a Normal Human Cell Traversed by a Single Charged Particle. *Sci. Rep.* **2**, (2012).
13. Kadhim, M. A. *et al.* Genomic instability after targeted irradiation of human lymphocytes: Evidence for inter-individual differences under bystander conditions. *Mutat. Res. - Fundam. Mol. Mech. Mutagen.* **688**, 91–94 (2010).
14. Prise, K. M. *et al.* Single ion actions: the induction of micronuclei in V79 cells exposed to individual protons. *Adv. Space Res.* **25**, 2095–2101 (2000).
15. Durante, M. & Friedl, A. a. New challenges in radiobiology research with microbeams. *Radiat. Environ. Biophys.* **50**, 335–8 (2011).
16. Hable, V. *et al.* Recruitment kinetics of DNA repair proteins Mdc1 and Rad52 but not 53BP1 depend on damage complexity. *PLoS One* **7**, e41943 (2012).
17. Mosconi, M. *et al.* 53BP1 and MDC1 foci formation in HT-1080 cells for low- and high-LET microbeam irradiations. *Radiat. Environ. Biophys.* **50**, 345–352 (2011).
18. Guo, N. *et al.* Live cell imaging combined with high-energy single-ion microbeam. *Rev. Sci. Instrum.* **87**, (2016).
19. Tobias, F. *et al.* Spatiotemporal dynamics of early DNA damage response proteins on complex DNA lesions. *PLoS One* **8**, e57953 (2013).
20. Bourret, S. *et al.* Fluorescence time-lapse imaging of single cells targeted with a focused scanning charged-particle microbeam. *Nucl. Instruments Methods Phys. Res. Sect. B Beam Interact. with Mater. Atoms* **325**, 27–34 (2014).



21. Heiss, M. *et al.* Targeted Irradiation of Mammalian Cells Using a Heavy-Ion Microprobe. *Radiat. Res.* **165**, 231–239 (2006).
22. Jakob, B. *et al.* DNA double-strand breaks in heterochromatin elicit fast repair protein recruitment, histone H2AX phosphorylation and relocation to euchromatin. *Nucleic Acids Res.* **39**, 6489–99 (2011).
23. Siebenwirth, C. *et al.* Determination of the accuracy for targeted irradiations of cellular substructures at SNAKE. *Nucl. Instruments Methods Phys. Res. Sect. B Beam Interact. with Mater. Atoms* **348**, 137–142 (2015).
24. Zhou, H., Hong, M., Chai, Y. & Hei, T. K. Consequences of cytoplasmic irradiation: studies from microbeam. *J. Radiat. Res.* **50 Suppl A**, A59–65 (2009).
25. Desouky, O., Ding, N. & Zhou, G. Targeted and non-targeted effects of ionizing radiation. *J. Radiat. Res. Appl. Sci.* **8**, 247–254 (2015).
26. Kam, W. W.-Y. & Banati, R. B. Effects of ionizing radiation on mitochondria. *Free Radic. Biol. Med.* **65**, 607–619 (2013).
27. Tartier, L., Gilchrist, S., Burdak-Rothkamm, S., Folkard, M. & Prise, K. M. Cytoplasmic Irradiation Induces Mitochondrial-Dependent 53BP1 Protein Relocalization in Irradiated and Bystander Cells. *Cancer Res.* **67**, 5872–5879 (2007).
28. Chen, S. *et al.* Mitochondria-dependent signalling pathway are involved in the early process of radiation-induced bystander effects. *Br. J. Cancer* **98**, 1839–44 (2008).
29. Auer, S. *et al.* Survival of tumor cells after proton irradiation with ultra-high dose rates. *Radiat. Oncol.* **6**, 139 (2011).
30. Schmid, T. E. *et al.* Relative biological effectiveness of pulsed and continuous 20MeV protons for micronucleus induction in 3D human reconstructed skin tissue. *Radiother. Oncol.* **95**, 66–72 (2010).
31. Greubel, C. *et al.* Scanning irradiation device for mice in vivo with pulsed and continuous proton beams. *Radiat. Environ. Biophys.* **50**, 339–344 (2011).
32. Zlobinskaya, O. *et al.* Reduced side effects by proton microchannel radiotherapy: study in a human skin model. *Radiat. Environ. Biophys.* **52**, 123–133 (2013).
33. Schmid, T. E. *et al.* Low LET protons focused to submicrometer shows enhanced radiobiological effectiveness. *Phys. Med. Biol.* **57**, 5889–5907 (2012).
34. Ziegler, J. F. & Biersack, J. P. in *Treatise on Heavy-Ion Science: Volume 6: Astrophysics, Chemistry, and Condensed Matter* (ed. Bromley, D. A.) 93–129 (Springer US, 1985). doi:10.1007/978-1-4615-8103-1\_3
35. Nikjoo, H., Uehara, S., Emfietzoglou, D. & Cucinotta, F. A. Track-structure codes in radiation research. *Radiat. Meas.* **41**, 1052–1074 (2006).
36. Agostinelli, S. *et al.* GEANT4 - A simulation toolkit. *Nucl. Instruments Methods Phys. Res. Sect. A Accel. Spectrometers, Detect. Assoc. Equip.* **506**, 250–303 (2003).
37. Barberet, P. *et al.* Monte-Carlo dosimetry on a realistic cell monolayer geometry exposed to alpha particles. *Phys. Med. Biol.* **57**, 2189–2207 (2012).
38. Incerti, S. *et al.* Monte Carlo dosimetry for targeted irradiation of individual cells using a microbeam facility. *Radiat. Prot. Dosimetry* **133**, 2–11 (2009).
39. Tomita, M. & Maeda, M. Mechanisms and biological importance of photon-induced bystander responses: Do they have an impact on low-dose radiation responses. *J. Radiat. Res.* **56**, 205–219 (2015).
40. Prise, K. M. & O’Sullivan, J. M. Radiation-induced bystander signalling in cancer therapy. *Nat. Rev. Cancer* **9**, 351–360 (2009).
41. Mothersill, C. & Seymour, C. B. Radiation-induced bystander effects--implications for cancer. *Nat. Rev. Cancer* **4**, 158–164 (2004).
42. Azzam, E. I., De Toledo, S. M. & Little, J. B. Oxidative metabolism, gap junctions and the ionizing radiation-induced bystander effect. *Oncogene* **22**, 7050–7057 (2003).

43. Hei, T. K., Zhou, H., Chai, Y., Ponnaiya, B. & Ivanov, V. N. Radiation induced non-targeted response: mechanism and potential clinical implications. *Curr. Mol. Pharmacol.* **4**, 96–105 (2011).
44. Klaunig, J. E., Kamendulis, L. M. & Hocevar, B. a. Oxidative stress and oxidative damage in carcinogenesis. *Toxicol. Pathol.* **38**, 96–109 (2010).
45. Gulston, M., de Lara, C., Jenner, T., Davis, E. & O'Neill, P. Processing of clustered DNA damage generates additional double-strand breaks in mammalian cells post-irradiation. *Nucleic Acids Res.* **32**, 1602–1609 (2004).
46. UNSCEAR. Biological Mechanisms of Radiation Actions At Low Doses. *United Nations* 1–45 (2012).
47. Löbrich, M. & Jeggo, P. A. The impact of a negligent G2/M checkpoint on genomic instability and cancer induction. *Nat. Rev. Cancer* **7**, 861–9 (2007).
48. Vadhavkar, N. *et al.* Combinatorial DNA Damage Pairing Model Based on X-Ray-Induced Foci Predicts the Dose and LET Dependence of Cell Death in Human Breast Cells. *Radiat. Res.* **000**, 273–281 (2014).
49. Carlson, D. J., Stewart, R. D., Semenenko, V. a & Sandison, G. a. Combined use of Monte Carlo DNA damage simulations and deterministic repair models to examine putative mechanisms of cell killing. *Radiat. Res.* **169**, 447–459 (2008).
50. Goodhead, D. T. Mechanisms for the biological effectiveness of high-LET radiations. *J. Radiat. Res.* **40 Suppl**, 1–13 (1999).
51. Höglund, H. & Stenerlöw, B. Induction and rejoining of DNA double-strand breaks in normal human skin fibroblasts after exposure to radiation of different linear energy transfer: possible roles of track structure and chromatin organization. *Radiat. Res.* **155**, 818–25 (2001).
52. Ciccia, A. & Elledge, S. J. The DNA Damage Response: Making It Safe to Play with Knives. *Mol. Cell* **40**, 179–204 (2010).
53. Zhang, Y., Rohde, L. H. & Wu, H. Involvement of nucleotide excision and mismatch repair mechanisms in double strand break repair. *Curr. Genomics* **10**, 250–8 (2009).
54. Okano, S., Lan, L., Caldecott, K. W., Mori, T. & Yasui, A. Spatial and temporal cellular responses to single-strand breaks in human cells. *Mol. Cell. Biol.* **23**, 3974–81 (2003).
55. Jiricny, J. The multifaceted mismatch-repair system. *Nat. Rev. Mol. Cell Biol.* **7**, 335–346 (2006).
56. Okano, S., Kanno, S., Nakajima, S. & Yasui, a. Cellular responses and repair of single-strand breaks introduced by UV damage endonuclease in mammalian cells. *J. Biol. Chem.* **275**, 32635–41 (2000).
57. Friedberg, E. C., McDaniel, L. D. & Schultz, R. a. The role of endogenous and exogenous DNA damage and mutagenesis. *Curr. Opin. Genet. Dev.* **14**, 5–10 (2004).
58. Bauer, N. C., Corbett, A. H. & Doetsch, P. W. The current state of eukaryotic DNA base damage and repair. *Nucleic Acids Res.* gkv1136 (2015). doi:10.1093/nar/gkv1136
59. West, S. C. Molecular views of recombination proteins and their control. *Nat. Rev. Mol. Cell Biol.* **4**, 435–445 (2003).
60. Caldecott, K. W. Single-strand break repair and genetic disease. *Nat. Rev. Genet.* **9**, 619–31 (2008).
61. Schae, D. & McBride, W. H. Opportunities and challenges of radiotherapy for treating cancer. *Nat. Rev. Clin. Oncol.* **12**, 1–14 (2015).
62. Hanawalt, P. C. Historical perspective on the DNA damage response. *DNA Repair (Amst)*. **36**, 2–7 (2015).
63. Fortini, P. The base excision repair: mechanisms and its relevance for cancer susceptibility. *Biochimie* **85**, 1053–1071 (2003).
64. Barnes, D. E. & Lindahl, T. Repair and genetic consequences of endogenous DNA base damage in mammalian cells. *Annu. Rev. Genet.* **38**, 445–76 (2004).

65. Campalans, A. *et al.* Distinct spatiotemporal patterns and PARP dependence of XRCC1 recruitment to single-strand break and base excision repair. *Nucleic Acids Res.* **41**, 3115–3129 (2013).
66. Polo, S. E., Kaidi, A., Baskcomb, L., Galanty, Y. & Jackson, S. P. Regulation of DNA-damage responses and cell-cycle progression by the chromatin remodelling factor CHD4. *EMBO J.* **29**, 3130–3139 (2010).
67. Chou, D. M. *et al.* A chromatin localization screen reveals poly (ADP ribose)-regulated recruitment of the repressive polycomb and NuRD complexes to sites of DNA damage. *Proc. Natl. Acad. Sci. U. S. A.* **107**, 18475–18480 (2010).
68. El-Khamisy, S. F., Masutani, M., Suzuki, H. & Caldecott, K. W. A requirement for PARP-1 for the assembly or stability of XRCC1 nuclear foci at sites of oxidative DNA damage. *Nucleic Acids Res.* **31**, 5526–5533 (2003).
69. Radulescu, I., Elmroth, K. & Stenerlöv, B. Chromatin organization contributes to non-randomly distributed double-strand breaks after exposure to high-LET radiation. *Radiat. Res.* **161**, 1–8 (2004).
70. Elmroth, K. & Stenerlow, B. Influence of chromatin structure on induction of double-strand breaks in mammalian cells irradiated with DNA-incorporated 125I. *Radiat Res* **168**, 175–182 (2007).
71. Beucher, A. *et al.* ATM and Artemis promote homologous recombination of radiation-induced DNA double-strand breaks in G2. *EMBO J.* **28**, 3413–27 (2009).
72. Woodbine, L., Brunton, H., Goodarzi, A. A., Shibata, A. & Jeggo, P. A. Endogenously induced DNA double strand breaks arise in heterochromatic DNA regions and require ataxia telangiectasia mutated and Artemis for their repair. *Nucleic Acids Res.* **39**, 6986–6997 (2011).
73. Soutoglou, M. T. and E. The Emerging role of nuclear architecture in DNA repair and genome maintenance. *Nat. Rev. Mol. Cell Biol.* **10**, 243–254 (2012).
74. Stiff, T. *et al.* ATM and DNA-PK Function Redundantly to Phosphorylate H2AX after Exposure to Ionizing Radiation. *Cancer Res.* **64**, 2390–2396 (2004).
75. Shanbhag, N. M., Rafalska-Metcalf, I. U., Balane-Bolivar, C., Janicki, S. M. & Greenberg, R. A. ATM-Dependent chromatin changes silence transcription in cis to dna double-strand breaks. *Cell* **141**, 970–981 (2010).
76. Paull, T. T. *et al.* A critical role for histone H2AX in recruitment of repair factors to nuclear foci after DNA damage. *Curr. Biol.* **10**, 886–895 (2000).
77. Bartocci, C. & Denchi, E. L. Put a RING on it: regulation and inhibition of RNF8 and RNF168 RING finger E3 ligases at DNA damage sites. *Front. Genet.* **4**, 128 (2013).
78. Mok, M. T. S., Cheng, A. S. L. & Henderson, B. R. The ubiquitin ligases RNF8 and RNF168 display rapid but distinct dynamics at DNA repair foci in living cells. *Int. J. Biochem. Cell Biol.* **57**, 27–34 (2014).
79. Dantuma, N. P. & van Attikum, H. Spatiotemporal regulation of posttranslational modifications in the DNA damage response. *EMBO J.* **35**, 6–23 (2016).
80. Kim, J. S. *et al.* Independent and sequential recruitment of NHEJ and HR factors to DNA damage sites in mammalian cells. *J. Cell Biol.* **170**, 341–347 (2005).
81. Shrivastav, M., De Haro, L. P. & Nickoloff, J. A. Regulation of DNA double-strand break repair pathway choice. *Cell Res. Cell Res. Cell Res.* **18**, 134–147 (2008).
82. Rothkamm, K., Kruger, I., Thompson, L. H. & Lobrich, M. Pathways of DNA Double-Strand Break Repair during the Mammalian Cell Cycle. *Mol. Cell. Biol.* **23**, 5706–5715 (2003).
83. Mahaney, B. L., Meek, K. & Lees-miller, S. P. Repair of ionizing radiation-induced DNA double strand breaks by non-homologous end-joining. *Biochem. J.* **417**, 639–650 (2009).
84. Lieber, M. R. The Mechanism of Double-Strand DNA Break Repair by the Nonhomologous DNA End-Joining Pathway. *Annu. Rev. Biochem.* **79**, 181–211 (2010).
85. Roberts, S. A. *et al.* Ku is a 5'-dRP/AP lyase that excises nucleotide damage near broken ends.

- Nature* **464**, 1214–7 (2010).
86. Mansour, W. Y., Rhein, T. & Dahm-Daphi, J. The alternative end-joining pathway for repair of DNA double-strand breaks requires PARP1 but is not dependent upon microhomologies. *Nucleic Acids Res.* **38**, 6065–6077 (2010).
  87. Jeggo, P. & Lavin, M. F. Cellular radiosensitivity: how much better do we understand it? *Int. J. Radiat. Biol.* **85**, 1061–1081 (2009).
  88. Williams, R. S., Williams, J. S. & Tainer, J. A. Mre11–Rad50–Nbs1 is a keystone complex connecting DNA repair machinery, double-strand break signaling, and the chromatin template. This paper is one of a selection of papers published in this Special Issue, entitled 28th International West Coast Chromatin a. *Biochem. Cell Biol.* **85**, 509–520 (2007).
  89. Jeggo, P. A., Geuting, V. & Löbrich, M. The role of homologous recombination in radiation-induced double-strand break repair. *Radiother. Oncol.* **101**, 7–12 (2011).
  90. Pellegrini, L. *et al.* Insights into DNA recombination from the structure of a RAD51–BRCA2 complex. *Nature* **420**, 287–293 (2002).
  91. Hei, T. K., Zhou, H., Chai, Y., Ponnaiya, B. & Ivanov, V. N. Radiation induced non-targeted response: mechanism and potential clinical implications. *Curr. Mol. Pharmacol.* **4**, 96–105 (2011).
  92. Zhou, C., Pan, W., Wang, X. P. & Chen, T. S. Artesunate induces apoptosis via a Bak-mediated caspase-independent intrinsic pathway in human lung adenocarcinoma cells. *J Cell Physiol* **227**, 3778–3786 (2012).
  93. Waldren, C. A. Classical radiation biology dogma, bystander effects and paradigm shifts. *Hum Exp Toxicol* **23**, 95–100 (2004).
  94. Kadhim, M. *et al.* Non-targeted effects of ionising radiation—Implications for low dose risk. *Mutat. Res. Mutat. Res.* **752**, 84–98 (2013).
  95. Hong, M. *et al.* Mechanism of genotoxicity induced by targeted cytoplasmic irradiation. *Br. J. Cancer* **103**, 1263–8 (2010).
  96. Wu, L.-J. *et al.* Targeted cytoplasmic irradiation with alpha particles induces mutations in mammalian cells. *Proc. Natl. Acad. Sci.* **96**, 4959–4964 (1999).
  97. Hu, B. *et al.* Intrachromosomal changes and genomic instability in site-specific microbeam-irradiated and bystander human-hamster hybrid cells. *Radiat. Res.* **177**, 25–34 (2012).
  98. Waypa, G. B. *et al.* Hypoxia triggers subcellular compartmental redox signaling in vascular smooth muscle cells. *Circ. Res.* **106**, 526–535 (2010).
  99. Sedelnikova, O. A. *et al.* Role of oxidatively induced DNA lesions in human pathogenesis. *Mutat. Res. - Rev. Mutat. Res.* **704**, 152–159 (2010).
  100. Zhou, X. *et al.* Effects of X-irradiation on mitochondrial DNA damage and its supercoiling formation change. *Mitochondrion* **11**, 886–892 (2011).
  101. Scaduto, R. C. & Grotyohann, L. W. Measurement of mitochondrial membrane potential using fluorescent rhodamine derivatives. *Biophys. J.* **76**, 469–77 (1999).
  102. Kroemer, G., Galluzzi, L. & Brenner, C. Mitochondrial Membrane Permeabilization in Cell Death. *Physiol. Rev.* **99**, 99–163 (2007). doi:10.1152/physrev.00013.2006.
  103. Chalfie, M., Tu, Y., Euskirchen, G., Ward, W. & Prasher, D. Green fluorescent protein as a marker for gene expression. *Science (80-. )*. **263**, 802–805 (1994).
  104. Lan, L. *et al.* In situ analysis of repair processes for oxidative DNA damage in mammalian cells. *Proc. Natl. Acad. Sci. U. S. A.* **101**, 13738–43 (2004).
  105. Campalans, A., Amouroux, R., Bravard, A., Epe, B. & Radicella, J. P. UVA irradiation induces relocalisation of the DNA repair protein hOGG1 to nuclear speckles. *J Cell Sci* **120**, 23–32 (2007).
  106. Mailand, N. *et al.* RNF8 Ubiquitylates Histones at DNA Double-Strand Breaks and Promotes Assembly of Repair Proteins. *Cell* **131**, 887–900 (2007).
  107. Britton, S., Coates, J. & Jackson, S. P. A new method for high-resolution imaging of Ku foci to

- decipher mechanisms of DNA double-strand break repair. *J. Cell Biol.* **202**, 579–595 (2013).
108. Kanda, T., Sullivan, K. F. & Wahl, G. M. Histone-GFP fusion protein enables sensitive analysis of chromosome dynamics in living mammalian cells. *Curr. Biol.* **8**, 377–385 (1998).
  109. Savino, T. M., Gébrane-Younès, J., De Mey, J., Sibarita, J. B. & Hernandez-Verdun, D. Nucleolar assembly of the rRNA processing machinery in living cells. *J. Cell Biol.* **153**, 1097–110 (2001).
  110. Narain, Y., Wyttenbach, a, Rankin, J., Furlong, R. a & Rubinsztein, D. C. A molecular investigation of true dominance in Huntington's disease. *J. Med. Genet.* **36**, 739–46 (1999).
  111. Dadachova, E. Cancer therapy with alpha-emitters labeled peptides. *Semin. Nucl. Med.* **40**, 204–8 (2010).
  112. Kelly, M. P. *et al.* Radioimmunotherapy with alpha-particle emitting <sup>213</sup>Bi-C-functionalized trans-cyclohexyl-diethylenetriaminepentaacetic acid-humanized 3S193 is enhanced by combination with paclitaxel chemotherapy. *Clin. Cancer Res.* **13**, 5604s–5612s (2007).
  113. Dekempeneer, Y. *et al.* Targeted alpha therapy using short-lived alpha-particles and the promise of nanobodies as targeting vehicle. *Expert Opin. Biol. Ther.* **16**, 1035–1047 (2016).
  114. Pugliese, M. *et al.* Inactivation of individual mammalian cells by single alpha-particles. *Int. J. Radiat. Biol.* **72**, 397–407 (1997).
  115. Aten, J. a *et al.* Dynamics of DNA double-strand breaks revealed by clustering of damaged chromosome domains. *Science* **303**, 92–5 (2004).
  116. Stap, J. *et al.* Induction of linear tracks of DNA double-strand breaks by  $\alpha$ -particle irradiation of cells. *Nat. Methods* **5**, 261–266 (2008).
  117. Lyckesvärd, M. N. *et al.* Alpha particle induced DNA damage and repair in normal cultured thyrocytes of different proliferation status. *Mutat. Res. - Fundam. Mol. Mech. Mutagen.* **765**, 48–56 (2014).
  118. Chauhan, V. & Howland, M. Gene expression responses in human lung fibroblasts exposed to alpha particle radiation. *Toxicol. Vitro.* **28**, 1222–1229 (2014).
  119. Wei, L. *et al.* Damage response of XRCC1 at sites of DNA single strand breaks is regulated by phosphorylation and ubiquitylation after degradation of poly(ADP-ribose). *J. Cell Sci.* **126**, 4414–4423 (2013).
  120. Mortusewicz, O., Leonhardt, H. & Cardoso, M. C. Spatiotemporal dynamics of regulatory protein recruitment at DNA damage sites. *J. Cell. Biochem.* **104**, 1562–1569 (2008).
  121. Gassman, N. R. & Wilson, S. H. Micro-irradiation tools to visualize base excision repair and single-strand break repair. *DNA Repair (Amst).* **31**, 52–63 (2015).
  122. Solarczyk, K. J., Kordon, M., Berniak, K. & Dobrucki, J. W. Two stages of XRCC1 recruitment and two classes of XRCC1 foci formed in response to low level DNA damage induced by visible light , or stress triggered by heat shock. *DNA Repair (Amst).* **37**, 12–21 (2016).
  123. Feng, L. & Chen, J. The E3 ligase RNF8 regulates KU80 removal and NHEJ repair. *Nat. Struct. Mol. Biol.* **19**, 201–206 (2012).
  124. Tobias, F., Durante, M., Taucher-Scholz, G. & Jakob, B. Spatiotemporal analysis of DNA repair using charged particle radiation. *Mutat. Res. Mutat. Res.* **704**, 54–60 (2010).
  125. Incerti, S. *et al.* Comparison of GEANT4 very low energy cross section models with experimental data in water. *Med. Phys.* **37**, 4692–4708 (2010).
  126. Bernal, M. A. *et al.* Track structure modeling in liquid water: A review of the Geant4-DNA very low energy extension of the Geant4 Monte Carlo simulation toolkit. *Phys. Medica* **31**, 861–874 (2015).
  127. Allison, J. *et al.* Recent developments in Geant4. *Nucl. Instruments Methods Phys. Res. Sect. A Accel. Spectrometers, Detect. Assoc. Equip.* **835**, 186–225 (2016).
  128. Asaithamby, A. & Chen, D. J. Mechanism of cluster DNA damage repair in response to high-atomic number and energy particles radiation. *Mutat. Res. Mol. Mech. Mutagen.* **711**, 87–99 (2011).
  129. Solarczyk, K. J., Kordon, M., Berniak, K. & Dobrucki, J. W. Two stages of XRCC1 recruitment

- and two classes of XRCC1 foci formed in response to low level DNA damage induced by visible light, or stress triggered by heat shock. *DNA Repair (Amst)*. **37**, 12–21 (2016).
130. Yan, J. & Jetten, A. M. RAP80 and RNF8, key players in the recruitment of repair proteins to DNA damage sites. *Cancer Lett.* **271**, 179–90 (2008).
  131. Thorslund, T. *et al.* Histone H1 couples initiation and amplification of ubiquitin signalling after DNA damage. *Nature* **527**, 389–93 (2015).
  132. Doil, C. *et al.* RNF168 Binds and Amplifies Ubiquitin Conjugates on Damaged Chromosomes to Allow Accumulation of Repair Proteins. *Cell* **136**, 435–446 (2009).
  133. Reits, E. A. & Neefjes, J. J. From fixed to FRAP: measuring protein mobility and activity in living cells. *Nat. Cell Biol.* **3**, E145–E147 (2001).
  134. Phair, R. D. & Misteli, T. High mobility of proteins in the mammalian cell nucleus. *Nature* **404**, 604–09 (2000).
  135. Louvet, E., Junéra, H. R., Le Panse, S. & Hernandez-Verdun, D. Dynamics and compartmentation of the nucleolar processing machinery. *Exp. Cell Res.* **304**, 457–70 (2005).
  136. Lippincott-Schwartz, J., Snapp, E. & Kenworthy, A. Studying protein dynamics in living cells. *Nat. Rev. Mol. Cell Biol.* **2**, 444–456 (2001).
  137. Merk, B. *et al.* Photobleaching setup for the biological end-station of the darmstadt heavy-ion microprobe. *Nucl. Instruments Methods Phys. Res. Sect. B Beam Interact. with Mater. Atoms* **306**, 81–84 (2013).
  138. Shao, C., Folkard, M., Michael, B. D. & Prise, K. M. Targeted cytoplasmic irradiation induces bystander responses. *Proc. Natl. Acad. Sci.* **101**, 13495–13500 (2004).
  139. Hanson, G. T. *et al.* Investigating Mitochondrial Redox Potential with Redox-sensitive Green Fluorescent Protein Indicators. *J. Biol. Chem.* **279**, 13044–13053 (2004).
  140. Vevea, J. D., Wolken, D. M. A., Swayne, T. C., White, A. B. & Pon, L. A. Ratiometric Biosensors that Measure Mitochondrial Redox State and ATP in Living Yeast Cells. 1–12 (2013). doi:10.3791/50633
  141. Sirri, V., Urcuqui-Inchima, S., Roussel, P. & Hernandez-Verdun, D. Nucleolus: the fascinating nuclear body. *Histochem. Cell Biol.* **129**, 13–31 (2008).
  142. Boisvert, F.-M., van Koningsbruggen, S., Navascués, J. & Lamond, A. I. The multifunctional nucleolus. *Nat. Rev. Mol. Cell Biol.* **8**, 574–585 (2007).
  143. Montgomery, P. O. & Hundley, L. L. Ultraviolet microbeam irradiation of the nucleoli of living cells. *Exp. Cell Res.* **24**, 1–5 (1961).
  144. Berns, M. W. & Cheng, W. K. Are chromosome secondary constrictions nucleolar organizers? *Exp. Cell Res.* **69**, 185–192 (1971).
  145. Sorokin, D. V *et al.* Localized movement and morphology of UBF1-positive nucleolar regions are changed by  $\gamma$ -irradiation in G2 phase of the cell cycle. *Nucleus* **6**, 301–13 (2015).



## **PART II**

***In vitro* evaluation of radiation sensitivity  
of sarcoma cell lines derived from  
patients**





In 1896 X-Rays were used for medical purpose to locate a piece of knife in the backbone of a drunken sailor, who was paralyzed until the fragment was removed by tracking its location. This new technology spread rapidly through Europe and United States, and the field of diagnostic radiology was born. Therapeutically, the surgeon Freund demonstrated the disappearance of a hairy mole following treatment with X-Rays. Medical uses of machine-produced radiations and radionuclides have also developed, and play a significant role in medical diagnosis and treatment. Controlled amounts of radiations in the form of X-Rays have been used for a century as aid in the diagnosis and treatment of diseases in humans and animals. Despite these recognized benefits, radiation has several well-established effects on human health, and cancer is considered the major long-term contributor to health risk. Radiation therapy, with surgery and chemotherapy, is one of the main modality involved in cancer treatments. Radiation therapy is based on the use of high-energy ionizing radiation to kill malignant cells or to control their proliferation. However, several associated side effects such as the damage inflicted to the surrounding healthy tissues and the appearance of the radiation resistance phenomena, are some of the main factors that influence the efficiency of this treatment.

To optimize and adapt the therapeutic benefit of radiation therapy, a lot of efforts are invested to improve the beam ballistics and to understand the mechanisms which cause the radiation resistance phenomena (that could be innate or consecutive to a radiation treatment).

The main current developments in radiation therapy are based on the final aim to increase the radiation-induced effects in the tumor volume, reduce secondary radiation induced-effects in healthy tissues and define sub-group of tumors that could be treated in the same manner. For these purpose, several strategies are investigated such as the use of heavy charged particles, the use of new techniques of irradiation, the addition of radiation sensitizing agents inside the tumor volume, and the analysis of the tumor genetics characteristics to develop new personalized therapies.

A better understanding of *in vitro* interaction of IR with biological systems is mandatory and must combine a realistic dosimetry in cells exposed to different IR, the ability to irradiate using different modalities, and the knowledge of the genetic characteristics that influence biological responses.

The aim of the second part of this project is to further develop our capabilities to evaluate the biological responses of cell lines exposed to different radiations. To achieve these objectives we developed irradiation protocols, based on realistic dosimetry obtained with Monte Carlo simulations, to evaluate the radiation sensitivity/resistance of two patient's derived sarcoma cell lines whose genetics is characterized. We defined the biological endpoints in order to compare the biological

effects induced by several doses of electrons (conventional particles used in radiation therapy), protons, and to compare two spatial energy distributions (broad beam *versus* focused microbeam).

The main body of this second part is divided in three parts: *Background* that deals with the overview of sarcomas, the radiation therapy techniques, the intrinsic mechanisms of cellular radiation sensitivity, and the use of microbeam in radiation biological studies; *Experimental results* that summarizes the results obtained; and *Discussion and Perspectives* that details the impact and the further possibilities opened by this work.

## Background

Today, one of the major health problems for humanity is cancer. The World Health Organization estimated 14.1 million new cases of cancer occurred worldwide, and 8.2 million cancer-related deaths in 2012<sup>1</sup>. The universal demand in oncology is early cancer diagnosis, and to remove cancer or precancerous growths. The armamentarium of cancer treatments includes surgery, radiotherapy and chemotherapy. Among them, treating cancer with a high-energy photon beam is a well-established therapeutic technique. Indeed, in developed countries, over 50% of cancer patients will undergo traditional X-Rays radiation therapy during their disease. Despite the benefits in destroying cancer IR therapy has also side effects as the damage can occur in healthy tissues surrounding the tumor. The process of ionization in living material necessarily changes atoms and molecules, at least transiently, and may thus damage cells. If cellular damage occurs and is not adequately repaired, the cell may not survive, reproduce or perform its normal function. Indeed, DNA damage from radiation is cumulative and can result in carcinogenesis or other adverse cellular events, months or years after exposure<sup>2</sup>. Further studies are needed because the carcinogenic potential of low and high dose of IR is not completely understood, and this uncertainty is much higher for cancer induced by charged particles<sup>3</sup>.

## Chapter 1

### *Sarcomas: particular types of cancer*

Cancer is a group of diseases caused by normal cells changing so that they grow in an uncontrolled way. It is possible to discriminate more than 100 different types of cancer. Sarcomas represent a heterogeneous group of rare tumors, accounting for approximately 1% of adult cancers with an estimated incidence averaging 5/100 000/year in Europe, and for nearly 21% of all pediatric solid malignant cancers<sup>4,5</sup>. Currently, more than 50 histological subtypes have been identified<sup>6</sup>. They are derived from mesenchymal tissue including bones (osteosarcoma), muscles, cartilages and other connective tissues (soft tissue sarcomas).

In summarizing the current knowledge on histology, clinical features, and specific molecular events that define tumor subtype, we can recognize four groups of sarcomas. Sarcomas of the first group have nonpleomorphic histology and known pathognomonic molecular events (e.g. GIST with activating KIT mutations). In the second group, we find sarcomas which affect younger patients and generally have nonpleomorphic histology and karyotypes of limited complexity, however pathognomonic molecular events have yet to be identified. The third group includes sarcomas which occur in the adult population, and show pleomorphic histology, but on a background of complex changes, it includes consistently identified molecular events (e.g. dedifferentiated liposarcoma with CDK4/MDM2 amplifications). Finally, the fourth group, the most common in adult population, have complex karyotypes, pleomorphic histology, and lack of identifiable molecular events<sup>7</sup>.

The sarcoma etiology is unknown, but external radiation therapy is a well-established risk factor for soft tissue sarcoma<sup>5,8</sup>. Indeed, sarcomas are a type of cancer that can be radiation-induced and they present a higher resistance to conventional radiation therapy. Studies devoted to deeper understand the susceptibility of radiation therapy-related cancers could be important in identifying high-risk individuals and may lead to clinical benefits if radiation exposure could be reduced in these patients<sup>9</sup>. When radiations are the etiologic factor, post-irradiation sarcomas are also called radiation-induced sarcoma or radiation-associated sarcomas. Evidences are given, for instance, by the mutation of *TP53* gene in 88% of post-irradiation sarcomas with respect to the 20% frequency of *TP53* mutations in sporadic soft-tissue sarcomas<sup>10</sup>.

Despite the sarcoma variety, the clinical behavior of most soft tissue sarcomas correlates with anatomic location, histological grade, and tumor size<sup>11</sup>. However, the variability in patients' clinical outcome underestimates the heterogeneity of the biological aggressiveness of these tumors, and the therapeutic management remains one of the most difficult tasks for oncologists. Contemporary management of sarcomas often includes a multidisciplinary approach involving a combination of surgery, radiation therapy, and chemotherapy specific for tumor type, histological grade, and stage of disease.

Surgery is the standard primary approach for all patients with adult-type, localized sarcoma. It must be performed by a surgeon specifically trained in the treatment of this disease. Chemotherapy is preferably given before surgery, in order to assess tumor response and thus modulate the length of treatment, and it is an option in non-resectable tumors. In this case, doxorubicin chemotherapy is the single most active broadly applicable anti-sarcoma chemotherapeutic but only has an approximate 30% overall response rate with additional breakthrough tumor progression and recurrence after initial chemo-responsiveness and further problematic features in sarcomas management. There clearly still remains a desperate need for new systemic therapies.

Radiation therapy is added for those patients with residual tumors following surgery, in the case of low-grade or superficial sarcomas, and or as neoadjuvant therapy. The optimal mode (external beam or brachytherapy), and timing (preoperative, intraoperative, or postoperative) of radiation therapy have yet to be defined<sup>12</sup>. But, in generally it should be administered postoperatively, with the best technique available, at a dose of 50-60 Gy, with fractions of 1.8-2 Gy, depending on presentation and quality of surgery<sup>4</sup>. Sarcoma radio-responsiveness is very variable and depends on the histology, etiology, and kind of radiation used for treatment<sup>13</sup>. Bone and soft-tissue tumors including several histological subtypes are generally very radiation resistant<sup>14</sup>. As these tumors are highly radiation resistant, sarcomas are ideal candidates for therapy with high-LET radiations. Nowadays, the proton beam therapy is employed for sarcomas treatment. It reduces healthy tissue radiation dose by up to 50-60% with respect to photon therapy and is increasingly the preferred treatment modality for pediatric sarcoma patients, where a higher risk for late radiation-associated malignancy is expected<sup>15,16</sup>.

## Chapter 2

### *Radiation biology for studying in vitro radiation resistance and radiation sensitivity*

Cancer is treated with both invasive and non-invasive treatment modalities, such as surgery, radiation therapy, chemotherapy, as well as other therapeutic modalities (e.g. immunotherapy, hormone therapy, photodynamic therapy), and a combination of these. Today, radiation therapy is one of the most common non-invasive way to treat cancer, and one million of patients each year undergo radiation therapy, which is a clinical modality dealing with the use of IR<sup>17</sup>. The fundamental challenge in radiation therapy is to deliver a precisely measured dose to a well-defined tumor volume with as minimal damage as possible to surrounding healthy tissue<sup>18</sup>. Considerable efforts are being devoted to improve radiation therapy. There are different ways in which such an improvement in radiation therapy might be obtained: (i) by focusing the delivered dose on the tumor; (ii) by raising the efficiency in cell killing; and (iii) by minimizing the energy deposition in healthy tissues.

Today, most radiation treatments are based on photon irradiations, but there is an increasing interest in proton and carbon ions radiation therapies because these particles have an impact on the above mentioned developments.

Radiobiological research includes investigation of the factors, which cause the different severity of damages induced by the same dose of IR and offers a fundamental basis in the understanding of how radiation therapy works. This knowledge is important in both planning radiation therapy and radiation protection.

The same dose of IR causes differential effects determined by the genetic and functional characteristics of the “targeted” type of cells, tissues, organs or organisms. Radiation therapy simplified this problem where the total dose is adjusted to the most sensitive individuals so that not more than 20% of the patients will have an adverse healthy tissue effects. For the same therapy treatment approximately 5% could experience some severe or even fatal effects from standard radiation therapy. As a consequence, the majority of the patients receive a suboptimal dose, as they would have tolerated a higher total dose and gained a better tumor control, without getting severe side effects<sup>19,20</sup>. Indeed, depending on the time of occurrence, an organ or tissue expresses response

to radiation damage either as an acute effect or as a late (chronic) reaction. Acute reaction induces endothelial cell dysfunction, which is characterized by increased permeability, detachment from the underlying basement membrane and apoptosis. Endothelial cell dysfunction and apoptosis contribute to post-irradiation inflammation and fibrosis. Early biological events are usually transient and normally resolved within 3 months of completing treatment. Late reactions occur after 3 months up to many years and may be caused by the absorption of radiation directly in the target tissue or consequential to damage in overlying tissue such as mucosa or epidermis. Furthermore, studies imply that patients with no acute tissue reactions to therapy have a higher incidence of local recurrence, indicating that all cancerous cells were not eradicated. And more, early and late responses of normal tissues to irradiation are dose-limiting factors in radiotherapy, affecting therapeutic efficacy as well as the quality of life of patients and these events also result in secondary malignancy<sup>21,22</sup>. Thus, if tumor therapy could be individualized based on radiation sensitivity, more patients would be cured and the most severe adverse reactions could be avoided.

Radiation sensitivity is the relative susceptibility of cells, tissues, organs, or organisms to the harmful effect of IR. It was suggested in one study by Safwat et al. that 80-90% of variability in late normal tissue radiation sensitivity was due to patient-related factors<sup>23</sup>. These uncertainties are considered as a problem in radiation protection practices where the dose limit applied aims to provide a robust protection for the whole population.

That variability in cellular radiation sensitivity may result from differences in efficiency and/or accuracy of DNA repair. DSB is the lesion most likely to be the cause of the lethal effects on cellular level. If left unrepaired, DSBs can result in permanent cell cycle arrest, induction of apoptosis, or mitotic cell death caused by loss of genomic material; if repaired incorrectly, they can lead to carcinogenesis through translocation, inversions, or deletions<sup>24,25</sup>. Also micronuclei and chromosomal rearrangements can result from non-repaired or misrepaired DNA damage induced by IR. Depending on the damage extent and the ability of damaged cell to cope with, damage may lead to defect/loss of cellular function, senescence, cessation of proliferation, cellular death, and mutagenesis, which may cause genomic instability<sup>26,27</sup>. *In vitro* assays normally measure only one particular cell function and multiple tests have been used and described to assess individual radiation sensitivity, which have a practical importance in the radiotherapy field<sup>28</sup>. The existing experimental end-points allow measurements of (i) induction of cellular death (loss of metabolic activity); (ii) apoptosis (programmed cell death); (iii) clonogenic survival; (iv) DNA repair capacity (pulsed field electrophoresis, comet assay, measurement of H2AX phosphorylation); (v) cytogenetic effects, micronuclei, chromosomal aberrations and chromosomal instability.



A general conclusion based on these studies is that individual sensitivity to radiation is likely to be multifactorial in its origin and several biomarkers/bioassays will be needed to gain the predictability necessary for implementation in the clinic.

## Chapter 3

### *Microbeam for radiation biological approaches*

The immense progress in the advancement of cellular and molecular biology techniques has raised the possibility to better understand the molecular consequences of particle irradiation in cells and (artificial) tissues. *In vitro* studies and the application of physics accelerators for radiation biological studies are necessary to improve the understanding of IR exposure. The long term aim of this thesis was to develop tools to assess the individual radiation sensitivity of sarcoma patient's cell lines and to better understand the mechanisms behind the radiation sensitivity and radiation effects after IR exposures.

Micro-irradiation devices are able to control the target area and to apply an established number of ions in such determined area. These characteristics permit different applications<sup>29-33</sup>, such as (i) the study of low-doses, where each targeted cells can be irradiated with a precise number of ions<sup>34,35</sup>; (ii) the analysis of molecular process at sites of DNA damage (this applications is the object of the first part of this PhD thesis); and (iii) study new approaches for tumor therapy extending studies from cell-culture models to more complex tissue models and *in vivo* systems<sup>30,36</sup>.

A series of reports have been addressed to evaluate new approaches for tumor therapy by irradiating cell systems and tissue models with a specially modified proton microbeam. Indeed microbeam offers the possibility to study the influence of the dose-rate on RBE. Schmid and colleagues administrated on a 3D human reconstructed skin model the same dose of 20 MeV protons either as a continuous or nanosecond pulsed proton beam. They analyzed several endpoints and concluded that there were no significant differences in RBE of continuous or pulsed applied protons, for the endpoints that were investigated, including clonogenic cell survival<sup>37-39</sup>.

Another example can be illustrated by the study of effects induced during microbeam radiation therapy (MRT). In general, the MRT is a novel radiotherapy method invented by Slatkin and coworkers in 1992<sup>40</sup> and it is based on a spatial fractionation of synchrotron-generated X-Ray beams where collimated, planar, quasi-parallel microbeams are delivered to the tumor. This technic leads to the radiation resistance of the skin and the radiation sensitization of the tumor tissue induced by mechanisms not yet completely understood<sup>41,42</sup>. Microbeam offers the opportunity to be focused to micrometer scale or defocused in order to study these mechanisms and at the SNAKE facility

different studies started with the scope of elucidating the dosimetry<sup>43</sup> and biological effects of different proton dose distributions<sup>44</sup>.

## Questions addressed in this work

The development of biomedical applications of ion beams is one objective of particular interest of the training program in which I participated during my PhD (SPRITE project). Transfer of knowledge from fundamental research to clinical applications is the final aim of this program. One fundamental issue that can be faced using standard research protocols is the evaluation *in vitro* of the radiation sensitivity or resistance in different biological samples. To achieve this purpose it is necessary to understand the biological mechanisms induced by electrons (commonly used in conventional radiation therapy), protons and different spatial energy distributions on patient's cell lines.

Developing protocols able to assess *in vitro* mechanisms that lead to radiation sensitivity or resistance of cancerous cells requires:

- to define biological samples which permit a correlation of radiation sensitivity of patient's derived sarcoma cell lines with their genetic characteristics. Two sarcoma cell lines were selected for their different genetics: a known amplicon based genetics and a complex genetics.
- the ability to compare different particles effects. Cells were irradiated with a medical linear accelerator (9 MeV electrons) and with the AIFIRA microbeam at CENBG (3 MeV protons). To ensure that the mean delivered dose by these two irradiation systems was equivalent, we performed the dosimetry at the cellular scale using Monte Carlo techniques.
- to evaluate the biological effects of two deposited energy distributions. For that, cells were irradiated with the same dose of protons but the energy at the cellular scale was deposited with different patterns. Indeed, the microbeam line allows us to focus the beam to the minimum beam spot size (2  $\mu\text{m}$ ) (microbeam) or to defocus it to obtain a homogeneous proton distribution (broad beam).
- to develop and validate protocols for deciphering *in vitro* radiation sensitivity. Several biological endpoints such as cell proliferation, surviving fraction, immunodetection of DNA damage signaling proteins (such as the phosphorylated proteins ATM and H2AX) were analyzed. For evaluating these end-points we developed two ImageJ routines: one is conceived for quantifying the radiation-induced foci per nucleus and the other one for counting the number of cells constituting a colony and the number of colonies after irradiation.

## Experimental results

To achieve the defined objectives, it is necessary to develop a multidisciplinary approach where biology, genetics, physics and medical physics are combined for a better understanding of radiation-induced effects. So that, I integrated diverse teams working on these different fields. (i) The team of Frederic Chibon works on the action of oncogenesis and implication of genetics and biology mechanisms in sarcomas at the Institut Bergonié (Inserm Unit 1218). By means of this collaboration, I got access to the wide collection of patient's sarcoma cell lines established and characterized from the genetic point of view by Chibon's group. Genetics is a relevant factor that influences cellular responses but more studies and more biomarkers identification will certainly improve the knowledge for patient's individualized treatments. Characterizing the response of different patient's cell lines is of main importance because could relate the cellular radiation sensitivity with that of patients. From this collection, two cell lines with different genetic (known amplicon-based genetics profile *versus* complex genetics) were selected to evaluate their radiation sensitivity under different irradiation modalities: dose, nature of IR and irradiation procedure (focalized *versus* broad beams); (ii) I worked with the Department of Radiation therapy of the Institut Bergonié and in particular with the radiation therapist Guy Kantor and the medical physicist Mikael Antoine. This partnership gave me access to a medical facility (Clinac) used at the Institut Bergonié for radiation therapy patient's treatment. A dosimetry was needed to develop irradiation protocols appropriate to irradiate the selected biological samples with controlled doses of electrons or photons; (iii) Taking advantage of the expertise of the iRIBio team, I adapted all protocols developed for a medical facility to proton microbeam irradiations in order to compare the responses of sarcoma cells exposed to these ionizing radiations. Protons are, in effect, particles used today in hadron therapy and analyze their effects on cancerous cells is essential. Despite the fact that the energy of our proton beam is not in the medical range (AIFIRA is able to deliver 3 MeV protons), the advantage of microbeam lies in its ability to control the dose, the time and the space of irradiation allowing to elucidate the impact of two energy distributions at the cellular level (proton broad beam *versus* proton microbeam). As mentioned in *Background* section, the use of microbeams and different spatial energy distributions are increasing for medical applications for which more knowledge is worth considering. The study of biological responses was matched with the micro-dosimetry at the cellular scale that displays the total deposited energy per nucleus and the deposited energy per spot.

The objective of this work was to combine all expertise above mentioned and to develop a methodology to assess radiation sensitivity of patient's derived cells. The methodology developed is schematized in Figure 13.

1. Selection of patient's cell lines	Culture of cells lines from patients after tumor biopsy at the Institut Bergonié by the Inserm Unit U1218			
	Sarcoma cell lines with different genetics well-characterized (known amplicon-based genetics <i>versus</i> complex genetics)			
2. Different IR		Medical device CLINAC	Fundamental research accelerator AIFIRA	
		Electrons 9 MeV Photons 6 MV	Protons 3 MeV	
3. Different modality	Proton broad beam Energy homogeneously distributed in the nucleus		Focused proton micro-beam Energy concentrate in micrometer spots	
	4. Evaluation of radiation sensitivity		<b>Immuno detection</b> of foci radiation-induced <b>EARLY RESPONSE</b>	<b>Proliferation</b> on cell population <b>TIME DEPENDENT</b>

Figure 13. Schematized procedures to study and characterize patient's cell lines radiation sensitivity.

To develop this methodology a multi-step work was necessary. The first approach tested in order to assess the radiation sensitivity of selected cells was the cytogenetic approach. Indeed, cytogenetic approaches are one of the ways that have enormously contributed to the understanding of radiation sensitivity. It enables to (i) precisely label the chromosomal location of any gene using different colored dots and (ii) identify cells that have lost or gained a specific chromosome, undergone a translocation event involving a specific set of chromosomes. To identify specific translocations radiation-induced, I performed a cytogenetic method called in multicolor fluorescence *in situ* hybridization (mFISH). This technique utilizes 24-color probes sets to label each human chromosome with a distinct color. Because each chromosome has its own color, chromosomal translocation are easily detected allowing researchers to detect small chromosomal rearrangements or chromosomal aberrations<sup>45</sup>. To estimate the chromosomal rearrangements, I started to perform mFISH assays in one cell type exposed to electron irradiations following the protocol described by Geigl *et al.*<sup>46</sup>. Figure 14 shows three karyotypes after exposure to 0, 2 and 6 Gy of electrons. From the performed analysis on these samples and from previous performed analysis on the same cell type after  $\alpha$ -particle

irradiations (Vincent Atallah's Master thesis), we confirmed that the high number of chromosome rearrangements already present in control cells makes impossible the identification of rearrangements due to irradiations.

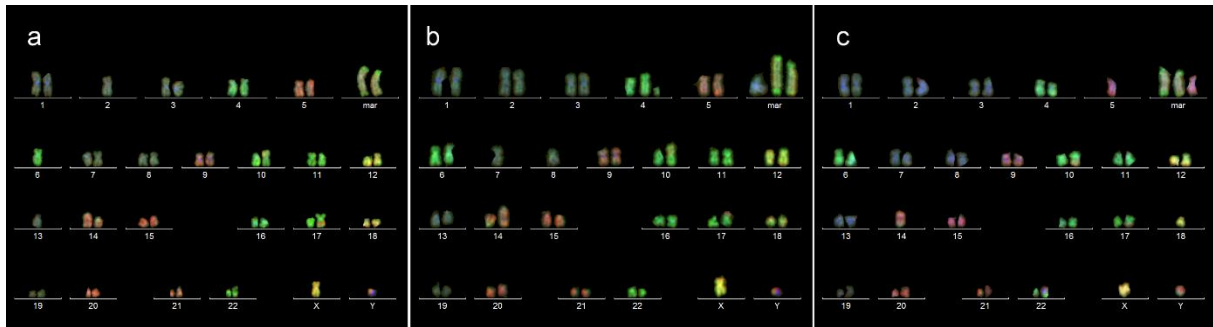


Figure 14. mFISH after electron irradiations. Chromosomes are stained with 5 fluorochromes where unique label combinations identify individual chromosome. Translocations result in chromosome composed of fragments with different color combinations. No differences are observed between (a) control, (b) 2 and (c) 6 Gy irradiated cells due to the high number of translocations already present before irradiation in control cells.

Then, another technique to perform genome-wide scans to identify chromosomal regions associated with loss or gain of genetic information is called microarray-based comparative genome hybridization (CGH). This method uses arrays containing thousands of base-pair fragments of the human genome adhered to a microchip. Each individual DNA fragment, which is located in a specific position on the chip, corresponds to a known DNA sequence that has been mapped to a specific chromosomal region. The same color-coded probes (green for the control group, and red for the experimental group) are then used in hybridization experiments with the CGH microarray platform, which can be scanned using an automated approach. Unaltered chromosome regions show equal binding of the green and red probes and a resulting orange/yellow color, whereas amplified and deleted chromosomal regions in the experimental group appear red and green, respectively<sup>47</sup>. By using this techniques, it is possible determine the chromosomal regions and genes that are amplified or missed. In this study and in previous studies performed at passages 2 and 5 after irradiation (Vincent Atallah's Master thesis) significant quantitative changes of the genomic profile with respect to control cells are not showed.

These two cytogenetic tests, mFISH and CGH, are not conclusive in our case due to the high complex genetic of samples which do not permit to correlate genetic/genomic alterations with radiation-induced effects.

For these reasons, I developed a multi-parametric methodology based on the more common assays aimed to evaluate the *in vitro* radiation sensitivity<sup>48</sup>. This methodology is well-detailed in the **Manuscript 4** and evaluates three biological endpoints, such as quantification and persistence over

time of DNA damage, proliferation and surviving fraction. These end points are analyzed for two types of ionizing radiations (electrons *versus* protons), two different energy distributions at the cellular scale (focused proton beam *versus* proton broad beam) and for two different sarcoma cell lines. This developed multi-parametric analysis required (i) the quantification over time of radiation-induced foci in a consistent number of cells, (ii) the quantification of colonies present in a cell dish and (iii) the quantification of cells belonging to each colony. To figure out with these difficulties, I validated two automatized routines *ImageJ* which allow the quantification of foci radiation-induced, the counting of colonies and the counting of cells in each colony by reducing the experimenter errors.

Using this approach, I observed that (i) radiation-induced effects and biological responses correlate with the delivered absorbed dose; (ii) protons induce more deleterious effects compared to electrons, independently from the dose distribution at the cellular scale; and (iii) one cell line is more sensitive than the other one for the endpoints analyzed. At first sight, this different radiation sensitivity can be associated to the genetics of samples; indeed, the higher radiation resistance is observed for the cell line with a complex genomic profile.



## Discussion and Perspectives

Despite the ability to build machine that deliver radiation with ever great accuracy and conformability progress, radiotherapy will continue to fall short of its promise. The next leap in progress will require radiation oncologists to immerse themselves in the biological basis of cancer and its response to radiation. The hallmarks of cancer represent potential routes to clinically useful biomarkers and targeted agents that will allow flexibility and undisputed therapeutic impact of radiation to find its full expression. No general biomarker of cellular radiation sensitivity has been identified yet. One probable reason for this is that the genetics behind radiation sensitivity is complex. It is also probable that the biology behind radiation sensitivity is diverse and caused by many different factors. A combination of biomarkers will most certainly improve the diagnostic and treatment power. However, many factors need to be carefully considered to achieve an individualized treatment for patients, such as acute radiation sensitivity, late radiation sensitivity, the risk of secondary cancers and the risk for local recurrences<sup>49,50</sup>.

Developing a 'system biology' approach to the radiation response, in which multidisciplinary expertise is used to analyze vast data sets, may identify the molecular targets that would probably yield tangible clinical benefits<sup>51</sup>. In this work, we developed protocols to evaluate two cell lines radiation sensitivity which genetics is known and seems to correlate with biological responses. Indeed, IB115 cells (cell line with a known amplicon-based genetics) show lower proliferation, higher number and lower rate of disappearance of DNA damages, revealing a higher radiation sensitivity with respect to IB106 (cell line with complex genetics). In addition, we show a considerably higher efficacy of protons in comparison to electrons on these sarcoma cells. More difficult was to define if differences occurred after proton broad beam and proton microbeam for the endpoints analyzed.

The main difficult of data analysis in this work is created by the use of patient's cell lines whose genomic profiles are complex. This complexity could be derived from the original biopsy and/or from the different nature of the cell lines analyzed. For example, IB106 cell line is constituted from cancerous and peritumoral cells and IB115 cell line shows the presence of more clones with similar but not identical genomic profiles. These particular characteristics could explain the impossibility to highlight specific radiation-induced chromosome rearrangements or genomic profile alterations.

A next step that could be considered to better understand the radiation-induced effects is the study of transcriptomics, also referred as expression profiling, which examines the expression level of mRNAs in a given cell population, often using high-throughput techniques based on DNA microarray

technology such as RNA-Seq<sup>52,53</sup>. The expression profile can reveal specific pathways radiation-induced.

These developed protocols can be improved by the addition of other end points but lay the groundwork for analyzing the radiation sensitivity of other patient's cell lines to verify first difference in response to ionizing radiations. In addition, the development of these well-defined protocols, allowed us to begin parallel works for the purpose of evaluating the effects of metal and metal oxide nanoparticles which use is a new increasing interesting approach in the battle against cancer. Metal and metal oxide nanoparticles have been proposed as potential contrast agents and represent an important improvement of the therapeutic ratio by increasing the local control (increasing dose to the target), or by decreasing the normal tissue complications. The amplification of radiation effects induced by the presence of intra-cellular high-Z nanoparticles are explained in terms of early stage physical processes that take place in the cells in the surrounding of nanoparticles. Nevertheless, the relation between biological effects and the radiation dose is not fully understood at present. These new approaches need to develop calculation methods with experimental validation to precisely predict dose-effect correlation in the context of IR and nanoparticles interaction in cancerous cell lines. In addition, is necessary to determine the physicochemical and bio-molecular mechanism induced *in cellulo* by IR and metal nanoparticles interaction. Tests of feasibility using different nanoparticles are in progress and are the objects of future studies.



## **Manuscript 4**

**“Multiparametric analysis of radiation sensitivity of two sarcoma cell lines derived from patients after both electron and proton irradiations”**

Muggioli G, Simon M, Devès G, Antoine M, Kantor G, Chibon F, Barberet P and Seznec H

**Scientific Reports (submitted)**

## **Multiparametric analysis of radiation sensitivity of two sarcoma cell lines derived from patients after both electron and proton irradiations.**

Giovanna Muggioli<sup>1,2</sup>, Marina Simon<sup>1,2</sup>, Guillaume Devès<sup>1,2</sup>, Mikael Antoine<sup>3</sup>, Guy Kantor<sup>1,3</sup>, Frédéric Chibon<sup>4</sup>, Philippe Barberet<sup>1,2</sup> and Hervé Seznec<sup>1,2,\*</sup>

<sup>1</sup>University of Bordeaux, Centre d'Etudes Nucléaires Bordeaux Gradignan (CENBG), UMR 5797, Gradignan, France; <sup>2</sup>CNRS, IN2P3, CENBG, UMR 5797, Gradignan, France; and <sup>3</sup>Department of Radiotherapy, Institut Bergonie, Bordeaux, France; <sup>4</sup>Genetics and Biology of Sarcomas INSERM U1218, Department of Biopathology, Institut Bergonié, Bordeaux, France

### **Abstract**

*In vitro* radiobiological studies permit to characterize the responses of cancerous cells exposed to ionizing radiations. A better understanding of radiation sensitivity of rare and resistant tumors exposed to different ionizing radiations is a today challenge and can be improved by a multi-parametric analysis of radiation induced biological responses.

We report the effects of (i) two types of ionizing radiations (electrons and protons), (ii) two modes of delivery using different dose distributions at the cellular scale (focused beam *versus* broad beam), and (iii) we take in account the genetic characteristics of two patient's derived sarcoma cell lines having a simple or complex genomic profile. First, we establish a method based on Monte Carlo simulations to ensure that the mean delivered dose on a cell monolayer is comparable for different irradiation modalities (9 MeV electrons and 3 MeV protons). Then, we evaluate the cellular response of two selected sarcoma cell lines to ionizing radiations by investigating three biological endpoints: radiation-induced DNA damage, proliferation and surviving fraction assays. For the endpoints analyzed, we show a higher efficacy of protons with respect to electrons and a marked radiation resistance associated with the complex genetics of one sarcoma cell line.

### **Introduction**

Optimizing the therapeutic benefit of radiation therapy requires the improvement of the beam ballistics and the Relative Biological Efficiency (RBE) of the radiation inside the tumor. The main current developments in radiation therapy are based on these ideas with the final aim to increase the radiation-induced effects in the tumor volume as well as decrease the dose delivered to the surrounding healthy tissues. Several strategies have shown interesting features such as the use of heavy charged particles having an high-LET (Linear Energy Transfer) such as hadrons and protons<sup>1-3</sup>, and nowadays Microbeam Radiation Therapy (MRT) with X-rays or heavy ions is largely studied<sup>4,5</sup>. However, the action mechanisms involved at the cellular scale and the biological efficacy of protons *versus* low-LET radiations are not completely understood<sup>6</sup>. And less is known about the biological efficacy of a millimeter-sized pencil beam, used in MRT, scanned on a determined area<sup>7</sup>. Additionally, the success

of radiation treatments not only depends on the total dose delivered to the tumor and on the protection of healthy tissues surrounding the tumor, but also from the intrinsic properties of the tumor cells<sup>8</sup>.

For a better understanding, it is crucial to carry out experiments on *in vitro* well-characterized biological models and in highly-controlled conditions<sup>9</sup>. Several parameters must be considered to obtain a correct evaluation of the cells radiation sensitivity such as the type of ionizing radiation (IR), the irradiation modalities, the genetic characteristics, and the biological endpoints considered.

In the present study, we considered all these parameters together. We compared two ionizing radiations: electrons and protons. Electrons are routinely used to treat patient's superficial tumors at the Institut Bergonié (Bordeaux) and are produced by a medical linear accelerator (Clinac 21EX© from VARIAN<sup>TM</sup>). Protons are delivered by an original irradiation setup based on a charged particle microbeam<sup>10</sup>, allowing to target living cells with a micrometer precision. This setup permits different energy depositions at the cellular scale, by using a proton microbeam or a proton broad beam. To ensure that the mean delivered dose by these two irradiation systems and by two irradiation modes is equivalent, we performed the dosimetry at the cellular scale using Monte Carlo techniques<sup>11</sup>.

We investigate the biological responses of two patient's derived sarcoma cell lines for different reasons. First, sarcomas are a group of tumors, which heterogeneity is defined by the anatomic sites, the patient's age and the varying histology. Second, they could be radiation-induced and have a very variable radio-responsiveness dependent on histology, genetics and type of radiation<sup>12-14</sup>. Third, radiation sensitivity of soft tissue sarcomas is generally low and requires high levels of dose. Thus, increasing the efficacy of radiation therapy represents a good strategy to improve sarcomas treatment and reduce associated side effects<sup>15</sup>. In addition, during last years, numerous studies are defined different representative group of sarcomas based on their genetic expression profiles<sup>8,16-20</sup>. In particular, Chibon *et al.* described three different genomic profiles recurrent in sarcomas<sup>17</sup>. According to this classification, sarcomas having a simple *amplicon* profile based on few co-amplifications belong to a first group, which is represented almost exclusively to dedifferentiated liposarcomas. A second group includes sarcomas with few alterations that involve a full chromosome arm or entire chromosomal gain or loss. And, a third group is constituted by all other unclassified sarcomas, which are characterized by a high level of chromosomal complexity and tumor aggressiveness. Two sarcoma cell lines were selected from the sarcoma collection of the Institut Bergonié (IB): a dedifferentiated liposarcoma (IB115) and an unclassified heterogenic sarcoma (IB106), belonging to the first and the third group, respectively<sup>17</sup>.

In this report, we evaluated the *in vitro* radiation sensitivity of these well-characterized sarcoma cell lines considering simultaneously three biological end points: (i) single cell *in situ* quantitative co-localization of phosphorylated H2AX (called  $\gamma$ H2AX) and ATM (called P-ATM) radiation-induced foci, (ii) cellular proliferation, and (iii) the commonly used survival fraction assay (SF).

The survival fraction is considered to be the optimal and well-recognized test for *in vitro* radiation studies<sup>21-25</sup>. However, it is limited by the ability of cells to form colonies, and is less reliable for cells

with a low colony-forming capability<sup>26,27</sup>. The estimation of cell growth by cell proliferation assay is a largely used test to evaluate the *in vitro* radiation sensitivity<sup>28,29</sup>. In addition, the analysis of induction and quantification at 2 and 20 h after irradiation of radiation-induced foci (IRIF) can be used as an endpoint to measure the cell radiation sensitivity<sup>26,27,30–36</sup>. In particular, the behavior of both P-ATM and  $\gamma$ H2AX, which are (i) two proteins involved in DNA damage and repair signaling, and (ii) phosphorylated on specific and well-characterized residues at DNA Double Strand Break (DSB) sites after ionizing radiation exposure is analyzed (in a time- and dose-dependent manner)<sup>32</sup>.

The performed multi-parametric analysis reveals a different radiation sensitivity of selected cell lines for the analyzed endpoints. In addition, we show that *in vitro* exposure to protons induces marked effects with respect to electrons. No differences are observed after two protons energy distributions at the cellular scale. It remains a challenge to explain the mechanisms that induce their respective responses. However, this work underlined the importance of *in vitro* radiation biological studies for investigation the effects induced by different particles on rare characterized tumors to develop and optimize therapeutic approaches.

## Results

### Irradiation, calibration and dosimetry

#### *Electron dosimetry*

Irradiation protocols using standard cell culture supports (6-well plate) and a medical facility (electron, 9 MeV, Clinac) were optimized by measuring the percentage of absorbed dose at a given depth (PDD) along the beam axis. Monte Carlo simulations (Geant4 10.1) describing the radiation sources (spectra and angular distributions of electrons and photons)<sup>37</sup> are in agreement with routine measurements performed by the medical physicists in according to IAEA TRS 398 protocols.

The PDD shows that the maximum relative dose is delivered at 22 mm in depth. As illustrated in Fig. 1, standard cell culture well (6-well plate) allows one to grow cells at 10 mm depth when covered with 9.6 ml of culture medium. By consequence, at this depth we reached 93% of the maximum relative dose as shown by experimental measurements and Monte Carlo simulations (Fig. 1).

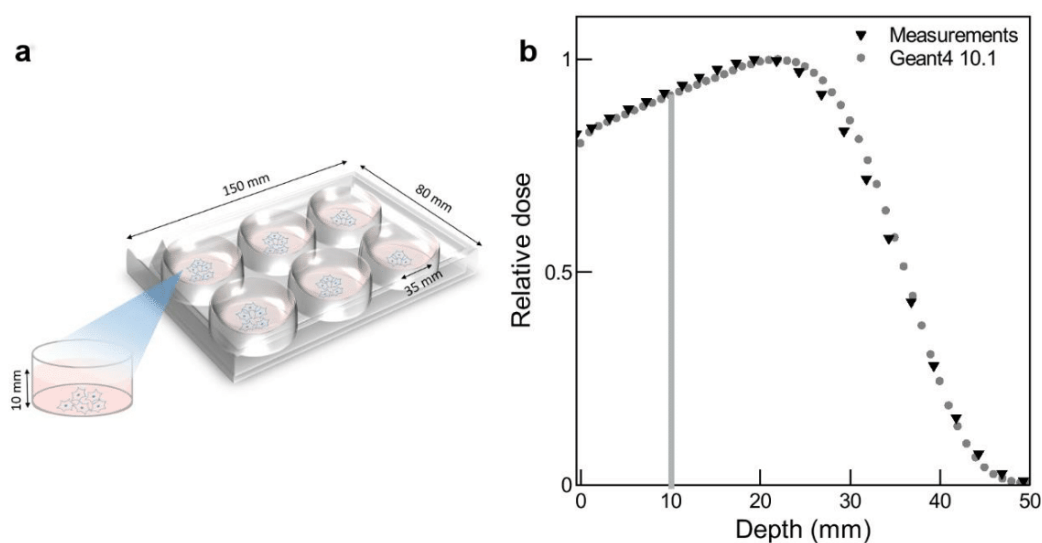


**Fig. 1. 9 MeV electrons relative dose measured at increasing depth.** (a) Representation of a 6-well plate used during electron irradiations with *zoom* on one cell dish at whose bottom were seeded cells. To achieve a 10 mm depth, 9.6 ml of culture medium were added in each well during whole irradiation time. (b) Absorbed relative dose as a function of depth. Experimental measurements and Geant4 10.1 Monte Carlo simulations showed that cells positioned at 10 mm under culture medium receive 93% of the maximum relative dose, as indicated by the gray line.

#### *Proton dosimetry*

3 MeV proton irradiations (Linear Energy Transfer =  $12 \text{ keV} \cdot \mu\text{m}^{-1}$ ) are performed on the AIFIRA facility using a microbeam line. To ensure an homogeneous dose distribution, we calculated by Geant4 10.1 Monte Carlo simulation<sup>11</sup>, that a mean absorbed dose of 2 Gy is achieved when the beam is scanned every  $5 \mu\text{m}$  in a regular pattern and 26 protons are delivered per beam position (Fig. 2). To obtain 1 and 6 Gy the mean number of protons delivered per beam position was 13 and 78, respectively. The beam can be either unfocused to obtain “broad beam” irradiations or focused down to the micrometer size (Fig. 2a and b). Using the method reported in a previous work<sup>38</sup>, we estimated the absorbed energy per pixel in cell nuclei, and we calculated the mean dose absorbed per nucleus for both unfocused and focused beams. Figure 2 shows that despite a mean dose of 2 Gy is delivered per nucleus, the absorbed energy at each beam spot after proton microbeam varies from 1 to 3 times the absorbed dose after proton broad beam.



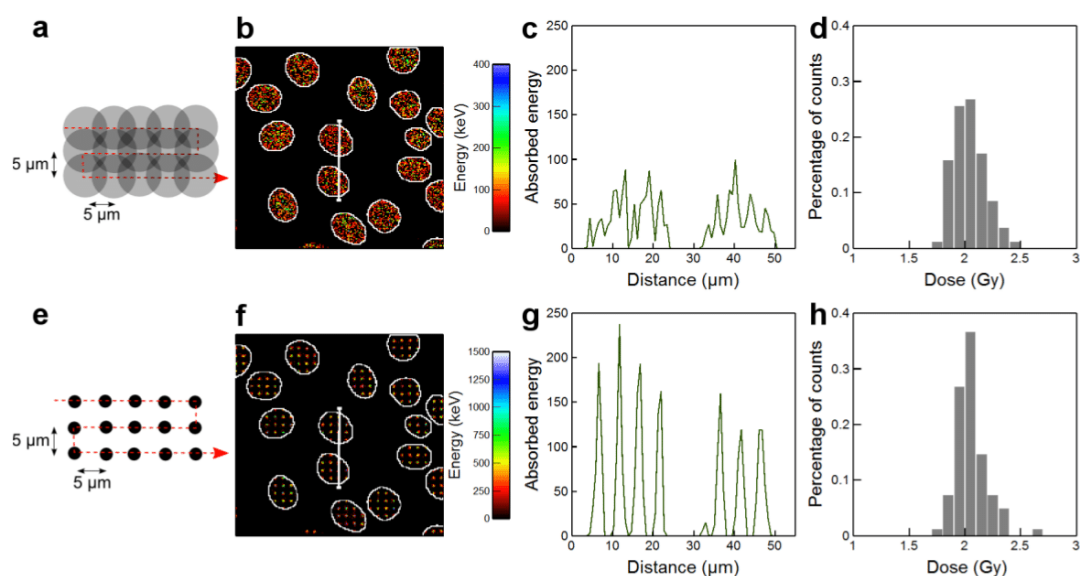


**Fig. 2. Microdosimetry at the cellular scale ensures the same mean dose of two proton irradiation modalities.** (a and e) The broad and micro beams are scanned every 5  $\mu\text{m}$  in regular pattern to obtain the desired dose. (b and f) Cell nuclei are delimited by white circles. Absorbed energies in cell nuclei were estimated by Monte Carlo simulations, and depicted with keV calibration bars. (c and g) Profiles of the absorbed energies plotted alongside the white line drawn on cell nuclei. The absorbed energy after microbeam irradiation is 1 to 3 times higher than after broad beam irradiation. (d and h) Histograms represent the percentage of cells that received from 1.5 to 2.5 Gy when 26 protons per point are delivered.

### **IB115 surviving fraction is dose- and IR-dependent.**

The strength of clonogenic assay relies on the independence of the Plating Efficiency that is assumed to be the same when different numbers of cells are inoculated in each experiment<sup>39</sup>.

First, we tested the IB115 plating efficiency (PE) by seeding different numbers of cells, from 200 to 1000 cells per well. The relative PE was calculated after 10 days in normal culture condition (Supplementary Table S3). The PE of IB115 varies from 12.4 to 16 for 500 and 200 plated cells, respectively. Whatever the PE variation, the number of colonies remains sufficiently elevated for the correct analysis of IB115 surviving fraction.

Second, we developed and validated a routine based on numerical acquisition of paraformaldehyde-fixed cell population. Nucleus staining using intercalating agent allows us to determine the number of colonies having more than 50 cells and also the number of cells per colony (see Supplementary Materials S3 for complete description). This methodology allowed us to measure the standard SF (Supplementary Fig. S3), the number of colonies with more than 50 cells (Fig. 3a) and the colony size distribution which takes in accounts the number of cells per colony (Fig. 3b).

The number of colonies of IB115 decreases as the dose increases, for both electron and proton irradiations. In addition, it is almost 20% lower when cells are irradiated with protons compared to electrons for both doses. No differences were observed after protons broad beam and proton

microbeam irradiations. The colony size distribution is also significantly reduced in a dose- and IR-dependent manner except for 1 Gy electron irradiation where the number of cells per colony does not significantly change.

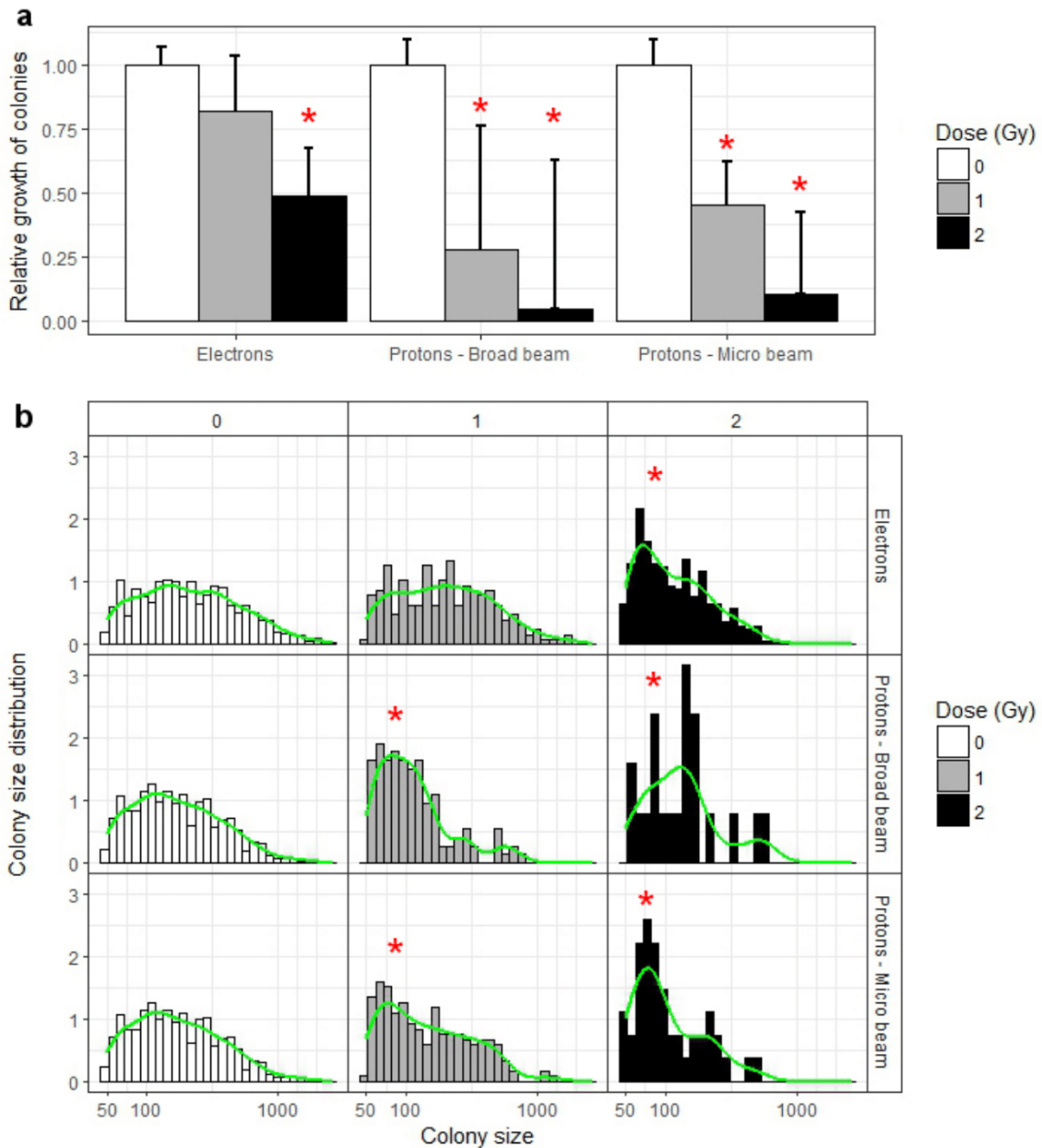


**Fig. 3. IB115 colonies number and colonies size distribution is dose- and IR-dependent except for 1 Gy electron irradiations.** (a) Relative growth of colonies above 50 cells *versus* incoming particles and irradiation doses. Significant change (\*,  $p < 0.05$ ) of the number of colonies was evaluated using multiple t-tests with Bonferroni correction. (b) Distribution of colony sizes (n cells per colony) *versus* incoming particle and irradiation doses. Significant changes of size distribution (\*,  $p < 0.05$ ) were compared using Kolmogorov-Smirnov test with Bonferroni correction.

As already done for IB115, we estimated the IB106 PE by plating from 200 to 1000 cells and showed that IB106 PE decreases from 10 to 2 when 1000 and 600 cells are seeded, respectively

(Supplementary Table S3). These data illustrate that the ability of IB106 to grow in colonies is drastically impaired and highlight the fact that the Colony Forming Assay may not be a suitable test for evaluating their radiation sensitivity.

### Proliferation rate is dose- and IR-dependent and highlights a first difference between IB115 and IB106.

As shown in Fig. 4a and b, the proliferation rate of IB115 exposed to 1 and 2 Gy with electrons decreases by 1.4 to 3.3 fold with respect to controls, respectively. The proliferation rate of IB115 exposed to 1 and 2 Gy with protons decreases by 3.3 to 10 fold with respect to controls, respectively. Moreover, the proliferation rate was not considerably modified by focusing the proton beam to micrometer dimension.

The analysis of cell proliferation highlights a difference between IB106 and IB115. For both doses of electrons, the IB106 proliferation rate decreases by 2 fold with respect to controls. For proton irradiations, the proliferation rate of IB106 exposed to 1 and 2 Gy decreases by 2 to 3 fold with respect to controls, respectively. The proliferation rate was not considerably modified between broad and focused proton irradiations for the tested doses (Fig. 4c and d).

However, we can observe a marked decrease in cell proliferation of IB115 in comparison to IB106, revealing a higher resistance to radiation of IB106.

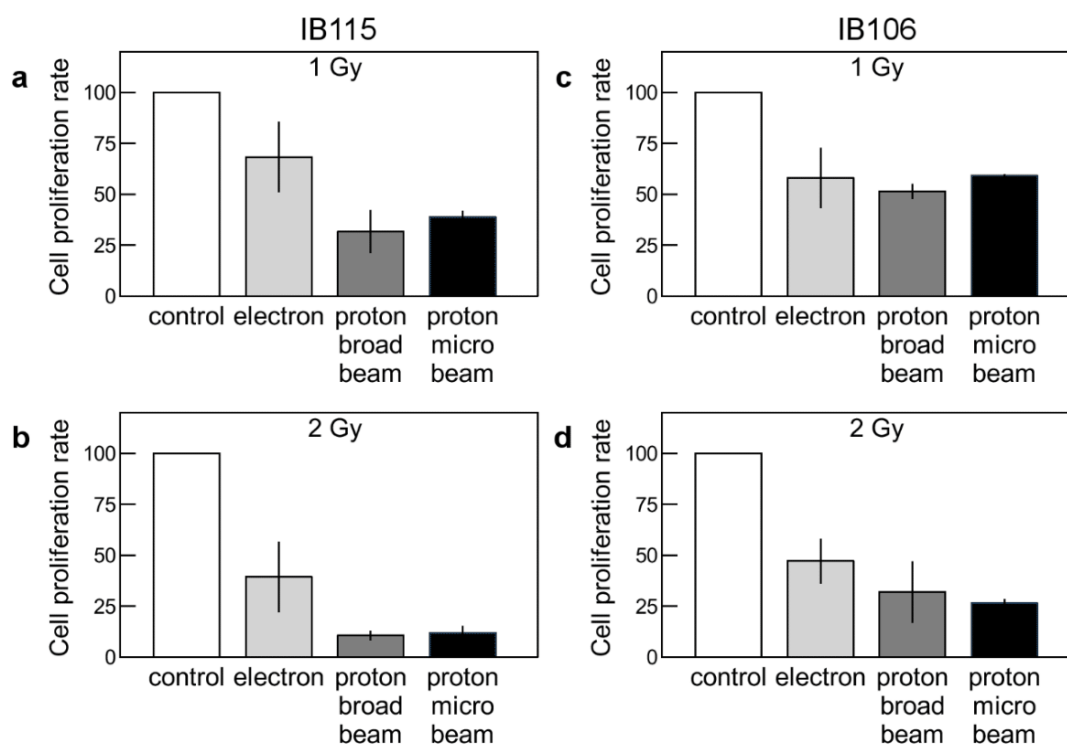


**Fig. 4. Proliferation rate reveals radiation sensitivity differences between IB115 and IB106.** IB115 proliferation not only depends on doses (a: 1 Gy and b: 2 Gy) but also on types of ionizing radiation. A higher decrease after 2 Gy with respect to 1 Gy, and after proton in comparison to

electron irradiations is observed. (c) IB106 proliferation after 1 Gy exposure is decreased 2 fold with respect to controls, but no differences are observed between electron and proton irradiations. (d) Following 2 Gy irradiation exposure, the IB106 proliferation rate is decreased 2 fold after electrons, and 3 fold after protons. Error bars represent mean +/- SD of three replicates from two independent experiments normalized to untreated controls.

### **Radiation-induced $\gamma$ H2AX and P-ATM foci number is dose-, IR-, time- and IR distribution-dependent.**

We detected and quantified the induction and persistence of both  $\gamma$ H2AX and P-ATM IRIF over time, as shown in previous studies<sup>32,40-42</sup> (Supplementary Fig. S4, S5 and S6). Box plots in Fig. 5 show the  $\gamma$ H2AX IRIF quantification per nucleus as a function of (i) the delivered dose, (ii) the ionizing radiation and (iii) the time post-irradiation.

For electron irradiations, the number of IRIF in IB115 increases in a dose-dependent manner, 2 h after irradiation (Fig. 5a). Then, it decreases to reach the controls baseline 20 h after irradiation (Fig. 5b).

For proton broad beam irradiations, the number of  $\gamma$ H2AX IRIF increases with respect to control cells after both doses, but no differences between 2 Gy and 6 Gy irradiated cells are observed (Fig. 5c). The number of  $\gamma$ H2AX IRIF at 6 Gy is probably underestimated. This could be due to the limit of optical microscopy resolution and the overlapping of DNA damages in the same area, as a consequence a high number of IRIF can appear as a single focus, as already showed by Costes *et al.*<sup>43</sup>. Persistence of  $\gamma$ H2AX IRIF is observed 20 h after proton broad beam irradiations; indeed, there is 3-fold increase of  $\gamma$ H2AX IRIF compared to control cells (Fig. 5d). For all conditions, a higher number of  $\gamma$ H2AX IRIF is observed in irradiated cells with proton broad beam compared to electrons, whatever the dose and the time after irradiation. These results highlight both the higher number and the duration persistence of protons induced-DNA damages compared to electrons as a function of the dose and time post-irradiation in IB115.

As for IB106, we detected and quantified the induction and persistence of both  $\gamma$ H2AX and P-ATM IRIF over time in IB106 (Supplementary Fig. S5 and S6). In IB106, 2 h after irradiations, the IRIF number increases in a dose-dependent manner and as a function of the IR used (Fig. 5e and g). A decrease of the IRIF number is observed for both electron and proton broad beams 20 h after irradiations (Fig. 5f and h). For each condition, the quantification of  $\gamma$ H2AX IRIF in IB106 showed that the number of IRIF per cell is reduced with respect to IB115.

As expected, a distinct distribution of  $\gamma$ H2AX IRIF per cell is observed after irradiation with proton microbeam in both IB115 and IB106. The number of IRIF remains low for both doses 2 h after irradiation reflecting the irradiation pattern (Fig. 5i and k). Twenty hour after proton microbeam irradiation, the IRIF number increases in both cell lines after 2 and 6 Gy irradiation doses (Fig. 5j and l). The increase in radiation-induced  $\gamma$ H2AX foci could be interpreted as a diffusion mechanism at the

site of damage where the chromatin relaxes, leading to more phosphorylation of H2AX, as suggested in other studies<sup>43,44</sup>.

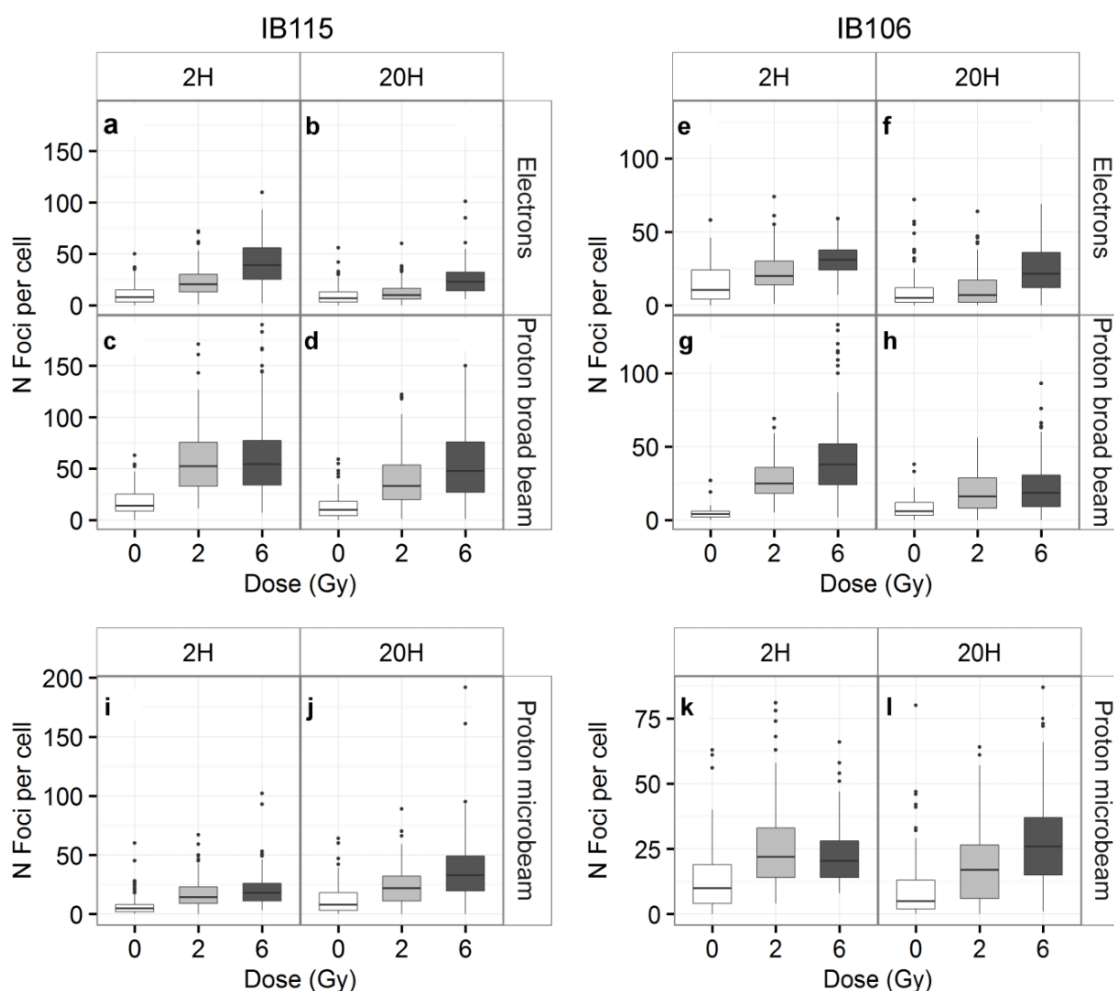


**Fig. 5. Radiation induced DNA damages are dose-, time-, IR-dependent and IR distribution-dependent.** (a and b) The number of  $\gamma$ H2AX IRIF observed after 2 h and 20 h after electron irradiations in IB115 is dependent on the dose delivered, with a decrease of the  $\gamma$ H2AX IRIF number at the later time point. (c) In IB115, 2 h after proton broad beam irradiations the number of IRIF is increased with respect to non-irradiated cells, and (d) 20 h after irradiation, IRIF number remains more elevated with respect to control and electron irradiated cells. (e and g) The number of  $\gamma$ H2AX IRIF observed in IB106, 2 h after electron and proton broad beam irradiations is dose-dependent but not differences are observed between the two ionizing radiations. (f and h) A decrease of the IRIF number 20 h after irradiation is observed for both electrons and proton broad beams. (i) In IB115, the number of  $\gamma$ H2AX IRIF observed 2 h after microbeam irradiation reflects the irradiation pattern hence not differences are observed between 2 and 6 Gy irradiated cells. (k) The same behavior is observed in IB106. (j and l) 20 h after proton microbeam irradiation the number of IRIF observed increase in a dose-dependent manner, in both IB115 and IB106. In all cases, the IRIF number observed in IB115 is higher than the IRIF number observed in IB106.

## Discussion

Understanding radiation-induced biological effects underlying the cellular radiation sensitivity can improve the radiation therapy benefits. Different ionizing radiations (photons, electrons, protons and carbon ions) are used today in radiation therapy. Thus, deciphering the *in vitro* biological impacts of these different ionizing radiations improve our knowledge and could enhance the personalized radiotherapy treatments.

We investigated the radiation-induced biological differences between 9 MeV electrons and 3 MeV protons homogeneously distributed, and 3 MeV proton focused to a micrometer-size beam spot and scanned over a cellular monolayer. To compare the delivered doses from a Clinac producing electrons and a Singletron Accelerator producing protons, we developed protocols based on the dosimetry at the cellular level obtained by Monte Carlo simulations, in agreement with the measurements at the Institut Bergonié, and to the electron beam characterization performed by Gobet and colleagues<sup>37</sup>.

In a previous work Williams *et al.* explains that “for a complete description of radiation sensitivity at least two parameters are needed and the radiation sensitivity is based on multiple distinct cell response mechanisms” (*sic*)<sup>45</sup>. For these reasons, we performed a multi-parametric analysis by measuring the survival fraction (SF), the number of colonies and the colony size distribution, the proliferation and we quantified  $\gamma$ H2AX IRIF. In addition to  $\gamma$ H2AX, we quantified the P-ATM IRIF which are a highly sensitive biological dosimeter that may use to probe DNA damage response and variations in cellular radiation sensitivity<sup>46</sup>.

The biological efficacy of electrons and protons is assessed firstly in IB115 sarcoma cells with a known amplicon based genetics. The SF of IB115 is decreased in a dose- and IR-dependent manner and reveals that protons have a greater efficacy with respect to electrons. These results are also confirmed with proliferation assay. And, the number of  $\gamma$ H2AX IRIF (low in control cells, as previously observed by Mac Manus *et al.* in both non-irradiated cancerous and primary human commercial cells, such as Hela and *Indian Muntjac skin* cells<sup>47</sup>) is increased in a dose-dependent manner and cells presented more IRIF 2 h after proton compared to electron irradiations. These data are in accordance to Rothkamm *et al.*, who showed that the IRIF frequency is proportional to the delivered dose<sup>32</sup>. A considerable reduction of the IRIF number in different cervical cancer cell lines, 20 h after irradiation, was previously showed by Banath *et al.*<sup>36</sup>. We found a reduction of the IRIF number after both electron and proton broad beam irradiations, 20 h after irradiation. Nevertheless, the number of IRIF remains higher after proton broad beam than after electron irradiations, in accordance with the higher LET of protons. Our results agreed with other published works showing more severe consequences of proton compared to electron irradiations<sup>48,49</sup>.

As previously mentioned, the ability to deliver the same dose in different patterns within cells is accessible using microbeams<sup>10,50,51</sup>. We compare the dose distribution obtained from focused proton beam, where the energy is deposited in small spots distributed in a regular pattern (microbeam) with

unfocused proton beam, where the energy is homogeneously distributed all over the cell monolayer (broad beam) (Supplementary Fig. S3). We observed that beam focusing leads to 3-fold increase of the energy deposited in the beam spot while keeping the mean dose constant. This highly concentrated energy deposit in micrometer size area is expected to produce more complex damage at the cellular level and thus to enhance the radiation-induced biological effects. The focused deposited energy is well-depicted by the  $\gamma$ H2AX IRIF distribution. Indeed, the number of  $\gamma$ H2AX IRIF 2 h after microbeam irradiations does not depend on the delivered dose, but it remains stable reflecting the irradiation pattern (as already explained, to obtain a mean dose of 1, 2 and 6 Gy, 13, 26 and 78 protons were delivered at each beam position, respectively). Twenty hours after irradiation the IRIF number increases in a dose-dependent manner. A change in the IRIF morphology together with an increase in the IRIF number and a decrease in the IRIF total size is observed over time. This phenomenon, demonstrated by other authors, can be due to the chromatin reorganization during which a sub-diffusion of damages can occurs<sup>30,52</sup>. Cell proliferation and SF do not reveal significant differences between proton micro- and broad- distributions. The team of Schmid and co-workers investigated the RBE enhancement after focused and homogenous low-LET proton beams. They demonstrated that focused protons result in an increased relative biological effectiveness for the induction of micronuclei and dicentric chromosomes<sup>53</sup>. This seems not to be the case for our experimental conditions. However, we cannot directly compare our results to their, because cell lines, biological endpoints and proton energy are different.

Once detailed the radiation-induced biological effects in IB115, we analyzed the biological responses of another patient-derived sarcoma cell line (IB106), known to have a complex genetics<sup>17</sup>. The first difference observed is the inability of IB106 to grow in colonies, hence the SF cannot be measured. The relative cell proliferation is dose-dependent after protons but not after electrons. However, we found that the proliferation rate after electron and proton irradiations decreases in the same way after 1 Gy. Regarding the  $\gamma$ H2AX IRIF quantification, we observed a lower IRIF number and a higher rate of disappearance compared to IB115. These two parameters, as already described by other authors<sup>35,54,55</sup>, confirm that IB106 are more radiation resistant than IB115.

We suggested different hypothesis to explain the radiation resistance of IB106. Due to their complex genetics and recurrent chromosome rearrangements, the lower number of IRIF in IB106 could be associated to a lack of phosphorylation mechanisms of H2AX and ATM. Another feature that could influence the different response to ionizing radiations is the cell cycle duration<sup>56</sup>. Indeed, the IB106 cell cycle is 10-times slower than the IB115 cell cycle. And, in agreement with our data, another study confirmed that liposarcoma (corresponding to our IB115 cell line) are known to belong to the more sensitive varieties of soft tissue sarcoma<sup>12</sup>.

In conclusion, we show that for radiation sensitivity assessment of cells derived from patients it is necessary to verify different biological endpoints, such as quantification and persistence over time of

DNA damage, proliferation and surviving fraction. These protocols highlighted different biological responses of the two cell lines exposed to ionizing radiations. We observe that protons induce more deleterious effects compared to electrons, independently from the dose distribution at the cellular scale. Our results lead to the conclusion that IB115 are more sensitive than IB106 for the endpoints analyzed.

## Methods and Materials

### Cells lines culture

Sarcoma cell lines were characterized, from a genetic point of view, in previous works from F. Chibon laboratory (described in Supplementary Material S1). Cell lines (IB115 and IB106) were maintained in RPMI 1640 GlutaMAX supplemented with Fetal Bovine Serum (10% v/v, FBS) and streptomycin/penicillin (100 µg/ml). Cells were kept in a humidified atmosphere at 37 °C and 5% (v/v) CO<sub>2</sub>. For both electron and proton irradiation experiments, 20,000 cells were seeded in a drop in specific cell dishes 20 h before irradiations. As a control, a mock sample was used, which was treated in the same way with the exception of irradiation.

### Irradiation systems

Electron irradiations were performed with a Clinical Linear Accelerator (CLINAC 21EX, Varian Medical Systems), used in routine at the Department of Radiotherapy, Institut Bergonié (Bordeaux, France). Cells were irradiated using 9 MeV electron beams with 1, 2 and 6 Gy delivered with a dose-rate of 2 Gy/min. These doses are selected as irradiation doses because 2 Gy is the fractionated dose used during patient treatments; 1 and 6 Gy are lower and higher doses with respect to this standard value. The electron beam was collimated in 15 x 15 cm<sup>2</sup> square field. A Source-Surface Distance (SSD) of 100 cm was applied, and the irradiations were carried out with a single beam oriented at 0° (single vertical beam). Cells were plated in the middle of a 6-well plate or on coverslips. The cell monolayer was covered by 10 mm of medium to achieve electronic equilibrium and reach 93% of the maximum dose. One hour before irradiation 9.6 ml of growth medium were added to achieve this depth.

Proton irradiations were carried out at the AIFIRA microbeam line (Applications Interdisciplinaires de Faisceaux d'Ions en Région Aquitaine)<sup>10</sup>. Cells were grown in a custom made support dish, described by Bourret *et al.*<sup>10</sup>, designed to keep the cells fully immersed in their culture medium during the irradiation procedure. A beam intensity of about 100,000 protons per second was used to irradiate a sufficient amount of cells in a reasonable time (20 min maximum for 6 Gy). The beam spot was scanned on a surface corresponding to the microscope field of view (690 x 520 µm<sup>2</sup>) by a fast electrostatic deflector. Then, this pattern was repeated on the adjacent microscope fields, following a mosaic of 9 x 12 fields, to cover an area of 6.2 x 6.2 mm (Supplementary Material S2A). The same



protocol was applied for either focused (microbeam, Supplementary Material S2B) or unfocused (broad beam, Supplementary Material S2C) beams, to study the impact of the energy deposition at the micrometer scale. The microbeam was focused to the minimum beam spot size (2  $\mu\text{m}$ ). The broad beam was unfocused to obtain a homogenous protons distribution on the cell population. In relation with the stability of the beam count rate over a few tens of minutes, 4% of uncertainties were estimated. The flux stability was checked every two samples for the three doses, by counting the incoming particles with a plastic scintillator (EJ-204, Scionix, The Netherlands) coupled to a photomultiplier tube (Model R9880U, Hamamatsu).

### Monte Carlo simulations

#### Electron beam

The percentage depth dose (PDD) was measured using standard protocols and cross-checked by Geant4 10.1 simulations<sup>11</sup>. The methodology was described previously by Gobet *et al.*<sup>37</sup>. Briefly, electrons are emitted isotropically in a cone of 4° half opening angle from the effective point source located 1 m above the water phantom surface. A Gaussian energy distribution (mean energy = 9 MeV, FWHM = 800 keV) was assumed from previous measurements<sup>37</sup>. The phantom is a 10x10x10 cm<sup>3</sup> filled with water. Voxels with dimensions of 0.1 x 0.1 x 0.1 cm<sup>3</sup> were defined along the vertical beam axis. The absolute absorbed dose at a given depth of the water phantom was defined by the ratio between the absorbed energy inside the voxel of interest and its mass. The G4EmLivermorePhysics library was used with a 100  $\mu\text{m}$  cut for electrons and photons.

#### Proton beam

To ensure that the mean delivered dose with protons was similar to the one obtained with electrons, the proton beam irradiation was simulated using a previously described methodology<sup>38</sup>. Briefly, a 3D confocal image of 82 cell nuclei is imported in Geant4 10.1 as a so-called cellular phantom. 3 MeV protons are delivered on Gaussian distributions of 0.5  $\mu\text{m}$  FWHM or 10  $\mu\text{m}$  FWHM focused and broad beam irradiation respectively. The beam is positioned every 5  $\mu\text{m}$  and 26 protons are delivered. The energy deposit in every nucleus is registered and the dose per nucleus is calculated as the absorbed energy normalized by the nucleus mass calculated from its volume and a density of 1 g.cm<sup>-3</sup>. The G4EmLivermorePhysics library was used with a 10 nm cut for electrons and photons.

### Cell surviving fraction

Cells were harvested with trypsin-EDTA (0.05%, v/v) right away irradiation, and 500 IB115 and 1000 IB106 were seeded in 12-well plate, respectively. After 12 days kept in standard culture conditions, cells were paraformaldehyde fixed (4%, w/v) in phosphate-buffered saline (PBS 1X, pH 7.4) for 15 min at room temperature. Cells nuclei were stained with Hoechst<sup>33342</sup> (1  $\mu\text{M}$ , 10 min, room temperature). Data acquisitions were performed with a Zeiss AxioObserver Z1 microscope (Carl Zeiss

MicroImaging, GmbH). Two independent experiments were performed in quadruplicates. Plating efficiency (PE) was determined for each dose and surviving fraction was calculated as the ratio of the PE for the irradiated cells to the control cells, as previously described by Franken<sup>25</sup>. Colonies were counted using an automated custom macro (See supplementary Material S3).

### Cellular proliferation

Right away irradiation, cells were harvested with trypsin-EDTA (0.05% v/v), and 300 IB115 or 500 IB106 cells were seeded in 30 wells of 96-well plate, respectively. Every day the culture medium was removed from 3 wells, cells were washed with PBS and harvest with trypsin-EDTA (0.05% v/v for 15 min, 37°C). For re-suspension and counting, FBS (4% v/v) in PBS was added and the totally of cells was counted with a flow cytometer (FACScalibur, BD Bioscience).

6 Gy irradiation inhibits cell division, independently of the ionizing radiations. Therefore data analysis of surviving fraction and proliferation rate was performed only for 1 and 2 Gy. Two independent experiments were performed for each dose of each ionizing radiation used. Each data point represents the average of triplicates. For IB115 cells, the cellular proliferation rate was calculated when the fold was 200 for the control cells number. For IB106 cells, the cellular proliferation rate was calculated when the fold was 20 for the control cells number. These respective folds were obtained 14 days following irradiation and the difference is due to the fact that IB106 cells have a slower population doubling time.

### Immunodetection

The co-immunostaining of  $\gamma$ H2AX and P-ATM was performed following the protocols described by Bennett<sup>57</sup>. Briefly, 2 or 20 h after irradiation, cells were paraformaldehyde fixed (4% w/v) in PBS for 15 min at room temperature. Then, cells were incubated using a blocking buffer (Triton X-100, 0.2% v/v and FBS, 10% v/v in PBS) for 30 min at room temperature. After three washes in PBS for 5 min, samples were incubated overnight, at 4 °C with anti-human  $\gamma$ H2AX rabbit monoclonal antibody (1:1000, 20E3, Cell signaling). After three more washes in PBS, samples were incubated for 3 h at room temperature with goat anti-rabbit conjugated to Alexa Fluor<sup>488</sup> antibody (1:2000 Molecular Probes, Invitrogen). The same process was repeated with anti-human P-ATM mouse monoclonal antibody (1:1000, 10H11.E12, Cell signaling), and goat anti-Mouse conjugated to Alexa Fluor<sup>594</sup> antibody (1:2000, Molecular Probes, Invitrogen). Nuclei were stained with Hoechst<sup>33342</sup> (1  $\mu$ M, 10 min at room temperature). The images acquisition was performed using a Carl Zeiss fluorescent microscope with a 63X/Oil immersion objective. The number of foci was counted in 40 to 60 cells per condition with a custom Image J macro (Supplementary Material S4).

### References

1. Durante, M. & Loeffler, J. S. Charged particles in radiation oncology. *Nat. Rev. Clin. Oncol.* **7**,

- 37–43 (2010).
2. McGovern, S. L. & Mahajan, A. Progress in Radiotherapy for Pediatric Sarcomas. *Curr. Oncol. Rep.* **14**, 320–326 (2012).
  3. DeLaney, T. F. & Haas, R. L. M. Innovative radiotherapy of sarcoma: Proton beam radiation. *Eur. J. Cancer* **62**, 112–123 (2016).
  4. Serduc, R. *et al.* Brain tumor vessel response to synchrotron microbeam radiation therapy: a short-term in vivo study. *Phys. Med. Biol.* **53**, 3609–3622 (2008).
  5. Bouchet, A., Serduc, R., Laissue, J. A. & Djonov, V. Effects of microbeam radiation therapy on normal and tumoral blood vessels. *Phys. Medica* **31**, 634–641 (2015).
  6. Zhang, X. *et al.* Therapy-Resistant Cancer Stem Cells Have Differing Sensitivity to Photon versus Proton Beam Radiation. *J. Thorac. Oncol.* **8**, 1484–1491 (2013).
  7. Nikitaki, Z. *et al.* Systemic mechanisms and effects of ionizing radiation: A new ‘old’ paradigm of how the bystanders and distant can become the players. *Semin. Cancer Biol.* **37-38**, 77–95 (2016).
  8. Barretina, J. *et al.* Subtype-specific genomic alterations define new targets for soft-tissue sarcoma therapy. *Nat. Genet.* **42**, 715–721 (2010).
  9. Tesei, A. *et al.* In vitro irradiation system for radiobiological experiments. *Radiat. Oncol.* **8**, 257 (2013).
  10. Bourret, S. *et al.* Fluorescence time-lapse imaging of single cells targeted with a focused scanning charged-particle microbeam. *Nucl. Instruments Methods Phys. Res. Sect. B Beam Interact. with Mater. Atoms* **325**, 27–34 (2014).
  11. Agostinelli, S. *et al.* GEANT4 - A simulation toolkit. *Nucl. Instruments Methods Phys. Res. Sect. A Accel. Spectrometers, Detect. Assoc. Equip.* **506**, 250–303 (2003).
  12. Rhomberg, W. The Radiation Response of Sarcomas by Histologic Subtypes: A Review With Special Emphasis Given to Results Achieved With Razoxane. *Sarcoma* **2006**, 1–9 (2006).
  13. Kim, K. S. *et al.* Radiation-Induced Sarcoma: A 15-Year Experience in a Single Large Tertiary Referral Center. *Cancer Res. Treat.* **48**, 650–657 (2016).
  14. Berrington de Gonzalez, A., Kutsenko, A. & Rajaraman, P. Sarcoma risk after radiation exposure. *Clin. Sarcoma Res.* **2**, 18 (2012).
  15. Cormier, J. N. & Pollock, R. E. Soft Tissue Sarcomas. *CA. Cancer J. Clin.* **54**, 94–109 (2004).
  16. Nielsen, T. O. & West, R. B. Translating gene expression into clinical care: Sarcomas as a paradigm. *J. Clin. Oncol.* **28**, 1796–1805 (2010).
  17. Chibon, F. *et al.* Validated prediction of clinical outcome in sarcomas and multiple types of cancer on the basis of a gene expression signature related to genome complexity. *Nat. Med.* **16**, 781–787 (2010).
  18. Taylor, B. S. *et al.* Advances in sarcoma genomics and new therapeutic targets. *Nat. Rev. Cancer* **11**, 541–57 (2011).
  19. Chibon, F. Cancer gene expression signatures-The rise and fall? *Eur. J. Cancer* **49**, 2000–2009 (2013).
  20. Italiano, A. *et al.* Genetic Profiling Identifies Two Classes of Soft-Tissue Leiomyosarcomas with Distinct Clinical Characteristics. *Clin. Cancer Res.* **19**, 1190–1196 (2013).
  21. Williams, J. R. *et al.* Overview of Radiosensitivity of Human Tumor Cells to Low-Dose-Rate Irradiation. *Int. J. Radiat. Oncol.* **72**, 909–917 (2008).
  22. Mansour, W. Y., Rhein, T. & Dahm-Daphi, J. The alternative end-joining pathway for repair of DNA double-strand breaks requires PARP1 but is not dependent upon microhomologies. *Nucleic Acids Res.* **38**, 6065–6077 (2010).
  23. Constanzo, J. *et al.* Radiograaff, a proton irradiation facility for radiobiological studies at a 4 MV Van de Graaff accelerator. *Nucl. Instruments Methods Phys. Res. Sect. B Beam Interact. with Mater. Atoms* **334**, 52–58 (2014).
  24. Munshi, A., Hobbs, M. & Meyn, R. E. in *Chemosensitivity* **110**, 021–028 (Humana Press, 2005).
  25. Franken, N. A. P., Rodermond, H. M., Stap, J., Haveman, J. & van Bree, C. Clonogenic assay of cells in vitro. *Nat. Protoc.* **1**, 2315–2319 (2006).
  26. Pauwels, B. *et al.* Comparison of the sulforhodamine B assay and the clonogenic assay for in vitro chemoradiation studies. *Cancer Chemother. Pharmacol.* **51**, 221–226 (2003).

27. Buch, K. *et al.* Determination of cell survival after irradiation via clonogenic assay versus multiple MTT Assay - A comparative study. *Radiat. Oncol.* **7**, 1 (2012).
28. Luttjeboer, M. *et al.* Strategies for the analysis of in vitro radiation sensitivity and prediction of interaction with potential radiation modifying agents. *Int. J. Radiat. Biol.* **86**, 458–66 (2010).
29. Quick, Q. A. & Gewirtz, D. A. Enhancement of radiation sensitivity, delay of proliferative recovery after radiation and abrogation of MAPK (p44/42) signaling by imatinib in glioblastoma cells. *Int. J. Oncol.* **29**, 407–12 (2006).
30. Costes, S. V., Chiolo, I., Pluth, J. M., Barcellos-Hoff, M. H. & Jakob, B. Spatiotemporal characterization of ionizing radiation induced DNA damage foci and their relation to chromatin organization. *Mutat. Res. Mutat. Res.* **704**, 78–87 (2010).
31. Kiltie, A. E. *et al.* A correlation between residual DNA double-strand breaks and clonogenic measurements of radiosensitivity in fibroblasts from preradiotherapy cervix cancer patients. *Int. J. Radiat. Oncol.* **39**, 1137–1144 (1997).
32. Rothkamm, K., Kruger, I., Thompson, L. H. & Lobrich, M. Pathways of DNA Double-Strand Break Repair during the Mammalian Cell Cycle. *Mol. Cell. Biol.* **23**, 5706–5715 (2003).
33. Ibañez, I. L. *et al.* Induction and Rejoining of DNA Double Strand Breaks Assessed by H2AX Phosphorylation in Melanoma Cells Irradiated with Proton and Lithium Beams. *Int. J. Radiat. Oncol. Biol. Phys.* **74**, 1226–1235 (2009).
34. Calugaru, V. *et al.* Involvement of the Artemis Protein in the Relative Biological Efficiency Observed With the 76-MeV Proton Beam Used at the Institut Curie Proton Therapy Center in Orsay. *Int. J. Radiat. Oncol.* **90**, 36–43 (2014).
35. Olive, P. L. & Banáth, J. P. Phosphorylation of histone H2AX as a measure of radiosensitivity. *Int. J. Radiat. Oncol.* **58**, 331–335 (2004).
36. Banath, J. P. Radiation Sensitivity, H2AX Phosphorylation, and Kinetics of Repair of DNA Strand Breaks in Irradiated Cervical Cancer Cell Lines. *Cancer Res.* **64**, 7144–7149 (2004).
37. Gobet, F. *et al.* Experimental and Monte Carlo absolute characterization of a medical electron beam using a magnetic spectrometer. *Radiat. Meas.* **86**, 16–23 (2016).
38. Barberet, P. *et al.* Monte-Carlo dosimetry on a realistic cell monolayer geometry exposed to alpha particles. *Phys. Med. Biol.* **57**, 2189–2207 (2012).
39. Pomp, J. *et al.* Cell density dependent plating efficiency affects outcome and interpretation of colony forming assays. *Radiother. Oncol.* **40**, 121–125 (1996).
40. Petrini, J. The cellular response to DNA double-strand breaks: defining the sensors and mediators. *Trends Cell Biol.* **13**, 458–462 (2003).
41. Burma, S. ATM Phosphorylates Histone H2AX in Response to DNA Double-strand Breaks. *J. Biol. Chem.* **276**, 42462–42467 (2001).
42. Bakkenist, C. J. & Kastan, M. B. DNA damage activates ATM through intermolecular autophosphorylation and dimer dissociation. *Nature* **421**, 499–506 (2003).
43. Costes, S. V *et al.* Imaging features that discriminate between foci induced by high- and low-LET radiation in human fibroblasts. *Radiat. Res.* **165**, 505–515 (2006).
44. Reitsema, T. J., Banáth, J. P., MacPhail, S. H. & Olive, P. L. Hypertonic saline enhances expression of phosphorylated histone H2AX after irradiation. *Radiat. Res.* **161**, 402–408 (2004).
45. Williams, J. R., Zhang, Y., Russell, J., Koch, C. & Little, J. B. Human tumor cells segregate into radiosensitivity groups that associate with ATM and TP53 status. *Acta Oncol. (Madr)*. **46**, 628–638 (2007).
46. Lavaf, A., Kao, J. & Peters, S. ATM Phosphorylation Kinetics as a Biological Reporter of Cellular Radiosensitivity. *Int. J. Radiat. Oncol.* **69**, S65–S66 (2007).
47. McManus, K. J. & Hendzel, M. J. ATM-dependent DNA Damage-independent Mitotic Phosphorylation of H2AX in Normally Growing Mammalian Cells. *Mol. Biol. Cell* **16**, 5013–5025 (2005).
48. Grutters, J. P. C. *et al.* Comparison of the effectiveness of radiotherapy with photons, protons and carbon-ions for non-small cell lung cancer: A meta-analysis. *Radiother. Oncol.* **95**, 32–40 (2010).
49. Green, L. M. *et al.* Response of Thyroid Follicular Cells to Gamma Irradiation Compared to Proton Irradiation. I. Initial Characterization of DNA Damage, Micronucleus Formation,

50. Apoptosis, Cell Survival, and Cell Cycle Phase Redistribution. *Radiat. Res.* **155**, 32–42 (2001).
51. Prise, K. M. & Schettino, G. Microbeams in radiation biology: review and critical comparison. *Radiat. Prot. Dosimetry* **143**, 335–339 (2011).
52. Zlobinskaya, O. *et al.* Reduced side effects by proton microchannel radiotherapy: study in a human skin model. *Radiat. Environ. Biophys.* **52**, 123–133 (2013).
53. Girst, S. *et al.* Subdiffusion supports joining of correct ends during repair of DNA double-strand breaks. *Sci. Rep.* **3**, 2511 (2013).
54. Schmid, T. E. *et al.* Low LET protons focused to submicrometer shows enhanced radiobiological effectiveness. *Phys. Med. Biol.* **57**, 5889–5907 (2012).
55. Taneja, N. *et al.* Histone H2AX Phosphorylation as a Predictor of Radiosensitivity and Target for Radiotherapy. *J. Biol. Chem.* **279**, 2273–2280 (2004).
56. Goodarzi, A. A. & Jeggo, P. A. Irradiation induced foci (IRIF) as a biomarker for radiosensitivity. *Mutat. Res. Mol. Mech. Mutagen.* **736**, 39–47 (2012).
57. Pawlik, T. M. & Keyomarsi, K. Role of cell cycle in mediating sensitivity to radiotherapy. *Int. J. Radiat. Oncol.* **59**, 928–942 (2004).
58. Bennett, B. T., Bewersdorf, J. & Knight, K. L. Immunofluorescence imaging of DNA damage response proteins: Optimizing protocols for super-resolution microscopy. *Methods* **48**, 63–71 (2009).

### Acknowledgements

The AIFIRA facility and the microbeam line have been financially supported by the Region Aquitaine (IOPRA, POPRA). MS is supported by the Region Aquitaine (POPRA). We would kindly thank Frédéric Chibon for its patient's sarcoma cell lines (IB115 and IB106). This work has been partly supported by the European Community as an Integrating Activity “Support of Public and Industrial Research Using Ion Beam Technology” (SPIRIT) under the EC contract n° 227012. GM is supported by the European Community as an “Integrating Activity Supporting Postgraduate Research with Internships in Industry and Training Excellence” (SPRITE) under EC contract no. 317169. BNCD membrane development was supported by the French national centre for scientific research (CNRS, Mission Interdisciplinaire).

### Author Contributions

GM and MS planned, performed the experiments and wrote the manuscript; PB and MA performed irradiations, dosimetry measurements and simulations; HS conceived and supervised this project; GK is POPRA coordinator and permits the access to the Clinac facility; FC provides the IB115 and IB106 cell lines; MG, MS, GD, PB and HS contributed to the data analysis and interpret the results; all authors review the manuscript.

### Additional information

Supplementary information accompanies this paper

**Competing financial interests.** The authors declare no competing financial interests.

## Supplementary Methods and Materials

### Material S1: Cell lines and characterization

#### IB115 and IB106 characterization

The *IB115* cell line was obtained from a dedifferentiated liposarcoma of a para-testicular tumor after surgery at the Institut Bergonié. This sarcoma cell line has a simple genetic profile based on many known limited amplifications of the *MDM2/CDK4* genes on the chromosome 12q15. The *IB115* genomic stability over time has been evaluated over 50 passages. The Comparative Genomic Hybridization (CGH) profile remains unmodified, as shown by the overlap of two CGH profiles after 30 and 50 passages of culture underlying the genomic high-stability of *IB115* line (Figure S1a).

The *IB106* cell line is an unclassified sarcoma from paravertebral mass with heterogenic pleomorphic cells. This cell line is considered having a complex genetics, and the highly genetic stability over time is depicted by the overlap of the blue and red CGH profiles obtained at passages 30 and 50, as shown in Figure S1b.

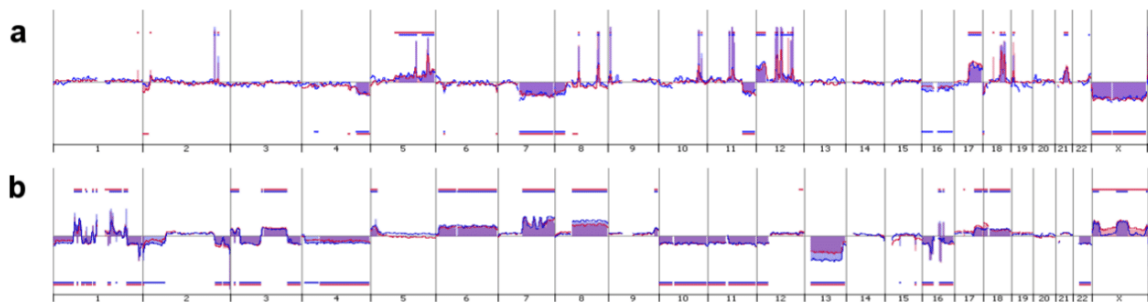


**Fig. S1. CGH profiles of *IB115* and *IB106* show a highly genomic stability.** (a) The *IB115* profile shows the characteristic alterations of dedifferentiated liposarcoma with amplifications (vertical peaks pointing upwards) and some localized deletions (areas under the midline). Localized known amplifications of *MDM2* and *CDK4* genes on the chromosome 12q15 are typically found in the liposarcomas. The superposition of CGH profiles of *IB115* cells at passages 30 (blue) and 50 (red) showed the genomic stability over time [P. Lagarde et al., CTOS poster 2010]. (b) The *IB106* profile shows alterations of this unclassified sarcoma. Many more amplifications (vertical peaks pointing upwards) and deletions (areas under the midline) are present in this cell line, with respect to *IB115*. All these alterations define the complex genetics of this tumor. CGH profiles at passages 30 and 50 showed the stability of this cell line.

## Material S2: Irradiation systems

### Solid state track detectors

To ensure the reliability of the dose distribution as well as the total irradiated area with proton beams, CR39 solid state track detectors were irradiated following a mosaic of 9 x 12 fields, to cover an area of 6.2 x 6.2 mm. CR39 slabs were positioned at the position of the cell monolayer at a distance of 250  $\mu\text{m}$  from the beam exit window. After irradiation, CR39 were etched in concentrated KOH (12 M, at 80 °C) for 3 min. Irradiated patterns were imaged using phase contrast imaging with a Zeiss AxioObserver Z1 microscope (CarlZeiss MicroImaging, GmbH).

### Protons micro and broad beam irradiations

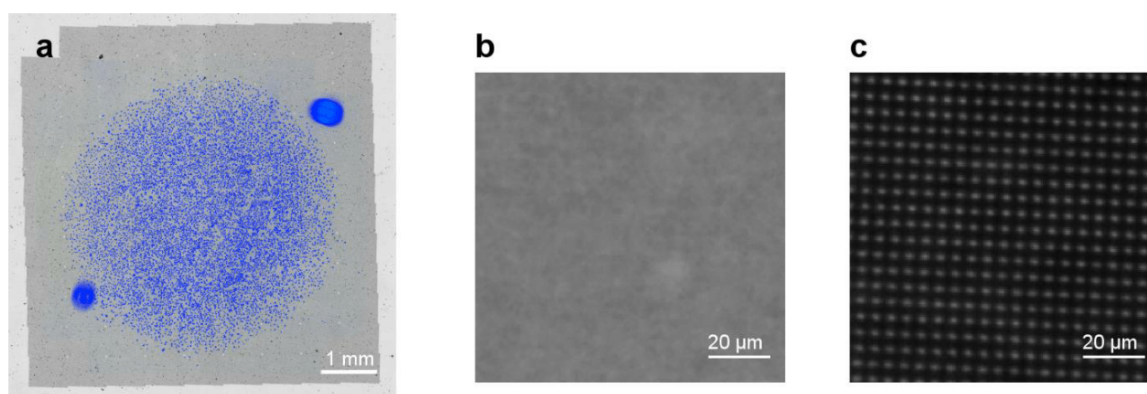


**Fig. S2. Protons micro and broad beam irradiations.** (a) Merge of a CR39 post irradiation and *IB115* monolayer. A total area of 6.2 x 6.2 mm<sup>2</sup> is irradiated with a focused or broad beams. The gray square is the irradiated area, obtained after irradiation of a CR39 Solid State Nuclear Track Detector. In blue 10000 cell nuclei are stained with Hoechst<sup>33342</sup> and merged with the CR39 image to show the irradiated area by comparison with the area where cells were seeded. (b and c) Proton broad beam and proton microbeam patterns shown on YAG:Ce scintillators.

### Material S3: Cell surviving fraction

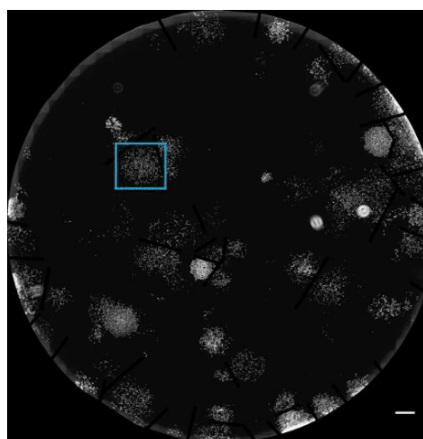
#### Development of an automated acquisition and ImageJ macro for colonies counting

A custom-made routine ImageJ for automatically colonies counting was developed to avoid human errors. The macro is detailed in Table S1. An automated acquisition of the whole well was obtained with an epifluorescence microscope (Carl Zeiss MicroImaging, GmbH) equipped with a 10X objective. A picture for each microscope field ( $877 \times 670 \mu\text{m}^2$ ) was taken following a mosaic of 856 fields. This corresponds to the total size of well. The image was stitched to obtain the whole well image (Step A). The intensity threshold was manually defined to detect single cells and a filter was set to identify each colony (Step B). Subsequently, colonies were scanned using the ImageJ macro and for each colony the number of cells was counted (Step C).

#### STEP A

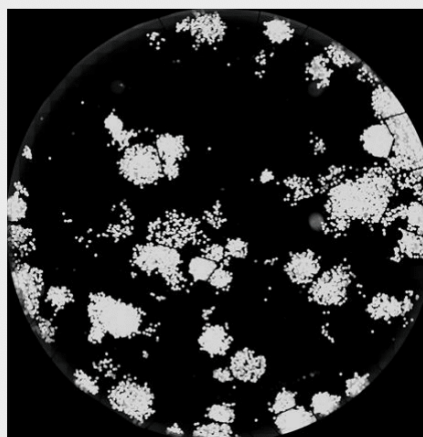
- Mosaic acquisition of 856 fields by an epifluorescence microscope
- Reconstruction of the whole well picture by stitching all images
- Image conversion into a 8-bit image using imageJ software

Scale bar: 1000  $\mu\text{m}$



#### Step B

- Application of a filter for each cell. Filter does gray scale dilatation by replacing each pixel in the image with the largest pixel value in that pixel's neighborhood. In this way cells in each colonies are fused and colonies can be identified
- Identification of each colony by setting a manual intensity threshold

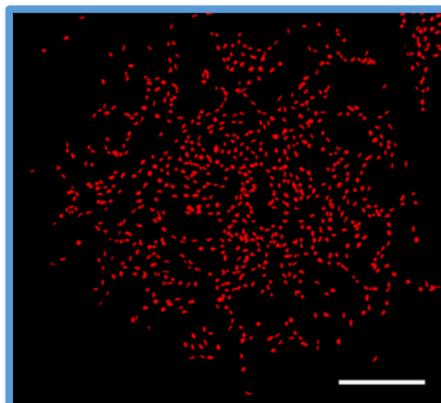




---

**Step C**

- The whole dish is scanned and all colonies are detected and numbered
- To illustrate the following steps the colony selected in the blue square is enlarged
- Single cells are recognized by analyzing particles with a size ranging from 100 to 2500 pixels
- For each colony a list file containing the number of colonies and the number of cells per colonies which is saved in the defined folder is created.



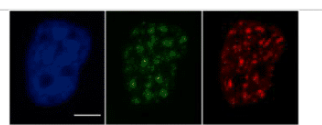
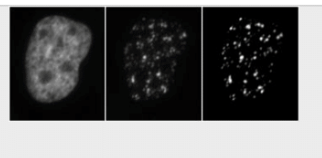
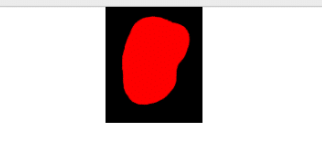
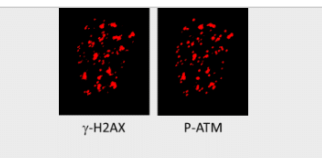
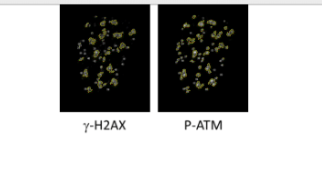
Scale bar: 500  $\mu\text{m}$

---

**Table S1.** Custom-made colonies counter routine

**Material S4: Immuno-detection**Development of an automated acquisition and ImageJ macro for IRIF counting

Pictures through various filters were taken serially for different dyes: Hoechst<sup>33342</sup>, AlexaFluor<sup>488</sup> and AlexaFluor<sup>594</sup>. Z-stacks of at least 15 slices were taken from each sample, to cover all the nuclear volume. Images were processed using Image-J software and the total number of  $\gamma$ H2AX and P-ATM IRIF per cell was determined using a custom-made macro in ImageJ (Table S2). Series of images of three channels were imported (Step A) and converted to 8-bit format (Step B). The intensity threshold was manually adjusted to recognize nuclei in the focal plan of Hoechst channel (Step C) and each nucleus was numbered. A Z-stack projection was applied for  $\gamma$ H2AX and P-ATM channels. Then, the image with the highest fluorescence intensity (6 Gy irradiated cells) was used to select the threshold gray value to visualize IRIF in both channels,  $\gamma$ H2AX and P-ATM. The intensity threshold was applied to all images for IRIF counting (Step D). Minimum and maximum IRIF sizes of  $0.100 \mu\text{m}^2$  and  $200 \mu\text{m}^2$ , respectively, were fixed (Step E). Data analysis provides the number of IRIF per nucleus (Step F).

<b>Step A</b> Open an image with three channels corresponding to nucleus (blue), $\gamma$ H2AX (green) and P-ATM (red) using ImageJ. Scale bar: $10 \mu\text{m}$	
<b>Step B</b> Convert the image in 8-bit format.	
<b>Step C</b> Select the first channel (Hoechst): manually select intensity threshold to identify cell nucleus. In this way, all cell nuclei are recognized and numbered.	
<b>Step D</b> Select the second and third channels ( $\gamma$ H2AX and P-ATM, respectively): manually select intensity threshold to define each focus. Used these two values for all images treatment.	
<b>Step E</b> Define the minimum and maximum size of IRIF: min $0.100 \mu\text{m}^2$ and max $200 \mu\text{m}^2$ . Starts the foci counting in each nucleus for the two channels.	
<b>Step F</b> A listing with all IRIF in each nucleus is created.	

**Table S2.** Schematization of custom-made macro for IRIF counting

## Supplementary Results

Cell lines	N of cells seeded	Mean colonies number	Plating Efficiency	N wells analyzed
<i>IB115</i>	500	62.9 ± 6.67	12.4	10
	200	32.77 ± 4.7	16	18
<i>IB106</i>	1000	100 ± 8.6	10	6
	600	12.25 ± 3.7	2.04	8

**Table S3.** *IB115* relative Plating Efficiency is not significantly affected by the initial number of seeded cell. In *IB106*, the variation in the number of cells seeded influences negatively the Plating Efficiency.

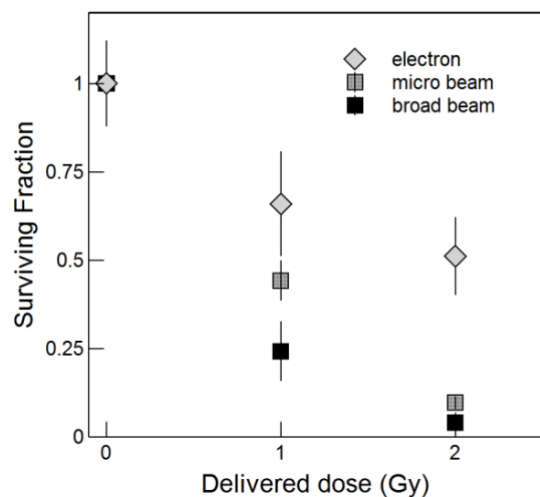


**Fig. S3.** *IB115* survival fraction is dose- and IR-dependent and particle distribution-dependent at 1 Gy. The cell capability of forming colonies is observed after irradiations with different doses of electrons, proton microbeam and proton broad beam. The error bars represent the SD of the mean of four replicates of two independent experiments.

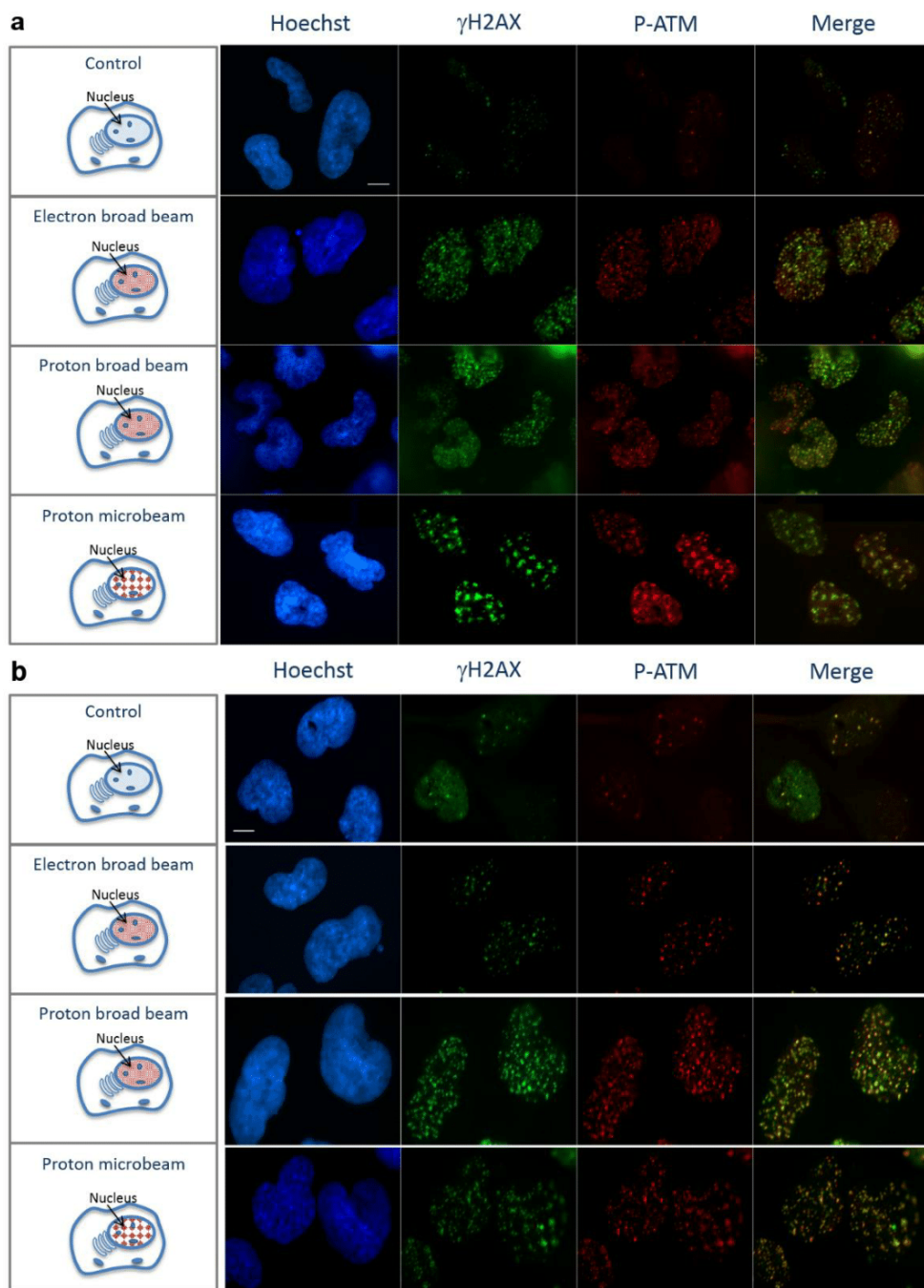


**Fig. S4.  $\gamma$ H2AX and P-ATM IRIF in *IB115* after electron and proton irradiations.** (a) Immunodetection 2 h after 6 Gy irradiations. Control cells show a weak presence of foci in the cell nuclei. Cells irradiated with electron and proton broad beams display a homogeneous IRIF distribution. In cells irradiated with proton microbeam, the IRIF distribution reflects the regular irradiation pattern. (b) Immunodetection 20 h after 6 Gy irradiations. The presence of foci in control cells remains stable. In cells irradiated with electrons the number of IRIF appears decreased and their size increased in comparison to 2 h post-irradiated cells. After broad proton beam, the IRIF number remains stable in comparison to cells analyzed 2 h after irradiation. After proton microbeam, the irradiation pattern is not distinguishable; smaller foci appear in the nuclei compared to 2 h irradiated cells. Scale bar: 10  $\mu$ m.

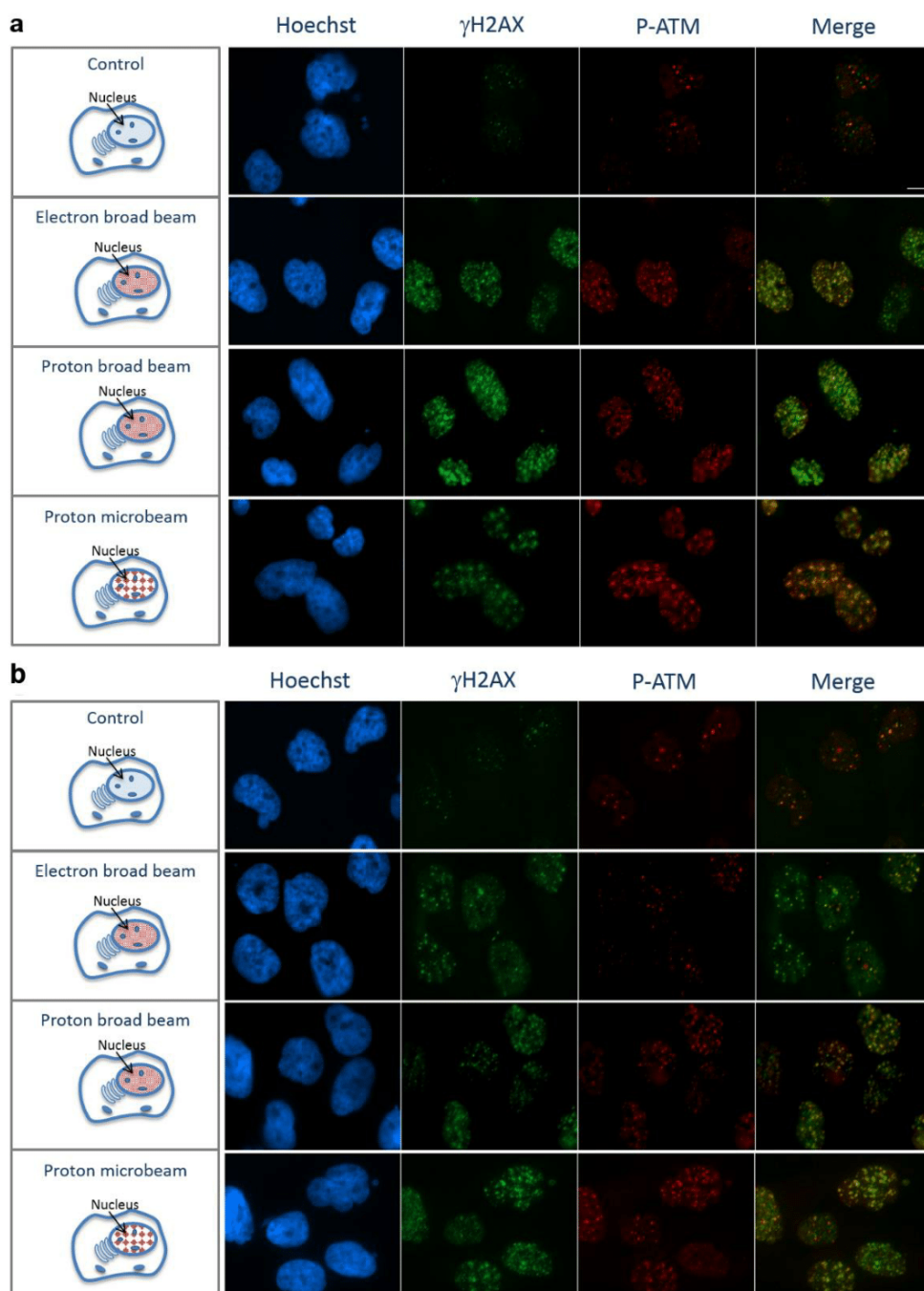


**Fig. S5.  $\gamma$ H2AX and P-ATM IRIF in *IB106* cells after electron and proton irradiations.** Immunodetection 2 h (a) and 20 h (b) after 6 Gy irradiations. Control cells show low foci presence in the nucleus for both phosphorylated H2AX and ATM at both time after irradiation. 2 h after irradiation, cells irradiated with electron and proton broad beams show homogeneous and comparable IRIF distributions. In cells irradiated with proton microbeam, the IRIF distribution reflects the regular pattern of irradiation. 20 h after irradiation, cells irradiated with electrons and broad proton beam showed a lower presence of IRIF compared to 2 h irradiated cells. 20 h after proton micro beam irradiation, the irradiation pattern is still distinguishable in the most of cells. Scale bar 10  $\mu$ m.

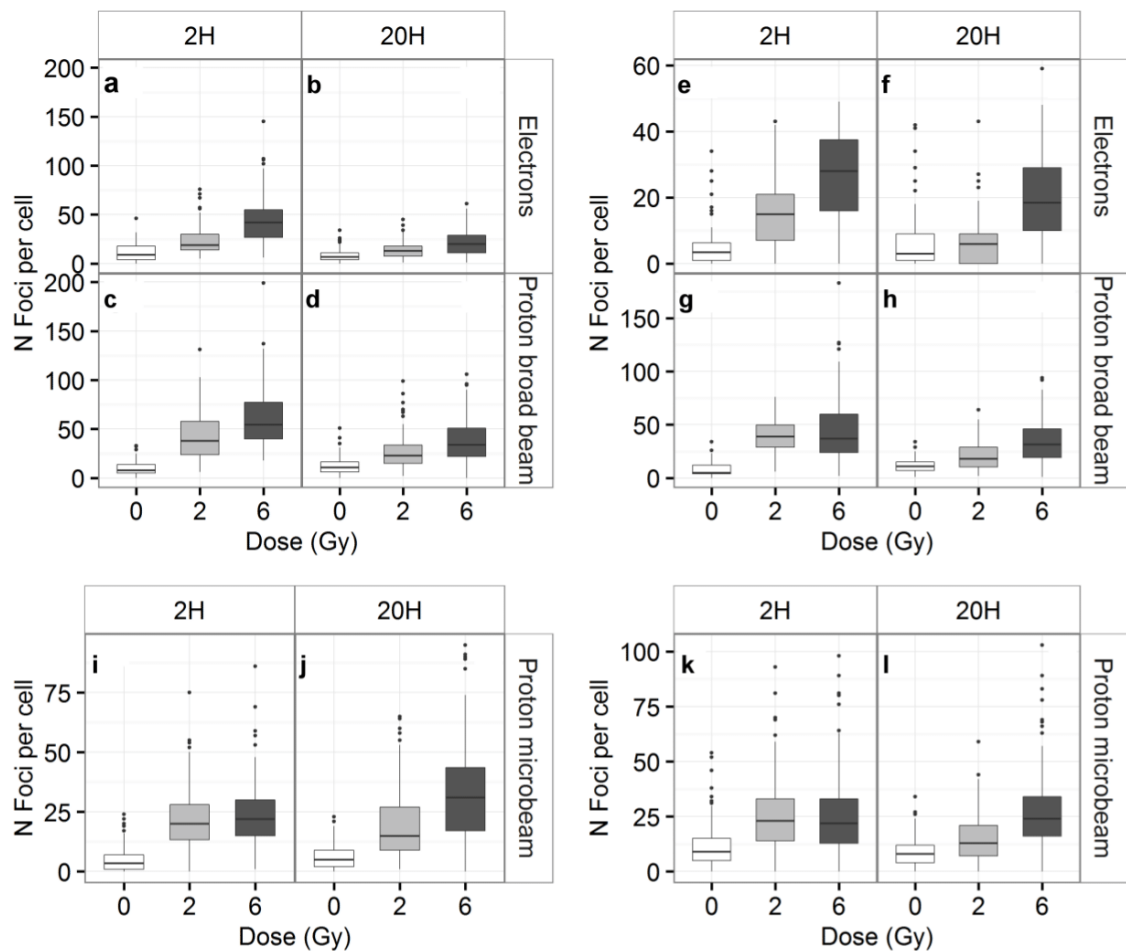


**Fig. S6. Quantification of P-ATM IRIF in *IB115* and *IB106*.** The number of IRIF observed in *IB115* after electrons (a) 2 h and (b) 20 h after irradiation is dependent on the dose delivered, and a decrease of the IRIF number over time is observed. (c) 2 h after protons broad beam the IRIF number increases in a dose-dependent manner, and (d) 20 h after irradiation remains more elevated with respect to electrons irradiated cells. (i and j) IRIF number after proton microbeam in *IB115*. The number of IRIF observed 2 h after irradiation reflects the irradiation pattern hence not differences are observed between 2 and 6 Gy irradiated cells. 20 h after irradiation an increment of IRIF is observed. Chromatin movements contribute to their fragmentation in smaller foci.

In *IB106*, the IRIF number observed after electrons (e) 2 h and (f) 20 h after irradiation is dependent on the dose delivered, with a decrease of the IRIF number over time. (g) 2 h after protons broad beam the number of IRIF increases as a function of the dose, and (h) 20 h after irradiation the IRIF number decreases. (k) 2 h after proton microbeam irradiation, the IRIF number observed reflects the irradiation pattern hence not differences are observed between 2 and 6 Gy irradiated cells. (l) 20 h after proton microbeam irradiation the IRIF number is not considerably changed.

## Bibliography

1. WHO. Global status report on noncommunicable diseases 2014. *World Health* 176 (2014). doi:ISBN 9789241564854
2. Hall, E. J. intensity-modulated radiation therapy, protons, and the risk of second cancers (Int J Radiat Oncol Biol Phys 2006;65:1-7). *Int. J. Radiat. Oncol. Biol. Phys.* **66**, 1593–4; author reply 1595 (2006).
3. Durante, M. & Cucinotta, F. a. Heavy ion carcinogenesis and human space exploration. *Nat. Rev. Cancer* **8**, 465–472 (2008).
4. Casali, P. G. & Blay, J. Y. Soft tissue sarcomas: ESMO clinical practice guidelines for diagnosis, treatment and follow-up. *Ann. Oncol.* **21**, 198–203 (2010).
5. Burningham, Z., Hashibe, M., Spector, L. & Schiffman, J. D. The Epidemiology of Sarcoma. 1–16 (2012).
6. C.D.M. Fletcher, K. Unni, F. M. World Health Organization Classification of Tumours Pathology and Genetics of Tumours of Soft Tissue and Bone. *Cancer* **177**, 1365–76 (2002).
7. Nielsen, T. O. & West, R. B. Translating gene expression into clinical care: Sarcomas as a paradigm. *J. Clin. Oncol.* **28**, 1796–1805 (2010).
8. Helman, L. J. & Meltzer, P. Mechanisms of sarcoma development. *Nat. Rev. Cancer* **3**, 685–694 (2003).
9. Berrington de Gonzalez, A., Kutsenko, A. & Rajaraman, P. Sarcoma risk after radiation exposure. *Clin. Sarcoma Res.* **2**, 18 (2012).
10. Patel, S. R. Radiation-induced sarcoma. *Curr. Treat. Options Oncol.* **1**, 258–61 (2000).
11. Mocellin, S., Rossi, C. R., Brandes, A. & Nitti, D. Adult soft tissue sarcomas: Conventional therapies and molecularly targeted approaches. *Cancer Treat. Rev.* **32**, 9–27 (2006).
12. Cormier, J. N. & Pollock, R. E. Soft Tissue Sarcomas. *CA. Cancer J. Clin.* **54**, 94–109 (2004).
13. Rhombert, W. The Radiation Response of Sarcomas by Histologic Subtypes: A Review With Special Emphasis Given to Results Achieved With Razoxane. *Sarcoma* **2006**, 1–9 (2006).
14. McGovern, S. L. & Mahajan, A. Progress in Radiotherapy for Pediatric Sarcomas. *Curr. Oncol. Rep.* **14**, 320–326 (2012).
15. DeLaney, T. F. & Haas, R. L. M. Innovative radiotherapy of sarcoma: Proton beam radiation. *Eur. J. Cancer* **62**, 112–123 (2016).
16. Yoon, S. S. *et al.* Proton-beam, intensity-modulated, and/or intraoperative electron radiation therapy combined with aggressive anterior surgical resection for retroperitoneal sarcomas. *Ann. Surg. Oncol.* **17**, 1515–29 (2010).
17. Tubiana, M., Feinendegen, L. E., Yang, C. & Kaminski, J. M. Linear No-Threshold Relationship Is Inconsistent with Radiation Biologic and Experimental Data. *Radiology* **251**, 13–22 (2009).
18. DeVita V., Hellman S., R. S. Cancer: principles and practice of oncology. (2001).
19. Alsbeih, G., Story, M. D., Maor, M. H., Geara, F. B. & Brock, W. A. Chromosomal fragility syndrome and family history of radiosensitivity as indicators for radiotherapy dose modification. *Radiother. Oncol.* **66**, 341–344 (2003).
20. Dahl, O., Horn, A. & Mella, O. Do Acute Side-Effects During Radiotherapy Predict Tumour Response in Rectal Carcinoma? *Acta Oncol. (Madr)*. **33**, 409–413 (1994).
21. Barker, H. E., Paget, J. T. E., Khan, A. A. & Harrington, K. J. The tumour microenvironment after radiotherapy: mechanisms of resistance and recurrence. *Nat. Rev. Cancer* **15**, 409–425 (2015).
22. Fleet, A. Radiobiology for the Radiologist: 6th edition, Eric J. Hall, Amato J. Giaccia, Lippincott Williams and Wilkins Publishing; ISBN 0-7817-4151-3; 656 pages; 2006; Hardback; £53. *J. Radiother. Pract.* **5**, 237 (2006).
23. Safwat, A., Bentzen, S. M., Turesson, I. & Hendry, J. H. Deterministic rather than stochastic

- factors explain most of the variation in the expression of skin telangiectasia after radiotherapy. *Int. J. Radiat. Oncol. Biol. Phys.* **52**, 198–204 (2002).
24. Cline, S. D. & Hanawalt, P. C. Who's on first in the cellular response to DNA damage? *Nat. Rev. Mol. Cell Biol.* **4**, 361–373 (2003).
  25. DIKOMEY J. DAHM-DAPHI I. BRAMMER R., E. Correlation between cellular radiosensitivity and non-repaired double-strand breaks studied in nine mammalian cell lines. *Int. J. Radiat. Biol.* **73**, 269–278 (1998).
  26. Obe, G. *et al.* Chromosomal aberrations: Formation, identification and distribution. *Mutat. Res. - Fundam. Mol. Mech. Mutagen.* **504**, 17–36 (2002).
  27. Schar, P. Spontaneous DNA damage, genome instability, and cancer--when DNA replication escapes control. *Cell* **104**, 329–332 (2001).
  28. Joubert, A. *et al.* DNA double-strand break repair defects in syndromes associated with acute radiation response: at least two different assays to predict intrinsic radiosensitivity? *Int. J. Radiat. Biol.* **84**, 107–25 (2008).
  29. Drexler, G. A. & Ruiz-Gómez, M. J. Microirradiation techniques in radiobiological research. *J. Biosci.* **40**, 629–643 (2015).
  30. Prise, K. M. & Schettino, G. Microbeams in radiation biology: review and critical comparison. *Radiat. Prot. Dosimetry* **143**, 335–339 (2011).
  31. Schettino, G., Al Rashid, S. T. & Prise, K. M. Radiation microbeams as spatial and temporal probes of subcellular and tissue response. *Mutat. Res. - Rev. Mutat. Res.* **704**, 68–77 (2010).
  32. Funayama, T., Hamada, N., Sakashita, T. & Kobayashi, Y. Heavy-Ion Microbeams - Development and Applications in Biological Studies. *IEEE Trans. Plasma Sci.* **36**, 1432–1440 (2008).
  33. Barberet, P. & Seznec, H. Advances in microbeam technologies and applications to radiation biology. *Radiat. Prot. Dosimetry* **166**, 182–187 (2015).
  34. Bigelow, A. *et al.* Expanding the question-answering potential of single-cell microbeams at RARAF, USA. *J. Radiat. Res.* **50 Suppl A**, A21–8 (2009).
  35. Prise, K. M. *et al.* Investigating the cellular effects of isolated radiation tracks using microbeam techniques. *Adv. Sp. Res.* **30**, 871–876 (2002).
  36. Durante, M. & Friedl, A. a. New challenges in radiobiology research with microbeams. *Radiat. Environ. Biophys.* **50**, 335–8 (2011).
  37. Schmid, T. E. *et al.* Relative biological effectiveness of pulsed and continuous 20MeV protons for micronucleus induction in 3D human reconstructed skin tissue. *Radiother. Oncol.* **95**, 66–72 (2010).
  38. Auer, S. *et al.* Survival of tumor cells after proton irradiation with ultra-high dose rates. *Radiat. Oncol.* **6**, 139 (2011).
  39. Greubel, C. *et al.* Scanning irradiation device for mice in vivo with pulsed and continuous proton beams. *Radiat. Environ. Biophys.* **50**, 339–344 (2011).
  40. Slatkin, D. N., Spanne, P., Dilmanian, F. A. & Sandborg, M. Microbeam radiation therapy. *Med. Phys.* **19**, 1395–1400 (1992).
  41. van der Sanden, B. *et al.* Tolerance of Arteries to Microplanar X-Ray Beams. *Int. J. Radiat. Oncol.* **77**, 1545–1552 (2010).
  42. Sabatasso, S. *et al.* Microbeam Radiation-Induced Tissue Damage Depends on the Stage of Vascular Maturation. *Int. J. Radiat. Oncol.* **80**, 1522–1532 (2011).
  43. Friedland, W., Kundrát, P. & Schmitt, E. Modelling proton bunches focussed to submicrometre scales: low-LET radiation damage in high-LET-like spatial structure. *Radiat. Prot. Dosimetry* **166**, 34–37 (2015).
  44. Schmid, T. E. *et al.* Low LET protons focused to submicrometer shows enhanced radiobiological effectiveness. *Phys. Med. Biol.* **57**, 5889–5907 (2012).
  45. Schrock, E. *et al.* Multicolor Spectral Karyotyping of Human Chromosomes. *Science* (80- ).



- 273**, 494–497 (1996).
46. Geigl, J. B., Uhrig, S. & Speicher, M. R. Multiplex-fluorescence in situ hybridization for chromosome karyotyping. *Nat. Protoc.* **1**, 1172–1184 (2006).
  47. Pinkel, D. *et al.* High resolution analysis of DNA copy number variation using comparative genomic hybridization to microarrays. *Nat. Genet.* **20**, 207–211 (1998).
  48. Jeggo, P. & Lavin, M. F. Cellular radiosensitivity: how much better do we understand it? *Int. J. Radiat. Biol.* **85**, 1061–1081 (2009).
  49. Eschrich, S. *et al.* Systems Biology Modeling of the Radiation Sensitivity Network: A Biomarker Discovery Platform. *Int. J. Radiat. Oncol. Biol. Phys.* **75**, 497–505 (2009).
  50. Oh, J. H., Wong, H. P., Wang, X. & Deasy, J. O. A bioinformatics filtering strategy for identifying radiation response biomarker candidates. *PLoS One* **7**, 1–17 (2012).
  51. Good, J. S. & Harrington, K. J. The hallmarks of cancer and the radiation oncologist: Updating the 5Rs of radiobiology. *Clin. Oncol.* **25**, 569–577 (2013).
  52. Sokolov, M. V., Panyutin, I. V., Panyutin, I. G. & Neumann, R. D. Dynamics of the transcriptome response of cultured human embryonic stem cells to ionizing radiation exposure. *Mutat. Res. Mol. Mech. Mutagen.* **709-710**, 40–48 (2011).
  53. Young, A. *et al.* RNA-seq profiling of a radiation resistant and radiation sensitive prostate cancer cell line highlights opposing regulation of DNA repair and targets for radiosensitization. *BMC Cancer* **14**, 808 (2014).

## **PART III**

***In situ and in cellulo* detection and  
quantification of metal oxide  
nanoparticles. Toward the elucidation of  
nanotoxicity mechanisms and  
perspectives for cancer therapy**



Strategy to optimize radiation therapy relies on increasing the dose ratio between the tumor and the surrounding tissues to kill cancerous cells while minimizing the risk of secondary radiation-induced effects in healthy cells. Thus, the use of radiation enhancement with metal oxide nanoparticles (NPs) is a promising strategy to both improve cancer treatment and reduce associated radiation side effects. Increased radiation effects induced by the presence of intracellular high atomic number (Z) NPs is due to early stage physical processes that take place in cells around NPs. Nevertheless, the relation between the biological effects and the delivered dose is not fully understood at present. In addition, nanomaterials are used in diverse fields including food, cosmetic, and medical industries. However, the risks for their adverse health effects have not been clearly established. A better understanding of the *in vitro* interactions of NPs with biological systems is mandatory and requires a multidisciplinary approach covering chemical, physical, and biological aspects.

The AIFIRA platform at the CENBG allows not only the selective irradiation of a target with controlled doses of ionizing radiations (microbeam) but also allows *in vitro* quantification and localization of subcellular chemical elements at the single cell level (microprobe). This equipment represents a major resource to localize and quantify nanoparticles in both single cells and cell population. In particular, the iRIBio team has gained long-standing experience about titanium dioxide nanoparticles (TiO<sub>2</sub> NPs). These NPs are widely used for a wide variety of applications and are produced in diverse shapes, but it remains largely unknown how their modifications may alter bioavailability, biological effects and *in vitro* and *in vivo* toxicity.

There is a real need for the development of analytical methods able to *in situ* detect and quantify NPs, whatever their size, nature, and surface reactivity and whether they are native or functionalized. For this purpose, diverse TiO<sub>2</sub> NPs are synthesized, an approach based on correlative microscopies (fluorescence microscopy and ion beam analysis) is developed, and their effects on the cellular homeostasis responses are investigated.

This third part of this PhD thesis is divided in three sections: *Background*, which firstly describes the use of nanoparticles in nanomedicine with a particular regard to TiO<sub>2</sub> NPs and secondly the microprobe line of CENBG which allows the detection of NPs in biological systems; *Experimental Results* are summarized in two articles which present the protocols employed and NPs exposure consequences in cells. Finally, *Discussion and Perspectives* illustrate the impact of these researches and the future directions associated to these works.

# Background

## Chapter 1

### *Nanoparticles in nanomedicine*

The use of nanoparticles for biomedical applications is prevalent in the literature and continues to be a rapidly growing research field, with heavy emphasis on imaging and drug delivery. Nanomaterials and nanoparticles (NPs) are generally defined as any particulate material for which at least one dimension lies in the range of 1-100 nm<sup>1</sup>. NPs can exist in various shapes and sizes. The various chemical process that guide the synthesis of materials at the nanometer scale can be defined as nanochemistry, which play a critical role in tailoring the physical and chemical proprieties of NPs. For their unique mechanical, thermal, electrical, magnetic and optical properties, NPs are suitable for a wide range of applications, ranging from electronics, to energy storage, to communications, to biology and to medicine<sup>2</sup>.

Nanomedicine is the application of NPs in medicine and NPs intended for medical use have drawn inspiration from the various 'natural' nanoparticles discovered in the body. These include various nanosized vesicles, lipids, proteins, and complex biomacromolecules that regulate the natural functioning in the body, and may act as carries of active molecules. Alongside, an increasing awareness about novel medical applications of smaller, inorganic-based NPs, processing unique properties at the nanoscale, has led to a burst of research activities in the development of 'nanoprobes' for diagnostic medicine and agents for novel, externally activated therapies<sup>3,4</sup>.

Nanocarriers are the most common application because they have several key advantages over conventional molecular agents in medicine. They enable stable aqueous dispersions of active, but poorly water soluble molecular agents, for delivery in the biological medium. Their composition, size, shape and surface proprieties can protect the encapsulated agents from degradation by various endogenous defense mechanisms. Control of their structure allows them to be targeted to not only specifics organs/tissues in the body, but even with cellular and subcellular specificity<sup>3,5,6</sup>.

NPs are also commonly used to perform biomedical imaging. A nanoparticle platform provides optical, magnetic, and radioactive functionalities to enhance contrast in various imaging methods for early detection, screening, diagnosis, and image-guided treatment of life-threatening diseases and cancer<sup>3,5</sup>.

*Nanoparticles in radiation therapy.* Recent advances in nanochemistry have paved the way for new strategies for the development of efficient sensitizers to enhance the biological effects of X-irradiations. It is known that X-Rays and photons deposit most of their energy through secondary electrons that are generated by photoelectric or Compton effects. In principle, loading the tumor with high-Z materials could result in a greater photoelectric absorption or Compton effect, when keV or MeV energy photons are delivered, respectively, within the tumor itself and in the surrounding tissues, and thereby enhance the dose delivered to a tumor during radiation therapy<sup>7,8</sup>. The nanoparticles enhanced-dose effect need to be estimated *via* dosimetry systems, such as Monte Carlo simulations and electron spin resonance<sup>9,10</sup>. In pioneering studies, several groups demonstrated that high atomic number materials, such as Iodine, have radiosensitizing effects on cultured cells<sup>11,12</sup>. Then, several studies – including *in vitro* and *in vivo* experiments – investigated gold nanoparticles (AuNPs)<sup>8,13,14</sup>, as well as hafnium (HfNPs)<sup>15,16</sup> and titanium (TiNPs)<sup>17</sup> nanoparticles effects, to improve the radiation therapy effectiveness. Dose enhancement obtained by combining ionizing radiations and high-Z NPs has been simulated and showed by numerous *in silico* and *in vitro* studies<sup>9,18,19</sup>. These studies concluded that the increased density of ionization is significantly localized and occurred in short distances from the nanoparticles<sup>7-10,19,16,20</sup>. So an important factor, affecting the sensitizing properties, is the localization of nanoparticles, because the energy deposition occurs very close to the irradiated nanoparticles. It has generally been believed that localization in the nucleus gives a higher sensitization, however different studies show a localization of the nanoparticles only in the cytoplasm not in the cell nucleus<sup>21-23</sup>. Although nanoparticles may not be incorporated into cell nuclei, they could contribute to the cell killing by attacking cytoplasmic targets. Quantifying and localizing the amount of nanoparticles at the single cell level is a challenge that is being pursued in various laboratories worldwide.

While the promises of nanomaterials in medicine are numerous, it is also worthwhile to consider possible risks associated with their interactions with biological systems. Ideally, once delivered in the body for a particular medical intent, NPs should perform their desired function and exit from body without causing any deleterious effect. In reality, a number of investigations, ranging from simple *in vitro* analyses to clinical observations, have revealed that many NPs exhibit minor to major

hazardous/toxicological effects<sup>24</sup>. Thus, it is essential to comprehensively analyze various nanoparticles from their toxicological perspective.

The team iRIBio, in collaboration with the chemist Marie-Hélène Delville, achieved a strong expertise in designing, synthesizing and characterizing TiO<sub>2</sub> NPs of different shapes and sizes. Using ion beam techniques, the group developed a methodology to obtain an accurate quantification of exogenous and endogenous chemical element distribution in single cells.

*TiO<sub>2</sub> Nanoparticles.* The high photocatalytic and super-hydrophilic properties of titanium dioxide nanoparticles (TiO<sub>2</sub> NPs) have made them popular for a wide variety of applications. Titanium dioxide pigment (TiO<sub>2</sub>) is a white powder with high opacity, brilliant whiteness, excellent covering power, and resistance to color change<sup>25</sup>. These properties have made it a valuable pigment for a broad range of applications in white paints, household products, plastic goods, medications (pills), foods, orthopedic implants, paper and toothpaste. A very common application of TiO<sub>2</sub> NPs is as an additive in sunscreen cosmetics as UV-attenuating filter agents. In recent years, many studies have focused on the biomedical applications of TiO<sub>2</sub> NPs in areas such as cancer therapy, drug delivery systems, cell imaging, genetic engineering, biosensors, and biomedical experiments<sup>26,17,27</sup>.

TiO<sub>2</sub> is a natural mineral found primarily in rutile, anatase, and brookite forms. TiO<sub>2</sub> was previously classified as biologically inert but after such widespread use, its potential to penetrate skin (dermal penetration), gastrointestinal tract (ingestion), respiratory tract (inhalation) and blood circulation (injection), and its pathogenic role was re-examined.

TiO<sub>2</sub> NPs are produced in “spherical” shape (such as AEROXIDE P25) but could be engineered in terms of shapes and sizes. The reduction of the particle size leads to higher specific surface area. Tailoring sphere-shaped to fiber-shaped NPs such as nanowires, nanobelts and nanotubes is very attractive, because these nanomaterials have advantage in the application of photocatalysis, charge transfer and sensing due to its unique structures. For example, titanate scrolled nanosheets have been recently developed for their exceptional electronic, optical and photocatalytic performance<sup>26-29</sup>.

Despite promising new applications in industry and in nanomedicine, TiO<sub>2</sub> NPs may engender environmental and health risks due to their specific properties supported by their size and geometry what is attracting great concerns. Many studies have reported that TiO<sub>2</sub> NPs elicit a toxic response in different biological systems including animals, mammalian cells, model organisms, and bacteria<sup>30-39</sup>. Although there are many observations of these TiO<sub>2</sub> NPs toxicity, the detailed molecular mechanisms induced are not so clear. Recent studies report endoplasmic reticulum stress (ER stress) as a common mechanism in TiO<sub>2</sub> NPs related toxicity. The endoplasmic reticulum (ER) is an important organelle and functions in folding and assembling of cellular proteins, in synthesis of lipids and sterols, and in

regulating the maintenance of the calcium ion (intracellular calcium homeostasis), processes which are all dependent on the ER internal homeostasis. ER stress is usually a short-term response, which induces a series of transcriptional activities for cell survival; in a prolonged stress situation, ER stress activates apoptotic cell death pathways<sup>40-43</sup>. Finally, whereas there are evidences of TiO<sub>2</sub> NPs toxicity, the involved mechanisms are not fully elucidated.

To date, only a few studies have investigated the relationship between NPs morphology and their toxicity without providing any obvious correlations<sup>24,44-46</sup>. Their toxic potential remains largely unclear and it is a real challenge to detect, track and quantify the NPs in living and biological samples and to correlate this with toxicity effects.



## Chapter 2

### *Nuclear Microprobe techniques for chemical multi-elements micro-analysis*

One of the main applications of microbeams is the ability to perform the micro-analysis which measures the physical/chemical characteristics of a sample.

Since the 1960s, charged-particle microbeams have been used for quantitative elemental analysis of geological, historical and biological samples. Two-dimensional elemental maps are obtained by scanning a small ion beam across a sample and monitoring the X-Rays produced by sample elements. The interaction of charged particles and matter allows one to obtain quantitative information about the chemical composition of matter. The beam focalization and scanning on the sample give the spatial distribution of these chemical elements. These characteristics make the ion beam analysis a multi-elemental, quantitative, sensitive (down to few parts per million), and non-destructive powerful tool to investigate the composition of biological specimens<sup>23</sup>. It allows the measurement of trace elements at the single cell level (Fe, Cu, Zn, Se, S, ...), the study the intracellular homeostasis (Na, Mg, Cl, K, Ca) and the investigation of the presence of metal nanoparticles (Ti, Al, Hf, Pt).

Various techniques are available for ion beam analysis, but just some of them are used for biological samples. Principally, these methods are: (i) PIXE – Particle-Induced X-Ray Emission, (ii) RBS – Rutherford Backscattering Spectrometry, and (iii) STIM – Scanning Transmission Ion Microscopy (Figure 15). These techniques rely on the detection and energy analysis of characteristic radiations emitted by atoms and nuclei of the target when bombarded by MeV ion beams, because the energy of the emitted radiation is typical of the targeted material<sup>47</sup>.

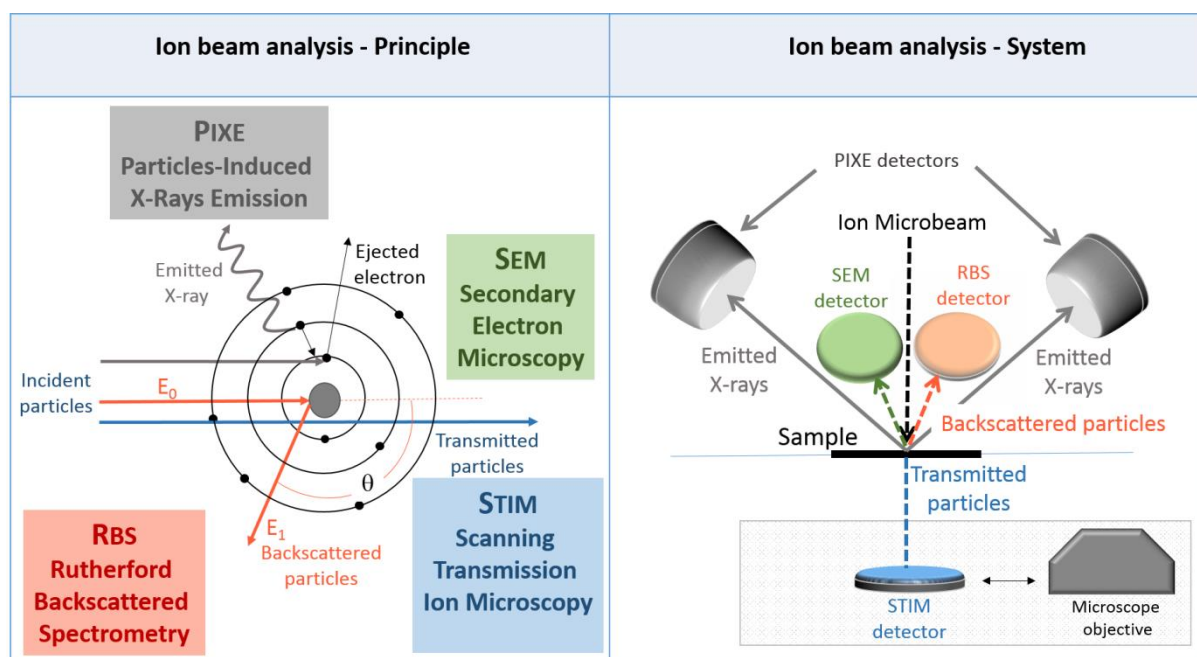


Figure 15. Ion Beam analysis principle and system for biological samples. STIM is used to map the cell density area by energy loss measurement. PIXE and RBS analyses provide the spatial distribution and quantification of chemical elements at the single cell level.

*Particle-Induced X-Rays Emission (PIXE).* PIXE is a spectrometry technique, which can be used for non-destructive, simultaneous elemental analysis. It is based on X-Rays emission after collision of incident protons with the inner shell electrons of the target atoms. The incident proton may remove an electron, creating a vacancy. The energies of the X-Rays, which are emitted when higher shell electrons fill the created vacancies, are characteristic of the element from which they originate. The number of X-Rays emitted is proportional to the mass of the element in the analyzed sample. Therefore, this technique provides not only the chemical composition of the sample, but also its two-dimensional elemental mapping of a specific region of interest (*ROI*) in defined cellular compartments. The distribution of trace elements, from sodium to heavy metals, is acquired simultaneously with a subcellular spatial resolution and high sensitivity<sup>23</sup>.

*Rutherford Backscattered Spectrometry (RBS).* This method is based on the energy measurement of backscattered protons after elastic collision with sample atom nuclei. The ion beam is directed onto a solid sample, it enters the sample, where it loses energy by inelastic collisions on electrons, it scatters on atomic nuclei and it travels back out with a characteristic energy distribution that can be detected. From it, it is possible to determine the dry mass of organic samples. Carried out simultaneously with PIXE, RBS allows identifying low-Z elements, such as carbon, nitrogen and oxygen.

*Scanning Transmission Ion Microscopy (STIM)*. In this technique, the particles are transmitted through the sample and the energy loss is measured. The magnitude of the energy loss depends on the thickness and density of the sample. Thereby the local change in cell density and cell structures such as the nucleus, nucleolus and cytoplasm can be deduced<sup>22</sup>. Thus, STIM can be used both as an imaging technique and as a thickness measurement. The transmitted particles are detected in the beam direction, allowing the use of very small beam currents, which makes it possible to focus the beam to about 300 nm.

The microprobe present at CENBG is used to quantify, localize and study the presence of inorganic elements in different tissues and at the single cell level. In this particular context, the capabilities of the microprobe are coupled to the classical imaging techniques, such as optical and fluorescence microscopy, to quantify and localize nanoparticles within cells. The importance of nanoparticles quantification is stressed not only in the study of their effects on cells homeostasis but also in their use in radiation therapy as a dose-enhancer agent.

## Questions addressed in this work

The work package 1 of the SPRITE project has been ideated to develop biomedical applications of ion beams and, in this context, the iRIBio expertise can be exploited to localize and quantify the intracellular content of nanoparticles and reveal chemical alterations due to nanoparticle and/or ionizing radiation exposure. Recently, the combined use on NPs and ionizing radiations have been extensively investigated for biomedical application, such as in radiation therapy. Indeed, different studies showed an increased density of ionization significantly localized in short distances from nanoparticles integrated in cells. Despite the use of nanoparticles are investigated for these reasons and also used in diverse field including food, cosmetic, and medical industries, the risks for their adverse health effects have not been clearly established. Their use in biological system still raises challenging questions about the internalization mechanisms, the localization and quantification in single cells. Another important parameter that merits attention is to define how modifications of NPs morphology may alter their bioavailability and then consequent effects on biological systems.

To answer these problematic issues, the goals of this work are to:

- develop an original imaging methodology that allows *in vitro* studies for the detection, tracking and quantification of NPs in biological systems.
- explore the toxicity of different forms of NPs and to define precisely the molecular and cellular mechanisms involved in the toxicity of NPs in eukaryotic cells.

## Experimental results

To optimize the therapeutic benefit of radiation therapy, a lot of efforts are invested to improve the beam ballistic and to increase the Relative Biological Effectiveness (RBE) of the radiation inside the tumor. The main current developments in radiation therapy are based on adding radiation sensitizing agents with the final aim to enhance the dose in the tumor volume and to reduce risks to healthy tissues. High-Z metal or metal oxide nanoparticles have been proposed as good candidates. Starting from the collaboration with the Institut Bergonié, I learnt of a clinical assay led by a private company (NANOBIOTIX) consisting in the injection within the tumor of Hafnium oxide NPs to increase the radiation effects. By working together with Marina Simon and based on the results previously obtained, we started to adjust these *in vitro* protocols for evaluating the potentiality of new emerging therapeutic agents. As mentioned before, nanotechnologies are emerging areas studied for increasing the dose-rate effects, and to enhance the therapeutic effectiveness of radiation therapy. Within this context, we collaborated with the private company NANOBIOTIX to study the effects of the combination of metal oxide nanoparticles ( $\text{HfO}_2$ ,  $\text{TiO}_2$ ) with IR. Preliminary confidential results are not discussed in this thesis but they originated important points to be clarified, such as the internalization, quantification and localization of nanoparticles in single cells. Indeed, besides the numerous physical and chemical advantages exhibited by NPs for medical applications, their use in biological systems still raises challenging questions: (i) How and where do accumulated NPs in cells? (ii) How to quantify *in situ* the intracellular NP content of exposed cells? (iii) How to clarify the interactions between NPs and biological systems? (iv) How do NPs interact with ionizing radiations?

To answer these questions, I contributed in collaboration with Marina Simon to quantify, localize and decipher the molecular mechanisms induced by NPs in cells. First, the research program tried to answer the following questions about  $\text{TiO}_2$  NPs: (i) What are the parameters influencing the  $\text{TiO}_2$  NP bio-availability and interaction? (ii) What are the  $\text{TiO}_2$  NP physicochemical properties that determine their bio-distribution, bioaccumulation and bio-persistence? (iii) What are the molecular and cellular mechanisms involved? (iv) What are the relations between bio-distribution and toxicity? Second, the goal was to apply the methodology developed for  $\text{TiO}_2$  NP analysis to other metal or metal oxide nanoparticles.

I participated in the development of a procedure suitable for *in situ* detection and *in vitro* quantification of chemical elements present in human cells. This method is well suited to any cell type and it is particularly useful for quantitative chemical analysis in single cells following *in vitro*

metal oxide nanoparticles exposure. By using this methodology, we showed that TiO<sub>2</sub> nanoparticles accumulate in the cytoplasm all around the nucleus and are excluded from nucleus and mitochondria. Interestingly, we also observed that the nanoparticles concentration can be 10 fold higher in one cell compared to another of the same exposed population. In addition, we noticed an increase of intracellular ions, such as potassium and calcium associated to the highest uptake of TiO<sub>2</sub> nanoparticles. The protocol describing all steps is detailed in the **Manuscript 5** and it is accompanied by a movie describing procedures. This work was invited for a publication in Journal of Visualized Experiments (*JoVE*).

The development of this original imaging and analytical methodology (multimodal and correlative microscopies) allowed me to participate in another *in vitro* study combining the detection, tracking, and quantification of TiO<sub>2</sub> NPs. The main goal was to define precisely the molecular and cellular mechanisms involved in the toxicity of TiO<sub>2</sub> NPs in eukaryotic cells. The main results obtained are summarized in the **Article 6**. Briefly, the study investigated the cellular homeostasis responses induced by different TiO<sub>2</sub> NPs (in terms of shape, size and surface reactivity) in different *in vitro* primary and immortalized human cell populations (human umbilical vein endothelial cells - HUVEC, human epidermal primary new-born keratinocytes – HEKn and, immortalized cancerous cell line - HeLa). A careful attention was paid to the quantification of NPs internalization in order to correlate it with the intracellular ion homeostasis, the ER stress response and the cell fate (differentiation, proliferation, death). We showed that (i) the presence of intracellular TiO<sub>2</sub> NPs is dependent on both their morphology and their bioavailability in biological media. In addition, we have established that (ii) a minimal intracellular content of TiO<sub>2</sub> NPs (minimal threshold) is needed to induce the positively correlated alteration of the intracellular calcium homeostasis (without any dysregulation of the calcium metabolism) and (iii) the induction of one specific ER stress-pathways associated with mitochondrial dysfunction that are strictly related to the nanotoxic responses. We also observed that (iv) the cellular function (endothelial *versus* epidermal), the cell type (primary *versus* immortalized/cancerous) and the heterogeneity of the intracellular distribution/content of TiO<sub>2</sub> NPs in a cell population/type deeply modify the cellular response.

## Discussion and perspectives

Nanotechnology is a fast-expanding area of science. This area of research is anticipated to lead to the development of novel, sophisticated, multifunctional applications which can recognize cancer cells, deliver drugs to target tissue, aid in reporting outcome of therapy, provide real-time assessment of therapeutic and surgical efficacy, and most importantly, monitor intracellular changes to help prevent precancerous cells from becoming malignant. On-going efforts by scientists, researchers, and medical personnel can sincerely ensure to 'do big thing using the very small'. The main challenge when working with very small particles is to provide a comprehensive study to fully explore the toxicity of these nanomaterials. A better knowledge of cellular mechanisms nano-induced may help to better understand their deleterious health effects and create environmentally friendly and biologically relevant nanoparticles.

The behavior of NPs inside living cells is still an enigma, and no metabolic responses induced by these NPs are understood so far. We took up this challenge to decipher the molecular events that regulate bioaccumulation, biopersistence, and toxicity of metal oxide NPs. In particular, we validate and integrated a methodology involving chemistry, physics and biology to predict potential effects of NPs. We investigated the toxicity of different TiO<sub>2</sub> NPs in terms of morphologies and the relation between intracellular titanium and calcium contents and a specific metabolic pathway: Endoplasmic Reticulum Stress. Our results show that TiO<sub>2</sub> NPs exerts different toxicity levels according to their morphologies (size, shape, surface reactivity), to their related behavior in biological media, and to the considered cell type (*in vitro*). Indeed, the morphology and the behavior of TiO<sub>2</sub> NPs in biological media will determine their capability to interact *in vitro* with the cell and then, to be internalized. According to this, it will favor heterogeneous distribution of the TiO<sub>2</sub> NPs within the cell population and an important variability in terms of titanium content at the single level. As we demonstrated that a minimal intracellular content of titanium (TiO<sub>2</sub> NPs) is mandatory to induce marked change of the cellular homeostasis, it is essential to consider the intracellular content (and not only the exposure concentration) of the considered NPs.

The fundamental and basic knowledge acquired will provide a unique opportunity to develop free-environmental risk nanomaterials and also offer new perspectives in cancer therapy. The future progresses of this project will address fundamental question in the emerging and promising fields of nanomedicine and will help us to (i) determine the physicochemical and bio-molecular mechanisms induced by ionizing radiation interactions and metal/metal oxide NPs *in cellulo* (with *in vitro*

distribution and quantification data), (ii) develop and validate predictive methodologies from chemistry, physics and biology (Monte Carlo simulation), (iii) develop calculation methods with experimental validation to precisely predict dose-effect correlation in the context of ionizing radiation and NPs interactions, (iv) identify adverse side effects due to potential NPs toxicity in relation to their physicochemical characteristics and the targeted cell type (cancerous *versus* normal cells), (v) define *in vitro* and preclinical assays to validate potential new radiation therapy protocol combining NPs and ionizing radiation. The physical and modeling aspect of the project, beam characterization and cell dosimetry in realistic conditions are some aspects of a PhD thesis in medical physics following my PhD work.





## **Manuscript 5**

***“In situ* detection and single cell quantification of  
metal oxide nanoparticles using Nuclear  
Microprobe Analysis”**

Muggiolu G, Simon M, Lampe N, Devès G, Barberet P,  
Michelet C, Delville MH, Seznec H

**JoVE (under revision)**



1 Alewife Center #200  
Cambridge, MA 02140  
tel. 617.945.9051  
[www.jove.com](http://www.jove.com)

**TITLE:** *In Situ* Detection and Single Cell Quantification of Metal Oxide Nanoparticles using Nuclear Microprobe Analysis.

**AUTHORS:**

Giovanna Muggioli<sup>1,2\*</sup>, Marina Simon<sup>1,2\*</sup>, Nathanael Lampe<sup>1,2</sup>, Guillaume Devès<sup>1,2</sup>, Philippe Barberet<sup>1,2</sup>, Claire Michelet<sup>1,2</sup>, Marie-Hélène Delville<sup>3,4</sup>, Hervé Seznec<sup>1,2</sup>

# The author wish it to be known, in their opinion, the first two authors (GM, MS) should be regarded as joint First Authors

<sup>1</sup> Université de Bordeaux, Centre d'Etudes Nucléaires Bordeaux Gradignan (CENBG), Chemin du solarium, 33175 Gradignan, France.

<sup>2</sup> CNRS, UMR5797, Centre d'Etudes Nucléaires Bordeaux Gradignan (CENBG), Chemin du solarium, 33175 Gradignan, France.

<sup>3</sup> CNRS, UPR9048, Institut de Chimie de la Matière Condensée de Bordeaux (ICMCB), 87 avenue du Dr. A. Schweitzer, Pessac, F-33608, France

<sup>4</sup> Université de Bordeaux, Institut de Chimie de la Matière Condensée de Bordeaux (ICMCB), 87 avenue du Dr. A. Schweitzer, Pessac, F-33608, France.

E-mail address: [muggioli@cenbg.in2p3.fr](mailto:muggioli@cenbg.in2p3.fr), [simon@cenbg.in2p3.fr](mailto:simon@cenbg.in2p3.fr), [lampe@cenbg.in2p3.fr](mailto:lampe@cenbg.in2p3.fr), [michelet@cenbg.in2p3.fr](mailto:michelet@cenbg.in2p3.fr), [deves@cenbg.in2p3.fr](mailto:deves@cenbg.in2p3.fr), [barberet@cenbg.in2p3.fr](mailto:barberet@cenbg.in2p3.fr), [delville@icmcb-bordeaux.cnrs.fr](mailto:delville@icmcb-bordeaux.cnrs.fr), [herve.seznec@cenbg.in2p3.fr](mailto:herve.seznec@cenbg.in2p3.fr)

**CORRESPONDING AUTHOR:** Hervé Seznec, [herve.seznec@cenbg.in2p3.fr](mailto:herve.seznec@cenbg.in2p3.fr)

**KEYWORDS:**

Nanoparticles, Chemical element mapping, *in situ* quantification, nuclear microprobe analysis, ImageJ, IBA-J, Single Cell Analysis, Fluorescence microscopy

**SHORT ABSTRACT:**

We present a procedure for the *in situ* detection and *in vitro* quantification of chemical elements present in human cells. The method is well suited to any cell type and is particularly useful for quantitative chemical analyses in single cells following *in vitro* metal oxide nanoparticle exposure.

**LONG ABSTRACT:**

Micro-analytical techniques based on chemical element imaging enable the localization and quantification of chemical elements at the single cell level, and offer new possibilities for the characterization of living systems. They are particularly appropriate for detecting, localizing and quantifying the presence of metal oxide nanoparticles both in biological specimens and the environment. This is due to the fact that they meet all relevant requirements in terms of (i) sensitivity (1 to 10  $\mu\text{g}\cdot\text{g}^{-1}$  dry mass), (ii) micrometer range spatial resolution, and (iii) multi-

element detection. Given these characteristics, micro-beam chemical element imaging can powerfully complement routine imaging techniques such as optical and fluorescence microscopy. Here, we detail a protocol to perform a nuclear microprobe analysis on cultured cells (HTB96 U2OS) exposed to titanium dioxide nanoparticles. Cells must grow on and be exposed directly in a specially designed sample holder used in the optical microscopy and in the nuclear microprobe analysis stages. Plunge-freeze cryogenic fixation of the samples permits the preservation of both the cellular organization and the chemical element distribution. Simultaneous nuclear microprobe analysis (scanning transmission ion microscopy, Rutherford backscattering spectrometry and particle induced X-ray emission) performed on the sample collect information about the cellular density, the spatial distribution of chemical elements and the amount of nanoparticles per cell. There is a developing need for such analytical tools within biology, especially in the emerging context of nanotoxicology and nanomedicine, to deepen our comprehension of the interactions between nanoparticles and biological samples. In particular, as nuclear microprobe analysis does not require that nanoparticles be labelled, nanoparticle abundances are quantifiable at the single cell level in cell populations, independent of their surface state.

#### **INTRODUCTION:**

Cellular homeostasis is determined by the regulation of uptake, assimilation, and intracellular distribution of trace chemical elements, such as ions, metals, or exogenous inorganic compounds. These elements are often present only at trace levels, but nevertheless play a considerable role in the physiology of biological systems. Thus, the study of cellular biochemistry in relation to function and structure in both normal and pathological/stressed conditions is a key step towards a complete understanding of cellular metabolic processes. In this sense, it is necessary to develop imaging and analytical methods that enable the investigation of intracellular chemical abundances, structural organization and their related metabolic functions. Very few methods give *in situ* quantitative information about the whole chemical composition of a sample. Apart from methods analyzing samples in the bulk form, *in situ* analyses consider biological samples in their integrity without losing mass and structural information, thereby preserving their constituent chemicals (trace elements and ions) and proteins. Furthermore, as the nanosciences continue to develop, it can be expected that improved imaging and analytical methods for environmental monitoring at the cellular scale will be necessary to observe and quantify nano-object behaviors and interactions.<sup>1</sup>

Nanoparticles (NPs) are defined as objects with at least one facial dimension between 1 and 100 nm.<sup>2</sup> Due to their unique physicochemical properties, NPs are extensively used in industry. NPs are employed in bio-applications such as therapeutics, antimicrobial agents, transfection vectors, and in nanomedicine.<sup>3,4</sup> Despite the numerous physical and chemical properties exhibited by NPs, the risks for adverse health effects due to prolonged or repetitive exposures at various concentration levels in both biological species and the environment have not yet been clearly established.<sup>5-8</sup> In particular, the behavior of NPs inside cells and the associated specific metabolic responses are, to date, not fully understood. This is partially due to the scarcity of methods that allow the detection and quantification of internalized NPs in a single cell.<sup>9</sup>

There are numerous analytical tools, including microscopy, mass spectrometry (MS), inductively coupled plasma MS (ICP-MS)<sup>10,11</sup> and liquid chromatography MS (LC-MS), which are used to estimate the cellular dose of NPs but they provide useful information at a macroscopic level. None of them can however give a precise identification of cellular NPs dose as well as NPs distribution without the use of fractionation methods. A systematic assessment of the dose-response is thus impossible with these methods, as opposed to methods based on atomic spectroscopy such as nuclear microprobe analysis<sup>12,13</sup>, synchrotron X-ray fluorescence microscopy<sup>14</sup>, Secondary Ion Mass Spectrometry (SIMS).<sup>15,16</sup> These methods are particularly interesting as they complement observations made using fluorescence microscopy, especially when NPs cannot be labeled with fluorescent tag molecules and are thus studied in their native state. To some extent, even when NPs are functionalized with fluorescent dyes, (i) quantification remains difficult because the level of tagging of a single NP is usually unknown and (ii) the chemical modification of the surface of a NP may alter its cellular distribution compared to the untagged state.

In this article, we will focus on a method based on a combination of nuclear microprobe techniques that aims to image the morphology and elemental composition of biological specimens in major, minor, and trace concentrations.

Nuclear microprobe analysis is particularly suitable for the measurement of trace elements in biological tissues. Both the spatial beam resolution (0.3 to 1  $\mu\text{m}$ ) and sensitivity in chemical element detection (from 1 to 10  $\mu\text{g.g}^{-1}$  dry mass) are well suited for studies at the cellular level. In short, ion microbeam techniques are based on the detection of particles (photons, electrons or ions) emitted after the ion beam (typically running at MeV energies) interacts with atoms present in the sample. The ion microbeam is repeatedly scanned over the sample surface, often over an area of 100 by 100  $\mu\text{m}^2$  containing several cells. Emitted particles are detected and their energy is recorded for each beam position. Sorting of particles according to the beam position, thus identifying the structure responsible for the emission of such particles is the aim of data treatment. Here, we describe precisely our approach based on fluorescence microscopy and nuclear microprobe analysis to detect and quantify NPs at the cellular scale of biological models, in order to investigate NP exposure consequences and interactions with living systems. We will particularly focus on the new possibilities offered by this method in terms of local quantification of titanium dioxide nanoparticle ( $\text{TiO}_2$  NPs) aggregates at the subcellular level.

## **PROTOCOL:**

### **1. Sample holder preparation**

#### **1.1) Sample holder design and preparation**

A custom sample holder suitable for cell culture and cell handling is required. It needs to be designed for cell culturing, *in vitro* observations using routine optical microscopy, and chemical elemental analysis and imaging. The choice of this support allows multiple treatments and multiple analyses on the same sample. This sample holder is made of a PEEK frame<sup>13</sup>. PEEK is a colorless thermoplastic organic polymer, resistant to thermal degradation (suitable for numerous cycles of sterilization by autoclaving), as well as to attack by both organic and

aqueous environments.

### 1.2) Sample holder preparation

The sample holder is covered with a 2- $\mu$ m thick polycarbonate foil. The polycarbonate film was chosen for its biocompatibility, its thickness and for its ability to resist different protocols and analytical constraints. Polycarbonate is a transparent polymer, which also shows a high resistance to the ion beam without stopping it. The polycarbonate foil is glued with a thin layer of Formvar solution (1 mg diluted in 100 ml chloroform, protect from light).

**Caution** – Chloroform is toxic. Avoid inhalation, ingestion or contact with skin. Always use a properly functioning chemical fume hood and appropriate filters.

### 1.3) Sample holder sterilization

Place the mounted sample holder in a conical flask with 50 ml of ethanol 70% (v/v) under agitation at 180 rpms and +37 °C overnight, using an incubator/agitator. Rinse the holder several times in sterile distilled water. Air dry them in sterile conditions and expose them to ultraviolet light (germicidal lamp from Biosafety bench, class II) for 30 min on each side.

Keep the samples in sterile 12-well plates (one sample holder per well) until ready to use.

**Pause point:** Multiple sample holders can be stored at room temperature in sterile and dry 12-well plates sealed with parafilm for several days.

## 2. Growth of cells in the appropriate sample holder.

**Caution:** Protocol must be carried out in a biosafety laminar flow bench (Class II) to exclude contaminating micro-organisms. Handle antibiotics (e.g. penicillin, streptomycin) with gloves. Respect best practices when handling biological materials (Cell lines, genetically modified derived human cells).

**Critical:** The cell lines used in your research should be regularly checked to ensure that they are authentic and not infected with *Mycoplasma*.

2.1) Transfect cells with the Matrix-roGFP (from ADDGEN, 49437)<sup>17-19</sup> plasmids using the appropriate transfection reagent (lipofection) in accordance to the protocol established by the manufacturer.

2.2) Check transfected cells by fluorescence microscopy to ensure the transfection has occurred and to confirm that they express the fluorescence protein and exhibit normal mitochondrial morphology.

**Pause point:** Cells can be frozen in liquid nitrogen for several years.

2.3) Prepare a stable transfected cell population by culturing the cells in an appropriate medium in order to obtain sub-confluent cell populations. Grow cells at + 37 °C, 5 % (v/v) CO<sub>2</sub> in a saturated water atmosphere.

2.4) Seed cells in a concentration, such as they are at 80% confluence the day of fixation. The protocol is applicable for all cellular types and the number of cells seeded is dependent of cell size and of cell doubling time. Harvest cells using 400  $\mu\text{L}$  of trypsin-EDTA 0.25 % (v/v) and incubate for 3 min at + 37 °C. Stop trypsin action with 1 mL of fresh culture medium. Pellet the cells by centrifugation for 5 min at 1200 rpms and + 4 °C, then remove the supernatant and add an appropriate volume of fresh culture medium.

**Caution:** Avoid subjecting trypsin, antibiotics, and serum to repeated freeze-thaw cycles. Keep them sterile. Divide the stock solution into aliquots and freeze them at -20 °C. Store the aliquots until the expiration date.

**Caution:** Carefully rinse the cell pellet in order to completely remove the trypsin. Traces of residual trypsin will delay and decrease the plating efficiency.

2.5) Count the cells and perform a dilution with fresh and thermo-stated complete culture medium in order to obtain a cell suspension with 500 cells per  $\mu\text{L}$  (to be adapted as a function of the cell type, in order to plate a 40  $\mu\text{L}$  drop).

2.6) Plate a 40  $\mu\text{L}$  drop onto the center of the polycarbonate foil. Carefully place the sample in the cell incubator for 2 hours at + 37 °C, 5 % (v/v)  $\text{CO}_2$  in a saturated water atmosphere.

**Critical:** Once the sample is placed in the incubator, limit as much as possible any mechanical movements to favor fast cell attachment.

**Critical:** According to the cell type, it could be necessary to incubate cells longer than 2 hours for optimal plating efficiency. Check that the incubator atmosphere is well saturated to prevent drops from evaporating.

2.6) Check that cells are well-attached on the polycarbonate foil using an optical microscope. Gently add 2 ml of fresh complete medium and keep for 24 h in appropriate culture conditions.

### 3. Nanoparticles preparation and exposure

Fluorescent dye-modified  $\text{TiO}_2$  NPs were designed, synthesized, and grafted with commonly used fluorophores such as tetramethyl rhodamine isothiocyanate (TRITC).<sup>20,21</sup> This surface modification allows nanoparticle detection, tracking and localization *in situ* and *in cellulo* in both living and fixed cells or multicellular organisms.<sup>12,13,18</sup>

**Caution:** Nanomaterials and Nanoparticles must be handled with care. Avoid inhalation, ingestion or contact with skin. To prevent dissemination in air, nanoparticles are maintained in solution (ultrapure water).

3.1) Prepare the  $\text{TiO}_2$  NPs suspension in ultrapure water at a concentration of 1 mg  $\text{mL}^{-1}$ . Disperse the  $\text{TiO}_2$  NPs using intense 1 minute sonication pulses at RT (750 W, 20 kHz, amplitude: 30%) using an ultra-sound generator and a dedicated 3MM conical microprobe.

3.2) Dilute TiO<sub>2</sub> NPs at the appropriate concentration in the culture medium in order to obtain an exposure suspension of 4 µg cm<sup>-2</sup> (final concentration).

Replace medium with the appropriate volume of medium containing NPs on cells and mix gently for homogeneous distribution of the TiO<sub>2</sub> NPs.

Prepare control cells similarly without the addition of TiO<sub>2</sub> NPs.

3.3) Incubate the cell populations for 24 hours at 37 °C, 5% (v/v) CO<sub>2</sub> and a saturated water atmosphere.

#### 4. Paraformaldehyde fixation and fluorescence microscopy.

4.1) Prepare a fresh solution of paraformaldehyde solution (PFA, 4 % w/v) buffered in Phosphate Buffer Saline (PBS, pH 7.4).

Dissolve 4 g of PFA in 100 ml of PBS. Heat the solution to 65 °C while stirring using a magnet and a magnetic stirrer in a fume hood. Increase the pH by adding 1 M NaOH one drop at a time until the solution clears. Cool the solution to room temperature and adjust the pH to 7.4. Use the freshly prepared solution immediately or keep at + 4 °C and protect from light.

**Caution:** PFA is toxic; avoid inhalation, ingestion or contact with skin. Always use a properly functioning chemical fume hood and appropriate filters.

4.2) Once, the incubation time has elapsed, remove the cell culture medium containing the TiO<sub>2</sub> NPs. Rinse the cell populations once with fresh culture medium and once with 2 ml of PBS. Remove the PBS and rinse quickly with an aliquot of fresh and cold PFA (4% w/v, +4 °C).

Add PFA (2 ml, 4% w/v, +4 °C). Incubate 15 min. at room temperature.

Remove the PFA and rinse the cells with PBS (2 ml, 3 times, 5 min) under agitation.

**Pause point:** These chemically fixed samples can be used for the “plunge-freeze” procedure after fluorescence imaging (go to step 5) or used only for fluorescence imaging (go to step 4.3).

4.3) Stain the nucleus with Hoechst<sup>33342</sup> incubating the cells for 10 min in PBS. Hoescht<sup>33342</sup> is used at a final concentration of 500 nM. After incubation remove the solution and rinse with PBS.

**Caution:** Hoechst<sup>33342</sup> is cell permeant and may be toxic. Avoid direct contact, and use gloves while preparing and using Hoechst<sup>33342</sup>.

**Critical:** Ensure that the Hoechst<sup>33342</sup> staining solution is freshly prepared and maintained in sterile conditions.

4.4). Fixed samples can be processed for *in situ* and single cell imaging using fluorescence microscopy (Figure 1).

#### 5. “Plunge freezing” fixation and dehydration



Chemical fixation is a common way to preserve biological samples (such as paraformaldehyde fixation). However, it is better to use physical fixation through cryogenic methods to preserve ultrastructure and biochemical integrity. "Plunge freezing" fixation provides a rapid cessation of the cellular activity within milliseconds without any addition of fixative compounds.

5.1) Prepare an aluminum transfer plate by cooling it in liquid nitrogen. Store the plate into a box filled with liquid nitrogen and maintain the plate surface above the liquid in the cold nitrogen vapor.

**Critical:** The box should be kept closed as much as possible in order to prevent water vapor deposition onto the cold plate surface.

**Critical:** The sample stored on the plate during preparation should not be covered by liquid nitrogen.

5.2) Rinse cells once in culture medium and then twice more, briefly, in sterile and ultrapure water to remove excess extracellular salts remaining from the culture medium.

**Critical:** Ensure that the media are freshly prepared and maintained in sterile conditions. All the media should be also heated at 37 °C before being used.

**Critical:** The rinse must be very brief (few seconds) and the excess of liquid on the samples removed as fast as possible.

5.3) Plunge-freeze the cells at -150 °C in liquid nitrogen chilled 2-methylbutane during 30 sec and place them onto the aluminum transfer plate. Samples are stored here during the preparation of all others samples. When samples are all cryofixed, transfer all-at-once by placing the transfer plate in a freeze-dryer.

**Critical:** The overall cryofixation process should not last more than 20 min in order to prevent structural modifications to appear in samples temporarily stored in the transfer box.

5.4) Freeze-dry the samples using the following sequences: 1) perform a primary desiccation for 12 to 24 hours (-99 °C,  $10^{-3}$  mbar) at low pressure and low temperature, then 2) perform a secondary desiccation phase for at least 24 hours, increasing the plate temperature to +40 °C while keeping the pressure low (+40 °C,  $10^{-3}$  mbar).

**Caution:** Liquid nitrogen is extremely cold and can cause severe frostbite or eye damage upon contact. Use adapted bench top containers for transport and wear safety equipment (cryogenic gloves, eye and face protection).

**Caution:** 2-Methylbutane is extremely flammable. A harmful contamination of the air can be reached rather quickly on evaporation of this substance at 20 °C. Avoid inhalation, ingestion or contact with skin. It is strongly advised not to let the chemical enter into the environment. Use breathing and eye protection, and protective gloves. Always use a properly functioning chemical fume hood. May be stored at 4 °C.

**Critical:** Use an appropriate thermometer (-150 °C) to monitor the 2-methylbutane temperatures during the “Plunge-freeze” session. The 2-methylbutane must be kept cool in a liquid phase.

**Critical:** Transferring cryofixed samples to the ambient atmosphere may cause cellular damage due to the temperature increase or water vapor condensing on the sample surface. Accordingly, the transfer should be made as fast as reasonably possible (30 sec)

**Pause point:** After cryofixation, samples can be stored at room temperature for several days in sterile and dry conditions (protected from dust and moisture). Carefully handle the samples with fine forceps and place them in a sterile 12-well plate sealed with parafilm. Dessicant can be used to dry the atmosphere.

## 6. Nuclear Microprobe Analysis

Chemical element imaging was carried out at the microprobe beam line of AIFIRA using the complementary ion beam analytical techniques  $\mu$ -PIXE and  $\mu$ -STIM. The facility is based on a 3.5 MV (HVEE, The Netherlands) singletron particle accelerator delivering light ion beams in the MeV energy range.<sup>22,23</sup>

**Pause point:** AIFIRA is an ion beam facility hosted by the University of Bordeaux that offers an access to national and international teams after scientific evaluation of the proposed experiment.

### 6.1) Scanning Transmission Ion Microscopy ( $\mu$ -STIM)

STIM is used to record areal density maps of cells after conversion of energy loss to cellular mass, taking advantage of the fact that the energy loss is proportional to the sample areal density (expressed in  $\mu\text{g cm}^{-2}$ ).

Use a 2 MeV Helium ( $\text{He}^+$ ) microbeam as a probe with a size in the focal plane of around 300 nm in diameter and at low fluency ( $2000 \text{ ions}\cdot\text{s}^{-1}$ ). Measure the energy of the transmitted ions with a planar silicon detector (Canberra PIPS detector,  $25 \text{ mm}^2$ , 11 keV energy resolution @ 5.4 MeV), placed behind the sample in the beam axis.

### 6.2) Particle induced X-ray Emission ( $\mu$ -PIXE) and Rutherford Backscattering Spectrometry ( $\mu$ -RBS).

$\mu$ -Pixe and  $\mu$ -RBS analyses provide the spatial distribution and quantification of chemical elements at the single cell level.

Use a 1.5 MeV proton ( $\text{H}^+$ ) microbeam (50–150 pA), focused down to a diameter of 1  $\mu\text{m}$  and scan over the same cells of interest spotted by STIM from 4 to 8 hours and around  $100 \times 100 \mu\text{m}^2$ .

Collect induced X-ray photons emitted from atoms present in the sample (from Na to Ti) by a high-resolution Si(Li) solid-state detector (Oxford Instruments, 145-eV energy resolution, @Mn-K $\alpha$ ) positioned at 45° from incoming beam axis. Use the detected photon energy to identify the nature of emitters (e.g. Z of element) and X-ray intensity to determine the element

concentration.

Simultaneously collect back-scattered protons at  $-135^\circ$  with a silicon detector (Canberra, partially depleted detector, 25 mm<sup>2</sup>, 11 keV FWHM @ 5.4 MeV) in order to measure the total number of incoming particles, in order to normalize X-ray intensities.

**Critical:** A collection of certified calibration standards for atomic concentration quantification is used in order to calibrate the X-ray detector response. Reference materials are a collection of thin atomic films deposited on 6.3- $\mu\text{m}$  thick mylar foils. Emitted X-Ray energies range from 0.6 (Li, K line) to 20.2 keV (Rh, K line).

## 7. Data analysis

7.1) Reconstruct chemical elemental maps using the IBA-J plugin for *ImageJ*.<sup>24</sup>

Dedicated software in the form of a plugin for ImageJ has been developed in order to process raw IBA data. Raw data correspond to a list of events arising from particle beam interaction with cells that are recorded along with the beam position as a chronological sequence. Use the IBA-J plugin to sort events according to their type: transmitted ion energy (STIM), backscattered ion energy (RBS) or X-ray photon energy (PIXE). Then, process separately each type of data:

(i) calculate STIM areal density map;

(ii) calculate average X-ray photon energy spectra and define for each chemical element of interest an energy window in order to retrieve the element spatial distribution.

(iii) define regions of interest (ROI) (e.g. individual cells, dense structure, aggregates, etc..) and calculate the corresponding x-ray spectra.

Then, using the Image J selection tools, select the region of interest (individual cells, grains, nucleus, etc..) and calculate the corresponding X-ray spectra.

7.2) Analyze the corresponding RBS spectra using the SIMNRA software in order to calculate the total number of incident particles.

7.3) Fit X-ray spectra using the Gupix software and RBS spectra using the SIMNRA software in order to determine the element concentration for each ROI. Typical limit of detection (LOD) for the method is in the range 1 to 10  $\mu\text{g g}^{-1}$  in dry mass depending on the atomic number of elements (LOD is decreasing with Z).

## REPRESENTATIVE RESULTS:

### Cell culture and fluorescence imaging of fluorescently labeled TiO<sub>2</sub> NPs

We designed a custom sample holder suitable for the cell culture, cell handling and preparation, and multimodal analysis. Specifically, it was important that the holder permit routine optical microscopy as well as chemical elemental analysis and imaging. This sample holder is made of a PEEK frame covered with a 2- $\mu\text{m}$  thick polycarbonate foil. Cells are directly grown on the polycarbonate foil. They are maintained in sterile culture conditions for several days and then used for different experimental conditions, such as NPs exposure.

Fluorescent dye-modified TiO<sub>2</sub> NPs were designed, synthesized, and grafted with fluorophores commonly used in biology (TRITC). This chemical surface modification allowed the detection and tracking of the NPs as well as their *in situ* and *in vitro* localizations in living or in paraformaldehyde fixed cells using fluorescence microscopy. The cell nucleus and mitochondria were stained using well-characterized fluorescent markers, the vital-dye Hoechst<sup>33342</sup> (blue) and the transfected Matrix-roGFP (green), respectively. This multiple staining allowed the intracellular localization of the TRITC-TiO<sub>2</sub> NPs (red) 20 h after exposure. NPs were exclusively found in the cytoplasm of exposed cells with no detection in the cell nucleus. NPs were randomly localized in the cytoplasm all around the nucleus (perinuclear region) but excluded from mitochondria (no overlapping between TRITC and GFP signals).

Although light microscopy is very informative and essential in localizing NPs inside exposed cells, it is still not possible to evaluate the exact number of NPs per cell. The main difficulty concerning the quantification of NPs using fluorescence microscopy mainly results from the uncertainty concerning (i) the amount of fluorophores attached to a single NP and its bleaching stability during the experiment and (ii) the aggregation state of the NPs inside the cell.

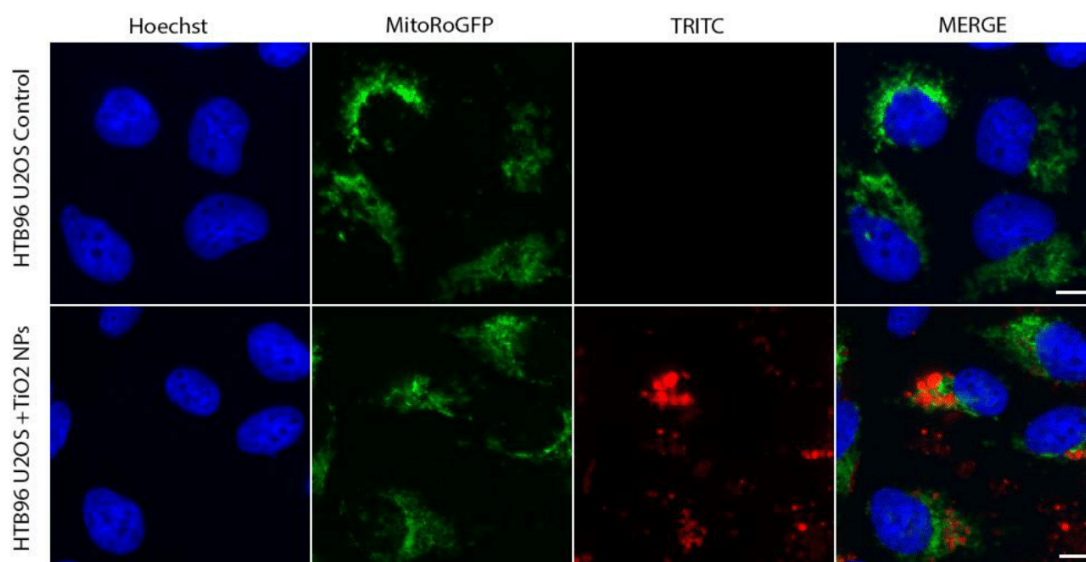


**Figure 1:** *in vitro* and *in situ* fluorescence imaging of HTB96 U2OS transgenic cells expressing MitoRoGFP and exposed to TRITC-TiO<sub>2</sub> NPs. HTB96 U2OS cells (top) marked with Hoechst<sup>33342</sup> (blue), Matrix-roGFP (green) are exposed to 4  $\mu\text{g cm}^{-2}$  TRITC-labeled TiO<sub>2</sub> nanoparticles (red) for 20 hours. Observations indicate that TiO<sub>2</sub> NPs aggregate in cells in a perinuclear region. Scale bar: 10  $\mu\text{m}$ .

To ameliorate these shortcomings, nuclear microprobe analyses techniques provide a complementary approach to conventional optical microscopy due to their sensitivity to the NPs with no need of an intermediate signal like fluorescence from a grafted molecule. Furthermore, they are also fully quantitative, giving access to information about (i) the intracellular biochemical content that is otherwise unknown, and (ii) the intracellular quantity of NPs at the single cell level.

### Cryofixation of cells after live imaging.

The main constraint in performing nuclear microprobe analysis is the need to perform analysis under vacuum conditions. We have developed a protocol for cell fixation enabling the preservation of the biological ultrastructure and the biochemical integrity of the biological specimen. Chemical fixation is known to modify the chemical composition of cells by replacement of their cellular medium with a polymer which seeks to preserve cellular ultrastructure. At the same time, the evacuation of water releases free ions and species thus modifying its composition. Hence, it is appropriate to give priority to physical fixation method, notably cryogenic methods. These cryogenic procedures provide rapid cessation of the cellular activity on the millisecond time scale.

### Nuclear microprobe analysis microscopy and quantification of NPs at the cellular scale.

After cryofixation and dehydration, the samples were analyzed by nuclear microprobe analysis to obtain precise quantitative data on their elemental chemical composition. Contrast in scanning transmission ion microscopy ( $\mu$ -STIM) images is due to local differences in density and allows the detection of cell structures such as the nucleus and cytoplasm. Although, the beam spatial resolution enables the observation of dense structures as narrow as 300 nm wide, like thin aggregates visible here in the cytoplasm, the STIM methods cannot discriminate between NP aggregates and other dense cellular structures. This is because, like for transmission electron microscopy, the physical process leading to variation in transmitted energy is the interaction of the incoming ion with the atomic electron cloud. Unlike TEM analysis however, because the entire cell volume is analyzed, local thickness variations prevent discrimination between high Z structures and a local increase of cellular density.

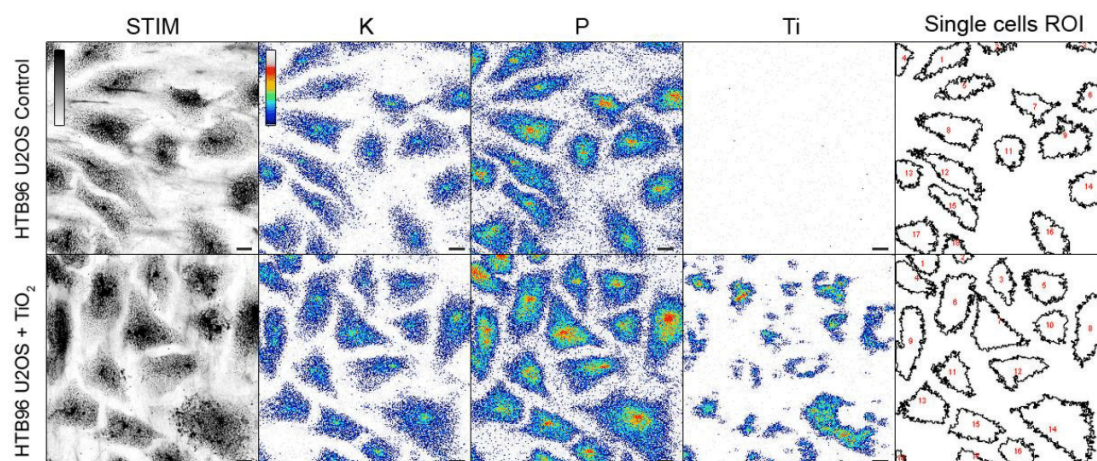


**Figure 2: Images of density and elemental distribution obtained by  $\mu$ -STIM and  $\mu$ -PIXE on cryo-fixed HTB96 U2OS cells.** HTB96 U2OS control cells (up) are compared to exposed cryo-fixed HTB96 U2OS cells (exposed to  $4\text{-}\mu\text{g cm}^{-2}$   $\text{TiO}_2$  NPs, down) and observed using nuclear microprobe analysis/microscopy. STIM microscopy (left, grayscale maps) revealed dense intra- or extra-cellular structures (nucleus, salt

aggregates, nanoparticles). The spatial resolution (300 nm) is comparable to fluorescence microscopy and shows structures such as NP aggregates in the perinuclear region. Identification of structures based only on their density may nevertheless be ambiguous. The  $\mu$ -PIXE elemental maps of K, P and Ti (thermal color scale) are complementary to  $\mu$ -STIM maps. They can be used to ensure the presence of NPs in cells. Each cell can be individually analyzed in terms of element concentration (see Figure 3). Scale bars: 10  $\mu$ m. Color scales range from minimum to maximum intensity.

As illustrated in Figure 2, the STIM rendering allows the recognition of individual cells within both a population and also intracellular sub-compartments such as the nucleolus and nucleus. Unfortunately, and as mentioned previously, NPs could not always be detected using  $\mu$ -STIM rendering.

Particle-induced X-ray emission ( $\mu$ -PIXE) analysis provides both the chemical composition of the sample and the elemental maps of chemical elements (Figure 2). During the interaction with the proton beam, the chemical elements present in the cells follow an atomic excitation-de-excitation process that eventually leads to the emission of a photon with a characteristic energy corresponding to the atomic number of the excited element. The sum of all the emitted photon events builds a characteristic peak spectrum, which may be considered as a chemical fingerprint of the sample.

Standard experimental setups and detectors used for  $\mu$ -PIXE experiments allow simultaneous quantification of all elements heavier than Na with a 1 to 10  $\mu$ g g<sup>-1</sup> dry mass detection limit. Accuracy in measuring elemental concentrations is usually limited to around 20% due to charge collection and detector efficiencies.

In this study, nuclear microprobe analysis is used to observe the distribution of cellular elements like phosphorus and potassium and to quantify the intracellular amount of TiO<sub>2</sub> NPs with titanium mapping. Chemical element maps are computed after sorting photons according to the beam position at the time of recording and selecting an energy window centered around a specific element. Maps usually represent the number of detected events at the beam position and are quantitative. Both noise and the background can be numerically simulated and filtered out. Furthermore, chemical element maps can be sorted in order to retrieve the local PIXE spectrum required for quantification.

As illustrated in Figure 2, phosphorus is found homogeneously distributed in the cell with a higher concentration in the nuclear area. Potassium is homogeneously distributed in the cytoplasm. Titanium is located in the cytoplasmic perinuclear region as aggregates, as previously observed using Fluorescence microscopy (Figure 1). NPs displayed the same perinuclear localization whatever their surface state that is either functionalized (Figure 1) or native (Figure 2). In the meantime, no trace of titanium was detected in control cells confirming that the titanium distribution observed by  $\mu$ -PIXE must be attributed to the TiO<sub>2</sub> NPs, in agreement with our previous observations by conventional fluorescence microscopy.

In addition, as illustrated in Figure 2, it is possible to extract the intracellular distribution of NPs and quantitative NPs concentrations from specific regions of interest. Based on the STIM maps and in correlation with the phosphorus/potassium distributions, single cell analysis is possible.

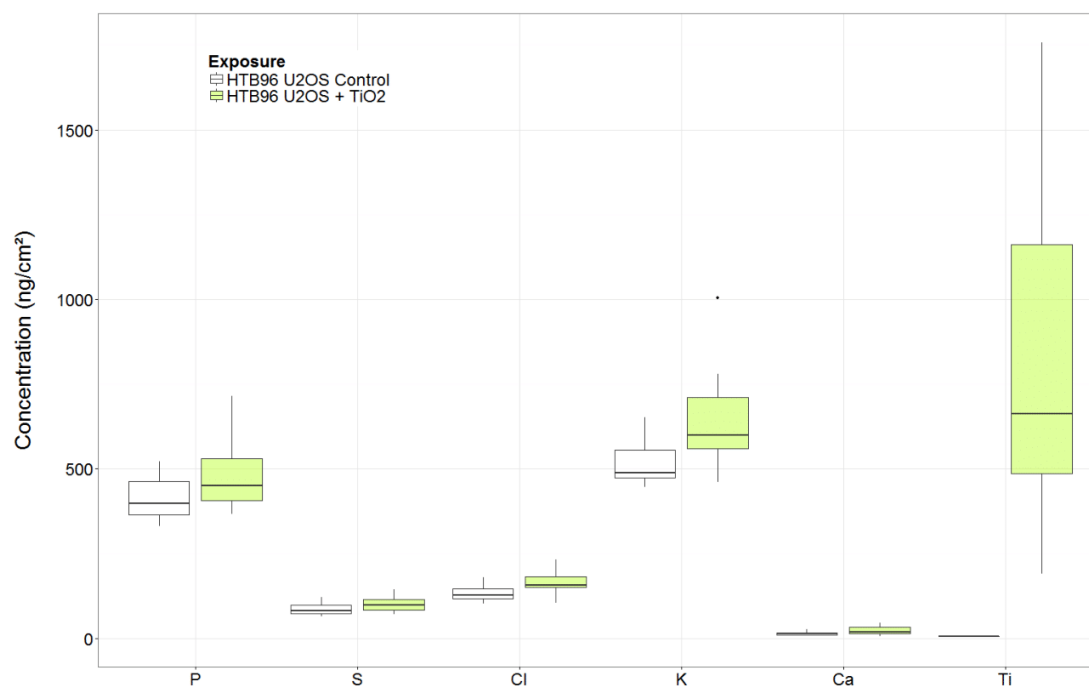


**Figure 3: Single cell quantitative analysis using  $\mu$ -PIXE.** Individual X-ray spectra calculated for cells shown in Figure 2 can be fitted in order to determine the element concentration at the cellular level. This feature is particularly interesting for NP analysis where cellular concentrations usually show strong variations inside the same population. For example here, for the same mean exposure, the Ti concentrations range from  $0.2 \mu\text{g cm}^{-2}$  up to  $1.8 \mu\text{g cm}^{-2}$ . Controls correspond to untreated cell populations. Exposure dose:  $4 \mu\text{g cm}^{-2}$ .

Accordingly, we have not only quantified the average content of titanium in a cell population but also shown the titanium distribution per cell in one population in a specific experimental condition. The median content of titanium presented here is quite low ( $500 \text{ ng cm}^{-2}$ ) compared to the  $4 \mu\text{g cm}^{-2}$  exposure dose of the cell population (Figure 3) and the variation between cells is large (Ti concentrations range from  $0.2 \mu\text{g cm}^{-2}$  up to  $1.8 \mu\text{g cm}^{-2}$  according to the analyzed cells). We also noticed an increase of free intracellular ions such as potassium and calcium in exposed samples suggesting a cellular alteration homeostasis induced by the presence of  $\text{TiO}_2$  NPs, as previously described by several authors.<sup>21,25</sup>

#### DISCUSSION:

Nuclear microprobe analysis can provide useful information beyond what is possible with other imaging techniques, especially at the subcellular level. In addition to its imaging ability, nuclear microprobe analysis also provides a quantification of chemical elements composing a biological sample, whatever its nature. In this case, it can analyze biological samples and focus on a chosen region of interest of a single cell. Its combination with other techniques provides both morphological cellular imaging and precise quantitative data on the elemental chemical

composition of the sample. These techniques present the following advantages: (i) a sample preparation which does not require chemical fixation, staining, nor sectioning; (ii) large observable areas with the option to focus on a given region of interest (ROI) of the sample; (iii) the quantification of the chemical elements content with a sensitivity of a few micrograms per gram ( $\mu\text{g g}^{-1}$ ); and (iv) the analysis of the overall cell volume with a sensitivity towards cell density changes, allowing the identification of cell compartments such as the nucleus, nucleolus and cytoplasm.

The accurate determination of dose when studying the internalization of NPs in cells is essential for quantitative NP toxicology and pharmacology. As suggested by the large discrepancy in the observed NP contents, which shows a 10-fold difference between the minimum and maximum observed concentrations (Figure 3), the mean cellular concentration might not be a relevant parameter to describe the phenomenon of particle exposure. This is all the more true when a threshold effect is supposed to take place because inhomogeneous dose exposure could lead to contradictory observations. Because the fractionated nature of nanoparticles appears clearly at cellular level, this study therefore poses again the question of the relevancy of methods based on analyzing global variables in addressing questions around the behavior of cells exposed to inhomogeneous doses of contaminants like nanoparticles.

As shown in the case studied here, the ability to observe and quantify NPs within individual cells allows us to better understand the bioaccumulation of endogenous/exogenous chemical elements such as metal oxide NPs. This is a crucial challenge for further applications of NPs in biomedicine, where a poor understanding of the underlying NP distribution of cells could lead to misinterpreted results.

This protocol highlighted the suitability of using nuclear microprobe analysis with other techniques concerning the future assessments of NP interactions with living cells. The quantitative approach gives information about the impact of these NPs in terms of detection, identification, localization, and quantification at the single cell level of both native and chemically modified NPs.

**ACKNOWLEDGMENTS:** Serge Borderes for directing and editing of the video. The French National Research Agency supports the research program TITANIUMS (ANR CES 2010, n° CESA 009 01). The CNRS and the European Community as an Integrating activity Support "Support of Public and Industrial Research Using Ion Beam Technology (SPIRIT)" under the EC contract n° 227012 support the research program. This work has been supported by Marie Curie Actions - Initial Training Networks (ITN) as an "Integrating Activity Supporting Postgraduate Research with Internships in Industry and Training Excellence" (SPRITE, D1.3) under EC contract no. 317169. The C'NANO Grand Sud Ouest and the Region Aquitaine support the research program TOX-NANO (n°20111201003) and the research program POPRA (n° 14006636-034).

**DISCLOSURES:** The authors have nothing to disclose



## REFERENCES

1. Krug, H. F. & Wick, P. Nanotoxicology: An Interdisciplinary Challenge. *Angewandte Chemie International Edition* **50** (6), 1260–1278, doi:10.1002/anie.201001037 (2011).
2. Van Hove, M. A. From surface science to nanotechnology. *Catalysis Today* **113** (3-4), 133–140, doi:10.1016/j.cattod.2005.11.059 (2006).
3. Le Trequesser, Q., Seznec, H., Delville, M.H. Functionalized nanomaterials: their use as contrast agents in bioimaging: mono- and multimodal approaches. **2** (2), 125–169, doi:10.1515/ntrev-2012-0080 (2013).
4. Oberdorster, G. Safety assessment for nanotechnology and nanomedicine: concepts of nanotoxicology. *journal of internal medicine*, 89–105, doi:10.1111/j.1365-2796.2009.02187.x (2009).
5. Savolainen, K., Pylkkanen, L., *et al.* Nanotechnologies, engineered nanomaterials and occupational health and safety - A review. *Safety Science* **48** (8), 957–963, doi:10.1016/j.ssci.2010.03.006 (2010).
6. Savolainen, K., Alenius, H., Norppa, H., Pylkkanen, L., Tuomi, T. & Kasper, G. Risk assessment of engineered nanomaterials and nanotechnologies - A review. *Toxicology* **269** (2-3), 92–104, doi:10.1016/j.tox.2010.01.013 (2010).
7. Arora, S., Rajwade, J. M. & Paknikar, K. M. Nanotoxicology and in vitro studies: The need of the hour. *Toxicology and Applied Pharmacology* **258** (2), 151–165, doi:10.1016/j.taap.2011.11.010 (2012).
8. Donaldson, K. Resolving the nanoparticles paradox. *Future Medicine* **1** (2), 229–234 (2006).
9. Schaumann, G. E., Philippe, A., *et al.* Understanding the fate and biological effects of Ag- and TiO<sub>2</sub>-nanoparticles in the environment: The quest for advanced analytics and interdisciplinary concepts. *Science of the Total Environment* **535**, 3–19, doi:10.1016/j.scitotenv.2014.10.035 (2014).
10. Olesik, J. W. *Inductively Coupled Plasma Mass Spectrometers. Treatise on Geochemistry*, doi:10.1016/B978-0-08-095975-7.01426-1 (Elsevier Ltd.: 2014).
11. Krystek, P. A review on approaches to bio-distribution studies about gold and silver engineered nanoparticles by inductively coupled plasma mass spectrometry. *Microchemical Journal* **105** (November 2011), 39–43, doi:10.1016/j.microc.2012.02.008 (2012).
12. Le Trequesser, Q., Saez, G., *et al.* Multimodal correlative microscopy for in situ detection and quantification of chemical elements in biological specimens. Applications to nanotoxicology. *Journal of Chemical Biology* **8** (4), 159–167, doi:10.1007/s12154-015-0133-5 (2015).
13. Le Trequesser, Q., Deves, G., *et al.* Single cell in situ detection and quantification of metal oxide nanoparticles using multimodal correlative microscopy. *Anal Chem* **86** (15), 7311–7319, doi:10.1021/ac501318c (2014).
14. Sutton, S. R. & Newville, M. *Synchrotron x-Ray Spectroscopic Analysis. Treatise on Geochemistry* **15**, doi:10.1016/B978-0-08-095975-7.01415-7 (Elsevier Ltd.: 2014).
15. Legin, A. A., Schintlmeister, A., *et al.* NanoSIMS combined with fluorescence microscopy as a tool for subcellular imaging of isotopically labeled platinum-based anticancer drugs.

- Chemical Science* **5**, 3135, doi:10.1039/c3sc53426j (2014).
16. McRae, R., Bagchi, P., Sumalekshmy, S. & Fahrni, C. J. In situ imaging of metals in cells and tissues. *Chemical Reviews* **109** (10), 4780–4827, doi:10.1021/cr900223a (2009).
  17. Waypa, G. B., Marks, J. D., *et al.* Hypoxia triggers subcellular compartmental redox signaling in vascular smooth muscle cells. *Circulation Research* **106** (3), 526–535, doi:10.1161/CIRCRESAHA.109.206334 (2010).
  18. Dooley, C. T., Dore, T. M., Hanson, G. T., Jackson, W. C., Remington, S. J. & Tsien, R. Y. Imaging Dynamic Redox Changes in Mammalian Cells with Green Fluorescent Protein Indicators. **279** (21), 22284–22293, doi:10.1074/jbc.M312847200 (2004).
  19. Hanson, G. T., Aggeler, R., *et al.* Investigating Mitochondrial Redox Potential with Redox-sensitive Green Fluorescent Protein Indicators. *Journal of Biological Chemistry* **279** (13), 13044–13053, doi:10.1074/jbc.M312846200 (2004).
  20. Chen, X. & Mao, S. S. Titanium dioxide nanomaterials: Synthesis, properties, modifications and applications. *Chemical Reviews* **107** (7), 2891–2959, doi:10.1021/cr0500535 (2007).
  21. Simon, M., Barberet, P., Delville, M.H., Seznec, H. Titanium dioxide nanoparticles induced intracellular calcium homeostasis modification in primary human keratinocytes. Towards an in vitro explanation of titanium dioxide nanoparticles toxicity. **5** (June), 125–139, doi:10.3109/17435390.2010.502979 (2011).
  22. Sorieul, S., Alfaut, P., Daudin, L., Serani, L., Moretto, P. Aifira: An ion beam facility for multidisciplinary research. *Nuclear Instruments and Methods in Physics Research, Section B: Beam Interactions with Materials and Atoms* **332**, 68–73, doi:10.1016/j.nimb.2014.02.032 (2014).
  23. Barberet, P., Daudin, L., *et al.* First results obtained using the CENBG nanobeam line: Performances and applications. *Nuclear Instruments and Methods in Physics Research, Section B: Beam Interactions with Materials and Atoms* **269** (20), 2163–2167, doi:10.1016/j.nimb.2011.02.036 (2011).
  24. Devès, G., Daudin, L., *et al.* An ImageJ plugin for ion beam imaging and data processing at AIFIRA facility. *Nuclear Instruments and Methods in Physics Research B* **348**, 62–67, doi:10.1016/j.nimb.2015.01.024 (2015).
  25. Yu, K., Chang, S., Park, S. J., Lim, J. & Lee, J. Titanium Dioxide Nanoparticles Induce Endoplasmic Reticulum Stress-Mediated Autophagic Cell Death via Mitochondria-Associated Endoplasmic Reticulum Membrane Disruption in Normal Lung Cells. *PLoS ONE*, 1–17, doi:10.1371/journal.pone.0131208 (2015).

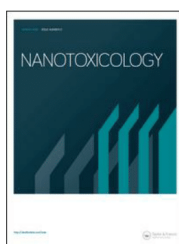


## Article 6

### ***“In situ* quantification of diverse titanium dioxide nanoparticles unveils selective endoplasmic reticulum stress-dependent toxicity”**

Marina Simon, Gladys Saez, Giovanna Muggiolu, Magali Lavenas, Quentin Le Trequesser, Claire Michelet, Guillaume Devès, Philippe Barberet, Eric Chevet, Denis Dupuy, Marie-Hélène Delville & Hervé Seznec (2017). *In situ* quantification of diverse titanium dioxide nanoparticles unveils selective endoplasmic reticulum stress-dependent toxicity.

**Nanotoxicology, 11:1, 134-145, DOI:  
10.1080/17435390.2017.1278803**



Nanotoxicology



ISSN: 1743-5390 (Print) 1743-5404 (Online) Journal homepage: <http://www.tandfonline.com/loi/inan20>


## In situ quantification of diverse titanium dioxide nanoparticles unveils selective endoplasmic reticulum stress-dependent toxicity

Marina Simon, Gladys Saez, Giovanna Muggiolu, Magali Lavenas, Quentin Le Trequesser, Claire Michelet, Guillaume Devès, Philippe Barberet, Eric Chevet, Denis Dupuy, Marie-Hélène Delville & Hervé Seznec

To cite this article: Marina Simon, Gladys Saez, Giovanna Muggiolu, Magali Lavenas, Quentin Le Trequesser, Claire Michelet, Guillaume Devès, Philippe Barberet, Eric Chevet, Denis Dupuy, Marie-Hélène Delville & Hervé Seznec (2017) In situ quantification of diverse titanium dioxide nanoparticles unveils selective endoplasmic reticulum stress-dependent toxicity, *Nanotoxicology*, 11:1, 134-145, DOI: [10.1080/17435390.2017.1278803](https://doi.org/10.1080/17435390.2017.1278803)

To link to this article: <http://dx.doi.org/10.1080/17435390.2017.1278803>

 [View supplementary material](#) 

 Accepted author version posted online: 03 Jan 2017.  
Published online: 25 Jan 2017.

 [Submit your article to this journal](#) 

 Article views: 43

 [View related articles](#) 

 [View Crossmark data](#) 

Full Terms & Conditions of access and use can be found at  
<http://www.tandfonline.com/action/journalInformation?journalCode=inan20>

NANOTOXICOLOGY, 2017  
<http://dx.doi.org/10.1080/17435390.2017.1278803>



## ORIGINAL ARTICLE

## *In situ* quantification of diverse titanium dioxide nanoparticles unveils selective endoplasmic reticulum stress-dependent toxicity

Marina Simon<sup>a,b,\*</sup>, Gladys Saez<sup>a,b,\*</sup>, Giovanna Muggioli<sup>a,b</sup>, Magali Lavenas<sup>c,d</sup>, Quentin Le Trequesser<sup>a,b,c,d</sup>, Claire Michelet<sup>a,b</sup>, Guillaume Devès<sup>a,b</sup>, Philippe Barberet<sup>a,b</sup>, Eric Chevet<sup>e,f</sup>, Denis Dupuy<sup>g,h</sup>, Marie-Hélène Delville<sup>c,d</sup> and Hervé Sez nec<sup>a,b</sup>

<sup>a</sup>Centre d'Etudes Nucléaires Bordeaux Gradignan (CENBG), Université de Bordeaux, Gradignan, France; <sup>b</sup>CNRS, UMR5797, Centre d'Etudes Nucléaires Bordeaux Gradignan (CENBG), Gradignan, France; <sup>c</sup>CNRS, UPR9048, Institut de Chimie de la Matière Condensée de Bordeaux (ICMCB), Pessac, France; <sup>d</sup>Institut de Chimie de la Matière Condensée de Bordeaux (ICMCB), Université de Bordeaux, Pessac, France; <sup>e</sup>INSERM, ERL440, "Oncogenesis Stress Signaling", Université Rennes 1, Rennes, France; <sup>f</sup>Centre de Lutte Contre le Cancer Eugène Marquis, Rennes, France; <sup>g</sup>INSERM, U869, IECB, Laboratoire ARNA, Bordeaux, France; <sup>h</sup>Université de Bordeaux, U869, IECB, Laboratoire ARNA, Bordeaux, France

## ABSTRACT

Although titanium dioxide nanoparticles (TiO<sub>2</sub> NPs) have been extensively studied, their possible impact on health due to their specific properties supported by their size and geometry, remains to be fully characterized to support risk assessment. To further document NPs biological effects, we investigated the impact of TiO<sub>2</sub> NPs morphology on biological outcomes. To this end, TiO<sub>2</sub> NPs were synthesized as nanoneedles (NNs), titanate scrolled nanosheets (TNs), gel-sol-based isotropic nanoparticle (INPs) and tested for perturbation of cellular homeostasis (cellular ion content, cell proliferation, stress pathways) in three cell types and compared to the P25. We showed that TiO<sub>2</sub> NPs were internalized at various degrees and their toxicity depended on both titanium content and NPs shape, which impacted on intracellular calcium homeostasis thereby leading to endoplasmic reticulum stress. Finally, we showed that a minimal intracellular content of TiO<sub>2</sub> NPs was mandatory to induce toxicity enlightening once more the crucial notion of internalized dose threshold beside the well-recognized dose of exposure.

## ARTICLE HISTORY

Received 29 July 2016  
 Revised 30 December 2016  
 Accepted 2 January 2017

## KEYWORDS

Titanium dioxide nanoparticles; morphology-dependent toxicology; ER stress; calcium homeostasis; *in situ* quantification

## Introduction

The high photocatalytic and super-hydrophilic properties of titanium dioxide nanoparticles (TiO<sub>2</sub> NPs) have made them popular for a wide variety of applications. Pigment grade titanium dioxide is widely used as a pigment due to its whiteness and high-refractive index. It can be found in paints, plastics, paper, inks, food, medicines (pills), and toothpaste. A very common application of TiO<sub>2</sub> NPs is as an additive in sunscreen cosmetics as a UV-attenuating filter agent. TiO<sub>2</sub> NPs have been engineered in terms of shapes and sizes for applications including their use as a functional component in self-cleaning cements, glass and paints; water purification systems, anti-fogging coatings for glass (Chen & Mao, 2007; Kaegi et al., 2008; Lee et al., 2010; Sadrieh et al., 2010). Tailoring sphere-shaped to fiber-shaped NPs such as nanowires, nanobelts and nanotubes is very attractive for their properties in photocatalysis, charge transfer and sensing due to their unique structures. TiO<sub>2</sub> NPs are produced in "pseudo-spherical" shape (such as the AEROXIDE P25) and also exist in low-dimensional TiO<sub>2</sub> nanomaterials such as one-dimensional nanotubes, nanorods, nanoneedles, nanobelts, and nanowires (Devan et al., 2012; Xia et al., 2003) or two-dimensional nanoplates (Zhuang et al., 2015) and titanate scrolled nanosheets (Liang et al., 2012) with different properties. For example, titanate scrolled nanosheets (TNs) have been recently developed for their exceptional electronic, optical and photocatalytic performance (Schwartzberg & Gray, 2012;

Yu et al., 2012). In recent years, many studies have also focused on the biomedical applications of TiO<sub>2</sub> NPs in areas such as cancer therapy, drug delivery systems, cell imaging, genetic engineering, and biosensors (Yin et al., 2013).

Parallel to these promising new applications in industry and in nanomedicine, TiO<sub>2</sub> NPs may generate environmental and health risks due to their specific properties supported by their size and geometry; this is actually source of great concerns. For many years, TiO<sub>2</sub> has been considered as biologically inert, suggesting that environmental or occupational exposure was relatively harmless and effectively cleared out of the body. However, their toxic potential remains largely unclear (Jovanovic, 2015; Kahru & Dubourguier, 2010; Yu et al., 2015b). Since NPs are used in therapy, it is a real challenge to detect, track and quantify them in living and biological samples and to correlate this with toxicity effects.

Many studies have reported that TiO<sub>2</sub> NPs elicit a toxic response in different biological systems including animals, mammalian cells, model organisms, and bacteria (Cai et al., 2011; Hamilton et al., 2009; Lewinski et al., 2008; Rahman et al., 2002; Setyawati et al., 2015b; Wang et al., 2013). Nevertheless, only a few ones have focused on the relationship between NPs morphology and toxicity (Zoroddu et al., 2014). It has been shown that longer TiO<sub>2</sub> nanobelts induced higher toxicity to both alveolar macrophages and mice than their shorter, spherical counterparts (Hamilton et al., 2009). Numerous *in vitro* studies have reported

CONTACT Hervé Sez nec [herve.seznec@cenbg.in2p3.fr](mailto:herve.seznec@cenbg.in2p3.fr) Marie-Hélène Delville [marie-helene.delville@icmb.cnrs.fr](mailto:marie-helene.delville@icmb.cnrs.fr)  
 \*Joint First Authors

Supplemental data for this article can be accessed [here](#).

© 2017 Informa UK Limited, trading as Taylor & Francis Group

65  
66  
67  
68  
69  
70  
71  
72  
73  
74  
75  
76  
77  
78  
79  
80  
81  
82  
83  
84  
85  
86  
87  
88  
89  
90  
91  
92  
93  
94  
95  
96  
97  
98  
99  
100  
101  
102  
103  
104  
105  
106  
107  
108  
109  
110  
111  
112  
113  
114  
115  
116  
117  
118  
119  
120  
121  
122  
123  
124  
125  
126  
127  
128

129 TiO<sub>2</sub> NPs toxicity in various cell types with different observations  
 130 (Federici et al., 2007; Lai et al., 2008; Li et al., 2008; Zoroddu et al.,  
 131 2014). As many NPs, TiO<sub>2</sub> NPs have been shown to localize within  
 132 the cells (Geiser et al., 2005; Osano et al., 2003; Simon et al.,  
 133 2011). It has been reported that a P25 suspension induces an  
 134 inflammation response in rat lungs. Fibrosis, pulmonary as well as  
 135 DNA damages have been described (Donaldson et al., 2001;  
 136 Oberdorster et al., 1994; Sager et al., 2008; Sayes et al., 2006; Sun  
 137 et al., 2012; Warheit et al., 2007; Zoroddu et al., 2014). TiO<sub>2</sub> NPs  
 138 are also able to generate free radicals and reactive oxygen species  
 139 (ROS), and raise DNA adduct formation in human lung fibroblasts  
 140 (Bhattacharya et al., 2009; Long et al., 2006; Toyooka et al., 2012;  
 141 Xia et al., 2006). In addition, in A549 cells, TiO<sub>2</sub> NPs induced mito-  
 142 chondrial injury in a dose-dependent way owing to reactive oxygen  
 143 species generation (Tang et al., 2013). Photogenotoxic  
 144 potential and genotoxicity have also been reported in different  
 145 cell systems (Oesch & Landsiedel, 2012; Vevers & Jha, 2008; Wang  
 146 et al., 2007). Tong et al. reported the effect of material morpho-  
 147 logy on the phototoxicity of TiO<sub>2</sub> NPs to bacteria *Escherichia coli*  
 148 and *Aeromonas hydrophila* (Tong et al., 2013).

149 Recent studies report the endoplasmic reticulum stress (ER  
 150 stress) as a common response in NPs related toxicity with studies  
 151 on TiO<sub>2</sub> NPs (Chen et al., 2014; Yu et al., 2015a; Zhang et al., 2012).  
 152 The endoplasmic reticulum (ER) is an important organelle, which  
 153 plays a role in folding and assembling of cellular proteins, in syn-  
 154 thesis of lipids and sterols, and in regulating the balance of the  
 155 intracellular calcium homeostasis, processes which are all depend-  
 156 ent on the ER internal homeostasis. The ER stress also known as  
 157 unfolded protein response (UPR) refers to an important cellular self-  
 158 protection mechanism, which can be activated to counteract the  
 159 cell situation of stress (overloading proteins or direct ER damage).  
 160 Previous works evidenced an alteration of calcium homeostasis in  
 161 different cell types after exposure to TiO<sub>2</sub> NPs (Koenen et al.,  
 162 2010; Simon et al., 2011). To date, only few studies have investi-  
 163 gated the relationship between NPs morphology and their toxicity;  
 164 they however, failed in providing any obvious links. Quantifying  
 165 NPs in biological systems is challenging but essential to elucidate  
 166 their interactions with the living organisms and the resulting toxic-  
 167 ity. Finally, whereas there are evidences of TiO<sub>2</sub> NPs toxicity, the  
 168 involved mechanisms are not yet fully elucidated.

169 As a consequence, the goal of this paper is to investigate and  
 170 rationalize the cellular homeostasis responses and ER stress induced  
 171 by different types of TiO<sub>2</sub> NPs (in terms of shape and size) in differ-  
 172 ent *in vitro* primary and immortalized human cell populations  
 173 (endothelial cells, epidermal keratinocytes and immortalized cancer-  
 174 ous cells). A careful attention was paid to the quantification of the  
 175 NPs internalization in order to establish a correlation with the subse-  
 176 quent intracellular ion homeostasis, the ER stress response as well  
 177 as the cell fate (differentiation, proliferation, death).

## 178 Methods

### 179 TiO<sub>2</sub> NPs synthesis and characterization

180 P25 nanoparticles (P25, AEROXIDE) were kindly provided by  
 181 Degussa/Evonik and used both for biological tests and as precursor  
 182 for all the synthesis performed in this study. Titanate scrolled  
 183 nanosheets (TNs) were produced *via* hydrothermal process  
 184 described by Kasuga (2006). Briefly, 2 g of P25 were introduced in  
 185 a 50 mL Teflon lined autoclave with 28 mL of 10 M sodium  
 186 hydroxide solution, sealed and heated at 130 °C for 20 h. The  
 187 white precipitate was washed with nitric acid (0.1 M) and water  
 188 for neutralization and identified as titanate scrolled nanosheets  
 189 (TNs). Nanoneedles (NNs) were obtained after a second

193 hydrothermal process applied on the TNs. An aqueous dispersion  
 194 of 660 mg of TNs was stabilized at pH 9, adjusted at 30 mL, and  
 195 sealed in the Teflon lined autoclave for a hydrothermal treatment  
 196 at 140 °C for 72 h (Nian & Teng, 2006). The resulting white powder  
 197 was then neutralized with water and identified as nanoobjects  
 198 called Nanoneedles (NNs) all along the paper. Isotropic NPs (INPs)  
 199 were finally synthesized using gel-sol method (Sugimoto et al.,  
 200 2003). Titanium isopropoxide (0.005 mol) was mixed with trietha-  
 201 nolamine (0.01 mol) and water reaching a final volume of 20 mL.  
 202 The solution was then sealed in Teflon lined autoclave for a  
 203 hydrothermal treatment at 140 °C for 72 h. The obtained white  
 204 powder was finally washed with deionized water. All the synthe-  
 205 sized NPs were kept in aqueous solution avoiding aggregation  
 206 issues. Mass concentrations were measured by drying a known  
 207 volume of solution and weighting the extracted powder.  
 208 Suspensions with concentration of 1 mg.mL<sup>-1</sup> were finally pro-  
 209 duced, sonicated and kept in the dark.

210 The physicochemical properties of TiO<sub>2</sub> NPs samples were char-  
 211 acterized by standard techniques. Specifically, the primary size and  
 212 morphological features of TiO<sub>2</sub> NPs were observed using  
 213 Transmission Electron Microscopy (TEM) using the Hitachi H7650  
 214 (120 kV). Powder X-ray diffraction was used to determine the phase  
 215 composition and crystallite size of each TiO<sub>2</sub> NPs and was per-  
 216 formed with Phillips PW1820 diffractometer. A Zeta potential ana-  
 217 lyzer (ZetaCompact®, CAD) was used to measure the zeta potential  
 218 and electrophoretic mobility of each TiO<sub>2</sub> NPs in the different  
 219 exposure media. The Hydrodynamic diameters were measured  
 220 using a Dynamic Light Scattering (Vasco, Cordouan technology).

### 221 Cell culture and TiO<sub>2</sub> NPs exposure

222 Human Epidermal Keratinocytes (HEK<sub>n</sub>) or Human Umbilical Vein  
 223 Endothelial Cells (HUVEC), derived from normal human tissues, were  
 224 obtained from Invitrogen (ThermoFischer Scientific). They were  
 225 respectively grown in EpiLife® (ThermoFischer Scientific,  
 226 MEPICFPRF500) or M200PRF® (ThermoFischer Scientific, M200PR  
 227 F500) complemented with LSGS™ with 100 mg.mL<sup>-1</sup> penicillin/  
 228 streptomycin. EpiLife® medium is a medium prepared without cal-  
 229 cium chloride for long-term and serum-free culture of human epi-  
 230 dermal keratinocytes supplemented with Human Keratinocyte  
 231 Growth Supplement (HKGS, S-001-5). M200-PRF® is a sterile liquid  
 232 medium for the culture of large vessel endothelial cells supple-  
 233 mented with Low-Serum Growth Supplement (LSGS, S-003-10).  
 234 Detailed formulation of these media can be found on the man-  
 235 ufactures' web site. HeLa cells (ATCC® CCL-2™) were obtained from  
 236 LGC-standards (Molsheim, France) and were grown in DMEM com-  
 237 pleted 2 mM L-glutamine and 100 mg.mL<sup>-1</sup> penicillin/streptomycin  
 238 (ThermoFischer Scientific). HUVEC, HEK<sub>n</sub> and HeLa cells were grown  
 239 in defined medium at 37 °C in a 5% (v/v) CO<sub>2</sub> humidified atmos-  
 240 phere and passages are realized at 80% confluency. The suspen-  
 241 sions of TiO<sub>2</sub> NPs were prepared in ultrapure water at a  
 242 concentration of 1 mg.mL<sup>-1</sup>. TiO<sub>2</sub> NPs were dispersed by intense  
 243 sonication pulses of 1 min at RT (750 W, 20 kHz, with 30% ampli-  
 244 tude) using a Vibra-Cell™ and a dedicated 3MM conical microprobe  
 245 (ThermoFischer Scientific). Suspensions were hereby known as  
 246 "stock suspensions". Stock suspensions were diluted at the appro-  
 247 priate concentration in defined culture medium in order to obtain  
 248 exposure suspension ranging from 0 to 20 µg.cm<sup>-2</sup> (final  
 249 concentration).

### 250 Cell preparation for high-resolution ion beam micro-analysis 251 (IBA)

252 Cell cultures (HUVEC, HEK<sub>n</sub> and HeLa) were cultured directly onto  
 253 ion beam microprobe sample holders as adapted from previous  
 254  
 255  
 256

Q3

studies (Le Trequesser et al., 2014). Briefly, cells were directly grown at high confluence on 2  $\mu\text{m}$ -thick polycarbonate foil for 24 h in appropriate culture medium, and then exposed to  $\text{TiO}_2$  NPs for 16 to 24 h. Control cells were prepared similarly with no addition of  $\text{TiO}_2$  NPs. Cells were rinsed once in culture medium, and very briefly rinsed twice in ultrapure water to remove excess of extracellular salts from culture medium. Finally, cells were plunge-frozen at  $-150^\circ\text{C}$  into liquid nitrogen chilled 2-methylbutane (ReagentPlus,  $\geq 99\%$ , Sigma-Aldrich) and freeze-dried using a freeze-dryer (Christ alpha, ThermoFischer Scientific) in two phases: A phase of primary desiccation of 12 to 24 h ( $T^\circ\text{C} = -99^\circ\text{C}$ ,  $p = 0.001$  mbar) followed by a phase of secondary desiccation of 24 h ( $T^\circ\text{C} = +40^\circ\text{C}$ ,  $p = 0.001$  mbar). With no contamination and no ionic diffusion, freeze-drying was found to be the most adapted process.

#### Ion beam micro-analysis (IBA)

Single cell quantitative analysis of the chemical element (quantitative analysis and element distribution) were carried out with a high-resolution microprobe beam line (AIFIRA, CENBG) using complementary ion beam analytical techniques ( $\mu\text{-STIM}$   $\mu\text{-PIXE}$ ). Protocols are described in previous works (Devès et al., 2004; Le Trequesser et al., 2014; Simon et al., 2011).

#### Cell proliferation

Cell populations were seeded in six-well plates at a density of 10,000 cells/well for HeLa or 20,000 cells/well for HEK293 and HUVEC, respectively. For each condition, the following procedure was used: eight different wells were prepared (one for each day, numbered 1 to 8), filled with the cells and let alone for 24 h. One well for each counting day was seeded for each condition. After this delay of 24 h of culture, each cells well was exposed to 2 ml of fresh medium supplemented with the exposure suspensions containing P25, Titanate scrolled nanosheets (TNs), nanoneedles (NNs) or Isotropic NPs (INPs) at a final concentration of  $2 \mu\text{g}\cdot\text{cm}^{-2}$ . Well 1 was examined after 1 day, well 2 after 2 days and so on, so that the cell culture was not contaminated by any component used to proceed to the counting. Cells were then harvested using 400  $\mu\text{L}$  of trypsin-EDTA 0.25% (v/v) (Invitrogen). After 5 min of centrifugation at 1200 rpm, the cell pellet was resuspended in an appropriate volume of fresh culture medium. The same volume of Trypan blue was added and 10  $\mu\text{L}$  of the cell suspension is counted using a cell counter (TC20, BioRad). The operation was proceeded on the 8 wells, one per day. 1 ml of fresh culture medium was added every 2 days in each well. The experiment was performed in duplicate.

For HEK293, the same procedure was used, but cells are counted every two days, because of the slow proliferation rate of keratinocytes.

#### Quantitative real-time PCR

Total RNA was extracted from cells at different times (from 1 to 24 h) after NPs exposure using the RNeasy mini kit (Qiagen) according to the manufacturer's instructions. Complementary DNA synthesis from 300 to 500 ng of total RNA was performed using random hexamer primers and QuantiTect Reverse Transcription kit (Qiagen). Quantitative real-time PCR were realized on a LightCycler<sup>®</sup>96 (Roche Diagnostics) using the Fast start essential Green master (Roche Diagnostics), according to the manufacturer's instructions. Reaction volumes of 20  $\mu\text{L}$  are subjected to the following cycles: a pre-incubation phase ( $95^\circ\text{C}$ , 10 min), followed by

45 cycles of a 3-step amplification phase ( $95^\circ\text{C}$ , 10 s,  $60^\circ\text{C}$ , 10 s and  $72^\circ\text{C}$ , 10 s) and finally, a melting phase ( $95^\circ\text{C}$ , 10 s,  $65^\circ\text{C}$ , 60 s and  $97^\circ\text{C}$ , 1 s). Results were normalized with the *hGAPDH* and *h18S* genes and analyzed using software LightCycler<sup>®</sup>96 SW 1.1 (Roche Diagnostics). The primers sequences used in these experiments are described in Table S3 (supplementary data).

#### In situ mitochondrial staining with TMRM (TetraMethylRhodamine)

TMRM diluted in DMSO was added to the cell culture medium at a final concentration of 500 nM. Cells were incubated in presence of  $\text{TiO}_2$  NPs for from 1 to 20 h and then with TMRM for 30 min at  $37^\circ\text{C}$  in the cell incubator. Cell culture medium was changed and rinsed before observation using live fluorescence microscopy.

#### In cellulo ER stress detection - CHOP immunodetection

Cell populations are seeded on glass slides and grown for 24 h. Then, cells are exposed to  $\text{TiO}_2$  NPs for 16 or 24 h. Tunicamycin treatment (20 h incubation,  $5 \mu\text{g}\cdot\text{mL}^{-1}$ , Calbiochem) is used as positive control for ER stress induction. Tunicamycin, an inhibitor of protein glycosylation, is used as model drug for disrupting the ER homeostasis-induced Unfolded Protein Response (UPR). After exposure, cells were fixed with 2% (w/v) paraformaldehyde (Sigma) in phosphate-buffered saline (PBS) medium (pH 7.4, without  $\text{Ca}^{2+}$  and  $\text{Mg}^{2+}$ , Invitrogen) for 15 min at room temperature (RT), under agitation. Then, cell permeabilization and saturation were performed using a solution containing 0.2% (v/v) Triton X-100 (Sigma), 10% FCS (Dutscher) in PBS for 30 min, at room temperature. Cells were incubated overnight at  $4^\circ\text{C}$  with anti-human CHOP mouse monoclonal antibody (L63F7, Cell Signaling) and 2 h at RT with goat anti-mouse IgG conjugated to AlexaFluor<sup>®</sup>488 antibody (Molecular Probes, Invitrogen) at 1/3200 and 1/2000 dilutions, respectively. Cells were then rinsed three times with PBS and nuclei stained with 10  $\mu\text{M}$  Hoechst<sup>®</sup>33342 in PBS. Slides were mounted using Prolong Gold Antifade Reagent (Invitrogen) and visualized on Zeiss AxioObserver Z1 (Carl Zeiss MicroImaging, GmbH).

#### Cell preparation for transmission electron microscopy (TEM)

Cells grown on 8-well Labtek II (Nunc) were exposed during 24 h to  $2 \mu\text{g}\cdot\text{cm}^{-2}$  of the different  $\text{TiO}_2$  NPs. Protocols are described in previous works (Simon et al., 2011).

#### Statistical analysis

Each experiment was repeated at least three times, independently. Data from all the experiments were analyzed using the "R" software. Comparison between element concentrations in exposed cells were made using non-parametric Kruskal-Wallis test in order to test null hypothesis, followed when necessary by a post-hoc Nemenyi test to identify groups presenting differences in their concentration. Relation between calcium, iron and titanium concentrations were tested using a linear model by both ordinary least square regression method (OLS-LM) and an alternative robust fitting of linear model less sensitive to points with a high leverage. Significance was set at  $p < 0.05$  (\*).

## Results

### Synthesis and physicochemical properties of the different $\text{TiO}_2$ NPs

In the current study, we synthesized  $\text{TiO}_2$  nanoneedles (NNs) (Nian & Teng, 2006), titanate scrolled nanosheets (TNs) (Kasuga, 2006)

321  
322  
323  
324  
325  
326  
327  
328  
329  
330  
331  
332  
333  
334  
335  
336  
337  
338  
339  
340  
341  
342  
343  
344  
345  
346  
347  
348  
349  
350  
351  
352  
353  
354  
355  
356  
357  
358  
359  
360  
361  
362  
363  
364  
365  
366  
367  
368  
369  
370  
371  
372  
373  
374  
375  
376  
377  
378  
379  
380  
381  
382  
383  
384



4 M. SIMON ET AL.

385 from AEROXIDE P25 (P25, classical spherical shape with hetero-  
386 geneous crystallinity) as well as isotropic NPs (INPs, pure ana-  
387 tase) from titanium alkoxides (Sugimoto et al., 2003). These TiO<sub>2</sub>  
388 NPs, along with the AEROXIDE P25, allowed us to examine the  
389 effects of material morphologies as well as crystallinity on TiO<sub>2</sub>  
390 nanotoxicity. Their characteristics are summarized and shown in  
391 Figure 1 with representative transmission electron microscopy  
392 (TEM) images.

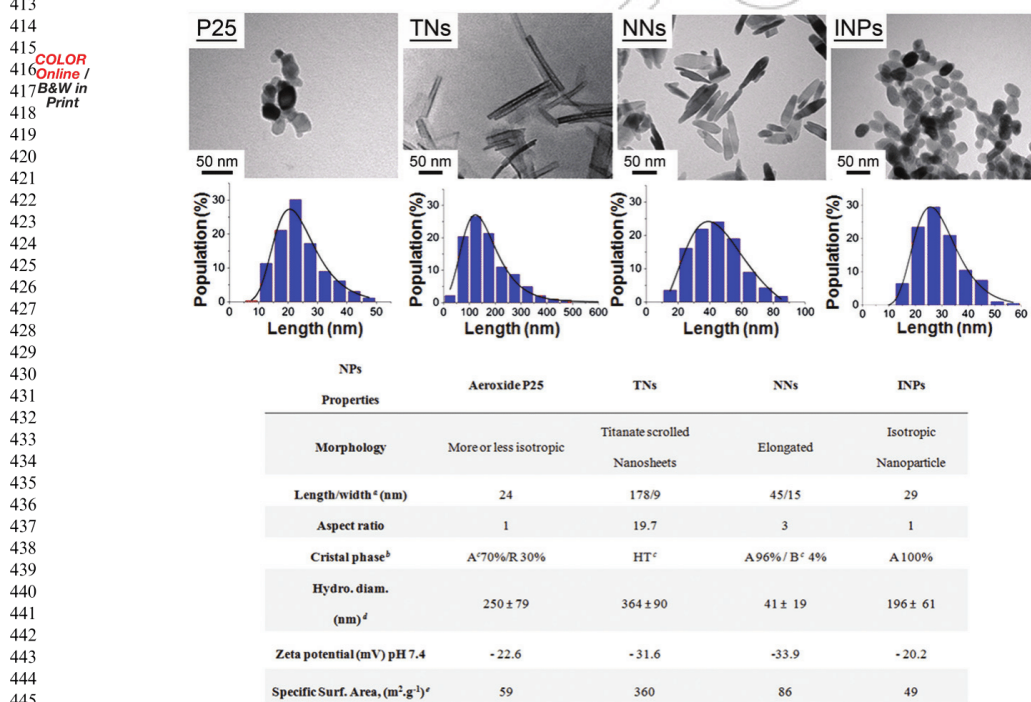
393 All along the synthesis procedure, the TiO<sub>2</sub> NPs were kept in  
394 solution to avoid aggregation due to drying. Nevertheless, and  
395 despite their negative surface at physiological pH (pH 7.4), these  
396 NPs exhibited a tendency to agglomerate in water and in the dif-  
397 ferent biological media used as illustrated by the hydrodynamic  
398 diameter variations (Figure S1). The latter also showed that P25  
399 and TNs were subjected to swift re-agglomeration after sonication  
400 as opposed to the much more stable colloidal NNs. The use of dif-  
401 ferent and specific culture media such as EpiLife®, M200-PRF® or  
402 DMEM strongly modified the behavior and agglomeration state of  
403 the NPs. Indeed, TNs and P25 flocculated in such media most  
404 likely due to their content in amino acids, vitamins, and inorganic  
405 salts (Figure S1).

406 These observations strongly indicate that the behavior of TiO<sub>2</sub>  
407 NPs in biological media can be drastically modified and should be  
408 considered an important factor that could influence the results of  
409 the toxicity evaluation.

#### Multi-parametric influences of TiO<sub>2</sub> NPs on cell proliferation

450 To evaluate the toxic effects of the different TiO<sub>2</sub> NPs, we studied  
451 the cell proliferation of the three different cells lines upon expos-  
452 ure to NPs. All TiO<sub>2</sub> NPs (P25, INPs, NNs, TNs) were toxic pointing  
453 HUVEC cells and toxicity was both morphology- (Figure 2(a)) and  
454 dose-dependent (Figure S2). The impact of TiO<sub>2</sub> NPs morphology  
455 on toxicity was obvious at a concentration of 2 μg.cm<sup>-2</sup> and after  
456 8 days of exposure. Indeed, P25, INPs and TNs dramatically  
457 affected proliferation, whereas NNs were harmless under these  
458 conditions. To determine the impact of the exposure dose for  
459 each type of TiO<sub>2</sub> NPs, a dose response from 0.5 μg.cm<sup>-2</sup> to  
460 20 μg.cm<sup>-2</sup> was performed. Toxic effects of INPs and TNs were  
461 observed at doses as low as 0.5 μg.cm<sup>-2</sup> (Figure S2). An exposure  
462 dose higher than 20 μg.cm<sup>-2</sup> was necessary to observe a decrease  
463 of the cell proliferation to less than 50% for NNs, by contrast with  
464 the other TiO<sub>2</sub> NPs (Figure S2).

465 The same sets of TiO<sub>2</sub> NPs were also incubated with HEK293T  
466 (Figure 2(b)), the resulting proliferation assays indicated that P25,  
467 NNs, and INPs exhibited a moderate dose-dependent toxicity even  
468 after several days. The most striking impact was observed for the  
469 elongated TNs, which dramatically and significantly decreased the  
470 HEK293T viability to about 20% of that of the control (2 μg.cm<sup>-2</sup> and  
471 8 days exposure, Figure 2(b)). Moreover, HeLa cells proliferation  
472 was only impaired at the highest doses (>20 μg.cm<sup>-2</sup> for INPs and  
473 >4 μg.cm<sup>-2</sup> for TNs) while no significant difference could be  
474



446  
447  
448  
449  
450  
451  
452  
453  
454  
455  
456  
457  
458  
459  
460  
461  
462  
463  
464  
465  
466  
467  
468  
469  
470  
471  
472  
473  
474  
475  
476  
477  
478  
479  
480  
481  
482  
483  
484  
485  
486  
487  
488  
489  
490  
491  
492  
493  
494  
495  
496  
497  
498  
499  
500  
501  
502  
503  
504  
505  
506  
507  
508  
509  
510  
511  
512

Figure 1. Physical and chemical characterizations of the different morphologies of TiO<sub>2</sub> NPs. Top: Transmission Electron Microscopy images of P25 and synthesized TiO<sub>2</sub> NPs (TNs, NNs and INPs) and their respective size distributions based on at least 300 NPs. Down: Physical characteristics <sup>a</sup>From TEM, <sup>b</sup>From XRD, <sup>c</sup>A = Anatase, R = Rutile, HT = Hydrogen Titanate, B = Brookite, <sup>d</sup>From DLS analysis, <sup>e</sup>From calculations or BET analysis.

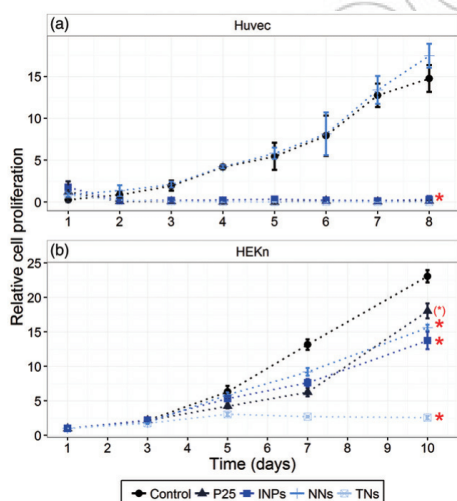
513 seen with P25 or NNs (Figure S2). Thus, according to these observa-  
514 tions, TiO<sub>2</sub> NPs impact on cell viability/proliferation not only  
515 depends on the dose and on the morphology of NPs but also on  
516 the cell types.

#### 517 TiO<sub>2</sub> NPs toxicity is related to the titanium intracellular content

518 To define the relationship between toxicity, titanium intracellular  
519 concentration and NPs type, we quantified the concentrations of  
520 titanium and the overall intracellular ion content (such as phos-  
521 phorus, potassium, calcium, ...) in single cell using  $\mu$ -PIXE (Le  
522 Trequesser et al., 2014).  $\mu$ -PIXE was performed on the three differ-  
523 ent cell types exposed to TiO<sub>2</sub> NPs at 2  $\mu\text{g}\cdot\text{cm}^{-2}$  for 20 h. This anal-  
524 ysis revealed a marked heterogeneity of the intracellular titanium  
525 content per cell in a given population, and also depending on the  
526 nature of TiO<sub>2</sub> NPs and the cell type (Figure 3). Indeed, titanium  
527 intracellular content in HEKn was in average lower than in HUVEC  
528 cells. As for example with P25, the intracellular titanium content is  
529 10 times lower in HEKn (0.14  $\pm$  0.1  $\mu\text{g}\cdot\text{cm}^{-2}$ ) than in HUVEC  
530 (1.36  $\pm$  0.1  $\mu\text{g}\cdot\text{cm}^{-2}$ ) (Table S1 and S2). Interestingly, a strong cor-  
531 relation was observed between the toxicity level (Figure 2) and  
532 the titanium content (Figure 3). NNs, which show no sign of *in*  
533 *vitro* toxicity towards HUVEC also exhibit a significantly low-intra-  
534 cellular titanium amount as exemplified by the single cell quanti-  
535 tative analysis (Figure 3(c)). In the case of HEKn, when the cells  
536 were exposed to P25, INPs and NNs they presented the same toxic-  
537 ity reply despite different intracellular titanium contents (Figure  
538 3(c)) suggesting that a minimal intracellular titanium content in a  
539 minimal number of cells per population is necessary but not suffi-  
540 cient to induce *in vitro* toxicity, which is also strongly dependent  
541 on the intrinsic morphology of the NPs.

542 Finally, the chemical distribution maps of titanium (Ti) at the  
543 single cell level (phosphorus distribution was used to delineate  
544 the cellular area) in HUVEC (Figure 3(a)) and HEKn cells (Figure  
545 3(b)) showed high heterogeneity of the titanium content within

552 COLOR  
553 Online /  
554 B&W in  
555 Print



573 **Figure 2.** Effect of TiO<sub>2</sub> NPs morphologies (P25, INPs, NNs, TNs) on human cell  
574 proliferation. Relative cell proliferation of (a) HUVEC and (b) HEKn. Exposure dose  
575 is 2  $\mu\text{g}\cdot\text{cm}^{-2}$ . Asterisks indicate significant differences with untreated groups at  
576 respectively day 8 (HUVEC) and day 10 (HEKn) (Kruskal-Wallis test (\*):  $p < 0.05$ ;  
577 (†):  $p < 0.06$ ) and Nemenyi post hoc test.

577 cell population as well as between the two cell types. NPs toxicity  
578 was noticeable when a minimal number of cells containing a min-  
579 imal amount of titanium per cell is reached (in HUVEC,  
580  $>5 \mu\text{g}\cdot\text{cm}^{-2}$ ,  $p > 0.005$ ).

581 Thus, TiO<sub>2</sub> NPs toxicity with regards to a given cell is a function  
582 of the intracellular titanium content most likely conditioned by  
583 the ability of the cells to internalize NPs and NPs behavior in bio-  
584 logical medium. To confirm this observation, we exposed HEKn to  
585 10  $\mu\text{g}\cdot\text{cm}^{-2}$  of TiO<sub>2</sub> NPs for 20 h (Figure 3). The resulting quanti-  
586 tative analysis revealed that the intracellular titanium content was  
587 effectively increased but in a limited way suggesting that the *in*  
588 *vitro* toxicity was much more related to the intracellular content  
589 of TiO<sub>2</sub> NPs than to the initial exposure dose.

#### 590 TiO<sub>2</sub> NPs internalization modifies the intracellular ionic 591 homeostasis

592 P25 internalization in human primary keratinocytes was previously  
593 described to induce an elevated and related accumulation of  
594 intracellular calcium (Simon et al., 2011). For HUVEC cells, a clear  
595 correlation between toxicity, intracellular titanium and intracellular  
596 calcium contents was established (Figure 4) for a NPs dose of  
597 exposure of 2  $\mu\text{g}\cdot\text{cm}^{-2}$  for 16–20 h. The results observed for NNs  
598 (low titanium and calcium contents) are coherent with the absence  
599 of toxicity detected for these TiO<sub>2</sub> NPs (Figure 2(a) and  
600 Table S1).

601 In the case of HEKn, a correlation between the increase of the  
602 intracellular calcium content and the internalized titanium content  
603 was established when the threshold of 0.01  $\mu\text{g}\cdot\text{cm}^{-2}$  in intracel-  
604 lular titanium content was reached and this for all the types of TiO<sub>2</sub>  
605 NPs (Figure S3). We also tested the effect of varying the extracel-  
606 lular calcium concentration in the culture medium of HEKn. Ac-  
607 cording to this protocol, we induced the keratinocyte differenti-  
608 ation by increasing by a factor of 20, the extracellular calcium  
609 concentration in the culture medium (1.2 mM). We then per-  
610 formed  $\mu$ -PIXE analysis to measure the intracellular content of  
611 titanium and calcium after 20 h of exposure of the different TiO<sub>2</sub>  
612 NPs. As illustrated in Figure S4, the control cells showed similar  
613 intracellular calcium contents (around 0.1  $\pm$  0.02  $\mu\text{g}\cdot\text{cm}^{-2}$ ) no mat-  
614 ter the calcium concentrations in culture media. In high calcium  
615 condition, HEKn cells exhibited the same intracellular calcium con-  
616 centration whether they were exposed or not to NPs (Table S2).  
617 When exposed, their internal titanium content remains very low  
618 (ranging from 0 to 0.04  $\mu\text{g}\cdot\text{cm}^{-2}$ , for TNs and INPs, respectively)  
619 and in the same range whatever the NPs type (Figure S4 and  
620 Table S2). This suggests that the regulation of the cellular calcium  
621 metabolism is not impaired in differentiated HEKn cells (they  
622 remain able to control the calcium efflux between their extra- and  
623 intracellular compartments) and that HEKn are far less permeable  
624 to TiO<sub>2</sub> NPs internalization than HUVEC.

625 The fact that the titanium intracellular content in differentiated  
626 HEKn is lower than in the proliferating cells and independent of  
627 the type of NPs could suggest a role of the cellular function with  
628 regards to a potential sensitivity to TiO<sub>2</sub> NPs uptake and the sub-  
629 sequent toxicity issues. To confirm this observation, we exposed  
630 the undifferentiated HEKn (low-calcium medium) to a higher dose  
631 of TiO<sub>2</sub> NPs (10  $\mu\text{g}\cdot\text{cm}^{-2}$ ), and measured the resulting titanium  
632 intracellular content (Figure 3). This set of experiments showed  
633 that even at doses as high as 10  $\mu\text{g}\cdot\text{cm}^{-2}$  (incubation for 20 hours),  
634 the intracellular uptake of titanium remains independent of the  
635 external concentration and coherent with the observations made  
636 at 2  $\mu\text{g}\cdot\text{cm}^{-2}$  (Table S2). Moreover, the intracellular contents for  
637 both calcium and iron, were elevated with positive correlation for  
638 NNs, which are the most internalized in the HEKn cells. It is also  
639 640

6 M. SIMON ET AL.

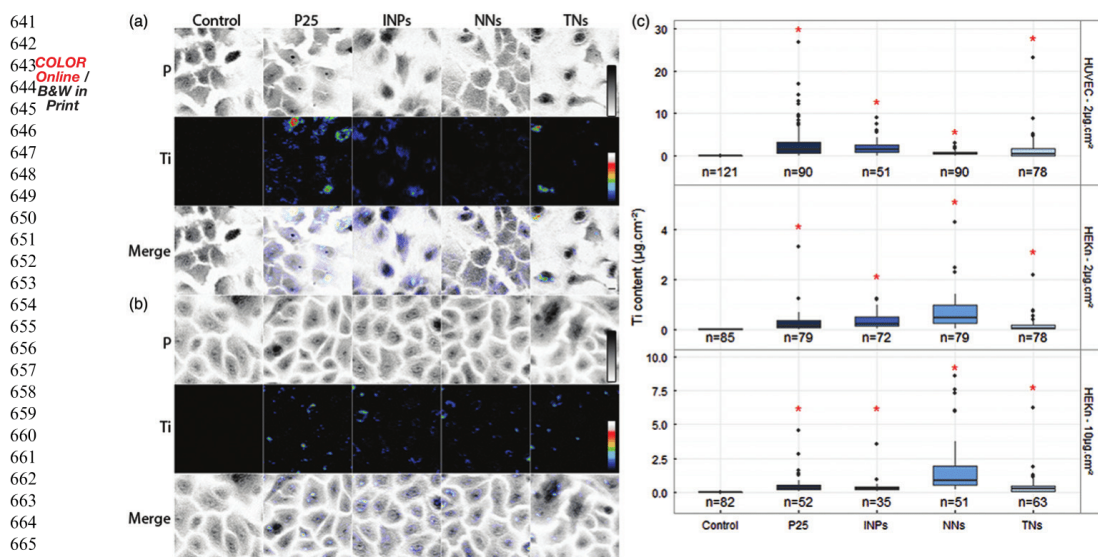


**Figure 3.**  $\mu$ -PIXE analysis of HUVEC and HEK293 after incubation with different  $\text{TiO}_2$  NPs (P25, INPs, NNs, TNs). (a,b) Chemical mapping of the titanium intracellular content in HUVECs (a) and HEK293 (b). The distribution maps for phosphorus and titanium are depicted. Two-dimensional mapping of distributions and intracellular contents of phosphorus (P) and titanium (Ti) are expressed in gray scale and in false color scale (blue-green-red), respectively. Merge of P and Ti distributions. Scale bar: 10  $\mu\text{m}$ . (c) Intracellular titanium content per cell in HUVEC (top), HEK293 (middle) (dose of exposure: 2  $\mu\text{g}\cdot\text{cm}^{-2}$ ) and in HEK293 (down) (dose of exposure: 10  $\mu\text{g}\cdot\text{cm}^{-2}$ ). (n) corresponds to the number of cells analyzed per condition. Asterisks over distributions indicate significant differences with untreated groups (Kruskal–Wallis test ( $p < 0.05$ ) and post hoc Nemenyi test ( $p < 0.05$ )). When not specified, experiments were performed 16 to 20 h after exposure with 2  $\mu\text{g}\cdot\text{cm}^{-2}$  of  $\text{TiO}_2$  NPs. Controls correspond to untreated cell populations.

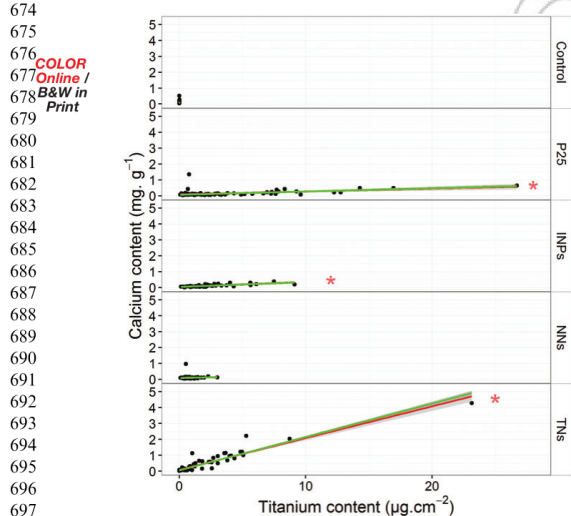


**Figure 4.** Effect of the  $\text{TiO}_2$  NPs on cellular homeostasis. Single cell quantitative analysis of the intracellular titanium (in  $\mu\text{g}\cdot\text{cm}^{-2}$ ) and calcium concentrations (in  $\text{mg}\cdot\text{g}^{-1}$ ) measured by  $\mu$ -PIXE in HUVEC exposed to 2  $\mu\text{g}\cdot\text{cm}^{-2}$  of different  $\text{TiO}_2$  NPs morphologies (P25, INPs, NNs and TNs). A black dot corresponds to one cell. The heterogeneity of the titanium intracellular content per cell is also well depicted. Relations between calcium and titanium contents were evaluated using a linear model with ordinary least square regression (red) or robust fitting (green). Asterisks indicate significant positive slopes for linear model ( $p < 0.05$ ).

interesting to note that the content of iron was also elevated in this condition. EpiLife<sup>®</sup> contains ferric sulfate ( $\text{Fe}_2(\text{SO}_4)_3 - 7\text{H}_2\text{O}$ ) and calcium chloride ( $\text{CaCl}_2 - 2\text{H}_2\text{O}$ ). This observation could suggest that  $\text{TiO}_2$  NPs favor (i) the internalization of free positively charged ions in the intracellular compartment, (ii) ionic homeostasis modifications and the subsequent metabolic consequences (cell stress, cell differentiation, cell death).

#### ***TiO<sub>2</sub> NPs internalization induced marked ER stress***

$\text{TiO}_2$  NPs induced a clear disruption of the calcium homeostasis, itself related to many of stress pathways (ROS, ER stress) (Djurišić et al., 2015; Jacobson & Duchon, 2002). To better characterize the influences of  $\text{TiO}_2$  NPs on these different stress pathways, selected target gene expression was examined by Real Time quantitative Polymerase Chain Reaction (RT-qPCR) assay (Higa et al., 2014). HUVEC cells were exposed to 2  $\mu\text{g}\cdot\text{cm}^{-2}$  of the diverse types of  $\text{TiO}_2$  NPs for 20 h. Total RNA was extracted and analyzed using RT-qPCR. The expression analysis was performed using both *hGAPDH* and *h18S*, as internal standards.

#### ***ROS pathway***

SOD1, SOD2, CAT1, CAT2, GPX expression were tested. Gene expression analysis revealed some differences between controls and exposed HUVEC cells. No difference was found for the superoxide dismutase1 (SOD1), the catalases (CAT1 and 2) or the glutathione peroxidase (GPX1). However, after 6 h of NPs exposure, the expression level of SOD2 was significantly increased and depended on the type of NPs (10 times higher in the presence of TNs, and 2 to 4 times when incubated with INPs and P25).

705  
706  
707  
708  
709  
710  
711  
712  
713  
714  
715  
716  
717  
718  
719  
720  
721  
722  
723  
724  
725  
726  
727  
728  
729  
730  
731  
732  
733  
734  
735  
736  
737  
738  
739  
740  
741  
742  
743  
744  
745  
746  
747  
748  
749  
750  
751  
752  
753  
754  
755  
756  
757  
758  
759  
760  
761  
762  
763  
764  
765  
766  
767  
768

769  
770  
771 **COLOR**  
772 *Online /*  
773 *B&W in*  
774 *Print*

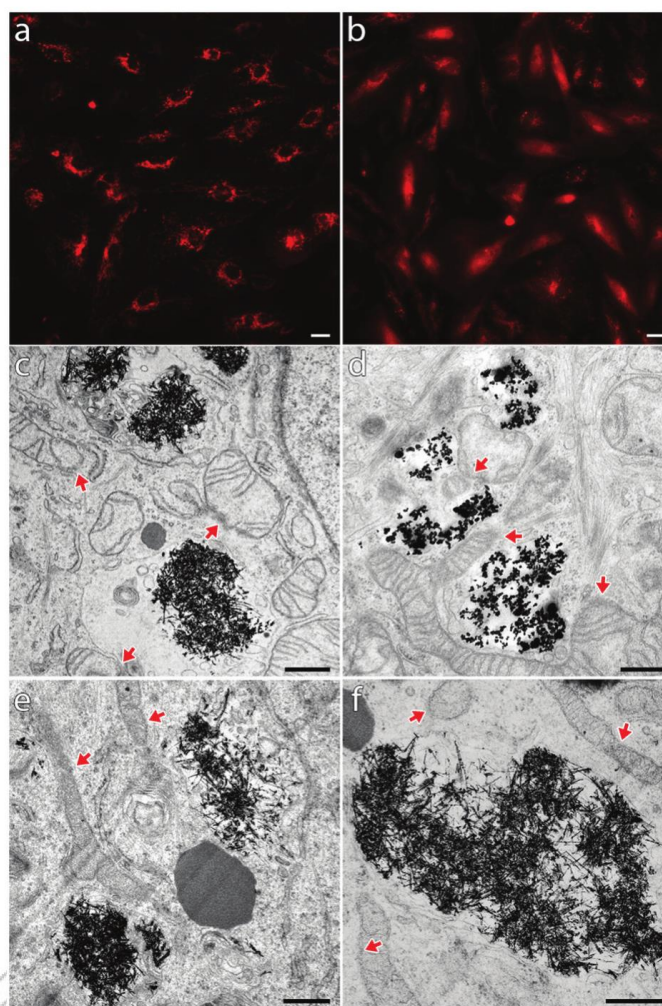


**Figure 5.** Effect of  $\text{TiO}_2$  NPs on the mitochondria. (a and b) The mitochondrial membrane potential ( $\Delta\Psi_m$ ) was monitored using TMRM staining. The intensity of TMRM fluorescence was detected using live cell imaging and fluorescent microscopy. HUVEC cells were loaded with TMRM (500 nM) during 30 min after 6 h exposure with  $2 \mu\text{g}\cdot\text{cm}^{-2}$  of  $\text{TiO}_2$  NPs. (a) HUVEC cells (control). (b) HUVEC cells exposed to TNs ( $2 \mu\text{g}\cdot\text{cm}^{-2}$ , 6 hours). Scale bar:  $10 \mu\text{m}$ . (c–f) Transmission electron microscopy analysis of HeLa and HUVEC cells exposed to  $2 \mu\text{g}\cdot\text{cm}^{-2}$  for 20 h to diverse morphologies of  $\text{TiO}_2$  NPs. (c and d) HeLa cells with TNs (c) and P25 (d). (e and f) HUVEC exposed to TNs.  $\text{TiO}_2$  NPs are visualized as dark and dense aggregates. Arrows signal damaged mitochondria (\*). Scale bar:  $500 \text{ nm}$ .

This suggested that the ROS production in the presence of  $\text{TiO}_2$  NPs may preferentially be associated to mitochondrial dysfunction.

#### Mitochondria

As the ROS pathway analysis pointed towards the mitochondria as a site potentially affected by  $\text{TiO}_2$  NPs, we evaluated the mitochondrial membrane potential ( $\Delta\Psi_m$ ) using Tetramethylrhodamine Methyl Ester (TMRM). Untreated cells exhibited a homogenous and intense labeling of their mitochondrial network at both single cell and cell population levels. By contrast, after their exposure to  $\text{TiO}_2$  NPs, TMRM labeling was

diffuse, heterogeneous and weak (Figure 5(a,b)). This observation corroborates marked mitochondrial and metabolic dysfunctions in relation to the presence of the  $\text{TiO}_2$  NPs. Moreover, as TMRM is also an indicator of cell death, this observation is in agreement with our previous findings on cell proliferation and toxicity.

To confirm this observation between  $\text{TiO}_2$  NPs toxicity and mitochondrial dysfunction, we also performed TEM analysis on both HUVEC and HeLa exposed to  $\text{TiO}_2$  NPs with  $2 \mu\text{g}\cdot\text{cm}^{-2}$  for several hours and confirmed the micro-structural alterations of mitochondria in the vicinity of internalized  $\text{TiO}_2$  NPs aggregates (Figure 5(c–f)). These alterations correspond mainly to a mitochondrial membrane disruption and internal matrix disorganization.

833  
834  
835  
836  
837  
838  
839  
840  
841  
842  
843  
844  
845  
846  
847  
848  
849  
850  
851  
852  
853  
854  
855  
856  
857  
858  
859  
860  
861  
862  
863  
864  
865  
866  
867  
868  
869  
870  
871  
872  
873  
874  
875  
876  
877  
878  
879  
880  
881  
882  
883  
884  
885  
886  
887  
888  
889  
890  
891  
892  
893  
894  
895  
896

8 M. SIMON ET AL.

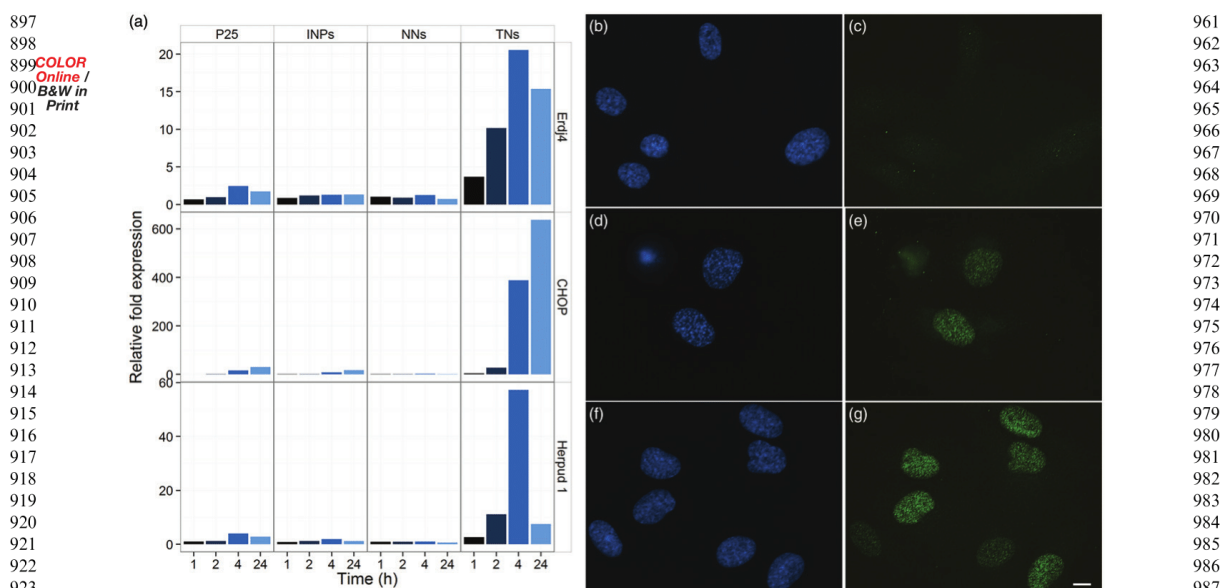


**Figure 6.** Time-dependent induction of ER stress markers related to the level of  $\text{TiO}_2$  NPs toxicity in HUVEC. (a) Time-response of *Erdj4*, *CHOP* and *Herpud 1* transcript levels induced by  $\text{TiO}_2$  NPs at  $2 \mu\text{g}\cdot\text{cm}^{-2}$ . The results are expressed as mean of at least three independent experiments.  $*p < 0.01$  compared to the control. (b–g) *in cellulo* detection of *CHOP*, a specific ER stress marker in HUVEC cells. Paraformaldehyde-fixed cell nuclei are stained by Hoechst<sup>33342</sup> (blue, b, d, f) and counterstained with anti-murine antibody targeted to the human protein *CHOP* (L63F7, Cell Signaling) coupled to Goat anti-mouse AF488 secondary antibody (green, c, e, g). b, c) HUVEC cells (control). d, e) HUVEC cells exposed to  $2 \mu\text{g}\cdot\text{cm}^{-2}$  of TNs during 16 h. f, g) Positive-control used to specifically induced *CHOP* expression and specific subcellular localization by incubating cells 20 h to Tunicamycin ( $5 \mu\text{g}\cdot\text{mL}^{-1}$ ). Scale bar:  $10 \mu\text{m}$ .

Taken together, these results showed that  $\text{TiO}_2$  NPs induced (i) calcium homeostasis alteration, (ii) moderate ROS production and (iii) mitochondrial dysfunction.

#### ER stress

The expression of *chop*, *Erdj4*, *Herpud1* was quantified in HUVEC cells exposed to different types of  $\text{TiO}_2$  NPs ( $2 \mu\text{g}\cdot\text{cm}^{-2}$ ) in a time course mode using RT-qPCR (Figure 6(a)). Correlation between the time-response and the level of expression of the selected genes was strongly dependent on the nature of  $\text{TiO}_2$  NPs and therefore on their level of toxicity. Indeed the most toxic TNs (cell proliferation threshold to zero for the smallest content of titanium per cell) induced the expression of *DDIT3/chop*, *Erdj4*, *Herpud1* after only 2 h of exposure ( $>30$  fold for *DDIT3/chop*) and maintained up-regulated during the following 20 h. By contrast, for NNs, which are scarcely internalized in HUVEC cells, the expression level of these three genes exhibited very little change. Moderate and time-dependent increases of expression levels were observed for the cells incubated with P25 and INPs ( $>8$  fold for *DDIT3/chop*, 4 h after incubation). Despite their higher content in the cells as compared to TNs, they showed less detrimental consequences, phenomenon likely to be attributable to their lower surface area and the scrolled structure of the TNs, which allows a higher interface with the environment. In addition, this positive correlation between the level of  $\text{TiO}_2$  NPs toxicity and the expression of ER stress markers at the RNA level was confirmed at the protein levels by the presence of nuclear CHOP in exposed cells (Figure 6(d,e)). CHOP protein is expressed in ER stressed cells and reveals a restricted nuclear localization. CHOP induces a cell cycle stop in G1/S (Ron & Habener, 1992; Vittoria Barone et al., 1994).

#### Discussion

$\text{TiO}_2$  NPs are widely used, produced in diverse shapes, but it remains largely unknown how modification of the  $\text{TiO}_2$  NPs morphology (size, geometry...) may alter their bioavailability, their effects on biological systems and the resultant *in vitro* and *in vivo* toxicity. In particular, the behavior of NPs inside living cells is still an enigma, and no metabolic responses induced by  $\text{TiO}_2$  NPs have been fully identified so far. To answer this question, we developed an interdisciplinary approach (combining biophysics, analytical chemistry, nanochemistry, cellular and molecular biology) to outline the cellular mechanisms that linked the bioaccumulation and the *in vitro* toxicity of diverse morphologies of  $\text{TiO}_2$  NPs.

We established a strong correlation between the rate of internalized titanium and (i) the intracellular calcium content and (ii) a specific metabolic pathway: ER stress.  $\text{TiO}_2$  NPs exhibit different toxicity levels strongly depending not only on their morphologies (size, shape) and their related behavior in biological media, but also on the considered cellular type.

According to our observations,  $\text{TiO}_2$  NPs impact on cell proliferation/viability not only depends on the dose and on the morphology of NPs but also on the cell type. Indeed, P25, INPs and TNs dramatically affected proliferation, whereas NNs were harmless in HUVEC cells. On the contrary, in HEK293T, proliferation assays indicated that P25, NNs, and INPs exhibited a moderate dose-dependent toxicity even after several days. To explain the toxicity disparity observed for the different NPs, different hypotheses can be made among which: (i) the aggregation states of the  $\text{TiO}_2$  NPs in the different media, (ii) a specific shape-induced chemistry.

1025 For example, TNs are far from being well-identified objects but  
1026 exhibit a structure made of parallel-corrugated ribbons of edge-  
1027 sharing  $\text{TiO}_6$  octahedra. This scrolled nanosheet structure results  
1028 in some local structural variations, such as changes of the Ti-O  
1029 bond lengths and bond angles in the octahedra, which are then  
1030 more distorted and more reactive. These scrolled nanosheets  
1031 exhibit as well a much larger surface area than the other well-  
1032 crystallized NPs increasing the exchanges with cell membranes  
1033 and the intracellular medium (Gao et al., 2009).

1034 A third hypothesis is that the toxicity is determined by the  
1035 effective content of titanium that each cell type is susceptible to  
1036 internalize and not directly correlated with the exposure concen-  
1037 tration. Indeed, the aggregation states of the  $\text{TiO}_2$  NPs changed in  
1038 the different culture media what could modify the deposition rate  
1039 of the NPs and the real delivered doses as illustrated further on  
1040 and previously discussed in the literature (Cohen et al., 2013,  
1041 2014; Deloid et al., 2014; Pal et al., 2016). One challenge in nano-  
1042 toxicology is to quantify the real dose of exposure within a cell.  
1043 Indeed, the use of mass concentration commonly used to assess  
1044 bulk material toxicity or either the exposure dose in toxicology  
1045 studies are not appropriate to nanotoxicology evaluation (Zhao  
1046 et al., 2013). Here, we assess the intracellular quantity of  $\text{TiO}_2$   
1047 nanoparticles at the single cell level using  $\mu$ -PIXE analysis.

1048 We have shown that the intracellular content of titanium is  
1049 heterogeneous from one cell to another and is dependent on  
1050 both the NPs morphologies, and the cell type. This result corrob-  
1051 orates a previous *in silico* study which showed that the internaliza-  
1052 tion rate of NPs can be modified by a 60-fold factor as a function  
1053 of the NPs shape (Nangia & Sureshkumar, 2012). Moreover, an *in*  
1054 *vivo* study confirmed this observation showing that different  
1055 shapes of silica NPs differentially altered physiological functions in  
1056 exposed rats (Li et al., 2015).

1057 Furthermore, we previously showed that P25 internalization in  
1058 keratinocytes induced an elevated and related accumulation of  
1059 intracellular calcium (Simon et al., 2011). Here, we confirmed and  
1060 generalized this observation to the other morphologies of  $\text{TiO}_2$   
1061 NPs and to two other primary cell types (HUVEC and HEK293).

1062 We also showed that a minimal intracellular content of tita-  
1063 nium is necessary and mandatory to induce a marked calcium  
1064 homeostasis alteration, which is also cell-type dependent. In addi-  
1065 tion, intracellular calcium homeostasis is constantly found corre-  
1066 lated to the intracellular titanium content (independently of the  
1067 extracellular calcium content). Even if this phenomenon has been  
1068 previously evidenced by different methods (Koeneman et al.,  
1069 2010; Simon et al., 2011), the subsequent consequences for the  
1070 cells remain to be clearly identified and correlated (or not) with  
1071 NPs-mediated toxicity. Potential explanations are as follows (i)  
1072  $\text{TiO}_2$  NPs are negatively charged in culture media (physiological  
1073 pH) and thus can fix calcium ions on their surface when entering  
1074 the cell, or (ii) that  $\text{TiO}_2$  entry in cells could induce biological path-  
1075 ways modifying the calcium influx.

1076 Calcium is known to be a key modulator of fundamental pro-  
1077 cesses involving mitochondria, the ER stress and the regulation of  
1078 major metabolic pathways such as proliferation, differentiation (for  
1079 example for keratinocytes), inflammation, necrosis/apoptosis.

1080 Previous studies reported ROS pathway as a key player in NPs  
1081 toxicity response (reviewed in Djurišić et al., 2015). In this study,  
1082 we observed a minor change in the ROS metabolism (as a sup-  
1083 posed result of a mitochondrial dysfunction) and suggested that  
1084  $\text{TiO}_2$  NPs toxicity was not primarily induced by this pathway.

1085 Previous data suggested that  $\text{TiO}_2$  NPs (P25) internalization was  
1086 linked to ER stress apparition in human bronchial epithelial cells  
1087 (16HBE14o-) and in HUVEC (Chen et al., 2014; Yu et al., 2015a;  
1088 Zhang et al., 2012). Our data show that the internalization of

titanium ( $\text{TiO}_2$  NPs), besides increasing the cell calcium content,  
1089 does also induce the expression of CHOP (ATF4 pathway) and acti-  
1090 vates (i) the ER stress in HUVEC cells and (ii) differentiation in ker-  
1091 atinocytes. In addition, ER stress and disruption of cellular calcium  
1092 homeostasis are strongly associated with mitochondrial dysfunc-  
1093 tion (Zhang et al., 2012). Here, we show that this mitochondrial  
1094 alteration is effective for a minimal content of  $\text{TiO}_2$  NPs defining  
1095 here the level of toxicity. Our results also bring out further infor-  
1096 mation on these processes because they provide a quantitative  
1097 analysis of these phenomena (including dose threshold), stressing  
1098 not only on the effective quantity of exogenous element internal-  
1099 ized in individual cells but also on the dose the cells have been  
1100 exposed to. These two parameters, ER stress and intracellular cal-  
1101 cium concentration, should be considered as cardinal and early  
1102 markers of the *in vitro* toxicity evaluation not only of  $\text{TiO}_2$  NPs,  
1103 but also of other metal oxide nanoparticles. These results (minimal  
1104 threshold to induce toxicity and the resulting cellular responses)  
1105 are summarized in Figure S5. As  $\text{TiO}_2$  NPs are able to cross natural  
1106 barriers such as the intestine and the blood-brain barrier, these  
1107 markers should also be taken in consideration to evaluate the  
1108 *in vivo* nanotoxicity of NPs (Brun et al., 2012; Setyawati et al.,  
1109 2013; Setyawati et al., 2015a; Yamashita et al., 2011).

1110 Ultimately, the present results indicate that the ATF4 pathway  
1111 (induction of CHOP expression) is activated in HUVEC cells con-  
1112 firming the strong link between the level of  $\text{TiO}_2$  NPs toxicity  
1113 (which is also shape dependent), the intracellular titanium and cal-  
1114 cium contents, the ER stress induction and mitochondrial altera-  
1115 tions. We show that these different parameters give rise to the  
1116 establishment of a level of toxicity based on the morphology in  
1117 between the different  $\text{TiO}_2$  NPs; the TNs presenting the highest  
1118 level of toxicity (the lowest proliferation rate for the smallest inter-  
1119 nalized rate).

## 1120 Conclusion

1121 We showed that  $\text{TiO}_2$  NPs are internalized at various degrees and  
1122 their toxicity depends (i) on titanium content and nanoparticle  
1123 shape, which impact on intracellular calcium homeostasis thereby  
1124 leading to endoplasmic reticulum stress for a given cell line and  
1125 (ii) on the considered cell type. Lastly, we showed that a minimal  
1126 intracellular content of titanium is mandatory to induce detectable  
1127 toxicity enlightening once more the crucial notion of internalized  
1128 dose threshold beside the well-recognized dose of exposure. Our  
1129 research highlights the understanding of the toxic effect induced  
1130 by  $\text{TiO}_2$  NPs according to their bioavailability and behavior in bi-  
1131 ological media. We also stress the central role played by the ER  
1132 stress and the intracellular calcium homeostasis as molecular sen-  
1133 sors of the NPs toxicity detection.

1134 The manuscript was written through contributions of all  
1135 authors. All authors have given approval to the final version of  
1136 the manuscript.

## 1137 Acknowledgements

1138 This research was undertaken on the high-resolution microbeam  
1139 line at the AIFIRA facility ("Applications Interdisciplinaires des  
1140 Faisceaux d'Ions en Région Aquitaine"). We also wish to thank the  
1141 technical staff members of the AIFIRA facility (Ph. Alfaut, S.  
1142 Sorieul), the Bordeaux Imaging Center (TEM facility, E. Gontier and  
1143 M. Petrel). The Région Aquitaine supported financially the AIFIRA  
1144 facility and the technical development of the microbeam line. The  
1145 authors acknowledge the Evonik (Degussa) Company (Düsseldorf,  
1146 Germany) for their generous gift (P25  $\text{TiO}_2$  NPs). This work has  
1147

- 1153 been partly supported by the European Community as an  
1154 Integrating Activity "Support of Public and Industrial Research Using  
1155 Ion Beam Technology" (SPIRIT) under the EC contract n° 227012  
1156 and as an "Integrating Activity Supporting Postgraduate Research  
1157 with Internships in Industry and Training Excellence" (SPRITE) under  
1158 EC contract no. 317169. The CNRS, the French National Research  
1159 Agency (ANR CES2010, n° CESA 009 01, TITANIUMS) and the  
1160 Région Aquitaine (TOX-NANO n° 20111201003/POPRA n°  
1161 14006636-034) support the research program and the funding of  
1162 QLT, GS, GM, MS.
- 1163
- 1164 **Disclosure statement**
- 1165 The authors report no conflicts of interest.
- 1166
- 1167
- 1168 **Funding**
- 1169 This work has been partly supported by the European Community  
1170 as an Integrating Activity "Support of Public and Industrial Research  
1171 Using Ion Beam Technology" (SPIRIT) under the EC contract n°  
1172 227012 and as an "Integrating Activity Supporting Postgraduate  
1173 Research with Internships in Industry and Training Excellence"  
1174 (SPRITE) under EC contract no. 317169. The CNRS, the French  
1175 National Research Agency (ANR CES2010, n° CESA 009 01,  
1176 TITANIUMS) and the Région Aquitaine (TOX-NANO n°  
1177 20111201003/POPRA n° 14006636-034) support the research  
1178 program and the funding of QLT, GS, GM, MS.
- 1179
- 1180 **References**
- 1181
- 1182 Bhattacharya K, Davoren M, Boertz J, Schins RP, Hoffmann E, Dopp  
1183 E. 2009. Titanium dioxide nanoparticles induce oxidative stress  
1184 and DNA-adduct formation but not DNA-breakage in human  
1185 lung cells. *Particle Fibre Toxicol* 6:17.
- 1186 Brun E, Carrière M, Mabondzo A. 2012. *In vitro* evidence of dysre-  
1187 gulation of blood-brain barrier function after acute and  
1188 repeated/long-term exposure to TiO<sub>2</sub> nanoparticles.  
1189 *Biomaterials* 33:886–96.
- 1190 Cai K, Hou Y, Hu Y, Zhao L, Luo Z, Shi Y, et al. 2011. Correlation of  
1191 the cytotoxicity of TiO<sub>2</sub> nanoparticles with different particle  
1192 sizes on a sub-200-nm scale. *Small* 7:3026–31.
- 1193 Chen R, Huo L, Shi X, Bai R, Zhang Z, Zhao Y, et al. 2014.  
1194 Endoplasmic reticulum stress induced by zinc oxide nanopar-  
1195 ticles is an earlier biomarker for nanotoxicological evaluation.  
1196 *ACS Nano* 8:2562–74.
- 1197 Chen X, Mao SS. 2007. Titanium dioxide nanomaterials: synthesis,  
1198 properties, modifications and applications. *Chemical Rev*  
1199 107:2891–959.
- 1200 Cohen J, Deloid G, Pyrgiotakis G, Demokritou P. 2013. Interactions  
1201 of engineered nanomaterials in physiological media and impli-  
1202 cations for *in vitro* dosimetry. *Nanotoxicology* 7:417–31.
- 1203 Cohen JM, Teeguarden JG, Demokritou P. 2014. An integrated  
1204 approach for the *in vitro* dosimetry of engineered nanomateri-  
1205 als. *Particle Fibre Toxicol* 11:1–12.
- 1206 Deloid G, Cohen JM, Darrah T, Derk R, Rojanasakul L, Pyrgiotakis  
1207 G, et al. 2014. Nanomaterials for *in vitro* dosimetry. *Nature*  
1208 *Commun* 5:1–10.
- 1209 Devan RS, Patil RA, Lin JH, Ma YR. 2012. One-dimensional metal-  
1210 oxide nanostructures: recent developments in synthesis, charac-  
1211 terization, and applications. *Adv Funct Mater* 22:3326–70.
- 1212 Devès G, Cohen-Bouhacina T, Ortega R. 2004. Scanning transmis-  
1213 sion ion microscopy mass measurements for quantitative trace  
1214 element analysis within biological samples and validation using  
1215 atomic force microscopy thickness measurements. *Spectrochimica Acta Part B* 59:1733–8.
- 1216 Djurišić AB, Leung YH, Ng AMC, Xu XY, Lee PKH, Degger N, Wu  
1217 RSS. 2015. Toxicity of metal oxide nanoparticles: Mechanisms,  
1218 characterization, and avoiding experimental artefacts. *Small*  
1219 11:26–44.
- 1220 Donaldson K, Stone V, Clouter A, Renwick L, MacNee W. 2001.  
1221 Ultrafine particles. *Occup Environ Med* 58:211.
- 1222 Federici G, Shaw BJ, Handy RD. 2007. Toxicity of titanium dioxide  
1223 nanoparticles to rainbow trout (*Oncorhynchus mykiss*): Gill  
1224 injury, oxidative stress, and other physiological effects. *Aquatic*  
1225 *Toxicol.* 84:415–30.
- 1226 Gao T, Fjellvåg H, Norby P. 2009. Crystal structures of titanate  
1227 nanotubes: a Raman scattering study. *Inorganic Chem*  
1228 48:1423–32.
- 1229 Geiser M, Rothen-Rutishauser B, Kapp-N, Schürch S, Kreyling W,  
1230 Schulz H, et al. 2005. Ultrafine particles cross cellular mem-  
1231 branes by nonphagocytic mechanisms in lungs and in cultured  
1232 cells. *Environ Health Perspect* 113:1555–60.
- 1233 Hamilton RF, Wu N, Porter D, Buford M, Wolfarth M, Holian A.  
1234 2009. Particle length-dependent titanium dioxide nanomaterials  
1235 toxicity and bioactivity. *Particle Fibre Toxicol* 6:35.
- 1236 Higa A, Taojui S, Lhomond S, Jensen D, Fernandez-Zapico ME,  
1237 Simpson JC, et al. 2014. Endoplasmic reticulum stress-activated  
1238 transcription factor ATF6 $\alpha$  requires the disulfide isomerase  
1239 PDI5 to modulate chemoresistance. *Mol Cell Biol* 34:1839–49.
- 1240 Jacobson J, Duchon MR. 2002. Mitochondrial oxidative stress and  
1241 cell death in astrocytes – requirement for stored Ca<sup>2+</sup> and sus-  
1242 tained opening of the permeability transition pore. *J Cell Sci*  
1243 115:1175–88.
- 1244 Jovanović B. 2015. Review of titanium dioxide nanoparticle photo-  
1245 toxicity: developing a phototoxicity ratio to correct the end-  
1246 point values of toxicity tests. *Environ Toxicol Chem* 34:1070–7.
- 1247 Kaegi R, Ulrich a, Sinnet B, Vonbank R, Wichser a, Zuleeg S, et al.  
1248 2008. Synthetic TiO<sub>2</sub> nanoparticle emission from exterior  
1249 facades into the aquatic environment. *Environ Pollut* 156:233–9.
- 1250 Kahru A, Dubourguier HC. 2010. From ecotoxicology to nanoeco-  
1251 toxicology. *Toxicology* 269:105–19.
- 1252 Kasuga T. 2006. Formation of titanium oxide nanotubes using  
1253 chemical treatments and their characteristic properties. *Thin*  
1254 *Solid Films* 496:141–5.
- 1255 Koeneman BA, Zhang Y, Westerhoff P, Chen Y, Crittenden JC,  
1256 Capco DG. 2010. Toxicity and cellular responses of intestinal  
1257 cells exposed to titanium dioxide. *Cell Biol Toxicol* 26:225–38.
- 1258 Lai JCK, Lai MB, Jandhyam S, Dukhande VV, Bhushan A, Daniels  
1259 CK, Leung SW. 2008. Exposure to titanium dioxide and other  
1260 metallic oxide nanoparticles induces cytotoxicity on human  
1261 neural cells and fibroblasts. *Int J Nanomed* 3:533–45.
- 1262 Lee J, Mahendra S, Alvarez PJJ. 2010. Nanomaterials in the con-  
1263 struction industry: a review of their applications and environ-  
1264 mental health and safety considerations. *ACS Nano* 4:3580–90.
- 1265 Lewinski N, Colvin V, Drezek R. 2008. Cytotoxicity of nanoparticles.  
1266 *Small* 4:26–49.
- 1267 Li L, Liu T, Fu C, Tan L, Meng X, Liu H. 2015. Biodistribution, excre-  
1268 tion, and toxicity of mesoporous silica nanoparticles after oral  
1269 administration depend on their shape. *Nanomed Nanotechnol*  
1270 *Biol Med* 11:1915–24.
- 1271 Li Q, Mahendra S, Lyon DY, Brunet L, Liga MV, Li D, Alvarez PJJ.  
1272 2008. Antimicrobial nanomaterials for water disinfection and  
1273 microbial control: potential applications and implications. *Water*  
1274 *Res* 42:4591–602.
- 1275 Liang YT, Vijayan BK, Lyandres O, Gray K. a, Hersam MC. 2012.  
1276 Effect of dimensionality on the photocatalytic behavior of  
1277 1278 1279 1280

- 1281 carbon-titania nanosheet composites: charge transfer at nano-  
1282 material interfaces. *J Phys Chem Lett* 3:1760–5.
- 1283 Long TC, Saleh N, Tilton RD, Lowry GV, Veronesi B. 2006. Titanium  
1284 Dioxide (P25) produces reactive oxygen species in immortalized  
1285 brain microglia (BV2): implications for nanoparticle. *Environ Sci  
1286 Q4 Technol* 7–13.
- 1287 Nangia S, Sureshkumar R. 2012. Effects of nanoparticle charge and  
1288 shape anisotropy on translocation through cell membranes.  
1289 *Langmuir* 28:1766.
- 1290 Nian JN, Teng H. 2006. Hydrothermal synthesis of single-crystalline  
1291 anatase TiO<sub>2</sub> nanorods with nanotubes as the precursor. *J Phys  
1292 Chem B* 110:4193–8.
- 1293 Oberdorster G, Ferin J, Lehnert BE. 1994. Correlation between partic-  
1294 le size, *in vivo* particle persistence, and lung injury. *Environ  
1295 Health Perspect* 102 (Suppl5):173–9.
- 1296 Oesch F, Landsiedel R. 2012. Genotoxicity investigations on nano-  
1297 materials. *Arch Toxicol* 86:985–94.
- 1298 Osano E, Kishi J, Takahashi Y. 2003. Phagocytosis of titanium partic-  
1299 les and necrosis in TNF-alpha-resistant mouse sarcoma L929  
1300 cells. *Toxicol In Vitro* 17:41–7.
- 1301 Pal AK, Bello D, Cohen J, Demokritou P, Program B. 2016.  
1302 Q5 Nanotoxicology 9:871–85.
- 1303 Rahman Q, Lohani M, Dopp E, Pemsel H, Jonas L, Weiss DG,  
1304 Schiffmann D. 2002. Evidence that ultrafine titanium dioxide  
1305 induces micronuclei and apoptosis in syrian hamster embryo  
1306 fibroblasts. *Environ Health Perspect* 110:797–800.
- 1307 Ron D, Habener JF. 1992. CHOP, a novel developmentally regu-  
1308 lated nuclear protein that dimerizes with the transcription factors  
1309 C/EBP and LAP and functions as a dominant negative  
1310 regulator of gene transcription. *Genes Dev* 6:439.
- 1311 Sadrieh N, Wokovich AM, Gopee NV, Zheng J, Haines D, Parmiter  
1312 D, et al. 2010. Lack of significant dermal penetration of titanium  
1313 dioxide from sunscreen formulations containing nano- and sub-  
1314 micron-size TiO<sub>2</sub> particles. *Toxicol Sci* 115:156–66.
- 1315 Sager TM, Kommineni C, Castranova V. 2008. Pulmonary response  
1316 to intratracheal instillation of ultrafine versus fine titanium diox-  
1317 ide: role of particle surface area. *Particle Fibre Toxicol* 5:17.
- 1318 Sayes CM, Wahi R, Kurian PA, Liu Y, West JL, Ausman KD, et al.  
1319 2006. Correlating nanoscale titania structure with toxicity: a  
1320 cytotoxicity and inflammatory response study with human der-  
1321 mal fibroblasts and human lung epithelial cells. *Toxicol Sci*  
1322 92:174–85.
- 1323 Schwartzberg KC, Gray KA. 2012. Nanostructured Titania: the  
1324 current and future promise of Titania nanotubes. *Catalysis Sci  
1325 Technol* 2:1617.
- 1326 Setyawati MI, Tay CY, Chia SL, Goh SL, Fang W, Neo MJ, et al.  
1327 2013. Titanium dioxide nanomaterials cause endothelial cell  
1328 leakiness by disrupting the homophilic interaction of VE-cad-  
1329 herin. *Nature Commun* 4:1673.
- 1330 Setyawati MI, Tay CY, Docter D, Stauber RH, Leong DT. 2015a.  
1331 Understanding and exploiting nanoparticles' intimacy with the  
1332 blood vessel and blood. *Chem Soc Rev* 44:8174–99.
- 1333 Setyawati MI, Tay CY, Leong DT. 2015b. Mechanistic investigation  
1334 of the biological effects of SiO<sub>2</sub>, TiO<sub>2</sub>, and ZnO nanoparticles  
1335 on intestinal cells. *Small* 11:3458–68.
- 1336 Simon M, Barberet P, Delville MH, Moretto P, Sezec H. 2011.  
1337 Titanium dioxide nanoparticles induced intracellular calcium  
1338 homeostasis modification in primary human keratinocytes.  
1339 Towards an *in vitro* explanation of titanium dioxide nanopar-  
1340 ticles toxicity. *Nanotoxicology* 5:125–39.
- 1341 Sugimoto T, Zhou X, Muramatsu A. 2003. Synthesis of uniform  
1342 anatase TiO<sub>2</sub> nanoparticles by gel – sol method 3. Formation  
1343 process and size control. *J Colloid Interface Sci* 259:43–52.
- 1344 Sun Q, Tan D, Ze Y, Sang X, Liu X, Gui S, et al. 2012. 1345  
1346 Pulmotoxicological effects caused by long-term titanium diox-  
1347 ide nanoparticles exposure in mice. *J Hazardous Mater*  
1348 235–236:47–53.
- 1349 Tang Y, Wang F, Jin C, Liang H, Zhong X, Yang Y. 2013. 1350  
1351 Mitochondrial injury induced by nanosized titanium dioxide in  
A549 cells and rats. *Environ Toxicol Pharmacol* 36:66–72.
- 1352 Tong T, Shereef A, Wu J, Thi C, Binh T, Kelly JJ, Gray KA. 2013. 1353  
1354 Effects of material morphology on the phototoxicity of nano-  
TiO<sub>2</sub> to bacteria. *Environ Sci Technol* 47:12486–95.
- 1355 Toyooka T, Amano T, Ibuki Y. 2012. Titanium dioxide partic-  
1356 les phosphorylate histone H2AX independent of ROS  
1357 production. *Mutat Res/Genet Toxicol Environ Mutagen*  
1358 742:84–91.
- 1359 Le Trequesser Q, Devès G, Saez G, Daudin L, Barberet P,  
1360 Michelet C, et al. 2014. Single cell *in-situ* detection and quanti-  
1361 fication of metal oxide nanoparticles using multimodal correla-  
1362 tive microscopy. *Anal Chem* 86: 7311–9.
- 1363 Vevers WF, Jha AN. 2008. Genotoxic and cytotoxic potential of  
1364 titanium dioxide (TiO<sub>2</sub>) nanoparticles on fish cells *in vitro*.  
1365 *Ecotoxicol* 17:410–20.
- 1366 Vittoria Barone M, Crozat A, Tabaei A, Philipson L, Ron D. 1994. 1367  
1368 CHOP (GADD153) and its oncogenic variant, TLS-CHOP, have  
opposing effects on the induction of G1/S arrest. *Genes Dev*  
8:453–64.
- 1369 Wang JJ, Sanderson BJS, Wang H. 2007. Cyto- and genotoxicity of  
1370 ultrafine TiO<sub>2</sub> particles in cultured human lymphoblastoid cells.  
1371 *Mutat Res. Genet Toxicol Environ Mutagen* 628:99–106.
- 1372 Wang Y, Chen Z, Ba T, Pu J, Chen T, Song Y, et al. 2013. 1373  
1374 Susceptibility of young and adult rats to the oral toxicity of  
titanium dioxide nanoparticles. *Small* 9:1742–52.
- 1375 Warheit DB, Webb TR, Reed KL, Frerichs S, Sayes CM. 2007. 1376  
1377 Pulmonary toxicity study in rats with three forms of ultrafine-  
TiO<sub>2</sub> particles: Differential responses related to surface proper-  
1378 ties. *Toxicology* 230:90–104.
- 1379 Xia T, Kovochich M, Brant J, Hotze M, Sempf J, Oberley T, et al. 1380  
1381 2006. Comparison of the abilities of ambient and manufactured  
nanoparticles to induce cellular toxicity according to an oxida-  
1382 tive stress paradigm. *Nano Lett* 6:1794–807.
- 1383 Xia Y, Yang P, Sun Y, Wu Y, Mayers B, Gates B, et al. 2003. 1384  
1385 One-dimensional nanostructures: synthesis, characterization, and  
applications. *Adv Mater* 15:353–89.
- 1386 Yamashita K, Yoshioka Y, Higashisaka K, Mimura K, Morishita Y,  
1387 Nozaki M, et al. 2011. Silica and titanium dioxide nanoparticles  
1388 cause pregnancy complications in mice. *Nat Nanotechnol*  
1389 6:321–8.
- 1390 Yin ZF, Wu L, Yang HG, Su YH. 2013. Recent progress in biomed-  
1391 ical applications of titanium dioxide. *Phys Chem Chem Phys*  
1392 15:4844–58.
- 1393 Yu J, Jaroniec M, Yu H, Fan W. 2012. Synthesis, characterization,  
1394 properties, and applications of nanosized photocatalytic materi-  
1395 als. *J Nanomater* 2012:2–5.
- 1396 Yu K, Chang S, Park SJ, Lim J, Lee J. 2015a. Titanium dioxide nano-  
1397 particles induce endoplasmic reticulum stress-mediated auto-  
1398 phagic cell death via mitochondria- associated endoplasmic  
1399 reticulum membrane disruption in normal lung cells. *PLoS One*  
1400 1–17.
- 1401 Yu Z, Sun Q, Pan W, Li N, Tang B. 2015b. A near-infrared triggered 1402  
1403 nanophotosensitizer inducing domino effect on mitochondrial  
1404 reactive oxygen species burst for cancer therapy. *ACS Nano*  
1405 9:11064–74.
- 1406 Zhang R, Piao MJ, Kim KC, Kim AD, Choi JY, Choi J, Hyun JW. 1407  
1408 2012. Endoplasmic reticulum stress signaling is involved in



12 M. SIMON ET AL.

1409	silver nanoparticles-induced apoptosis. <i>Int J Biochem Cell Biol</i>	Zhuang M, Zheng Y, Liu Z, Huang W, Hu X. 2015. Shape-dependent performance of TiO <sub>2</sub> nanocrystals as adsorbents for methyl orange removal. <i>RSC Adv</i> 5:13200–7.	1473
1410	44:224–32.		1474
1411	Zhao Y, Nel A, Riehemann K. 2013. Filling knowledge gaps that distinguish the safety profiles of nano versus bulk materials. <i>Small</i> 9:1426–7.	Zoroddu MA, Medici S, Ledda A, Nurchi VM, Lachowicz JI, Peana M. 2014. Toxicity of nanoparticles. <i>Curr Med Chem</i> 21:3837–53.	1475
1412			1476
1413			1477
1414			1478
1415			1479
1416			1480
1417			1481
1418			1482
1419			1483
1420			1484
1421			1485
1422			1486
1423			1487
1424			1488
1425			1489
1426			1490
1427			1491
1428			1492
1429			1493
1430			1494
1431			1495
1432			1496
1433			1497
1434			1498
1435			1499
1436			1500
1437			1501
1438			1502
1439			1503
1440			1504
1441			1505
1442			1506
1443			1507
1444			1508
1445			1509
1446			1510
1447			1511
1448			1512
1449			1513
1450			1514
1451			1515
1452			1516
1453			1517
1454			1518
1455			1519
1456			1520
1457			1521
1458			1522
1459			1523
1460			1524
1461			1525
1462			1526
1463			1527
1464			1528
1465			1529
1466			1530
1467			1531
1468			1532
1469			1533
1470			1534
1471			1535
1472			1536

*Supplementary Material*

<b>Exposure type</b>	<b>Ca content (mg.g<sup>-1</sup>)</b>	<b>Ti content (µg.cm<sup>-2</sup>)</b>
<i>Control</i>	0.08 +/- 0.03	0.006 +/- 0.002
<b>P25</b>	0.09 +/- 0.02	1.67 +/- 1.03
<b>INPs</b>	0.08 +/- 0.03	1.64 +/- 0.74
<b>NNs</b>	0.09 +/- 0.02	0.57 +/- 0.22
<b>TNs</b>	0.091 +/- 0.05	0.50 +/- 0.5

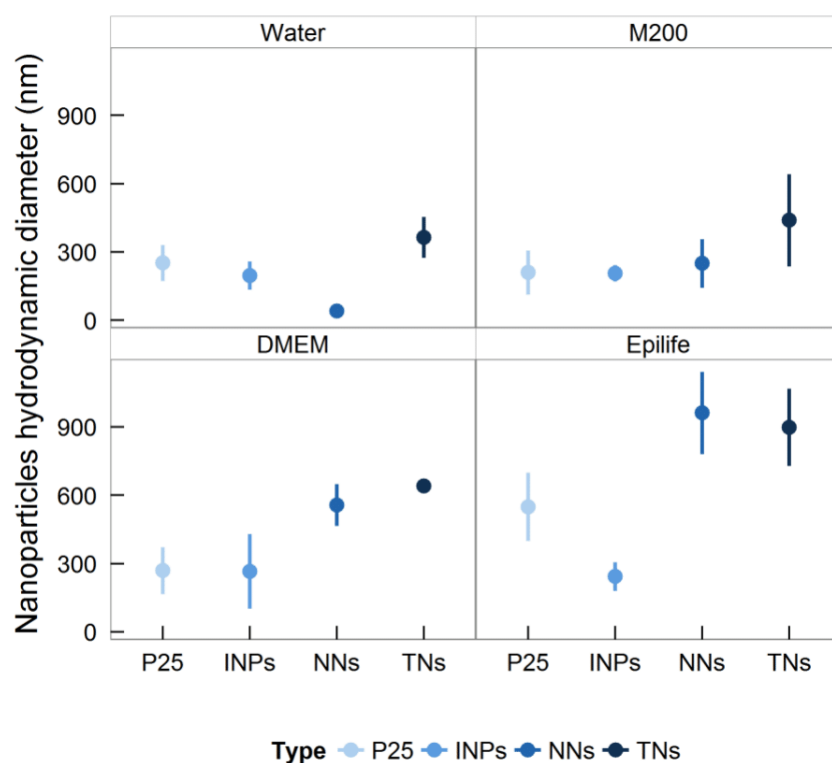
**Table S1:** Single cell intracellular calcium and titanium concentrations (in mg.g<sup>-1</sup> and µg.cm<sup>-2</sup>, respectively) measured by µ-PIXE in HUVEC cells exposed to 2 µg.cm<sup>-2</sup> of different TiO<sub>2</sub> NPs morphologies (P25, INPs, NNs and TNs). Results are expressed as median values +/- median absolute deviation.

	<b>Exposure type</b>	<b>Ca content (mg.g<sup>-1</sup>)</b>	<b>Ti content (µg.cm<sup>-2</sup>)</b>
0.06 mmol Calcium	<i>Control</i>	0.1 +/- 0.02	0.008 +/- 0.003
	<b>P25</b>	0.1 +/- 0.04	0.13 +/- 0.1
	<b>INPs</b>	0.14 +/- 0.07	0.2 +/- 0.17
	<b>NNs</b>	0.17 +/- 0.06	0.46 +/- 0.5
	<b>TNs</b>	0.14 +/- 0.05	0.045 +/- 0.05
1.2 mmol Calcium	<i>Control</i>	0.09 +/- 0.03	0.003 +/- 0.001
	<b>P25</b>	0.09 +/- 0.02	0.033 +/- 0.05
	<b>INPs</b>	0.08 +/- 0.02	0.035 +/- 0.05
	<b>NNs</b>	0.1 +/- 0.03	0.012 +/- 0.01
	<b>TNs</b>	0.1 +/- 0.04	0.003 +/- 0.002

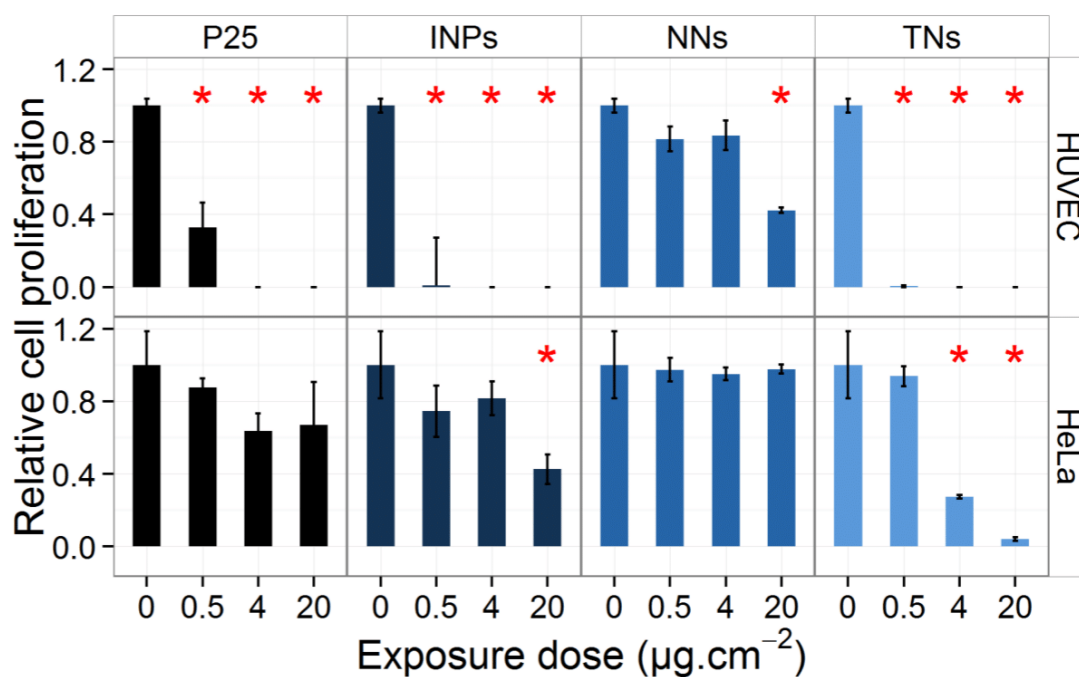
**Table S2:** Single cell intracellular calcium and titanium concentrations (in mg.g<sup>-1</sup> and µg.cm<sup>-2</sup>, respectively) measured by µ-PIXE in HEK293 cells exposed to 2 µg.cm<sup>-2</sup> of different TiO<sub>2</sub> NPs morphologies (P25, INPs, NNs and TNs) in low- and high-calcium concentration culture media. Results are expressed as median values +/- median absolute deviation.

Table S3- RTqPCR Primers list.

Gene	GenBank	Forward primer	Reverse Primer
<i>hBIP</i>	NM_005347.4	5'- GCTTATGGCCTGGATAA GAGG-3'	5'- CCACAACCTCGAAGAC ACCAT-3'
<i>hDDIT3/chop</i>	NM_00119505 3.1	5'- ACCAAGGGAGAACCAGG AAACG-3'	5'- TCACCATTCGGTCAATC AGAGC-3'
<i>hHERPUDI</i>	NM_014685.3	5'- TCCTCCTCCTGACGTTGT AAA-3'	5'- TGCTCGCCATCTAGTAC ATCC-3'
<i>hErdj4</i>	NM_012328.2	5'- CTTCGTTGAGTGACAGT CCTGC-3'	5'- TGGTGGTTCCAGTAGA CAAAGG-3'
<i>hGAPDH</i>	NM_00128974 6.1	5'- AAGGTGAAGGTCGGAGT CAA-3'	5'- CATGGGTGGAATCATA TTGG-3'
<i>h SOD1</i>	NM_000454.4	5'- AAAGATGGTGTGGCCGA TGT-3'	5'- CAAGCCAAACGACTTC CAGC-3'
<i>hSOD2 (isof. 1- 2)</i>	NM_000636.2	5'- GGCCTACGTGAACAACC TGA-3'	5'- GTTCTCCACCACCGTTA GGG-3'
<i>hCAT</i>	NM_001752.3	5'- AGTGATCGGGGATTCC AGA-3'	5'- AAGTCTCGCCGCATCTT CAA-3'
<i>hGPX1 (isof. 1)</i>	NM_000581.2	5'- TATCGAGAATGTGGCGT CCC-3'	5'- TCTTGGCGTTCTCCTGA TGC-3'
<i>hGPX1 (isof. 2)</i>	NM_201397.1	5'- AACCAGTTTGGGCATCA GGT-3'	5'- CCAAGGGCGGAGAGGA ATTT-3'
<i>hI8S</i>	NR_046235.1	5'- GGCCGTTCTTAGTTGGTG GA-3'	5'- CCCGGACATCTAAGGG CATC-3'



**Figure S1.** TiO<sub>2</sub> NPs behavior in biological media such as water, M200-PRF<sup>®</sup>, DMEM and Epilife<sup>®</sup>. The hydrodynamic diameter is expressed in nm and is shown to be medium-dependent. Water is used as synthesis medium and for stock solution composition. M200-PRF<sup>®</sup>, DMEM and Epilife<sup>®</sup> are sterile and defined culture media provided by the manufacturer and correspond to the culture media used for HUVEC, HeLa, and HEK293T cell lines, respectively.



**Figure S2.** Dose-dependent effect TiO<sub>2</sub> NPs morphologies (P25, INPs, NNs, TNs) on human cell culture proliferation. Relative cell proliferation of human endothelial cells (HUVEC, top) and immortalized and cancerous cell line (HeLa, down). Measurements performed 8 days after exposure. Exposure doses: 0.5, 4 and 20  $\mu\text{g}\cdot\text{cm}^{-2}$ . Data expressed as mean $\pm$  SD of at least three independent experiments normalized to untreated controls, \*  $P < 0.01$  compared to the control (*i.e.*, non-exposed cell populations).

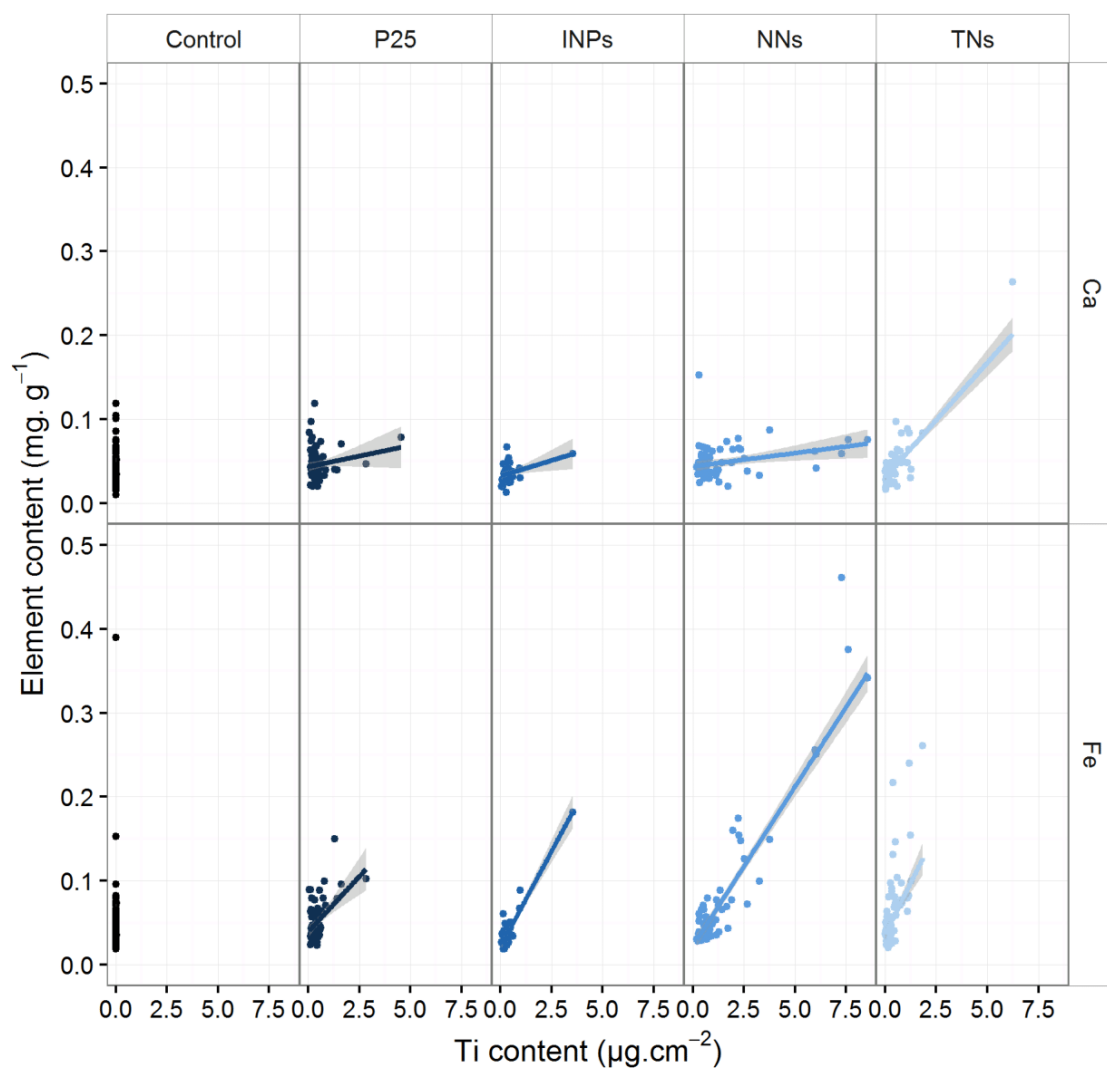


**Figure S3.** Relation between intracellular titanium content and intracellular chemical elements (iron and calcium). Single cell intracellular titanium ( $\mu\text{g}\cdot\text{cm}^{-2}$ ), calcium and iron contents ( $\text{mg}\cdot\text{g}^{-1}$ ) measured by  $\mu$ -PIXE in human primary cell line (HEK293) exposed to  $2 \mu\text{g}\cdot\text{cm}^{-2}$  of different  $\text{TiO}_2$  NPs morphologies (P25, INPs, NNs and TNs). The single cell quantitative analysis revealed a positive correlation between the intracellular titanium and intracellular calcium (top) and iron (down) contents. The heterogeneity of the titanium intracellular content per cell is also well depicted.

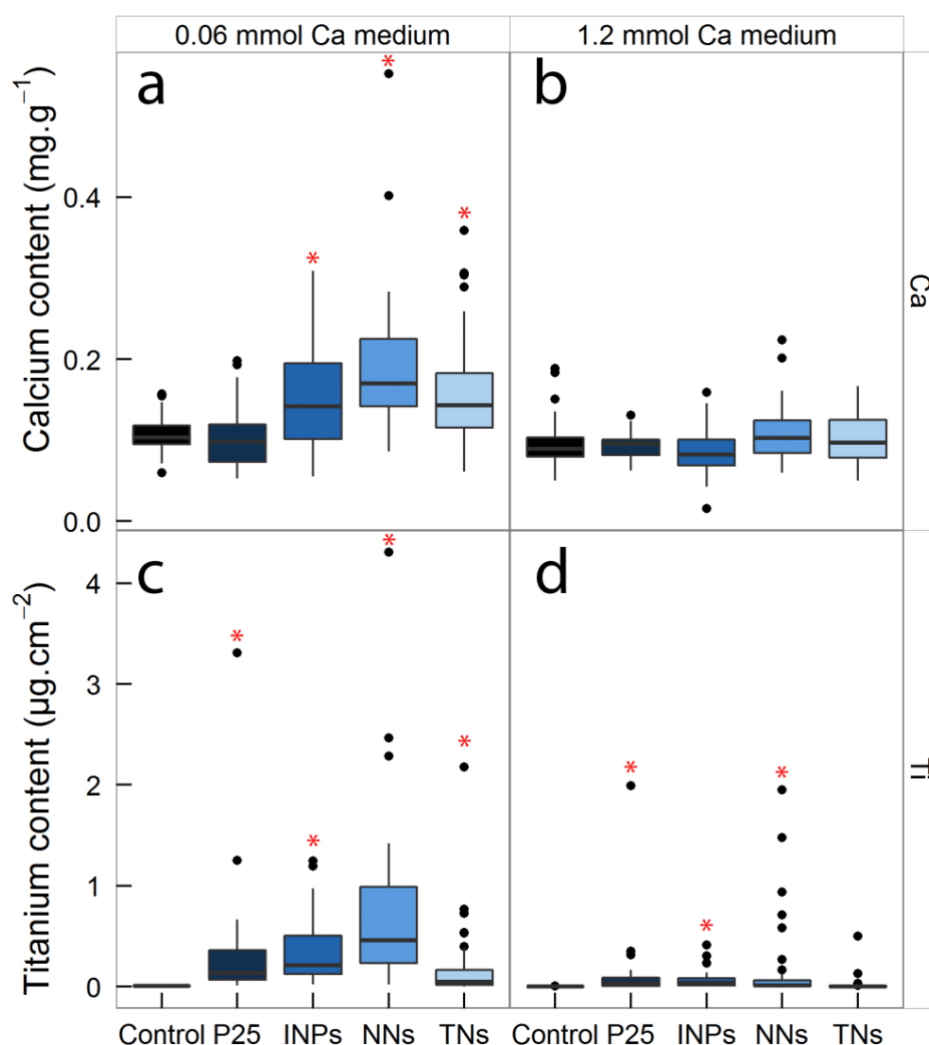


**Figure S4.** Effect of the extracellular calcium concentration on the intracellular TiO<sub>2</sub> NPs content in primary human keratinocytes (HEK293). Single cell quantitative analysis of the intracellular titanium and calcium concentrations (% dry mass per cell) were measured by  $\mu$ -PIXE in cells exposed to 2  $\mu\text{g}\cdot\text{cm}^{-2}$  of different TiO<sub>2</sub> NPs morphologies (P25, INPs, NNs and TNs) in low- and high-calcium concentration culture medium (0.06 and 1.2 mM, respectively) a, c). Intracellular calcium and titanium contents in low-calcium condition. b, d) Intracellular calcium and titanium contents in high-calcium conditions. Asterisks over distributions indicate significant differences with untreated groups (Kruskal-Wallis test ( $p < 0.05$ ) and post hoc Nemenyi test ( $p < 0.05$ ))

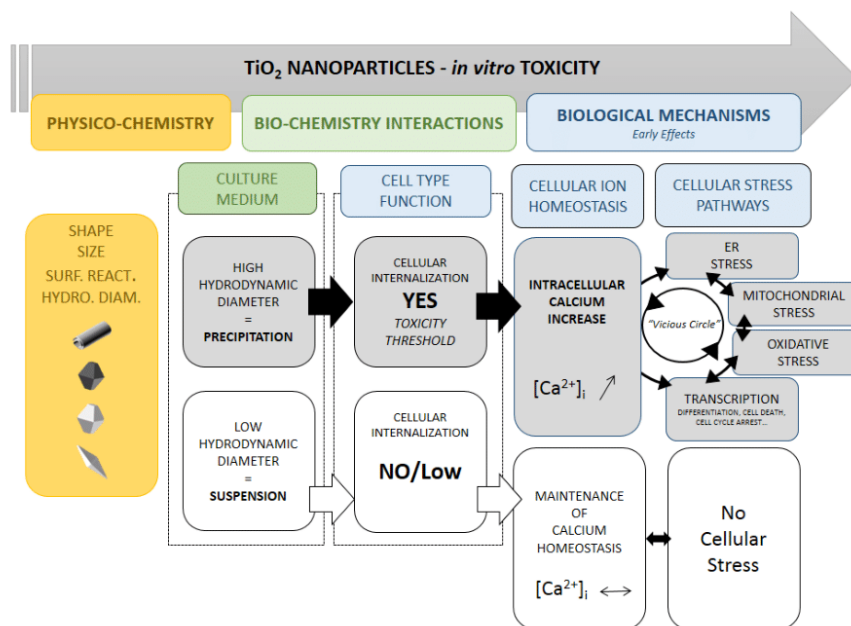


**Figure S5.** Schematic representation of the proposed methodology to evaluate TiO<sub>2</sub> NPs toxicity.



## Bibliography

1. Krug, H. F. & Wick, P. Nanotoxicology: An Interdisciplinary Challenge. *Angew. Chemie Int. Ed.* **50**, 1260–1278 (2011).
2. Prasad, P. N. Introduction to Nanomedicine and Nanobioengineering. *Wiley-Interscience Hoboken, NJ* (2012).
3. Chen, G., Roy, I., Yang, C. & Prasad, P. N. Nanochemistry and Nanomedicine for Nanoparticle-based Diagnostics and Therapy. *Chem. Rev.* **116**, 2826–2885 (2016).
4. Chen, G., Qiu, H., Prasad, P. N. & Chen, X. Upconversion nanoparticles: Design, nanochemistry, and applications in Theranostics. *Chem. Rev.* **114**, 5161–5214 (2014).
5. Doane, T. L. & Burda, C. The unique role of nanoparticles in nanomedicine: imaging, drug delivery and therapy. *Chem. Soc. Rev.* **41**, 2885–911 (2012).
6. Sinha, R. Nanotechnology in cancer therapeutics: bioconjugated nanoparticles for drug delivery. *Mol. Cancer Ther.* **5**, 1909–1917 (2006).
7. Kobayashi, K., Usami, N., Porcel, E., Lacombe, S. & Le Sech, C. Enhancement of radiation effect by heavy elements. *Mutat. Res.* **704**, 123–31 (2010).
8. Chang, M. Y. *et al.* Increased apoptotic potential and dose-enhancing effect of gold nanoparticles in combination with single-dose clinical electron beams on tumor-bearing mice. *Cancer Sci.* **99**, 1479–1484 (2008).
9. Wolfe, T., Guidelli, E. J., Gómez, J. a, Baffa, O. & Nicolucci, P. Experimental assessment of gold nanoparticle-mediated dose enhancement in radiation therapy beams using electron spin resonance dosimetry. *Phys. Med. Biol.* **60**, 4465–4480 (2015).
10. Zhang, S. X. *et al.* Quantifying tumor-selective radiation dose enhancements using gold nanoparticles: A monte carlo simulation study. *Biomed. Microdevices* **11**, 925–933 (2009).
11. Matsudaira, H., Ueno, A. M. & Furuno, I. Iodine Contrast Medium Sensitizes Cultured Mammalian Cells to X Rays but Not to  $\gamma$  Rays. *Radiat. Res.* **84**, 144 (1980).
12. Nath, R., Bongiorno, P., Rossi, P. I. & Rockwell, S. Enhanced IUdR radiosensitization by  $^{241}\text{Am}$  photons relative to  $^{226}\text{Ra}$  and  $^{125}\text{I}$  photons at 0.72 Gy/hr. *Int. J. Radiat. Oncol.* **18**, 1377–1385 (1990).
13. Wolfe, T. *et al.* Targeted gold nanoparticles enhance sensitization of prostate tumors to megavoltage radiation therapy in vivo. *Nanomedicine Nanotechnology, Biol. Med.* **11**, 1277–1283 (2015).
14. Yasui, H., Takeuchi, R., Nagane, M., Meike, S. & Nakamura, Y. Radiosensitization of tumor cells through endoplasmic reticulum stress induced by PEGylated nanogel containing gold nanoparticles. **347**, 151–158 (2014).
15. Chen, M.-H. *et al.* Hafnium-doped hydroxyapatite nanoparticles with ionizing radiation for lung cancer treatment. *Acta Biomater.* **37**, 2–10 (2016).
16. Marill, J. *et al.* Hafnium oxide nanoparticles : toward an in vitro predictive biological effect ? **9**, 1–11 (2014).
17. Mirjolet, C. *et al.* The radiosensitization effect of titanate nanotubes as a new tool in radiation therapy for glioblastoma : A proof-of-concept q. *Radiother. Oncol.* **108**, 136–142 (2013).
18. Usami, N., Kobayashi, K., Furusawa, Y. & Le Sech, C. in *Nanobiomaterials in Cancer Therapy* 471–503 (Elsevier, 2016). doi:10.1016/B978-0-323-42863-7.00014-1
19. McMahon, S. J. *et al.* Biological consequences of nanoscale energy deposition near irradiated heavy atom nanoparticles. *Sci. Rep.* **1**, 18 (2011).
20. Yasui, H. *et al.* Radiosensitization of tumor cells through endoplasmic reticulum stress induced by PEGylated nanogel containing gold nanoparticles. *Cancer Lett.* **347**, 151–158 (2014).
21. Usami, N. *et al.* Mammalian cells loaded with platinum-containing molecules are sensitized to

- fast atomic ions. *Int. J. Radiat. Biol.* **84**, 603–11 (2008).
22. Le Trequesser, Q. *et al.* Single cell in situ detection and quantification of metal oxide nanoparticles using multimodal correlative microscopy. *Anal Chem* **86**, 7311–7319 (2014).
  23. Simon, M., Barberet, P., Delville, M.-H., Moretto, P. & Seznec, H. Titanium dioxide nanoparticles induced intracellular calcium homeostasis modification in primary human keratinocytes. Towards an in vitro explanation of titanium dioxide nanoparticles toxicity. *Nanotoxicology* **5**, 125–139 (2011).
  24. Rivera Gil, P., Oberdörster, G., Elder, A., Puentes, V. & Parak, W. J. Correlating physico-chemical with toxicological properties of nanoparticles: The present and the future. *ACS Nano* **4**, 5227–5231 (2010).
  25. Buettner, K. M. & Valentine, A. M. Bioinorganic Chemistry of Titanium. *Chem. Rev.* **112**, 1863–1881 (2012).
  26. Chen, X. & Mao, S. S. Titanium dioxide nanomaterials: Synthesis, properties, modifications and applications. *Chem. Rev.* **107**, 2891–2959 (2007).
  27. Schwartzberg, K. C. & Gray, K. A. Nanostructured Titania: the current and future promise of Titania nanotubes. *Catal. Sci. Technol.* **2**, 1617 (2012).
  28. Xia, Y. *et al.* One-Dimensional Nanostructures: Synthesis, Characterization, and Applications. *Adv. Mater.* **15**, 353–389 (2003).
  29. Devan, R. S., Patil, R. A., Lin, J. H. & Ma, Y. R. One-dimensional metal-oxide nanostructures: Recent developments in synthesis, characterization, and applications. *Adv. Funct. Mater.* **22**, 3326–3370 (2012).
  30. Shi, H. *et al.* Titanium dioxide nanoparticles: a review of current toxicological data. *Part. Fibre Toxicol.* **10**, 15 (2013).
  31. Hong, F. TiO<sub>2</sub> nanoparticles induced hippocampal neuroinflammation in mice. *PLoS One* **9**, e92230 (2014).
  32. Hu, R. *et al.* Neurotoxicological effects and the impairment of spatial recognition memory in mice caused by exposure to TiO<sub>2</sub> nanoparticles. *Biomaterials* **31**, 8043–8050 (2010).
  33. Trouiller, B., Reliene, R., Westbrook, A., Solaimani, P. & Schiestl, R. H. Titanium dioxide nanoparticles induce DNA damage and genetic instability in vivo in mice. *Cancer Res.* **69**, 8784–8789 (2009).
  34. Hamzeh, M. & Sunahara, G. I. In vitro cytotoxicity and genotoxicity studies of titanium dioxide (TiO<sub>2</sub>) nanoparticles in Chinese hamster lung fibroblast cells. *Toxicol. Vitro.* **27**, 864–873 (2013).
  35. Aruoja, V., Dubourguier, H. C., Kasemets, K. & Kahru, A. Toxicity of nanoparticles of CuO, ZnO and TiO<sub>2</sub> to microalgae *Pseudokirchneriella subcapitata*. *Sci. Total Environ.* **407**, 1461–1468 (2009).
  36. Kasemets, K., Ivask, A., Dubourguier, H. C. & Kahru, A. Toxicity of nanoparticles of ZnO, CuO and TiO<sub>2</sub> to yeast *Saccharomyces cerevisiae*. *Toxicol. Vitro.* **23**, 1116–1122 (2009).
  37. Fisichella, M. *et al.* Intestinal toxicity evaluation of TiO<sub>2</sub> degraded surface-treated nanoparticles: a combined physico-chemical and toxicogenomics approach in caco-2 cells. *Part. Fibre Toxicol.* **9**, 18 (2012).
  38. Menard, A., Drobne, D. & Jemec, A. Ecotoxicity of nanosized TiO<sub>2</sub>. Review of in vivo data. *Environ. Pollut.* **159**, 677–684 (2011).
  39. Fujita, K. *et al.* Effects of ultrafine TiO<sub>2</sub> particles on gene expression profile in human keratinocytes without illumination: Involvement of extracellular matrix and cell adhesion. *Toxicol. Lett.* **191**, 109–117 (2009).
  40. Raturi, A. & Simmen, T. Where the endoplasmic reticulum and the mitochondrion tie the knot: The mitochondria-associated membrane (MAM). *Biochim. Biophys. Acta - Mol. Cell Res.* **1833**, 213–224 (2013).
  41. Malhotra, J. D. & Kaufman, R. J. The Endoplasmic Reticulum and the Unfolded Protein Response. *Semin Cell Dev Biol* **18**, 716–731 (2009).

42. Schroder, M. & Kaufman, R. J. ER stress and the unfolded protein response. *Mutat Res* **569**, 29–63 (2005).
43. Yu, K. N. *et al.* Titanium dioxide nanoparticles induce endoplasmic reticulum stress-mediated autophagic cell death via mitochondria-associated endoplasmic reticulum membrane disruption in normal lung cells. *PLoS One* **10**, 1–17 (2015).
44. Ju-Nam, Y. & Lead, J. R. Manufactured nanoparticles: An overview of their chemistry, interactions and potential environmental implications. *Sci. Total Environ.* **400**, 396–414 (2008).
45. Wu, Q. *et al.* Small sizes of TiO<sub>2</sub>-NPs exhibit adverse effects at predicted environmental relevant concentrations on nematodes in a modified chronic toxicity assay system. *J. Hazard. Mater.* **243**, 161–168 (2012).
46. Hamilton, R. F. *et al.* Particle length-dependent titanium dioxide nanomaterials toxicity and bioactivity. *Part. Fibre Toxicol.* **6**, 35 (2009).
47. Giuntini, L. A review of external microbeams for ion beam analyses. *Anal. Bioanal. Chem.* **401**, 785–793 (2011).

# **CONCLUSIONS AND PERSPECTIVES**



Since the discovery of X-Ray in 1895 by Rontgen, ionizing radiation (IR) has been employed as a powerful tool for imaging and radiotherapy. In the early days after the discovery of radiation, scientists were interested in understanding the physics of different types of IR as well as their applications. It did not take a long time to discover the hazards of radiation. Skin erythema due to high doses of radiation was among the first symptoms observed. Eventually it was noticed that radiation is a potential risk for cancer induction by observing the cancer incidence of exposure to radiations, among them Marie Curie and her daughter. IR is known as a double edged sword that could cause or be used to eradicate cancer. IR has been studied mainly by its effects, however all mechanisms of action are still not fully understood.

The European project SPRITE, in which I was recruited, aimed to exploit the ion beam techniques and their applications. All along my PhD, I utilized ion microbeam abilities to expand the fundamental knowledge of IR effects on biological systems (microbeam for micro-irradiation) and to exploit the interactions between IR and matter to obtain information on the chemical elements distribution in cells (microprobe for multi-elements chemical analysis). All together these techniques aimed to decipher IR-induced mechanisms at the single cell level or in cell population which would be exploited for improving cancer management or treatment.

In response to IR, cells activate DNA repair and cell signaling processes to protect their genetic pool either by repairing or by causing cell death in order to avoid adverse effects, such as mutation, chromosome aberration, and cancer. DNA repair plays the central role in the cell response to radiation. Intensive laboratory research is evolving in DNA repair and cell signaling process, however the link from DNA damage to mutation, cancer and cell death is not easily formed. The advances in understanding the mechanisms of DNA repair and cell signaling pathways and human genome research have opened up opportunities to develop new approaches. These approaches are aimed at linking induced DNA damage through cellular DNA repair processes with the dose of IR, the type of IR and with the potential adverse health consequences (cancer and hereditary effects) that may ensue. The first part of this work focused on the study of induced DNA damages, the repair processes and the responses activate after exposure to IR. We developed a system able to control the dose of different IR, in space and time, and deliver them on living cells. The AIFIRA microbeam, indeed, permits to correlate charged particles-induced responses and dose-response at the cellular level.

$\alpha$ -particles that are increasingly studied because constituting significant part of the radioactive natural background and increasingly considered in medical applications. Up to now, the knowledge about  $\alpha$ -particles effects on living cells is acquired by using radioactive sources with which we cannot

precisely control the number of traversals at the single cell scale and it is difficult to correlate the biological responses with the traversal. Microbeam can control the number and the position of delivered particles. However, two major issues needed to be solved due to the low energy of  $\alpha$ -particles: the  $\alpha$ -particles detection without stopping them and the observation of induced damages in real time. During my PhD, the collaboration with Michal Pomorski led to the development of a thin Boron-doped Nano-Crystalline Diamond membranes able to detect single  $\alpha$ -particles without modifying their trajectory and energy. In addition, the biological marker GFP-RNF8 protein permitted to visualize and follow the DNA damages induced by single  $\alpha$ -particles in real time. These technical developments allowed us, for the first time, to irradiate and visualize in real time the GFP-RNF8 protein that accumulates at DNA damage sites induced by one  $\alpha$ -particle. These results open a series of studies devoted to elucidate the effects of low doses in living.

Then, our facility was used to investigate repair processes activated after different types of damages induced by increasing numbers of charged particles with different LET. Increasing number (from 1 to 1000) of protons ( $\text{LET} = 12 \text{ keV} \cdot \mu\text{m}^{-1}$ ) or  $\alpha$ -particles ( $\text{LET} = 148 \text{ keV} \cdot \mu\text{m}^{-1}$ ) were delivered on living cells to create cluster of DNA damages with different complexities. The responses of GFP-RNF8 and GFP-XRCC1, involved in two DNA repair mechanisms, were followed after irradiations. The correlations between their recruitment time to damages and both deposited energies and particle structures were done. With this study, I showed that two proteins acting in two DNA repair mechanisms react in two different manners. In response to IR, GFP-RNF8 exhibits a kinetics significantly dependent on the spatial distribution of damages, while the kinetics of GFP-XRCC1 is mainly dependent on the deposited energy. These results indicate a coherence between the protein function and the biological response to IR and open new challenging questions for understanding how the repair machinery acts in response to different types of damages, particles and doses.

In addition during my PhD, I developed not only transfected cell lines to support the DNA irradiation but also stable transfected cell lines that allow the visualization and targeting of others sub-cellular compartments such as Matrix-roGFP2 and GFP-Nop52 to visualize mitochondria and nucleoli, respectively. We made these cell lines available to other research teams which triggers a collaboration with the Munich University. By establishing the cell line expressing Matrix-roGFP2 which is a sensor of mitochondrial matrix, I had the opportunity to participate in the PhD project of Dieter Walsh. The goals of Dieter's project are to target and irradiate mitochondria for evaluating their role in response to IR. Irradiations were performed at both facilities SNAKE (in Munich) and AIFIRA (in Bordeaux) with carbon ions and protons, respectively. Mitochondrial membrane

depolarization without disrupting membrane integrity was shown after charged particle irradiations. Despite the mechanisms of mitochondrial depolarization remain unclear and further studies are necessary to explain such behavior, we demonstrated that this depolarization was not due to the membrane rupture ensured by the constant presence of Matrix-roGFP2 in the mitochondrial matrix.

Recently, the microbeam line end-station has been implemented with a 488 nm laser able to bleach the GFP which allowed us to perform Fluorescence Recovery after Photobleaching experiments. I was involved in the calibration and validation of this new system that was achieved partly thanks to the development of stable GFP-H2B and GFP-Nop52 cell lines. Now this system can be combined with micro-irradiation experiments to measure the exchange and binding behavior of repair proteins recruited at the DNA damaged sites.

The repair processes activated after IR-induced damages if not well-completed could lead to cellular modifications and then trigger mechanisms for cancer genesis and/or radiation resistance. In collaboration with the Institut Bergonié, I studied the responses of sarcoma cell lines exposed to particles and doses commonly used in medical conditions and particles produced by a fundamental research accelerator. Two patients-derived sarcoma cell lines were selected for their genetic characteristics and were irradiated with 9 MeV electrons and 3 MeV protons. Additionally, protons were delivered by following two energy depositions at the cellular scale: homogeneous *versus* focused beams. Protocols to elucidate the radiation resistance after irradiation were developed and validated. In particular, automated *ImageJ* routines for DNA damage quantification and colonies counting were improved. Three biological end-points (radiation-induced foci, surviving fraction and proliferation) allowed us to show that (i) the biological responses are related to the genetic characteristics, (ii) the protons have more pronounced effects than electrons, and (iii) no differences are noticed between two energy distributions.

Implementation of protocols to assess radiation sensitivity or resistance in patient cell lines drives to study the characterization of biological effects induced by IR in the presence of metal nanoparticles. The use of nanoparticles is an emerging field in radiation therapy with the objective to improve the deposit of IR in the tumor sparing the healthy tissues. As nanoparticles are relatively new technologies, it is necessary to elucidate the effects that nanoparticles could induce in biological systems. It is worth to know the cellular localization and concentration after exposure to define the effects of these agents. To this purpose, protocols to localize, quantify and study the effects of nanoparticles in cells were improved. Nuclear microprobe analysis are exemplary techniques allowing the investigation of nanoparticles bioaccumulation and consequent effects. By participating



in the project of Marina Simon, I could observe the effects induced by different nanoparticle shapes and sizes in different cell types. We showed that nanoparticles induced biological effects positively correlated to ion homeostasis balance disequilibrium (calcium) and to the induction of metabolic stress pathways (Endoplasmic Reticulum stress). These published data validated an original methodology (multimodal and correlative microscopies) that allows *in vitro* detection, tracking, and quantification of TiO<sub>2</sub> NPs in parallel to the use of biological indicators for ion homeostasis, cell metabolism and cell fate.

All these data, obtained thanks to the multidisciplinary expertise of the team I worked with, contributed to improve the knowledge about the interactions of IR and living. By combining DNA repair targeting and new radiation therapy approaches the radiation therapeutic benefits could be enhanced and uprising of radiation resistant cancers could be reduced. The deeper understanding of these mechanisms (IR or/and NPs induced effects) gives new insights to fundamental and therapeutic approaches.

***Numerous works are started and need to be continued at CENBG thanks to the wide versatility of the microbeam lines.***

Other biological markers are under development and investigation, such as GFP-Ku70 and GFP-Ku80 for elucidating NHEJ pathway, GFP-OGG1 for studying the ROS effects; beyond DNA, other substructures as nucleoli and cytoplasmic changes deserve attention and for these reasons stable transfected cell lines are under development such as GFP-FBL and GFP-PolyQ mutants. The use of these different constructs permits the characterization of different mechanisms induced by IR. The validation of the laser system permits now to move towards studies direct to combine microirradiation and FRAP experiments. These performances can elucidate, in addition to the kinetics, the dynamics of investigated proteins present at the damaged sites. In addition, PCR-based approaches constitute a suitable technique for DNA-damage quantification. LORD-Q PCR allows to accurate quantification of DNA damage in both nuclear DNA and mitochondrial DNA.

For a complete characterization of the radiation sensitivity or resistance of cancerous cells to examine in depth others biological markers such as the cellular death, the cell cycle arrest, changes of genomic profiles can improve the radiation therapy protocols and estimate genetic and carcinogenic risks to human populations exposed to IR. In addition, several stress pathways could be modified after IR exposure or nanoparticles exposure, such as the ER stress induced by certain nanoparticles. To characterize different stress pathways activated after IR and/or nanoparticles exposure, a collaboration with the platform BMYScreen has been established. This platform develops

approaches consisting in screening molecular stress pathways such as ER stress, inflammatory response and oxidative stress (Figure 16).

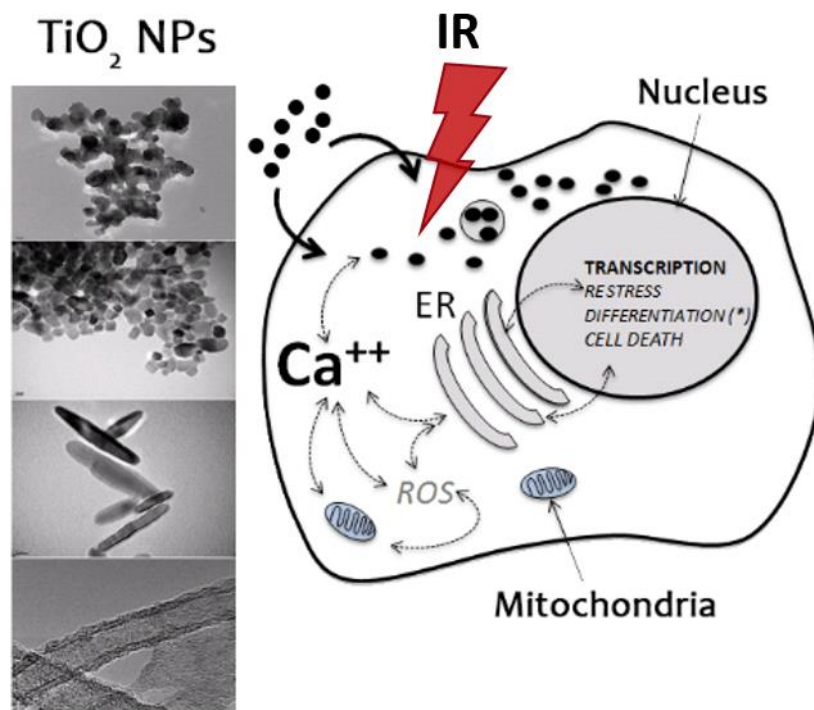


Figure 16. The influence of TiO<sub>2</sub> nanoparticles or/and IR can be investigated at the single cell level. The NPs internalization as well as IR alter the intracellular ion homeostasis, leading to endoplasmic reticulum stress and can activate other different stress pathways.

Elucidating the mechanisms of targeted and non-targeted effects calls for further researches; moving away from the conventional DNA target effect framework, future studies should concentrate on exploring more complex experimental system instead of single cells. The resulting data may need evaluation by an approach to study of cellular communication and 3-D tissue system. There is also a need for further development of more relevant *in vivo* models. There is a growing evidence for the role of epigenetic mechanisms in the transmission of genomic instability as well as in the formation of bystander effects-induced DNA breaks. The rapid development of high-throughput epigenetic screening technologies opens new avenues for the understanding of the interaction of genome and environment, including the effects of ionizing radiation. A key question for evaluation of low dose radiation induced cancer risk is the relative contribution of DNA-targeted and non-targeted effects at low and high doses



## **Etude des effets biologiques radio-induits et micro-irradiation par particules chargées. Des mécanismes moléculaires aux thérapies émergentes anti-cancéreuses**

Ces dernières années, le paradigme de la radiobiologie selon lequel les effets biologiques des rayonnements ionisants ne concernent strictement que les dommages à l'ADN et les conséquences liées à leur non réparation ou à leur réparation défectueuse, a été remis en question. Ainsi, plusieurs études suggèrent que des mécanismes «non centrés» sur l'ADN ont une importance significative dans les réponses radio-induites. Ces effets doivent donc être identifiés et caractérisés afin d'évaluer leurs contributions respectives dans des phénomènes telle que la radorésistance, les risques associés au développement de cancers radio-induits, les conséquences des expositions aux faibles doses. Pour ce faire, il est nécessaire : (i) d'analyser la contribution de ces différentes voies de signalisation et réparation induites en fonction de la dose et de la zone d'irradiation; (ii) d'étudier les réponses radio-induites suite à l'irradiation exclusive de compartiments subcellulaires spécifiques (exclure les dommages spécifiques à l'ADN nucléaire); (iii) d'améliorer la connaissance des mécanismes moléculaires impliqués dans les phénomènes de radiosensibilité/radorésistance dans la perspective d'optimiser les protocoles de radiothérapie et d'évaluer *in vitro* de nouvelles thérapies associant par exemple les effets des rayonnements ionisants et de nanoparticules d'oxydes métalliques.

Les microfaisceaux de particules chargées offrent des caractéristiques uniques pour répondre à ces questions en permettant (i) des irradiations sélectives et en dose contrôlée de populations cellulaires et donc l'étude *in vitro* des effets « ciblés » et « non ciblés » à l'échelle cellulaire et subcellulaire, (ii) de caractériser l'homéostasie de cultures cellulaires en réponses à des expositions aux rayonnements ionisants et/ou aux nanoparticules d'oxydes métalliques (micro-analyse chimique multi-élémentaire). Ainsi, au cours de ma thèse, j'ai validé et exploité des méthodes d'évaluation qualitatives et quantitatives (i) *in cellulo* et en temps réel de la réponse radio-induite de compartiments biologiques spécifiques (ADN, mitochondrie, ...); (ii) *in vitro* de la radiosensibilité de lignées sarcomateuses issues de patients; et (iii) *in vitro* des effets induits par des expositions à des nanoparticules d'oxydes métalliques afin d'évaluer leur potentiel thérapeutique et anti-cancéreux.

**Mots clés :** Micro-irradiation ciblé, Dommages ADN radio-induits, Irradiations bas/haut TEL, Radiosensibilité, Nanoparticules

---

## **Deciphering the biological effects of ionizing radiations using charged particle microbeam: from molecular mechanisms to perspectives in emerging cancer therapies**

Few years ago, the paradigm of radiation biology was that the biological effects of ionizing radiations occurred only if cell nuclei were hit, and that cell death/dysfunction was strictly due to unrepaired/misrepaired DNA. Now, next this “DNA-centric” view several results have shown the importance of “non-DNA centered” effects. Both non-targeted effects and DNA-targeted effects induced by ionizing radiations need to be clarified for the evaluation of the associated radiation resistance phenomena and cancer risks. A complete overview on radiation induced effects requires the study of several points: (i) analyzing the contribution of different signaling and repair pathways activated in response to radiation-induced injuries; (ii) elucidating non-targeted effects to explain cellular mechanisms induced in cellular compartments different from DNA; and (iii) improving the knowledge of sensitivity/resistance molecular mechanisms to adapt, improve and optimize the radiation treatment protocols combining ionizing radiations and nanoparticles.

Charged particle microbeams provide unique features to answer these challenge questions by (i) studying *in vitro* both targeted and non-targeted radiation responses at the cellular scale, (ii) performing dose-controlled irradiations on a cellular populations and (iii) quantifying the chemical element distribution in single cells after exposure to ionizing radiations or nanoparticles.

By using this tool, I had the opportunity to (i) use an original micro-irradiation setup based on charged particles microbeam (AIFIRA) with which the delivered particles are controlled in time, amount and space to validate *in vitro* methodological approaches for assessing the radiation sensitivity of different biological compartments (DNA and cytoplasm); (ii) assess the radiation sensitivity of a collection of cancerous cell lines derived from patients in the context of radiation therapy; (iii) study metal oxide nanoparticles effects in cells in order to understand the potential of nanoparticles in emerging cancer therapeutic approaches.

**Keywords:** Targeted irradiation, DNA damage, low/high LET irradiations, Radiation sensitivity, Nanoparticles